

UNIVERSITÉ SORBONNE PARIS NORD

École doctorale Galilée
Laboratoire des Sciences des Procédés et des Matériaux

Mechanics of Displacive Instabilities in Solids

Par OĞUZ UMUT SALMAN

Habilitation à Diriger des Recherches

Devant un jury composé de:

MAURINE MONTAGNAT, DIRECTRICE DE RECHERCHE	CNRS	Rapporteuse
MUHITTIN MUNGAN, PROFESSEUR	University of Cologne	Rapporteur
AURÉLIEN VATTRÉ, MAÎTRE DE RECHERCHE	Onera, Université Paris-Saclay	Rapporteur
VÉRONIQUE LAZARUS, PROFESSEURE	ENSTA Paris	Examinaterice
NICOLAS AUFRAY, PROFESSEUR	Sorbonne Université	Examinateur
DENIS GRATIAS, DIRECTEUR DE RECHERCHE	CNRS	Examinateur
DAMIEN FAURIE, PROFESSEUR	USPN	Examinateur
IOAN R. IOANESCU, PROFESSEUR	USPN	Examinateur

Declaration

Author's declaration: aware of legal responsibility I hereby declare that I have written this dissertation myself and all the contents of the dissertation have been obtained by legal means.

Abstract

When crystalline materials are subjected to mechanical loading beyond their elastic limit, the activation of complex microstructural mechanisms drives the material into a macroscopic nonlinear regime, where stress and strain are no longer proportional. This nonlinear behavior encompasses phase transitions, progressive plastic deformation, and, ultimately, fracture, all of which arise from microscale structural rearrangements. Understanding how these interconnected mechanisms govern macroscopic material response remains a central challenge in materials science and solid mechanics.

Phase transitions, plasticity, and fracture are traditionally studied by distinct communities, each with its own tools, models, and perspectives. Yet, these phenomena share deep underlying similarities: they exhibit complex energy landscapes, avalanche-like responses, and strongly coupled spatial-temporal patterns. Despite their disciplinary boundaries, they are fundamentally intertwined in real materials—where phase transformation can trigger plastic deformation, or where plasticity can precede and localize fracture. Unraveling the full richness of material behavior demands computational models capable of bridging these processes, capturing their interactions, and revealing the underlying mechanisms that govern them. This work explores how such unified modeling approaches, rooted in nonlinear physics and multiscale computation, can offer fresh insights into the mechanics of both crystals and engineered metamaterials.

The need for such unified approaches becomes particularly important when examining materials at small scales. Recent advancements in nano- and micro-scale engineering have unveiled remarkable mechanical behaviors in crystalline solids. At these reduced dimensions, crystals defy conventional expectations—withstanding stresses far beyond their predicted elastic limits and exhibiting size-dependent phenomena absent in bulk materials. Yet this exceptional performance comes with a critical trade-off: mechanical instabilities including buckling, shear banding, and fracture emerge unpredictably across length scales, fundamentally limiting their deployment in next-generation technologies.

A striking characteristic of small-scale materials is the presence of intermittent fluctuations during steady plastic deformation and incipient fracture and martensitic phase transformations. These fluctuations, now routinely detected through acoustic emission techniques, reveal fundamental material behaviors that contradict conventional assumptions. Contrary to traditional beliefs that such signals represent Gaussian noise, recent studies demonstrate that these fluctuations exhibit long-tailed distributions and complex correlations indicative of critical dynamics. The emitted acoustic signals contain rich information about the material’s microstate, offering invaluable insights for predicting the remaining structural lifespan of components and systems.

In a strategic departure from conventional methods, we propose to utilize a recent mesoscopic model of crystal plasticity that coherently integrates molecular-scale features with continuum mechanics concepts such as strain and stress. This innovative atomic-continuum framework enables us to connect atomistic-scale information with macroscopic fields measured at the continuum level. In our approach, defect nucleation and interaction are modeled using atomic interactions, while computational work is performed at the continuum scale—making it readily adaptable for engineering applications.

Beyond crystalline materials, this thesis extends the investigation to architected metamaterials, proposing a novel design consisting of breakable spring chains reinforced by pantographic substructures. We develop discrete and continuum models for this system, demonstrating that the pantographic reinforcement enables damage delo-

calization mechanisms that cannot be captured by conventional phase-field fracture theories. This finding reveals that metamaterial architecture introduces genuinely new physics beyond gradient-enhanced continuum models, establishing the need for specialized theoretical frameworks. The comparative analysis between our metamaterial model and classical phase-field approaches provides both fundamental insights into fracture mechanics and practical design principles for damage-tolerant structures.

Acknowledgements

Contents

1	Introduction	7
1.1	Context	7
1.2	Preliminaries	12
1.2.1	Notions of Crystallography	12
1.2.2	Bravais Lattices in \mathbf{C} Space	15
1.3	Continuum Mechanics Framework and the Cauchy-Born Rule	18
1.3.1	Kinematics of Deformation	18
1.3.2	Strain Measures and the Metric Tensor	18
1.3.3	Displacement Field Formulation	19
1.3.4	Connection to Crystal Lattices	19
1.3.5	The Cauchy-Born Rule	19
1.3.6	Frame Indifference and Material Symmetry	19
1.3.7	Comments	20
2	Mesoscopic Tensorial Model	22
2.1	Introduction	22
2.1.1	Atomistic-Scale Methods	22
2.1.2	Mesoscale Dislocation Dynamics Approaches	23
2.1.3	Multi-Scale Bridging Methods	24
2.2	Mesoscopic Tensorial Model for Crystal Plasticity	25
2.2.1	The Mesoscopic Tensorial Model (MTM)	26
2.3	The model	26
2.3.1	Elastic energy	27
2.3.2	Finite element representation	30
2.3.3	General comments	32
3	Solid-to-Solid Phase Transformations	35
3.1	Introduction	35
3.2	Slip-dominated structural transitions	36
3.2.1	Preliminaries	37
3.2.2	Molecular dynamics	39
3.2.3	Molecular statics	44
3.3	Discussion	46
3.3.1	Conclusions	49
4	Plastic flow in crystals	50
4.1	Introduction	50
4.2	Numerical experiments	51
4.2.1	A Single Dislocation	51

4.2.2	Amorphisation of a perfect crystal	53
4.3	Rebonding algorithm	61
4.4	Conclusions	64
5	Fracture Phenomena: Gradient-Enhanced Materials and Damage Pattern Evolution	66
5.1	Fracture Phenomena: Gradient-Enhanced Materials and Damage Pattern Evolution	67
5.2	The design idea	68
5.3	Continuum analog	72
5.4	Elastic background	75
5.5	Conventional fracture: Evolution in a Gradient Damage Fracture Model	80
5.5.1	Introduction	80
5.5.2	Irreversible evolutions and stability	86
5.6	Conclusions	90
6	Perspectives	92
6.1	Atomistic-Continuum Framework for Failure Precursors in Crystalline Solids	92
6.1.1	Fracture in thin films:	94
A	Algorithm	98
A.1	Appendix: Numerical Algorithm	98
B	Curriculum Vitae	99

Chapter 1

Introduction

This introductory chapter aims to present the physical phenomena governing solid-to-solid phase transitions, crystal plasticity, and fracture mechanics through a unifying lens that transcends traditional disciplinary boundaries. These phenomena although each considered as a distinct branch in materials science share deep underlying similarities: they exhibit complex energy landscapes, avalanche-like responses, and strongly coupled spatial-temporal patterns. Despite their disciplinary boundaries, they are fundamentally intertwined in real materials—where phase transformation can trigger plastic deformation, or where plasticity can precede and localize fracture. Following this conceptual foundation, we examine the elementary mechanisms that govern these processes, presenting the theoretical frameworks necessary to understand their collective behavior across multiple length and time scales.

1.1 Context

Crystalline solids are characterized at the fundamental level by their periodic lattice structure, where atomic positions follow precise geometric relationships that extend coherently over macroscopic distances. This crystalline periodicity serves as a crucial advantage for understanding complex material behavior, since the well-defined reference state enables precise tracking of structural evolution and deformation mechanisms. Both martensitic phase transformations and plastic deformation can be fundamentally described through shear processes acting on the underlying crystal lattice, yet they operate at distinctly different scales and magnitudes. Displacive martensitic transformations primarily involve coordinated shear of the crystal lattice from a high-symmetry austenitic phase to a lower-symmetry martensitic variant, typically involving relatively small atomic displacements that do not involve any change in the initial neighboring of atoms. In contrast, plastic deformation occurs through the relative motion of atomic planes via lattice-invariant shears—dislocation glide and slip—that accommodate much larger deformations while maintaining the overall crystal structure. On the other hand, fracture involves breaking atomistic bonds without any reconnection, representing an irreversible severing of the crystal lattice that fundamentally differs from the shear-based mechanisms of phase transformation and plasticity. Here we ignore diffusion-like phenomena which are outside of our scope. Although fundamental distinctions exist, each of these phenomena can be described by a single measure which is "strain"—whether it represents the transformation strain accompanying phase change, the plastic strain accumulating through dislocation motion, or the critical strain at which bonds fail catastrophically. This unifying framework of strain provides a common language for describing these seemingly disparate processes and their complex interactions in real materials.

Crucially, the appearance of strain in crystalline materials implies the generation of elastic energy that must be minimized, leading to the formation of characteristic patterns and microstructures. This energy minimization principle governs the morphological evolution across all three phenomena, albeit through different mechanisms. In martensitic transformations, the lattice mismatch between the high-symmetry austenitic phase and the lower-symmetry martensitic variants creates substantial elastic energy that drives the formation of complex self-similar patterns. Generally, the martensitic transition leads to very complicated self-similar patterns that consist of inter-

twinning laminates on a wide range of length scales. The important mechanism at the origin of these morphologies is the large lattice mismatch between the different variants of the low-symmetry martensite and the austenite. Specifically, lattice continuity at the interfaces between two variants and between any variant and the austenite enforces long-range elastic interactions. The resulting strain energy can be relaxed only through specific relative arrangements of twinned laminates (together with rigid body rotations) that lead to a stress-free state characterized, at the scale of the laminates, by an invariant plane strain and, at a larger scale, by a very small average strain.

Similarly, in plastic deformation, the motion of dislocations creates regions of sheared and unsheared material, generating elastic distortions that organize into characteristic dislocation structures. These arrangements—including cell structures, persistent slip bands, and dislocation walls—represent energy-minimizing configurations that accommodate the imposed strain while reducing the overall elastic energy of the dislocation ensemble. The patterns emerge from the long-range elastic interactions between dislocations, leading to spatial segregation and the formation of low-energy boundaries.

In fracture processes, the concentration of elastic energy at crack tips drives both the propagation direction and the formation of characteristic surface patterns. The elastic energy release associated with crack advancement creates fracture surface morphologies—from river patterns to hackle marks—that reflect the local stress state and energy dissipation mechanisms. Even the branching instabilities observed in dynamic fracture arise from the system’s attempt to minimize the elastic energy stored ahead of the propagating crack front. In Figure 1.1, we show different patterns experimentally observed in each case: (a) martensitic twin laminates, (b) dislocation cell structures, and (c) fracture morphologies.

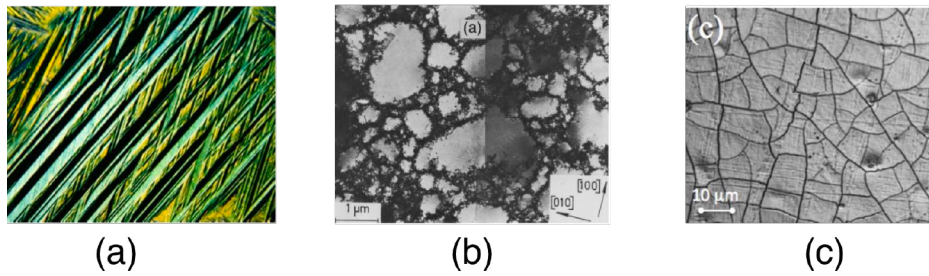


Figure 1.1: A selection of patterns: (a) Formation of polyvariant martensitic patterns: optical micrography with polarized light showing the self-similar intertwined laminate structure in a Cu-Zn-Al alloy during cubic-to-monoclinic transformation. Taken from [1]. (b) Formation of dislocation patterns: transmission electron micrograph revealing the self-organized cell structure in a [100]-oriented copper single crystal after plastic deformation to 75.6 MPa at room temperature, after [2]. (c) Formation of fracture patterns: crack morphologies observed ex situ in Nickel thin films see [3].

Another interesting similarity between these three phenomena is their avalanche-like dynamics, characterized by intermittent, scale-free bursts of activity that exhibit remarkable statistical universality. Rather than proceeding through smooth, continuous processes, martensitic transformations, plastic deformation, and fracture all display sudden, collective events where small perturbations can trigger cascades of activity across multiple length and time scales. In martensitic transformations, the nucleation of a single variant can trigger avalanches of further transformations as the elastic fields generated by the initial transformation destabilize neighboring regions. These transformation avalanches manifest as acoustic emission bursts and sudden changes in strain, with event sizes following power-law distributions characteristic of critical phenomena. The autocatalytic nature of the process means that local transformations create long-range elastic fields that promote further transformations, leading to intermittent dynamics rather than gradual, uniform conversion. Similarly, plastic deformation in crystals occurs through dislocation avalanches where the motion of individual dislocations triggers the collective movement of entire dislocation populations. These plastic avalanches are particularly evident in small-scale systems and single crystals, where stress drops and strain bursts follow the same statistical laws observed in earthquakes—including the Gutenberg-Richter distribution for event magnitudes and temporal clustering described by Omori’s law. The

underlying mechanism involves long-range elastic interactions between dislocations, where the motion of one dislocation modifies the stress field experienced by others, creating the conditions for cascading failure. In fracture processes, crack propagation exhibits avalanche dynamics through the intermittent advance of crack fronts and the formation of damage cascades. Rather than smooth crack extension, fracture often proceeds through sudden jumps and arrests, with the size and frequency of these events following power-law statistics. Micro-crack coalescence and the formation of process zones ahead of crack tips create conditions for avalanche-like failure events, where local bond breaking can trigger widespread damage cascades. This avalanche behavior reflects the underlying criticality of these systems, where they operate near phase boundaries or instability thresholds. The scale-free nature of these events suggests that similar physical principles—related to long-range interactions, disorder, and metastability—govern the dynamics across all three phenomena, providing another unifying framework for understanding these seemingly distinct processes.

For instance, in the case of plastic deformation, with the advance of nanotechnology and the shift towards broad fabrication of nano-scale parts, the focus in the study of materials science has shifted to submicron dimensions. At these scales, describing the cross-over from mild plastic flow in high-symmetry bulk materials to ‘wild’ scale-free intermittent plastic response of sub-micron scale micropillars requires a significant paradigm change. Figure 1.2 illustrates this size-dependent transition through SEM images of micropillars after compression testing at different scales. The images reveal a striking evolution in deformation behavior as sample size decreases. In the smallest samples 500 nm and 1000 nm, we observe highly anisotropic, single slip plane character of the local plastic deformation pattern, with crystallographically exact slip traces clearly visible (Fig. 1.2(a,b)). This localized deformation reflects the dominance of individual dislocation sources and the limited availability of slip systems in confined geometries. In contrast, larger 1500 nm crystals exhibit more isotropic plastic flow, displaying locally a multi-slip deformation pattern that begins to resemble the homogeneous deformation characteristic of bulk materials. This transition demonstrates how the fundamental nature of plastic deformation changes as external dimensions approach internal microstructural length scales.

In Fig. 1.3(a), we juxtaposed the stress-strain curves for Mo pillars with diameters from 500 nm to 1500 nm, all showing a characteristic set of abrupt discontinuities. For the chosen pillar orientation, the slip systems with maximum Schmid factor S are $(101)\langle 111 \rangle$ and $(011)\langle 111 \rangle$. Accordingly, after deformation, we observed the most significant plasticity on the planes $\{110\}$. The cumulative probability distributions $P(X)$ are shown in Fig. 1.3(b) for all three sample sizes. A statistical analysis of these distributions, which involved the comparison of the p -values and the likelihood ratios, allows us to conclude that: (i) for 500 nm Mo micro-pillars the outliers observed above $X \approx 3$ nm are statistically significant and indicate super-criticality; (ii) for 1000 nm Mo micro-pillars, the power-law distribution is strongly supported; (iii) for 1500 nm Mo micro-pillars, both the power-law with a cut-off and the log-normal distribution are more favorable than the power-law distribution, but the log-normal distribution is more likely.

These size-dependent transitions in statistical behavior highlight a fundamental challenge in interpreting power-law distributions in finite systems: the crossover from critical to non-critical regimes as sample dimensions change relative to characteristic length scales of the underlying physical processes. The observed progression from super-critical behavior in the smallest pillars to log-normal statistics in the largest ones reflects the complex competition between system-spanning correlations that drive power-law scaling and geometric constraints that inevitably truncate or modify the scaling behavior. The presence of power-law, scale-free behavior makes it inherently difficult to provide a smooth, continuous description of plastic deformation in small-scale crystals.

Besides, these dislocation avalanches are not without consequences for fatigue and fracture behavior. The intermittent, burst-like nature of plastic deformation fundamentally alters damage accumulation mechanisms compared to smooth, continuous plasticity observed in bulk materials. In fatigue applications, avalanche events create localized stress concentrations and microstructural heterogeneities that can serve as preferential sites for crack nucleation. This becomes particularly critical in dwell fatigue scenarios, where sustained stress holds provide time for dislocation pile-ups to develop and trigger cascading avalanche events that progressively build toward failure [4, 5]. Moreover, the unpredictable timing and magnitude of these avalanches compromise the reliable

mechanical response required for engineering applications, particularly in MEMS devices and other micro-scale systems where consistent performance is critical [6–8]. The probabilistic nature of avalanche dynamics introduces uncertainty in lifetime predictions, as failure can occur through rare, large-magnitude events rather than gradual damage accumulation, necessitating probabilistic approaches to design and reliability assessment.

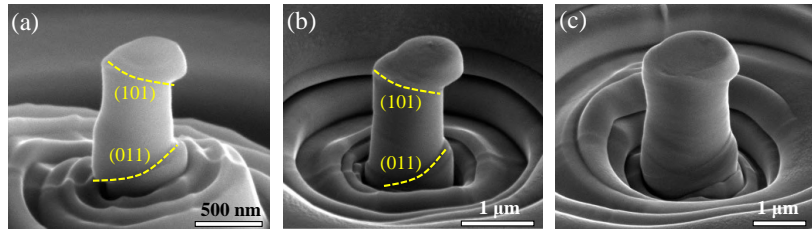


Figure 1.2: SEM images of [112]-oriented micro-pillars after compression: (a) 500 nm, (b) 1000 nm and (c) 1500 nm. The marked slip traces in (a) and (b) indicate the locally single-slip nature of the plastic flow in 500 nm and 1000 nm crystals, see [9].

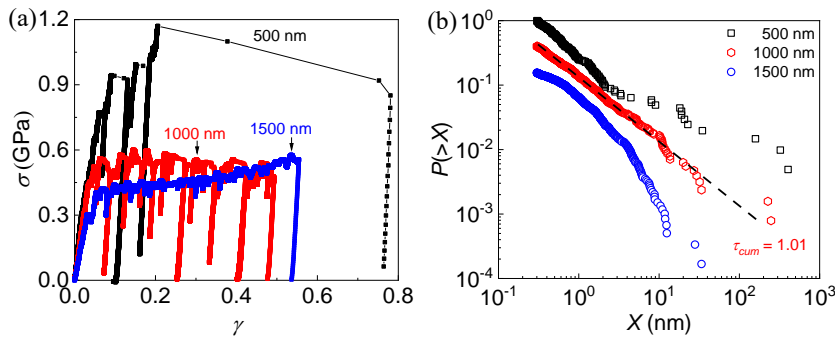


Figure 1.3: Compression tests on pure Mo sub-micron pillars: (a) stress-strain curves (shear); (b) cumulative distribution of plastic displacements X detected over the entire loading process; here $\tau_{\text{cum}} = \tau_{\text{in}} - 1$ where τ_{in} is the stress integrated exponent, see [10]

From a theoretical modeling perspective, it is clear that the intermittent dislocation avalanches defy self-averaging and challenge any attempt at continuous description. Engineering crystal plasticity (CP) is usually formulated within classical continuum mechanics and involves macroscale constitutive relations. The inelastic component of the strain tensor is parametrized by a finite number of order parameters representing amplitudes of pre-designed plastic mechanisms; in rate-independent limit, each of them is assumed to be governed by dry friction type dynamics [11–13]. The fact that fluctuations are effectively averaged out opens for CP access to macroscopic time and length scales. It allows one to model realistic 3D structures with generic geometries while accounting phenomenologically for such complex effects as hardening, lattice rotation, rate dependence, and polycrystallinity. Provided that the phenomenological constitutive laws are experimentally verified, this modeling approach can adequately describe the temporally and spatially averaged plastic response of most plastic crystals. CP modeling is at the heart of all contemporary approaches to materials deformation and failure, from civil engineering to metallurgy. However, the pure CP-based approach has been challenged fundamentally by an intermittent plastic activity observed in bulk HCP and FCC crystals as we mentioned above.

Consequently, the development of alternative computational tools accounting for the dislocation nature of plastic flows has become a priority. The lack of modeling tools compatible with intermittent microscale plasticity imposes severe restrictions on structural analysis of ultra-small crystals, limiting their utilization in engineering practice and inhibiting the progress in the related industries. Traditional continuum approaches that rely on averaged material responses are fundamentally inadequate when dealing with systems where individual dislocation events can dominate the mechanical behavior. Moreover, the coupling of phase transitions, fracture, and plasticity—all exhibiting similar avalanche-like dynamics and scale-free behavior—suggests the need for a unified theoretical framework that can capture their common underlying physics. This necessitates a paradigm shift to-

ward discrete, stochastic modeling frameworks that can capture the inherent randomness, scale-dependent nature of avalanche plasticity, and the complex interactions between these seemingly disparate but fundamentally related phenomena.

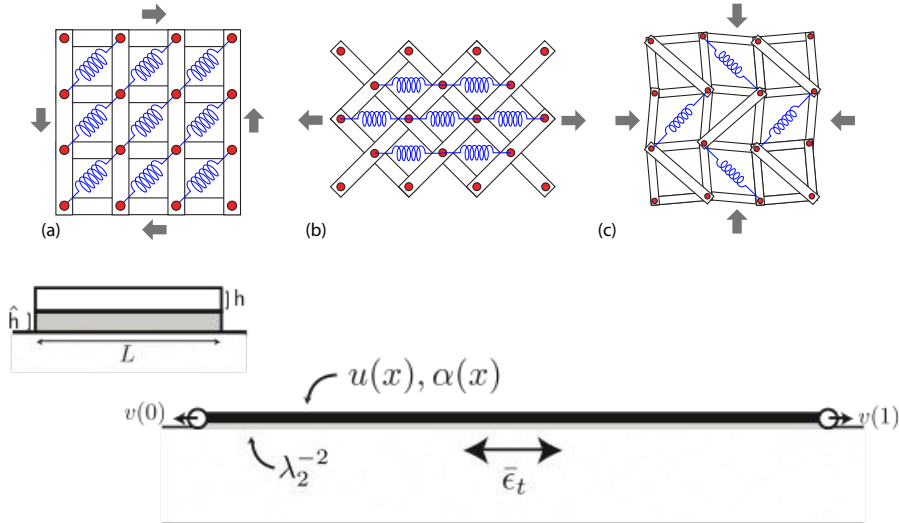


Figure 1.4: (a–c) Three configurations of 2D spring networks reinforced with compliant substructures that exhibit bending-dominated elasticity. These systems demonstrate fracture delocalization under different loading modes: (a) shear, (b) uniaxial tension, and (c) biaxial (hydrostatic) compression. (d) Schematic of the dimensionally-reduced thin film model, obtained from a 3D bilayer geometry consisting of a film (thickness h_{film}) bonded to a substrate via an interfacial layer (thickness h_{inter}) over a domain of length L .

Beyond the fundamental study of phase transitions, plasticity, and fracture in crystalline materials, this thesis explores how fracture behavior can be controlled through metamaterial design. In recent years, metamaterials have emerged as an alternative to classical bulk materials, offering the possibility to achieve desirable mechanical properties through structural architecture rather than material composition.

This thesis proposes a novel metamaterial design consisting of a primary chain of breakable springs reinforced by a pantographic substructure. The key innovation lies in coupling a load-bearing spring chain, which would typically exhibit brittle fracture through localized bond breaking, with a compliant pantographic frame that acts as a floppy reinforcement. This pantographic substructure—composed of interconnected beams with pivot points—introduces bending-dominated elasticity that fundamentally alters the failure mechanism of the primary spring chain. When the system is loaded, the pantographic reinforcement redistributes stress concentrations that would otherwise cause catastrophic failure in the spring chain, enabling controlled damage spread rather than abrupt fracture.

To analyze this reinforced spring-pantograph system, we develop a comprehensive mathematical framework spanning multiple scales. Starting from the discrete level, we formulate a mathematical model that captures both the extensional mechanics of the breakable springs and the bending kinematics of the pantographic substructure. We then systematically derive the continuum limit of this discrete system, obtaining an enriched continuum theory with higher-order gradient terms that emerge from the pantographic microstructure.

A crucial finding of this work is that conventional phase-field models of fracture fail to capture the unique damage-spreading behavior exhibited by our pantographic metamaterial. Without the nonlocal pantographic substructure, the spring chain behaves as a conventional brittle material that can be adequately described by gradient damage models [14–18] or phase-field fracture theories [19–22]. While these models incorporate internal length scales and can account for elastic foundations, we demonstrate that they cannot reproduce the broad microcracking domains and re-entrant behavior characteristic of our metamaterial. Instead, phase-field simulations consistently produce highly localized macro-cracks typical of conventional fracture, missing the fundamental damage delocalization enabled by the pantographic architecture.

This comparative analysis reveals that the pantographic substructure introduces genuinely new physics beyond what gradient-enhanced continuum theories can capture. The bending-dominated elasticity of the pantographic

frame creates nonlocal interactions that fundamentally differ from the gradient terms in phase-field models, enabling damage-spreading mechanisms impossible in conventional materials. This finding establishes the need for new theoretical frameworks specifically tailored to capture the mechanics of architected metamaterials.

1.2 Preliminaries

In the studies that will be presented in this work, we have examined various aspects of mechanical behavior mostly in crystalline materials, including plasticity mechanisms, damage evolution, and phase transitions, all of which are fundamentally governed by the underlying crystal structure and their symmetries. In parallel, this work has extensively employed continuum mechanics concepts such as deformation gradients, various strain and stress measures, and their geometric interpretations. The theoretical models that will be presented in this work are explicitly constructed to respect crystal symmetries while operating within the continuum mechanics framework, making it essential to establish the proper mathematical foundations from the outset. We begin by discussing some fundamental notions of crystallography, with particular emphasis on the mathematical framework underlying crystal symmetries and their implications for mechanical behavior, followed by a brief review of the relevant continuum mechanics concepts that form the backbone of our theoretical development. For a comprehensive treatment of crystallographic principles, we refer to [23] for deeper mathematical insights and [24] for continuum mechanical perspectives.

1.2.1 Notions of Crystallography

A crystal lattice can be mathematically described as a discrete set of points in space, generated by integer linear combinations of a finite set of basis vectors. A Bravais lattice is a structure that can be constructed by infinite integer translations of two linearly independent vectors $\{\mathbf{e}_I\}$, the *lattice basis*, in every space direction. More formally, in two dimensions:

$$\mathcal{L}(\mathbf{e}_I) = \{\mathbf{x} \in \mathbb{R}^2, \mathbf{x} = v_I \mathbf{e}_I, v_I \in \mathbb{Z}\}, \quad (1.1)$$

where Einstein summation convention is implied. Bravais lattices are also referred to as simple lattices. Crystals which are characterized by a more complex structure are called *multilattices*. In this case additional parameters \mathbf{p}_i , the *lattice shifts*, are needed in addition to the lattice basis $\{\mathbf{e}_I\}$ to describe the crystal structure and it outside of the scope of this work.

This seemingly simple representation conceals a profound geometric fact: the same physical lattice can be described by infinitely many different basis choices, all related by specific mathematical transformations. We can associate with any basis $\{\mathbf{e}_I\}$ a *metric tensor* \mathbf{C} with components:

$$C_{IJ} = C_{JI} = \mathbf{e}_I \cdot \mathbf{e}_J \quad (1 \leq I, J \leq 2). \quad (1.2)$$

The tensor \mathbf{C} is always symmetric and positive definite. Note that when linear maps are represented in matrix form, we are assuming a reference basis for the description of space \mathbb{R}^2 . Here, we will always assume as reference basis the Cartesian orthonormal basis $\{\mathbf{I}_I\}$ of \mathbb{R}^2 , coincident with the square symmetry lattice. The fact that we are implying a reference basis for the description of space \mathbb{R}^2 should not be confused with the fact that the same lattice in \mathbb{Z}^2 can be represented by several equivalent bases. Indeed, all these different equivalent bases are implicitly expressed in terms of $\{\mathbf{I}_I\}$, chosen for the representation of the space.

The key insight is that any two bases $\{\mathbf{e}_I\}$ and $\{\mathbf{f}_I\}$ generating the same lattice must be related by a linear transformation with integer coefficients and unit determinant. This constraint ensures that the transformation is invertible (unit determinant) and maps lattice points to lattice points (integer coefficients). Mathematically, the transformation can be written as:

$$\bar{\mathbf{e}}_J = m_{IJ} \mathbf{e}_I \quad \text{with } \mathbf{m} \in GL(2, \mathbb{Z}) . \quad (1.3)$$

The collection of all such transformations forms the *general linear group over the integers*, denoted $GL(2, \mathbb{Z})$, which is the set of reversible 2D integer matrices:

$$GL(2, \mathbb{Z}) = \{\mathbf{m}, m_{IJ} \in \mathbb{Z}, \det(\mathbf{m}) = \pm 1\} . \quad (1.4)$$

This group represents the complete set of lattice-preserving transformations and constitutes the fundamental symmetry group governing crystal structure. The group of all transformations leaving a lattice $\mathcal{L}(\mathbf{e}_I)$ invariant is known as the *global symmetry group* $G(\mathbf{e}_I)$ of the lattice:

$$\begin{aligned} G(\mathbf{e}_I) &:= \{\mathbf{H} \in Aut : \mathcal{L}(\mathbf{H}\mathbf{e}_I) = \mathcal{L}(\mathbf{e}_I)\} \\ &= \{\mathbf{H} \in Aut : \mathbf{H}\mathbf{e}_I = m_{JI}\mathbf{e}_J, \mathbf{m} \in GL(2, \mathbb{Z})\} . \end{aligned} \quad (1.5)$$

All 2D lattices are characterized by the same global invariance, as their symmetry is expressed by groups that, in suitable bases, all coincide with $GL(2, \mathbb{Z})$:

$$G(\mathbf{e}_I) = GL(2, \mathbb{Z}) . \quad (1.6)$$

Unlike the familiar finite point groups of classical crystallography, which only describe local rotational and reflection symmetries, $GL(2, \mathbb{Z})$ is infinite and encompasses all possible lattice-invariant deformations, including the shear transformations that are central to plastic deformation.

The corresponding symmetry for metric tensors \mathbf{C} under basis transformations is given by:

$$\bar{\mathbf{C}} = \mathbf{m}^T \mathbf{C} \mathbf{m} \quad \bar{C}_{IJ} = m_{KI} C_{KL} m_{LJ} . \quad (1.7)$$

Our discussion is deliberately limited to two-dimensional systems for several compelling reasons. First, this restriction allows us to work with $GL(2, \mathbb{Z})$ rather than the significantly more complex $GL(3, \mathbb{Z})$, providing a mathematically transparent yet physically meaningful framework. The configurational space of metric tensors in 2D can be visualized directly, enabling intuitive understanding of the energy landscape that governs plastic deformation mechanisms.

The choice of 2D systems reflects genuine physical relevance. In addition to its theoretical interest, the study of plasticity in 2D crystals is technologically relevant because such crystals have been recently found important in many applications [25–30]

From a theoretical standpoint, the $GL(2, \mathbb{Z})$ framework captures the essential physics of lattice invariant transformations while remaining computationally tractable. The infinite and discrete nature of this group gives rise to a periodic energy landscape in the space of strain tensors, where equivalent lattice configurations appear as wells separated by energy barriers corresponding to different plastic mechanisms.

To summarize, every time we perform a change of basis we are operating within the group $GL(2, \mathbb{Z})$. Similarly, every time the lattice is deformed into a symmetrically equivalent structure, such deformation can also be described as the action of $GL(2, \mathbb{Z})$ on the initial configuration. Equations (1.3) and (1.7) describe the action of the global symmetry group $GL(2, \mathbb{Z})$ on the configurational space \mathcal{B} of basis vectors (4D space of linearly-independent 2D vectors) and on the space \mathcal{Q}_2^+ of lattice metrics (the 3D space of positive definite symmetric second order tensors $\in \mathbb{R}^2$). In what follows we will mostly refer to the invariance with respect to configurational space \mathcal{Q}_2^+ , which naturally accounts for frame indifference.

The notion of global lattice symmetry based on $G(\mathbf{e}_I)$ may seem in contradiction with the classical notion of *crystallographic point group* $P(\mathbf{e}_I)$. This is the set of all the orthogonal transformations that leave the crystal invariant:

$$\begin{aligned} P(\mathbf{e}_I) &:= G(\mathbf{e}_I) \cap \mathcal{O} \\ &= \{\mathbf{Q} \in \mathcal{O} : \mathbf{Q}\mathbf{e}_I = m_{JI}\mathbf{e}_J, \mathbf{m} \in GL(2, \mathbb{Z})\} . \end{aligned} \quad (1.8)$$

where \mathcal{O} is the set of all orthogonal matrices $\mathbf{Q}^T \mathbf{Q} = 1$. The operations $\mathbf{Q} \in P(\mathbf{e}_I)$ are rotations and reflections (orthogonal transformations) mapping the lattice $\mathcal{L}(\mathbf{e}_I)$ in itself. In other words, $P(\mathbf{e}_I)$ is the orthogonal subset of $G(\mathbf{e}_I)$. We mention that both $P(\mathbf{e}_I)$ and $G(\mathbf{e}_I)$ are independent of the specific basis \mathbf{e}_I , but depend only on the lattice \mathcal{L} . Indeed the following is easily proved [24]:

$$G(\mathbf{e}_I) := G(m_{JI}\mathbf{e}_J) \quad \forall \mathbf{m} \in GL(2, \mathbb{Z}) \quad (1.9)$$

$$P(\mathbf{e}_I) := P(m_{JI}\mathbf{e}_J) \quad \forall \mathbf{m} \in GL(2, \mathbb{Z}). \quad (1.10)$$

However, while $G(\mathbf{e}_I)$ is an infinite group, $P(\mathbf{e}_I)$ is not. Indeed, given a certain lattice basis:

$$m_{JI} = \mathbf{e}_J \cdot \mathbf{Q}\mathbf{e}_I \Rightarrow |m_{JI}| \leq \|\mathbf{e}_J\| \|\mathbf{Q}\mathbf{e}_I\| = \|\mathbf{e}_J\| \|\mathbf{e}_I\| \quad (1.11)$$

which admits only finite integral solutions ($\|\mathbf{v}\|$ euclidean norm of vector \mathbf{v}). In some sense, the size of the point group $P(\mathbf{e}_I)$ of a certain lattice is indicative of the "amount of symmetry" of that lattice. This concept does not apply to $G(\mathbf{e}_I)$, which contains the infinite number of non-rigid mappings associated with the arbitrariness of the chosen lattice basis. The implied deformations are simple shears leaving the crystal invariant and can be written as:

$$\mathbf{S}\mathbf{e}_I = s_{IJ}\mathbf{e}_J, \quad \mathbf{S} = \mathbf{I} + \hat{\mathbf{a}} \otimes \hat{\mathbf{n}} \quad (s_{IJ}) \in GL(2, \mathbb{Z}), \quad (1.12)$$

where $\hat{\mathbf{a}}$ and $\hat{\mathbf{n}}$ are two orthogonal unit vectors; \mathbf{I} is the identity matrix. A detailed proof of this claim can be found in [31].

Since it is desirable to treat in the same manner lattices that are equivalent, one needs a suitable criterion for a classification of lattices with equivalent properties. The classical subdivision of lattices in *crystal systems* is based on conjugacy relations among their point groups. Indeed, when an orthogonal transformation $\mathbf{Q} \in \mathcal{O}$ is applied to basis $\{\mathbf{e}_I\}$, the associated point group is transformed to the \mathcal{O} -conjugate of itself:

$$P(\mathbf{Q}\mathbf{e}_I) = \mathbf{Q}P(\mathbf{e}_I)\mathbf{Q}^T. \quad (1.13)$$

Then, the two lattices \mathcal{L} and \mathcal{L}' are said belong to the same crystal system when their respective point groups are orthogonally conjugate. In 2D there are 4 different crystal systems: *oblique*, *rectangular*, *square* and *triangular*.

A finer classification is offered by the subdivision of lattices in *Bravais types* (also called *lattice types* in literature). This classification is based on conjugacy in $GL(2, \mathbb{Z})$, that is more restrictive condition than conjugacy in \mathcal{O} [24]. To explain how this classification is obtained, it is necessary to introduce the *lattice groups* $L(\mathbf{e}_I)$, that are integral representations of the point groups $P(\mathbf{e}_I)$:

$$L(\mathbf{e}_I) := \{\mathbf{m} \in GL(2, \mathbb{Z}) : m_{IJ}\mathbf{e}_J = \mathbf{Q}\mathbf{e}_I, \mathbf{Q} \in P(\mathbf{e}_I)\}. \quad (1.14)$$

Notice that, differently from $P(\mathbf{e}_I)$ and $G(\mathbf{e}_I)$, lattice group $L(\mathbf{e}_I)$ of a given lattice depends on the specific basis $\{\mathbf{e}_I\}$ chosen to describe that lattice. They are finite and coincide with the maximal subgroups of $GL(2, \mathbb{Z})$ acting orthogonally on a certain lattice. When a basis \mathbf{e}_I is transformed into an equivalent one $\mathbf{e}'_I = m_{JI}\mathbf{e}_J$ by the application of an integer matrix $\mathbf{m} \in GL(2, \mathbb{Z})$, the associated lattice group changes into a $GL(2, \mathbb{Z})$ -conjugate:

$$L(\mathbf{e}'_I) = \mathbf{m}^{-1}L(\mathbf{e}_I)\mathbf{m}. \quad (1.15)$$

We say that two lattices \mathcal{L} and \mathcal{L}' belong to the same Bravais type if their respective lattice groups $L(\mathbf{e}_I)$ and $L(\mathbf{e}'_I)$ are conjugate in $GL(2, \mathbb{Z})$, i.e. (1.15) holds for some $\mathbf{m} \in GL(2, \mathbb{Z})$. Also, when \mathcal{L} and \mathcal{L}' have the same Bravais type, there will be a certain choice for basis $\{\mathbf{e}'_I\}$ such that $L'(\mathbf{e}'_I)$ will be equivalent to $L(\mathbf{e}_I)$. Notice also that lattice group is not affected by orthogonal transformations, in the sense that:

$$L(\mathbf{Q}\mathbf{e}_I) = L(\mathbf{e}_I). \quad (1.16)$$

The concept of lattice group can be reformulated in terms of the correspondent metric tensor \mathbf{C} :

$$L(\mathbf{e}_I) = \{\mathbf{m} \in GL(2, \mathbb{Z}) : \mathbf{m}^T \mathbf{C} \mathbf{m}\} := L(\mathbf{C}). \quad (1.17)$$

In 2D, there are 5 Bravais types, *oblique*, *rectangular*, *rhombic*, *square* and *triangular* (the latter indicating an equilateral triangle with hexagonal symmetry). The corresponding groups, along with the classification of crystal systems, are reported in Table 1.1, taken from [32]. Note that the action (1.7) defines the relation between metric tensors of the same Bravais type. Then, it divides the configurational space of metric tensors \mathcal{Q}_2^+ in 5 orbits, each corresponding to a particular Bravais type.

Summarizing, there are two different criteria for the classification of simple lattices:

- Conjugacy of point groups $P(\mathbf{e}_I)$ in \mathcal{O} , resulting in the classifications of lattices in *crystal systems*. This classification is also known as *geometric symmetry* of simple lattices.
- Conjugacy of lattice groups $L(\mathbf{e}_I)$ in $GL(2, \mathbb{Z})$, resulting in the classifications of lattices in *Bravais types* (also *lattices types*), also called *arithmetic symmetry* of simple lattices.

Both of these classifications are based on the notion of crystallographic point group $P(\mathbf{e}_I)$, however the second is more suitable for the purpose of this Thesis, being directly compatible with $GL(2, \mathbb{Z})$ invariance. Indeed, it can be seen as the restriction of actions (1.3) and (1.7) to a suitable neighborhood of "small but finite" deformations, the so called Ericksen-Pitteri Neighborhoods (EPN) (see [33] and chapter 4 of [24] for more details).

Crystal system (International Symbol)	Lattice type (International Symbol)	Fixed set	Lattice group (up to inversion)
oblique (2)	oblique ($p2$)	$0 < C_{11} < C_{22}$ $0 < C_{12} < \frac{C_{11}}{2}$	$\begin{pmatrix} 1 & 0 \\ 0 & 1 \end{pmatrix}$
rectangular ($2mm$)	rectangular ($p2mm$)	$0 < C_{11} < C_{22}$ $C_{12} = 0$	$\begin{pmatrix} 1 & 0 \\ 0 & 1 \end{pmatrix}, \begin{pmatrix} -1 & 0 \\ 0 & 1 \end{pmatrix}$
	rhombic or centered- rectangular ($c2mm$)	Fixed set I $0 < C_{11} = C_{22}$ $0 < C_{12} < \frac{C_{11}}{2}$	$\begin{pmatrix} 1 & 0 \\ 0 & 1 \end{pmatrix}, \begin{pmatrix} 0 & 1 \\ 1 & 0 \end{pmatrix}$
		Fixed set II $0 < C_{11} < C_{22}$ $0 < C_{12} = \frac{C_{11}}{2}$	$\begin{pmatrix} 1 & 0 \\ 0 & 1 \end{pmatrix}, \begin{pmatrix} 1 & 1 \\ 0 & -1 \end{pmatrix}$
square ($4mm$)	square ($p4mm$)	$0 < C_{11} = C_{22}$ $C_{12} = 0$	$\begin{pmatrix} 1 & 0 \\ 0 & 1 \end{pmatrix}, \begin{pmatrix} 0 & -1 \\ 1 & 0 \end{pmatrix}$ $\begin{pmatrix} -1 & 0 \\ 0 & 1 \end{pmatrix}, \begin{pmatrix} 0 & 1 \\ 1 & 0 \end{pmatrix}$
triangular ($6mm$)	triangular ($p6mm$)	$0 < C_{11} = C_{22}$ $0 < C_{12} = \frac{C_{11}}{2}$	$\begin{pmatrix} 1 & 0 \\ 0 & 1 \end{pmatrix}, \begin{pmatrix} 0 & -1 \\ 1 & 1 \end{pmatrix}$ $\begin{pmatrix} 1 & 1 \\ -1 & 0 \end{pmatrix}, \begin{pmatrix} -1 & 0 \\ 1 & 1 \end{pmatrix}$ $\begin{pmatrix} 1 & 1 \\ 0 & -1 \end{pmatrix}, \begin{pmatrix} 0 & 1 \\ 1 & 0 \end{pmatrix}$

Table 1.1: The five Bravais types of simple lattices in 2D, and the fixed sets (sets of metrics with given lattice group) intersecting the fundamental domain D defined in Eq. 1.19, with the corresponding lattice groups (only one element of each pair $(m, -m)$ is tabulated).

1.2.2 Bravais Lattices in \mathbf{C} Space

Since the tensor \mathbf{C} is symmetric, we may represent all possible 2D Bravais lattices in the three dimensional space given by the coordinates C_{11}, C_{22}, C_{12} . This configurational space is very useful for visualizing the different lattice types and will be important for the understanding of the energy construction.

We remark that, because $\mathbf{C} \in \mathcal{Q}_2^+$ by definition, every admissible lattice metric \mathbf{C} belongs to the subspace limited by condition $\det(\mathbf{C}) > 0$, that is, the upper part of the 3D surface limited by the hyperbolic surface

$\det(\mathbf{C}) = \mathbf{C}_{11}\mathbf{C}_{22} - \mathbf{C}_{12}^2 > 0$. By restricting the description to the hyperbolic surface $\det(\mathbf{C}) = \mathbf{C}_{11}\mathbf{C}_{22} - \mathbf{C}_{12}^2 = 1$, we limit the analysis to lattices with the volume of a unit cell, chosen as reference, see Fig 1.5(a). This can be done without loosing generality since all the other hyperbolic surfaces are related homothetically.

The metric tensors \mathbf{C} can be projected onto the Poincaré disk using the rectangular coordinates

$$x = t(C_{11} - C_{22})/2, \quad y = tC_{12}, \quad (1.18)$$

where $t = 2(2 + C_{11} + C_{22})^{-1}$. This mapping is illustrated in Fig. 1.5(a) and the projected space is shown in 1.5(b). As we previously stated, a particular unit lattice has infinite representations on the $\det \mathbf{C} = 1$ surface, all in relation through action (1.7). As a consequence, the invariance subdivides the surface $\det \mathbf{C} = 1$ into a series of subdomains related by trivial symmetry operations. Each of these subdomains is a *fundamental domain* for the action (1.7), i.e. a subset of \mathcal{Q}_2^+ such that every $GL(2, \mathbb{Z})$ orbit, and then every Bravais lattice type, has one and just one element contained in it. In Fig. 4.4(b), this subdivision of the $\det \mathbf{C} = 1$ space is illustrated. Notice as higher symmetry lattices, triangular and square, are individuated by points, rhombic and rectangular lattices individuate lines, while generic obliquous lattice occupy all the remaining points of the $\det \mathbf{C} = 1$ surface.

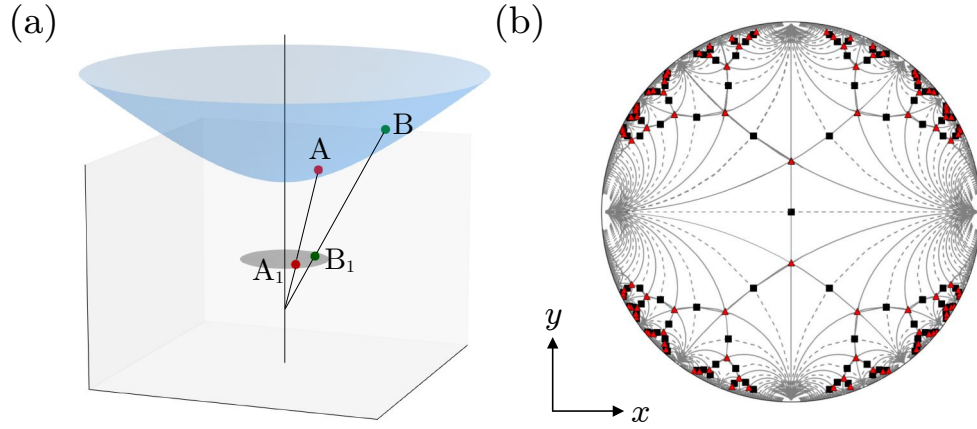


Figure 1.5: (a) 3D hyperbolic surface $C_{11}C_{22} - C_{12}^2 = 1$ in the configurational space of metric tensors C_{11}, C_{22}, C_{12} projected onto a Poincaré disk: the points A, B on such a surface are mapped to the points A_1, B_1 on the disk. (b) Poincaré disk: thin lines indicate the boundaries of minimal periodicity domains; points on the disk describing equivalent square and triangular lattices are marked by black squares and red triangles, respectively.

As we have already mentioned, the action of the infinite discrete symmetry group $GL(2, \mathbb{Z})$ divides the Poincaré disk into periodicity domains, as shown in Fig. 1.5(b). The minimal periodicity domain of this kind, known as the fundamental domain, can be represented in our case explicitly

$$\mathcal{D} = \{2C_{12} \leq \min(C_{11}, C_{22})\}, \quad (1.19)$$

see the dark gray area in Fig. 1.6(a). It corresponds to the ‘minimal’ choice for the lattice vectors $\tilde{\mathbf{e}}_1, \tilde{\mathbf{e}}_2$, which can be specified using the classical Lagrange reduction algorithm [23, 24, 32–37].

The three boundaries of the fundamental domain \mathcal{D}

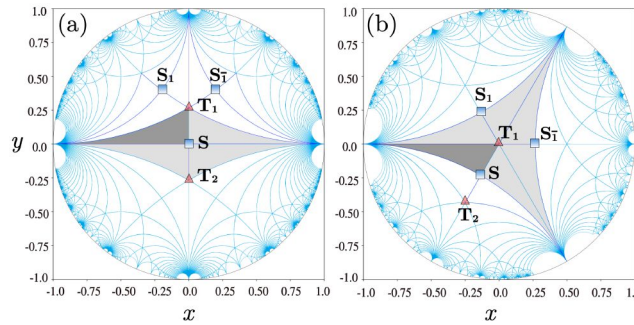


Figure 1.6: Stereographic projection on a Poincaré disk of the configurational space of metric tensors \mathbf{C} with $\det \mathbf{C} = 1$. In (a,b) the reference states are the square phase S and the triangular phase T_1 , respectively. Dark gray indicates the minimal periodicity domain, light gray – the minimal elastic domain; blue lines represent the tessellation induced by the $GL(2, \mathbb{Z})$ global symmetry. Two additional square variants $S_1, S_{\bar{1}}$, accessible from T_1 are also shown.

can be presented explicitly in the parametric form:

$$\mathbf{C} = \begin{pmatrix} \alpha^2 & 0 \\ 0 & \frac{1}{\alpha^2} \end{pmatrix}, 0 < \alpha \leq 1, \quad (1.20)$$

$$\mathbf{C} = \begin{pmatrix} \alpha^2/4 + 1/\alpha^2 & -\alpha^2/4 + 1/\alpha^2 \\ -\alpha^2/4 + 1/\alpha^2 & \alpha^2/4 + 1/\alpha^2 \end{pmatrix}, 0 < \alpha \leq \sqrt{2} \quad (1.21)$$

and

$$\mathbf{C} = \begin{pmatrix} \alpha^2 & \alpha^2/2 \\ \alpha^2/2 & \alpha^2/4 + 1/\alpha^2 \end{pmatrix}, 0 < \alpha \leq \gamma. \quad (1.22)$$

The $GL(2, \mathbb{Z})$ copies (replicas) of these boundaries, constitute the tessellation of the configurational space, represented in Fig. 1.6(a) by the thin lines which are divided in Fig. 1.5(b) into solid and dashed ones for easier identification, see [38, 39] for more details.

The *elastic domain*, represents the minimal set where the mechanical response is elastic. It is also known in the literature as the maximal Ericksen-Pitteri neighborhood [24, 32, 33]. The elastic domain can be generated from \mathcal{D} by applying discrete mappings representing the classical crystallographic point group $P(\mathbf{e}_I)$ containing only rigid rotations and used to characterize material symmetries within classical continuum elasticity [24, 32]. The elastic domain is identified in Fig. 1.6(a) by light gray color and can be represented by $D_{sq}^{elastic} = \{2|C_{12}| \leq \min(C_{11}, C_{22})\}$.

Our Fig. 1.6(a,b) provide equivalent information with the only difference that in Fig. 1.6(a) the \mathbf{C} -space is centered around the reference square lattice (point S), while in Fig. 1.6(b) the reference lattice is triangular (point T_1). In the latter case, the construction of the $GL(2, \mathbb{Z})$ induced tessellation of the Poincaré disk and recovery of the corresponding symmetry-induced periodicity structure in the space of metric tensors \mathbf{C} , proceeds through the following steps. We first represent the basis vectors of the triangular lattice T_1 in the coordinates of the basis of the square lattice S to obtain: $\mathbf{h}_1 = \{\gamma, 0\}$ and $\mathbf{h}_2 = \{\gamma/2, \gamma\sqrt{3}/2\}$, where $\gamma = (4/3)^{1/4}$. We then introduce a matrix \mathbf{H} whose columns are the vectors $\mathbf{h}_{1,2}$. Since $\mathbf{h}_j = \mathbf{H}\mathbf{e}_i$ the metric tensor in this new (triangular lattice) basis takes the form $\mathbf{C}' = \mathbf{H}^{-T}\mathbf{C}\mathbf{H}^{-1}$ where \mathbf{C} is the metric tensor in the square lattice basis. Next, the components of the tensor \mathbf{C}' are stereographically projected into the Poincaré disk using the same mapping as we used above which gives rise to a tessellation presented in Fig. 1.6(b). While in both cases shown in Fig. 1.6(a,b) the fundamental domain \mathcal{D} has the same triangular shape, the elastic domains are different reflecting the difference in the corresponding point groups. More specifically, the point group involves four rotations when the reference lattice is square and six rotations when it is triangular, which is illustrated by the different number light gray areas in Fig. 1.6(a,b). The elastic domain for the triangular lattice can then be represented by the inequalities $D_{tr}^{el} = \{0 \leq C_{12} \leq \min(C_{11}, C_{22})\}$, where metrics are defined in the coordinates of the basis of the square lattice.

1.3 Continuum Mechanics Framework and the Cauchy-Born Rule

Having established the crystallographic foundations, we now turn to the continuum mechanical description that forms the backbone of our theoretical framework. The connection between the discrete crystal structure and continuum mechanics is achieved through the deformation gradient tensor and the fundamental assumption known as the Cauchy-Born rule.

1.3.1 Kinematics of Deformation

In continuum mechanics, the motion of a material body is described by a mapping χ that relates material points in the reference configuration to their current positions. Let \mathbf{X} denote the position of a material point in the reference configuration and \mathbf{x} its position in the current configuration. The deformation mapping is then:

$$\mathbf{x} = \chi(\mathbf{X}, t) \quad (1.23)$$

The deformation gradient tensor \mathbf{F} is defined as the gradient of this mapping with respect to the reference coordinates:

$$\mathbf{F} = \frac{\partial \chi}{\partial \mathbf{X}} = \nabla_{\mathbf{X}} \mathbf{x} \quad (1.24)$$

This tensor captures the local deformation at each material point and contains complete information about the local stretching, rotation, and shearing of the material. The determinant $J = \det(\mathbf{F})$ represents the volumetric change ratio: $J > 1$ indicates volume expansion, $J < 1$ compression, and $J = 1$ isochoric deformation. The constraint $J > 0$ ensures physical admissibility and prevents material interpenetration.

Polar Decomposition: The deformation gradient can be uniquely decomposed as:

$$\mathbf{F} = \mathbf{R}\mathbf{U} = \mathbf{V}\mathbf{R} \quad (1.25)$$

where \mathbf{R} is an orthogonal rotation tensor ($\mathbf{R}^T \mathbf{R} = \mathbf{I}$, $\det(\mathbf{R}) = 1$), \mathbf{U} is the right stretch tensor, and \mathbf{V} is the left stretch tensor. Both \mathbf{U} and \mathbf{V} are symmetric positive definite tensors that describe pure stretching along principal directions. The right decomposition $\mathbf{F} = \mathbf{R}\mathbf{U}$ corresponds to stretch followed by rotation, while the left decomposition $\mathbf{F} = \mathbf{V}\mathbf{R}$ represents rotation followed by stretch.

The components of \mathbf{F} in index notation are:

$$F_{iI} = \frac{\partial x_i}{\partial X_I} \quad (1.26)$$

where i refers to spatial coordinates and I to material coordinates.

1.3.2 Strain Measures and the Metric Tensor

From the deformation gradient, various strain measures can be constructed. The right Cauchy-Green deformation tensor is defined as:

$$\mathbf{C} = \mathbf{F}^T \mathbf{F} = \mathbf{U}^2 \quad (1.27)$$

Similarly, the left Cauchy-Green tensor (Finger tensor) is:

$$\mathbf{B} = \mathbf{F}\mathbf{F}^T = \mathbf{V}^2 \quad (1.28)$$

The eigenvalues λ_i^2 of \mathbf{C} (or \mathbf{B}) are the squares of the principal stretches, representing how material line elements are stretched along the principal directions. The principal stretches $\lambda_1, \lambda_2, \lambda_3$ satisfy $J = \lambda_1 \lambda_2 \lambda_3$.

The Green-Lagrange strain tensor provides a useful measure of finite strain:

$$\mathbf{E} = \frac{1}{2}(\mathbf{C} - \mathbf{I}) = \frac{1}{2}(\mathbf{F}^T \mathbf{F} - \mathbf{I}) \quad (1.29)$$

For small deformations, this reduces to the linear strain tensor $\boldsymbol{\epsilon} = \frac{1}{2}(\mathbf{H} + \mathbf{H}^T)$.

1.3.3 Displacement Field Formulation

Working with the displacement field $\mathbf{u}(\mathbf{X}) = \mathbf{x} - \mathbf{X}$, the deformation gradient becomes:

$$\mathbf{F} = \mathbf{I} + \nabla_{\mathbf{X}} \mathbf{u} = \mathbf{I} + \mathbf{H} \quad (1.30)$$

The right Cauchy-Green tensor then reads:

$$\mathbf{C} = (\mathbf{I} + \mathbf{H})^T (\mathbf{I} + \mathbf{H}) = \mathbf{I} + \mathbf{H}^T + \mathbf{H} + \mathbf{H}^T \mathbf{H} \quad (1.31)$$

The quadratic terms $\mathbf{H}^T \mathbf{H}$ represent geometric nonlinearity. The Jacobian becomes $J = \det(\mathbf{I} + \mathbf{H}) = 1 + \text{tr}(\mathbf{H}) + \text{higher order terms}$, showing that $\text{tr}(\mathbf{H}) = \nabla \cdot \mathbf{u}$ governs volumetric changes to first order.

1.3.4 Connection to Crystal Lattices

The connection between continuum mechanics and crystal structure becomes explicit when we consider how lattice vectors transform under deformation. If $\{\mathbf{e}_I\}$ are the lattice basis vectors in the reference configuration, the deformed lattice vectors $\{\mathbf{f}_I\}$ are given by:

$$\mathbf{f}_I = \mathbf{F} \mathbf{e}_I \quad (1.32)$$

The metric tensor of the deformed lattice is then:

$$C_{IJ} = \mathbf{f}_I \cdot \mathbf{f}_J = (\mathbf{F} \mathbf{e}_I) \cdot (\mathbf{F} \mathbf{e}_J) = \mathbf{e}_I \cdot (\mathbf{F}^T \mathbf{F}) \mathbf{e}_J \quad (1.33)$$

This establishes the direct relationship between the deformation gradient and the crystallographic metric tensor introduced in the previous section.

1.3.5 The Cauchy-Born Rule

In the Cauchy-Born framework, the relative positions of atoms within a representative volume element (unit cell) are determined solely by the local deformation gradient, while the lattice vectors transform according to Eq. (1.32). Consequently, the energy of the deformed crystal can be expressed as a function of the deformation gradient, $W = W(\mathbf{F})$. More precisely, if $\mathbf{r}_\alpha^{(0)}$ represents the reference position of atom α relative to a lattice site, then its deformed position is given by

$$\mathbf{r}_\alpha = \mathbf{F} \mathbf{r}_\alpha^{(0)}. \quad (1.34)$$

This rule is exact for affine deformations and provides a good approximation for slowly varying deformation fields where the wavelength of deformation is much larger than the lattice spacing.

1.3.6 Frame Indifference and Material Symmetry

An important consequence of working with the metric tensor $\mathbf{C} = \mathbf{F}^T \mathbf{F}$ is that it automatically satisfies the principle of material frame indifference. Under a rigid body rotation \mathbf{Q} , the deformation gradient transforms as $\mathbf{F}^* = \mathbf{Q} \mathbf{F}$, but the metric tensor remains unchanged:

$$\mathbf{C}^* = (\mathbf{F}^*)^T \mathbf{F}^* = \mathbf{F}^T \mathbf{Q}^T \mathbf{Q} \mathbf{F} = \mathbf{F}^T \mathbf{F} = \mathbf{C} \quad (1.35)$$

This invariance under rigid rotations is essential for a physically consistent theory. Furthermore, the crystal symmetries we discussed in the previous section manifest as material symmetries in the continuum framework. The $GL(2, \mathbb{Z})$ invariance of the lattice translates to specific symmetries of the strain energy function $W(\mathbf{C})$:

$$W(\mathbf{C}) = W(\mathbf{m}^T \mathbf{C} \mathbf{m}) \quad \forall \mathbf{m} \in GL(2, \mathbb{Z}) \quad (1.36)$$

This symmetry requirement will be crucial in constructing the energy landscape that governs plastic deformation mechanisms.

The Cauchy-Born rule offers a powerful way to link atomistic and continuum descriptions of crystalline materials, but it has key shortcomings: it assumes affine deformation within each element, which breaks down near defects such as dislocations; it neglects surface effects and non-local interactions; and it becomes unreliable when deformations vary on the scale of the lattice spacing. Our theoretical framework overcomes these limitations by introducing a mesoscopic length scale that averages over several lattice constants, by incorporating the full $GL(2, \mathbb{Z})$ symmetry to account for lattice-invariant deformations, and by allowing discontinuous changes in the metric tensor to represent dislocation cores. In this way, the approach preserves the computational efficiency of continuum mechanics while capturing the essential physics of lattice structure and symmetry.

1.3.7 Comments

A comment regarding the geometric interpretation of deformation space is warranted here. We revisit the space of metric tensors as illustrated in Fig. 1.7, where the x and y axes represent the Poincaré projection of the metric tensor with $\det(\mathbf{C}) = 1$ using Eq. 1.18. To provide a more complete picture of deformation, we introduce a third dimension along the z -axis corresponding to $\det(\mathbf{C})$, which quantifies volumetric changes relative to the reference state, as indicated by the \odot symbol in Fig. 1.7.

The two magenta rectangles overlaid on this figure represent rectangular deformations of the reference square configuration. These rectangular deformations lie within the elastic domain and correspond to relatively small strains, similar to those observed in shape-memory alloys during reversible martensitic phase transitions. The elastic nature of these deformations ensures complete recoverability upon unloading.

In contrast, the high-symmetry triangular phase occupies a position at the boundary of the elastic domain, reminiscent of BCC-FCC structural transitions between high-symmetry crystallographic phases. The location of this triangular phase at the domain boundary makes it energetically accessible to neighboring elastic domains, thereby facilitating the onset of plastic deformation through lattice-invariant shears and dislocation-mediated processes.

The third dimension associated with volumetric changes ($\det(\mathbf{C}) \neq 1$) introduces an additional deformation mode that becomes particularly relevant in fracture mechanics, where void nucleation, growth, and coalescence lead to significant volume changes and eventual material failure. This three-dimensional representation thus encompasses the complete spectrum of deformation mechanisms: elastic deformation (within domain boundaries), plastic flow (transitions between domains), and fracture (volumetric expansion through damage).

Of course, this geometric representation provides a kinematic description of the physical phenomena occurring in the deformation space. To fully understand the material behavior and predict the transitions between different deformation modes, we must complement this kinematic framework with the energetics that govern these processes. The energy landscape associated with each region of this deformation space will be established in the following section.

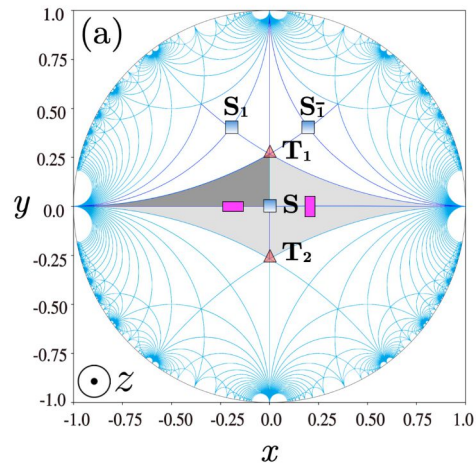


Figure 1.7: Stereographic projection on a Poincaré disk of the configurational space of metric tensors \mathbf{C} with $\det \mathbf{C} = 1$. In (a,b) the reference states are the square phase S and the triangular phase T_1 , respectively. To provide a more complete picture of deformation, we introduce a third dimension along the z -axis corresponding to $\det(\mathbf{C})$, which quantifies volumetric changes relative to the reference state, as indicated by the \odot symbol

Chapter 2

Mesoscopic Tensorial Model

2.1 Introduction

The mechanical behavior of crystalline materials at small scales presents a fundamental challenge that exposes the limitations of existing computational approaches. Recent advancements in nano- and micro-scale engineering have unveiled remarkable mechanical behaviors in crystalline solids, where materials defy conventional expectations by withstanding stresses far beyond their predicted elastic limits and exhibiting size-dependent phenomena absent in bulk materials. Yet this exceptional performance comes with critical trade-offs: mechanical instabilities including buckling, shear banding, and fracture emerge unpredictably across length scales, fundamentally limiting deployment in next-generation technologies.

Classical continuum plasticity (CP) theory has proven inadequate for modeling plastic flows in small samples. While CP successfully describes macroscopic crystal plasticity through smooth phenomena amenable to continuous description, it fundamentally fails at submicron scales. The theory cannot resolve intermittent stress-drops and strain-jumps, fails to explain catastrophic events in nanoparticles, nanowires, and nanopillars, and struggles with system-size dislocation avalanches that defy self-averaging assumptions. The core limitation stems from CP's assumption of zero microstructural length scale, which breaks down when sample sizes become comparable to defect patterning scales.

At macroscopic scales, plastic flow appears smooth because fluctuations are effectively averaged out, allowing CP to access realistic time and length scales for complex 3D structures. However, in ultra-small samples, plastic flows involve highly cooperative dislocational rearrangements that challenge any continuous description. The scale-free nature of these processes requires significant paradigm changes in modeling approaches. The following section provides essential background on the most successful modeling strategies developed in the literature. This foundation is crucial for contextualizing the scope of this thesis and highlighting the novel aspects of our proposed approach. We begin with a general overview and briefly discuss existing methods that have garnered significant attention within the scientific community. Our review maintains a minimal scope, focusing exclusively on athermal dynamics while omitting approaches that incorporate finite time scales.

2.1.1 Atomistic-Scale Methods

Molecular Dynamics and Molecular Statics

Molecular dynamics (MD) approaches, including Molecular Statics (MS) and Density Functional Theory (DFT), represent the most fundamental level of plastic deformation modeling. These methods accurately represent micro-mechanisms of plastic response while relying minimally on phenomenology. MD simulations have been particularly instrumental in studying homogeneous and heterogeneous dislocation nucleation, providing detailed insights into the atomic-scale processes governing yield behavior.

Despite their accuracy, atomistic simulations face significant limitations. They remain computationally expensive even at the small time and length scales of interest, restricting applications to very small systems and short time periods. Additionally, the problem of mapping atomistic results to macroscopic measurable quantities like stresses and strains is not yet fully resolved, creating challenges in connecting fundamental mechanisms to experimentally observable behavior.

Phase-Field Crystal Method

The Phase-Field Crystal (PFC) method emerged as a coarse-grained approach from partial temporal averaging of atomistic molecular dynamics [40]. This method provides a continuum description of atomic lattices while retaining some atomic-scale detail. PFC has been successfully applied to describe ensembles of few interacting dislocation dipoles and captures some cooperative features of crystal plasticity [41–43].

However, the detailed description of atomic lattices in PFC remains computationally demanding, particularly for developed plastic flows involving realistic numbers of interacting dislocations. While more efficient than full MD, PFC still faces scalability challenges for larger systems with extensive dislocation networks.

2.1.2 Mesoscale Dislocation Dynamics Approaches

Discrete Dislocation Dynamics

Discrete dislocation dynamics (DDD) was developed to overcome the temporal and spatial limitations of atomistic methods [44–46]. This approach treats long-range elastic interactions of dislocations adequately without resolving the fine structure of dislocation cores. Short-range interactions are handled through specific “local rules” governing phenomena like intersections and locks, often motivated by atomistic simulations.

DDD has emerged as an extremely useful tool for modeling the evolution of many interacting dislocations. The method can successfully incorporate lattice-scale effects through phenomenological constructs, making it valuable for studying dislocation ensemble behavior. However, significant challenges remain in accounting for large deformations, crystal symmetry, lattice rotation, and the emergence of non-disloational defects within the DDD framework.

Continuum Dislocation Dynamics

Continuum dislocation dynamics (CDD) represents a coarse-grained version of DDD that opens pathways toward modeling dislocation patterning. In CDD methods, dislocation microstructures are represented by continuum dislocation density fields rather than individual dislocation lines. This approach enables the study of larger systems and longer time scales compared to discrete methods [47, 48].

Various phenomenological closure relations have been proposed to model dislocation density evolution, but the systematic development of CDD remains hindered by fundamental challenges. Rigorous statistical averaging in ensembles of strongly interacting dynamic defects represents a significant theoretical obstacle that limits the predictive capability of these approaches.

Phase-Field Dislocation Dynamics

Phase-field dislocation dynamics (PFDD) offers a fully continuum framework for treating dislocations, evolved from the original Landau approach to phase transitions [49–52]. In PFDD, lattice slips are described by scalar order parameters, with energy wells representing quantized lattice invariant shears. Transition layers separating regions with different shear amounts represent dislocation line locations.

The method couples tensorial linear elastic energy with scalar lattice energy, whose periodic structure is typically informed by atomic-scale simulations using the Cauchy-Born rule. PFDD enables simulations of much larger crystal sizes and longer time scales than atomistic approaches. Recent extensions to finite strains have appeared, though challenges remain in accurately resolving lattice invariant shear structures using scalar order parameters [53].

2.1.3 Multi-Scale Bridging Methods

Quasi-Continuum Approach

The *Quasi-Continuum method* (QC) was originally proposed by Ortiz and co-authors in [54] and was then significantly developed in the following years [55–58]. Among methods aimed at the coupling of scales, it is probably the most known and used. It is based on the observation that a fully atomistic resolution is actually needed only in limited regions of the modeled problem, where deformation gradients are high. The majority of the modeled domain is instead characterized by slowly varying deformation fields and can be modeled by means of the classical continuum theory.

Considering this, authors subdivide the domain in a subdomain Ω^{cont} , where the formulation is continuum, and a subdomain Ω^{atom} , where the formulation is atomistic. In a quasistatic setting, equilibrium is found by parametric minimization of the total potential energy Π of the system. The latter is taken as a sum of potential energies on these two subdomains:

$$\Pi = \Pi^{cont} + \Pi^{atom}. \quad (2.1)$$

Potential energy Π^{atom} is evaluated as the sum of the site energies E_i of all atoms in Ω^{atom} :

$$\Pi^{atom} = \sum_{\Omega^{atom}} E_i, \quad (2.2)$$

In the continuum subdomain Ω^{cont} site energies E_i are replaced with a continuum energy density ϕ . Differently from the site energy E_i , which depends on the displacement \mathbf{u} of all other atoms within its cut-off radius, the continuum energy density $\phi(\mathbf{X})$ at a generic point \mathbf{X} depends only on the displacement gradient at that point. An important feature of QC is that the continuum energy density ϕ is evaluated directly on the basis of interatomic potentials. This can be done assuming that deformation gradient $\mathbf{F} = \nabla(\mathbf{X} + \mathbf{u})$ is homogeneous in the neighborhood of point \mathbf{X} and that the atomic lattice is deforming accordingly. Consequently, all site energies E_i of atoms in the lattice underlying continuum point \mathbf{X} are equivalent and depend only on the homogeneous deformation gradient $\mathbf{F}(\mathbf{X})$. This means that the corresponding continuum energy density ϕ is given simply by:

$$\phi(\mathbf{X}) = \frac{1}{\Omega_0} E_i(\mathbf{F}(\mathbf{X})), \quad (2.3)$$

where Ω_0 is the volume of the undeformed lattice cell.

Practically, in order to minimize (2.1) numerically, the continuum subdomain Ω^{cont} has to be subdivided in a number n_e of discrete elements with volume Ω^e such that $\Omega^{cont} = \sum_e^n \Omega^e$. The potential energy Π^{cont} is then approximated by:

$$\Pi^{cont} \approx \tilde{\Pi}^{cont} = \sum_e^n \Omega^e \phi(\mathbf{F}_e), \quad (2.4)$$

where \mathbf{F}^e is the homogeneous deformation gradient within element e . It is important to notice that computation of a continuum energy density by means of (2.3) implies the important physical assumption that the continuum deformation gradient \mathbf{F} actually describes the deformation of the underlying atomic lattice. This hypothesis is known as Cauchy-Born rule and has important consequences. An advantage of the QC method is that it is easily integrated in a Finite Element Method (FEM), a well developed technique for the numerical solution of continuum problems. Moreover, QC allows one to coordinate the evolution of Ω^{cont} and Ω^{atom} with the deformation process, in a way that the atomistic description can be limited only where it is truly needed. This can be done with automatic adaption schemes, which can expand the atomic region to the detriment of the continuum one and vice-versa [55]. Extension to the method to a dynamic setting for zero and finite temperature [59, 60], and to more complex lattice structures [55] have also been proposed.

A inherent weakness of the QC is given by the necessity of patching the continuum and discrete subdomains Ω^{cont} and Ω^{atom} through a sharp interface. Naturally, the differences between the two formulations generate

spurious forces, known as *ghost forces*. Their control is not straightforward, but the spurious effects may be reduced, given that some precautions have been taken[56, 61]. The QC method has been used in many applications, including the study of nano-indentation, deformation of grain-boundaries and crack tip evolution [56].

The somewhat contradictory nature of the interface connecting subdomains Ω^{cont} and Ω^{atom} led the authors to use, in some applications, a completely continuum formulation, known as the *local QC* [54]. In this case, potential energy is evaluated on the entire domain Ω by means of the Cauchy-Born based energy density (2.3) and we have $\Pi \approx \tilde{\Pi}^{cont}$, however, this energy can be attributed either to a continuum or to a lattice. This local QC is by itself a meso-scale method mixing continuum and atomistic features. More specifically, it is a mixed discrete-continuum formulation where the constitutive law relating stresses and strains is evaluated directly from interatomic potentials and not defined phenomenologically.

Some authors refer to the local QC model as *Cauchy-Born Theory of Crystal Elasticity*. This approach was shown to be capable of representing dislocations, even if in an approximated, coarsened, way. The success of this method is due to the fact that the use of the Cauchy-Born assumption imbues the continuum energy density with elastic non-linearity, and most importantly, with the correct crystal invariance¹. However, at the same time, it underrepresents some truly atomistic features, for instance, deformation gradients varying rapidly within the cut-off distance cannot be adequately represented. Among other approaches using the Cauchy-Born based continuum energies, we mention the *Interatomic Potential FEM* method (IPFEM) by Van Vliet and co-workers [62, 63]. This is an independently formulated local QC used for the study of homogeneous nucleation during nanoindentation.

As we have already mentioned, coupled atomistic methods different from QC were also proposed in literature, even if they did not reach the same attention. They also confront the issue of the continuum-atomistic interface. We refer the reader to the dedicated review of Miller and Curtin [64], to the more general review of McDowell [65] and also to the corresponding chapter in the book of Tadmor [61], which contains an exhaustive discussion of these techniques.

2.2 Mesoscopic Tensorial Model for Crystal Plasticity

Despite significant advances in computational methods for crystal plasticity, a sufficiently versatile approach that naturally couples different plastic mechanisms while addressing realistic space and time scales remains elusive. The fundamental challenge lies in developing a synthetic mesoscopic tensorial approach capable of handling large strains while correctly accounting for both anisotropy and discreteness of Bravais lattices.

Early attempts to address this challenge can be traced through various scalar approaches that generalized the minimalist 1D Frenkel-Kontorova model to 2D cases with single slip system activation. Despite their simplicity, these models achieved notable success in describing dislocation cores, simulating dislocation nucleation, and modeling plastic intermittency. However, they remained fundamentally limited by their scalar nature.

Progress toward more realistic descriptions emerged with tensorial models incorporating linearized kinematics. While these approaches produced more accurate representations of plastic flows, they still failed to adequately account for lattice-invariant shears associated with finite plastic slip, highlighting the need for geometrically nonlinear formulations.

The first attempts to incorporate geometrical nonlinearity appeared in models of reconstructive phase transitions that allowed for partial plastic accommodation. Subsequently, a finite strain model focused directly on plastic deformation was developed for highly anisotropic lattices of hexagonal close-packed (HCP) type with single slip systems. These developments represented different realizations of Ericksen's original program, which proposed making energy periodicity compatible with geometrically nonlinear kinematics of Bravais lattices.

Ericksen's coarse-grained approach was based on the fundamental assumption that mesoscale material elements experience an effective energy landscape that is globally periodic due to lattice invariant shears. From this Landau-type continuum theory perspective, plastically deformed crystals can be viewed as multi-phase mixtures

¹This is the reason why the local QC is similar, to some extent, to the model presented in this thesis

of equivalent phases, with an infinite number of equivalent energy wells.

2.2.1 The Mesoscopic Tensorial Model (MTM)

Building upon the theoretical foundations presented in the first chapter, the mesoscopic tensorial model represents a significant advancement in crystal plasticity modeling. In this kinematically nonlinear Landau-type theory with $GL(2, \mathbb{Z})$ symmetry, the metric tensor serves as the order parameter, with energy well bottoms corresponding to lattice invariant deformations.

The model addresses the necessarily degenerate ground state problem through regularization, where the regularizing internal length scale is associated with the mesh size generating discrete elastic elements. This mesh scale functions as a physical parameter defining the mesoscale. Due to the large magnitude of transformation strains, different phases become localized at the scale of these mesoscopic elements, with domain boundaries appearing macroscopically as linear defects that mimic dislocations.

Advantages and Capabilities: The MTM approach offers several significant advantages over previous methods. It formulates crystal plasticity in terms of macroscopically measurable quantities (stress and strain) while maintaining the ability to distinguish between different symmetry-induced configurations of dislocation cores. This capability enables adequate accounting for both long-range and short-range interactions between dislocations.

Most importantly, the model allows for topological transitions associated with dislocation nucleation and annihilation, even though these reactions appear blurred at the regularization scale. The approach can handle interactions of dislocations with various obstacles, including pinning by impurities and depinning from nucleation sources, without requiring ad-hoc constitutive relations.

Theoretical Foundations and Physical Interpretation: Within this framework, plastic yield can be interpreted as escape from the reference energy well, while plastic mechanisms can be linked to low-barrier valleys in the energy landscape. The friction-type dissipation that controls dynamics in continuum crystal plasticity emerges naturally as a result of homogenized description of overdamped athermal dynamics in a rugged energy landscape.

This theoretical foundation provides a bridge between atomistic mechanisms and continuum behavior, offering a path toward understanding the complex phenomena observed in submicron crystal plasticity while maintaining computational tractability for realistic system sizes and time scales. Behind the emergence of the continuum stresses and strains in MTM lies the spatial averaging over a mesoscopic length scale: the latter characterizes the size of a maximal cluster of atoms which can be assumed to deform homogeneously. The MTM belongs to the class of mesoscopic elasto-plastic models used in the studies of amorphous plasticity, but instead of using conventional Eshelby elastic propagator, it deals directly with geometrically and physically nonlinear elasticity of inhomogeneous solid bodies and instead of simplified description of plastic slip, it accounts adequately for crystallographically specific lattice invariant shears. The resulting approach has the advantage over DDD of describing without any special phenomenological assumptions, the topological changes in dislocation configurations such as nucleation, annihilation and interaction with obstacles, all in a self-consistent manner and only relying on the assumptions about the inter-atomic potential. Most importantly, it allows one to resolve scale-free dislocational avalanches, responsible for intermittent fluctuations accompanying steady plastic flows in low symmetry crystals. We mention that various other MTM-related approaches have been also explored in the literature [66–75].

2.3 The model

In overview, the MTM is a geometrically nonlinear theory of Landau-type where the role of the order parameter is played by the metric tensor (characterizing local deformation). In the corresponding 2D continuum theory, the elastic energy density is assumed to respect the full $GL(2, \mathbb{Z})$ symmetry of Bravais lattices represented by 3×3 invertible matrices \mathbf{m} with integer entries and unit determinants. This implies that such energy density is a multi-well function of the tensorial parameter, with the bottoms of the energy wells corresponding to lattice invariant deformations. In the numerical implementation of the MTM, the space of admissible deformations is reduced to

compatible piece-wise affine mappings. Therefore, the outcome of the numerical energy minimization depends on the value of the internal length representing the size of the mesoscopic finite element, which brings a cut-off scale into the theory. Given the large magnitude of the associated transformation strains, different phases end up being localized at the scale of mesoscopic elements, and the domain boundaries appear macroscopically as linear defects representing mesoscopic dislocations.

2.3.1 Elastic energy

In the 2D version of the MTM approach the configurational space of metric tensors is tessellated into an infinite number of equivalent domains, where equivalence is understood in terms of the symmetry transformations induced by the infinite group $GL(2, \mathbb{Z})$. If the energy density is known in one of such tensorial periodicity domains, it can be extended to the whole configurational space. To express the global lattice induced symmetry of the ensuing function

$$\phi = \phi(\mathbf{C}) \quad (2.5)$$

which goes beyond the conventional continuum mechanics point group, we need to recall that 2D Bravais lattices can be generated by two linearly independent vectors $\{\mathbf{e}_I\}$, $I = 1, 2$, which form a lattice basis. The two bases \mathbf{e}_I and $\bar{\mathbf{e}}_I$ describe the same lattice if $\mathbf{e}_J = m_{IJ}\bar{\mathbf{e}}_I$ with $m_{IJ} \in \mathbb{Z}$. In this sense, all 2D simple lattices are invariant under the action of a group

$$GL(2, \mathbb{Z}) = \{\mathbf{m}, m_{IJ} \in \mathbb{Z}, \det(\mathbf{m}) = \pm 1\}. \quad (2.6)$$

Therefore, to preserve a Bravais lattice, the strain energy density of a crystal must respect the symmetry

$$\phi(\mathbf{C}) = \phi(\mathbf{m}^T \mathbf{C} \mathbf{m}), \quad (2.7)$$

where \mathbf{m} belongs to $GL(2, \mathbb{Z})$.

In view of this global symmetry, the surface $\det \mathbf{C} = 1$ (isochoric deformations) is tessellated in the 3D space (C_{11}, C_{22}, C_{12}) into an infinite number of equivalent periodicity domains as already discussed in the previous chapter, see Figures 1.6(a,b).

As we have already mentioned, it is sufficient to define the energy density only in one minimal periodicity domain, D which is known in the mathematical literature on modular forms as a 'fundamental domain', see shaded domains in our Fig.1.6. We shall refer to the restriction of the energy density to the fundamental domain as $\phi_D(\tilde{\mathbf{C}})$ where $\tilde{\mathbf{C}}$ is the projection of a general \mathbf{C} into this domain. We can write $\tilde{\mathbf{C}} = \mathbf{m}^T \mathbf{C} \mathbf{m}$ where \mathbf{m} is the corresponding mapping of the metric tensor \mathbf{C} into the fundamental domain ensuring that $\phi(\mathbf{C}) = \phi_D(\tilde{\mathbf{C}})$.

In our 2D case, the fundamental domain can be chosen in the form [23, 24, 32, 76]

$$D = \left\{ C \in \det \mathbf{C} = 1, \quad 0 < C_{11} \leq C_{22}, \quad 0 \leq C_{12} \leq \frac{C_{11}}{2} \right\}. \quad (2.8)$$

Given a generic metric \mathbf{C} , the task of finding a unimodular matrix \mathbf{m} ensuring that $\tilde{\mathbf{C}} \in D$ (and therefore $\phi(\mathbf{C}) = \phi_D(\tilde{\mathbf{C}})$) can be formulated in the form of a recursive algorithm known as Lagrange reduction [23, 32]. Specifically, if we define the matrices :

$$\mathbf{m}_1 = \begin{pmatrix} 1 & 0 \\ 0 & -1 \end{pmatrix}, \quad (2.9)$$

$$\mathbf{m}_2 = \begin{pmatrix} 0 & 1 \\ 1 & 0 \end{pmatrix}, \quad (2.10)$$

and

$$\mathbf{m}_3 = \begin{pmatrix} 1 & -1 \\ 0 & 1 \end{pmatrix}. \quad (2.11)$$

we can formulate the reduction process in a form of an explicit algorithm. Thus, if we start with an assumption

that $\mathbf{m} = \mathbb{I}$, we can proceed through the following steps: (i) if $C_{12} < 0$, change sign to C_{12} , $\mathbf{m} \rightarrow \mathbf{m}\mathbf{m}_1$; (ii) if $C_{22} < C_{11}$, swap these two components, $\mathbf{m} \rightarrow \mathbf{m}\mathbf{m}_2$; (iii) if $2C_{12} > C_{11}$, set $C_{12} = C_{12} - C_{11}$, $\mathbf{m} \rightarrow \mathbf{m}\mathbf{m}_3$. As a commentary, we note that the action of the matrix \mathbf{m}_1 is a reflection which returns an acute angle between two lattice vectors \mathbf{e}_i . The action of the matrix \mathbf{m}_2 is also a reflection as it swaps two lattice vectors \mathbf{e}_i . Both of these operations belong to the point group and propagate the metric only inside the corresponding 'elastic domain' (Pitteri neighborhood) composed of the four copies of the minimal domain D [24]. Instead, the mapping defined by matrix \mathbf{m}_3 brings the metric outside the 'elastic domain' and therefore represents a quantized analog of the macroscopic plastic strain [77].

The single-period Landau potential $\phi_D(\tilde{\mathbf{C}})$ can be now constructed using the classical Cauchy-Born approach. Suppose that material points in a representative volume Ω undergo an affine deformation such that

$$\mathbf{y}(\mathbf{x}) = \mathbf{x} + \mathbf{u}(\mathbf{x}), \quad (2.12)$$

and the displacement vector $\mathbf{u}(\mathbf{x})$ is an affine function of \mathbf{x} , see Fig. 2.1. Specifically, if we define the vectors $\mathbf{R} = \mathbf{x} - \mathbf{x}'$ and $\mathbf{r} = \mathbf{y} - \mathbf{y}'$, connecting two atoms in the reference and in the deformed configurations, respectively, we can write $\mathbf{r} = \mathbf{F}\mathbf{R}$ where we introduced the homogeneous deformation gradient $F_{ia} = \partial y_i / \partial x_a = \delta_{ia} + \partial u_i / \partial x_a$. To compute the energy density $\phi(\mathbf{C})$, we need to account for the elongation or shortening of every atomic bond and then average over the domain Ω . Then, if the interatomic potential is $V(|\mathbf{r}|)$ which is defined within a given cutoff, we can write

$$\phi(\mathbf{C}) = \frac{1}{2\Omega} \sum_{\mathbf{x}} \sum_{\mathbf{x}' \in \mathcal{N}(\mathbf{x})} V\left(\sqrt{R_a C_{ab} R_b}\right), \quad (2.13)$$

where $C_{ab} = F_{ia} F_{ib}$ and the internal summations involves all points \mathbf{x}' belonging to the cutoff neighborhood $\mathcal{N}(\mathbf{x})$. After we compute the energy in this way inside the fundamental domain D , we can extend it to the whole configurational space by $GL(2, \mathbb{Z})$ periodicity. The ensuing Landau potential can be expected to become smooth only in the limit when the size of the domain Ω tends to infinity.

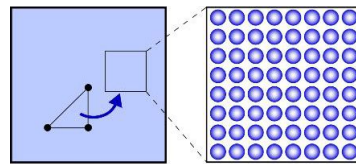


Figure 2.1: Schematic representation of the finite element containing a number of atomic units which are assumed to deform homogeneously.

One can also achieve a desired level of smoothness phenomenologically, by representing the energy density inside the domain \mathcal{D} using polynomial functions of different degrees. In this work we adopt, for simplicity, such an approach and without relying on any particular interatomic potential, use a prototypical sixth order polynomial energy density developed in [32, 36] which ensures stress continuity over the whole configurational space. Specifically, we assume that

$$\phi_0\left(\frac{\tilde{\mathbf{C}}}{(\det \tilde{\mathbf{C}})^{1/2}}\right) = \beta\psi_1\left(\frac{\tilde{\mathbf{C}}}{(\det \tilde{\mathbf{C}})^{1/2}}\right) + \psi_2\left(\frac{\tilde{\mathbf{C}}}{(\det \tilde{\mathbf{C}})^{1/2}}\right), \quad (2.14)$$

where

$$\psi_1 = I_1^4 I_2 - \frac{41}{99} I_2^3 + \frac{7}{66} I_1 I_2 I_3 + \frac{1}{1056} I_3^2, \quad (2.15)$$

$$\psi_2 = \frac{4}{11} I_2^3 + I_1^3 I_3 - \frac{8}{11} I_1 I_2 I_3 + \frac{17}{528} I_3^2. \quad (2.16)$$

and we introduced the following hexagonal invariants of the metric tensor:

$$I_1 = \frac{1}{3}(\tilde{C}_{11} + \tilde{C}_{22} - \tilde{C}_{12}), \quad (2.17)$$

$$I_2 = \frac{1}{4}(\tilde{C}_{11} - \tilde{C}_{22})^2 + \frac{1}{12}(\tilde{C}_{11} + \tilde{C}_{22} - 4\tilde{C}_{12})^2, \quad (2.18)$$

$$I_3 = (\tilde{C}_{11} - \tilde{C}_{22})^2(\tilde{C}_{11} + \tilde{C}_{22} - 4\tilde{C}_{12}) - \frac{1}{9}(\tilde{C}_{11} + \tilde{C}_{22} - 4\tilde{C}_{12})^3. \quad (2.19)$$

The potential (2.14) contains a single parameter β that enables the enforcement of specific symmetries on the reference state. We select here $\beta = -1/4$ which ensures that global energy minimizers correspond to square lattices. The total elastic energy, allowing one to deal with both shear and volumetric deformations, is taken in the form

$$\phi(\tilde{\mathbf{C}}) = \phi_0 \left(\frac{\tilde{\mathbf{C}}}{(\det \tilde{\mathbf{C}})^{1/2}} \right) + \phi_v(\det \tilde{\mathbf{C}}). \quad (2.20)$$

The volumetric part, which primarily influences dislocation core structures and controls the formation of voids, is assumed to be of a generic form

$$\phi_v(s) = \mu(s - \log(s)) \quad (2.21)$$

which prevents infinite compression. To maintain in our numerical experiments the strain field near the surface $\det C = 1$, we adopted a sufficiently high value of the bulk modulus, $\mu = 5$.

In Fig. 2.2 we illustrate the resulting energy landscape in the configurational space of metric tensors \mathbf{C} with $\det \mathbf{C} = 1$. It highlights the fact that any such landscape would have a network of low energy valleys along the directions representing simple shears along crystallographic slip planes. It also reminds us that the deepest energy wells correspond to the equivalent replicas of the reference square lattice furnished by rank one deformation gradient tensors representing lattice invariant simple shears. Instead, pure shear deformations lead to extremely large elastic energy levels.

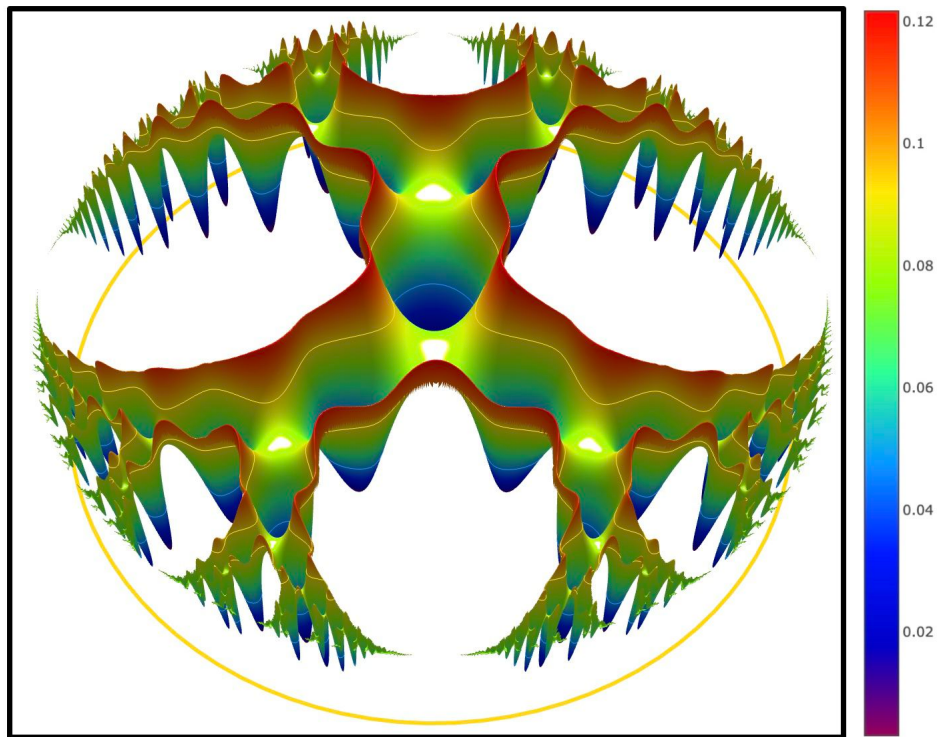


Figure 2.2: Energy landscape in the space of metric tensors. Color indicates the energy level with only the lowest energy levels shown. The deepest energy wells correspond to equivalent representations of the same square lattice.

2.3.2 Finite element representation

The account for quantized lattice invariant shears makes the energy $\phi(\mathbf{C})$ highly non convex. Therefore, the corresponding continuum (scale free) problem is highly degenerate. In particular, the energy minimization in such continuum setting can be expected to produce infinitely fine microstructures [78]. In fact, the lack of convexity of the potential is a property that the MTM shares with other similar Landau type continuum theories. The usual way of regularization in this case is the introduction of higher gradients (of the deformation, in our case) into the energy density and using the corresponding internal length scale as a cutoff parameter [79]. This would be an approach of a phase field theory which often leads to over-regulrization and the loss of sufficiently fine aspects of the microstructure which is acceptable near critical points but may compromise the inherent nonlocality by treating it only in the long wave limit. Inside such a framework it is also a nontrivial task to represent adequately the global lattice symmetry. In view of these limitations, in the MTM approach we take a different path and bring an internal scale into the model through an explicit spatial discretization. Essentially, we reduce the space of admissible deformations to a finite dimensional set of compatible, piece-wise affine mappings.

More specifically, we assume that a crystal can be represented at the mesoscale by a collection of $N \times N$ discrete elements organized in a mesoscopic lattice which preserves the symmetry of the atomic lattice. The original lattice is effectively coarse-grained with an introduction of a uniform mesoscale grid. The deformation is assumed to be piecewise linear and the elastic response is attributed to discrete material elements whose linear size h is viewed as a physical parameter of the model. The numerical implementation of MTM is then based on solving an elastic finite element problem, with elements imitating mesoscopic aggregates of atomic cells. To trace the mechanical response of the crystal we follow the displacements of the network of discrete nodes labeled by integer valued coordinates $I = 1, \dots, N^2$.

We assume further that each of the elements is a deformable triangle and employ standard finite element discretization with linear triangular 3-node elements [80]. We begin by writing the displacement field inside each of these triangles in the form

$$\mathbf{u}(\mathbf{z}) = \sum_a \mathcal{N}^a(\mathbf{z}; h) \mathbf{u}^a, \quad (2.22)$$

where $\mathcal{N}^a(\mathbf{z}; h)$ are compactly supported linear shape functions, \mathbf{u}^a are the amplitudes of the displacements of the nodes and summation is assumed over repeated indexes; the interpolation functions for each element are defined in terms of local dimensionless coordinate system. The mesoscopic deformation gradient is then

$$\mathbf{F}(\mathbf{z}; h) = \mathbb{I} + \mathbf{u}^a \otimes \nabla \mathcal{N}^a(\mathbf{z}; h). \quad (2.23)$$

In terms of macroscopic reference coordinates, the elastic energy inside each element can be computed using the simplest quadrature scheme

$$w(\mathbf{x}; h) = \frac{1}{2} \phi(\mathbf{F}(\mathbf{x}; h)) J(\mathbf{x}, h), \quad (2.24)$$

where J is the determinant connecting local (\mathbf{z}) and global (\mathbf{x}) coordinate systems.

We illustrate in Fig 2.3 our computational mesh which is a 2D lattice representing a scaled version of the original atomic lattice; a representative triangular finite element is, for instance, the element BAC adjacent to the node A. This element connects three nodes and therefore the index a associated with this element takes three values $a = 1, 2, 3$. We effectively assume in the MTM that the energy associated with the deformed element BAC depends on the three parameters: the deformed lengths of the bonds AB and AC and the deformed value of the angle BAC. To obtain these dependencies we use the Cauchy Born rule. Behind it is the assumption that the element deforms as if it was embedded into an infinite lattice undergoing a global affine (homogeneous) deformation. The latter is fully characterized by the same three parameters which we interpret as the components of the corresponding metric tensor C_{11} , C_{22} and C_{12} .

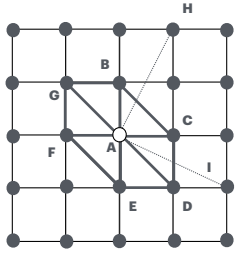


Figure 2.3: Six triangular finite elements which are immediately adjacent to a generic node A .

Finding solution of an elastic problem implies local minimization of the energy

$$W = \int_{\Omega} w(\mathbf{x}; h) d\mathbf{x}, \quad (2.25)$$

which is prescribed on a triangulated domain Ω . The conditions of mechanical equilibrium, formulated in terms of the first Piola-Kirchhoff stress tensor

$$\mathbf{P} = 2\mathbf{F}\mathbf{m} \frac{\partial w}{\partial \bar{\mathbf{C}}} \mathbf{m}^T, \quad (2.26)$$

take the form

$$\nabla \cdot \mathbf{P} = 0.$$

In the finite element representation these equations can be rewritten in the form

$$\frac{\partial W}{\partial \mathbf{u}^a} = \int_{\Omega} \mathbf{P}(\mathbf{x}; h) \nabla \mathcal{N}^a(\mathbf{x}; h) d\mathbf{x} = 0. \quad (2.27)$$

Referring again to our Fig 2.3, we observe that the elastic energy w dependence on the displacement of the node A has six contributions from the six adjacent triangular elements BAC, CAD, DAE, EAF, FAG and GAB. Therefore, in this setting, the node A interacts not only with all the nearest nodes B,C,E,F but also with some next to nearest neighbor nodes D and G. This interaction can be still interpreted as 'local', for instance, as it is shown in Fig 2.3, the node A does not interact with mode distant nodes H and I. The implied 'multibody' interaction suggests that the energy of the node A depends not only on the distances to the corresponding nodes B,C,D, E, F, G but also on the three-point configurations represented by the angles BAC, CAD, AED, EAF and AFG. In other words, the force balance for the node A includes not only responses to the elongation of the bonds but also the associated three-body contributions.

We emphasize that such non-pairwise interaction is a result of coarse graining. In this sense the MTM approach is not in any contradiction with the fact that in the corresponding atomic model the interaction between the actual atoms is pairwise while maybe extending far beyond nearest neighbors. Essentially, in the MTM approach the energy of a single elastic element (triangle in our case) is computed as if the surrounding deformation field was affine which means that the local inhomogeneity of the deformation is underplayed.

Note also that the MTM, with parameter h equal to atomic scale and with nodes identified with actual atoms, can be seen as an atomistic scale model in which the actual inhomogeneity of local environment of a given atom is neglected even if the deformation of the element itself is properly accounted for. Such effective coarse graining allows can be used as a way to save computational time but at the expense of misrepresenting some microscopic aspects of the problem. Still, despite the inevitable shortcomings accompanying this type of approximations, the MTM approach remains advantageous as an accelerated computational scheme allowing one to bridge the gap between continuum and atomistic descriptions. The implied acceleration is due to the fact that one does not need to keep track of all neighboring atoms of a given element as the energy of the element can be computed in a straightforward manner based only on the information about the local value of the deformation gradient. The acceleration comes, of course, at a price: in the presence of an internal cutoff length scale some aspects of a genuinely atomistic description are necessarily lost.

The ensuing mathematical problem can be solved numerically using a quasi-Newton method accompanied by the Newton–Raphson (NR) "refinement" when the initial guess is too far from the solution for Newton–Raphson method to converge [54]. It has the advantage of being computationally efficient as well as being able to handle nonconvexity of the problem by only dealing with positive-definite Hessian matrices. The numerical method performs the minimization of the energy functional iteratively. In very general terms, it begins with an initial guess of $\mathbf{u}(\mathbf{x})$ and a given approximation of the *inverse* Hessian matrix H_0 as well as known optimal number m of BFGS corrections to be stored. An iteration first finds a minimization direction by performing a (one-dimensional) line search and finding the optimal step-size. Next, the solution is updated along with other quantities necessary to compute the inverse Hessian matrix of the next step. The algorithm differs from BFGS in the way it handles the inverse Hessian matrix, which is approximated/updated by m corrections at each iteration.

More specifically, in our numerical experiments to find \mathbf{u}^a , we first use the L-BFGS algorithm [81] which builds a positive definite linear approximation allowing one to make a quasi-Newton step lowering the total energy. The iterations continue till the increment in the advance of the total energy becomes sufficiently small. The obtained approximate solution is then used as an initial guess \mathbf{w}^a to solve, using LU factorization [82, 83], the equations for the correction $d\mathbf{w}^a$ around an initial guess for the displacement field

$$\mathbf{u}^a = \mathbf{w}^a + d\mathbf{w}^a$$

. The corresponding system of linear equations can be written in the form

$$K_{ij}^{ab} dw_j^b + R_i^a = 0, \quad (2.28)$$

where

$$K_{ij}^{ab} = A_{ipjq}(\mathbf{F}) \frac{\partial \mathcal{N}^a}{\partial x_p} \frac{\partial \mathcal{N}^b}{\partial x_q}, \quad R_i^a = P_{ip}(\mathbf{F}) \frac{\partial \mathcal{N}^a}{\partial x_p}. \quad (2.29)$$

Note that here we used the Eulerian $i, j = 1, 2$ and the Lagrangian $K, L = 1, 2$ indexes and assumed summation on repeated indexes. We also defined

$$A_{iajb} = \frac{\partial^2 \phi_D(\tilde{\mathbf{C}})}{\partial F_{ia} \partial F_{jb}}. \quad (2.30)$$

the tensor of tangential elastic moduli. We note that the knowledge of the Eulerian acoustic tensor

$$Q_{ij} = F_{la} F_{mb} A_{iajb} n_l n_m, \quad (2.31)$$

where \mathbf{n} are vectors of the unit circle allows one to formulate the criterion of an elastic instability of the corresponding continuum body in the form [84, 85]:

$$\det(\mathbf{Q}) = 0. \quad (2.32)$$

2.3.3 General comments

Before we turn to the results of our numerical experiments, some general comments about the MTM approach may be suitable as the physical implications of these experiments depend on the chosen modeling framework.

Recall first that in molecular dynamics approach (or rather molecular statics (MS) in our quasi-static loading case) there is also a characteristic internal scale: the interatomic distance a which is a microscale parameter. In the mesoscopic approach of the MTM the coarse-graining scale h , defining the cutoff beyond which the deformation is considered homogeneous (affine), is necessarily larger than a since the goal is to accelerate the computations. Their relative magnitudes should be, of course, discussed in terms of dimensionless quantities. Thus, if the size of the macroscopic domain is L , its division into finite elements introduces a dimensionless internal scale $h = L/N$ and $\delta = 1/N$ where we recall that N^2 is the number of the nodes in the mesoscopic finite-element grid. The analogous microscale parameter is $\epsilon = a/L$ and while we are ultimately implying the limit $\epsilon \rightarrow 0$, $\delta \rightarrow 0$, we must assume

that $\delta \gg \epsilon$. To locate in this perspective the classical continuum approach, we recall that h can be interpreted as an effective size of a 'continuum particle'. Then, to obtain the continuum limit we first implicitly perform the limit $\epsilon \rightarrow 0$ and recover in this way local constitutive response by using, for instance, the Cauchy-Born rule. Then, to obtain a scale free theory we perform the second limit $\delta \rightarrow 0$. Essentially we consider a double asymptotics $\epsilon \rightarrow 0, \delta \rightarrow 0$, with $\delta \gg \epsilon$ which implies that $a \ll h \ll L$ and the only remaining length scale is L , see Fig. 2.4. Instead, in the MTM approach we effectively consider only a single limit $\epsilon \rightarrow 0$ which allows us still to use the Cauchy-Born rule. We then avoid the second limit and maintain a small but finite value of the parameter δ which then necessarily satisfies the constraint $\delta \gg \epsilon$. In this situation we have $a \ll h \sim L$ and both h and L survive in the limit $a/L \rightarrow 0$, see Fig. 2.4. In this sense the MTM is essentially a continuum theory with an internal length scale, like, say, phase field model and other similar 'quasi-continuum' approaches.

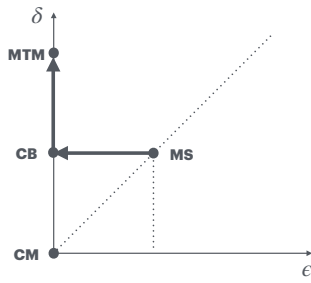


Figure 2.4: Schematic representation of the asymptotic ($\epsilon \rightarrow 0, \delta \rightarrow 0$) inter-relations between the molecular statics (MS), the continuum mechanics (CM) and the mesoscopic tensorial model (MTM). As the (normalized) atomic scale ϵ tends to zero, the elasticity can be approximated by the energy density obtained through the application of the Cauchy-Born rule (CB). If the mesoscopic scale δ is eliminated, we obtain CM and if it is kept finite and larger than the atomic scale, we obtain MTM.

As on all such theories, making the dimensional parameter h smaller is equivalent to making another dimensional parameter L larger. In this sense the assumption that δ is finite is equivalent to incorporating finite size effects. Thus, even though changes in δ will scale the size of the core regions of dislocations, they will preserve the nature of their long range interactions, at least far away from the boundaries. The use of Cauchy-Born coarse grained description, will also lead to some loss of microscopic details in the description of dislocation cores, however, the ensuing 'blurred' dislocations will still nucleate and self-lock adequately even if perhaps at different values of controlling parameters than in the corresponding MS simulations. Note also that at least some of the characteristic parameters including the core energy, the Peierls stress, the elasticity of a dislocation line, etc., may be matched by using δ dependent interatomic potential which will then affect the barrier structure in the corresponding Cauchy-Born energy density. The situation here is the same as in the case of phase field description of phase boundaries where the need to reproduce the realistic value of the surface energy requires the microscopic potential to be appropriately re-scaled.

Given the nature of the approximation provided by the MTM approach, it can be compared to other physical models with partial spatial resolution. An important example is the model of turbulence known as large eddy simulation (LES), e.g. [86, 87]. This computational approach deals with a similar problem of choosing an ultraviolet cutoff while describing the processes at the smaller scales by effective closure schemes. The principal idea behind LES is the same as in the MTM approach: to reduce the computational cost by ignoring the smallest length scales which turn out to be the most computationally expensive to resolve. In both LES and MTM, the omitted small scale details are mostly sacrificed in the interests of addressing the scale invariant aspects of the phenomena. As in the MTM, the sub-grid scales in the LES are not irrelevant, and their effect is modeled by sub-grid scale models which are not rigorously derived from the microscale but, instead, combine empirical information with some fundamental physical constraints. The choice of the grid size in LES is rooted in the idea that LES accurately captures the energy-containing large eddies while modeling the smaller ones only effectively to maintain a balance between accuracy and computational feasibility. Similarly, the choice of the cutoff scale h in the MTM, where the sub-grid description reduces to Cauchy-Born type representation of the energy density, is guided by the necessity

to capture within available computational resources the collective effects involving a large number of dislocations leading to intermittent avalanche behavior and attendant spatial complexity. In this perspective, the actual value of the parameter h in the MTM approach is irrelevant as long as the *quantitative* comparison with MS is not an issue and the computational domain is large enough so that the finite size effects due to interaction of enlarged dislocation cores with external boundary can be still neglected. In such settings, by changing h we end up capturing the same physical interactions even if they are viewed with different degree of resolution.

Therefore, we adopt a pragmatic approach to the choice of the mesoscopic length scale h and make it problem-specific. The idea is to ensure that the Cauchy-Born energy density, computed for a *finite* lattice fragment with scale h , can be considered as approximately periodic within the interesting range of strains. In other words, we would like to capture correctly the targeted energy wells while probably sacrificing the $GL(2, \mathbb{Z})$ periodicity beyond the actually reachable range. Since the exact global periodicity is recovered fully in the Cauchy-Born approach only in the limit of infinite sample size, our strategy suggests that the cutoff scale h should be increased when the goal is to capture the phenomenon of progressively larger slips along the same slip system.

Finally, it is important to stress that despite its unusual, for plasticity theory, 'nonlinear elasticity' appearance, the MTM approach is conceptually very close to the classical continuum plasticity (CP). For instance, both theories effectively account for the complexity of energy landscape by introducing low-energy valleys describing plastic 'mechanisms'. However, if in CP, additional phenomenological relations are needed to handle the coupling between different 'mechanisms' [11, 88–91], in the MTM approach, such coupling is automatic as the model has access to the height of the energy barriers separating different low-energy valleys. It also accounts for the barriers inside such valleys, moreover the finite element representation, creates an even broader set of metastable states. A mechanical system driven elastically in the ensuing 'bumpy' energy landscape experiences a rich repertoire of snap-through instabilities which are ultimately behind the dissipative nature of the MTM. Indeed, as we have already seen, such instabilities are described implicitly by an overdamped model with relaxation time much shorter than the characteristic time of the loading. Therefore the actual dissipative process is hidden inside the local energy minimization protocol which hides rate independent plasticity behind the nonlinear elasticity appearance.

Chapter 3

Solid-to-Solid Phase Transformations

Selected peer-reviewed articles

- [P1] O U Salman, A. Gaubert, Y. Le Bouar, A. Finel. Phase field methods: Microstructures, mechanical properties and complexity. *C. R. Phys.*, 11, (3), 245-256, 2010.
- [P2] O U Salman, B Muite, A Finel, Origin of stabilisation of macrotwin boundaries in martensites, *Eur. Phys. J. B* 92 (1), 20, (2019)
- [P3] C Baruffi, A Finel, Y Le Bouar, B Bacroix, O U Salman. Atomistic simulation of martensite microstructural evolution during temperature driven $\beta \rightarrow \alpha$ transition in pure titanium. *Comput. Mater. Sci.*, 203, 111057, 2022.
- [P4] K Ghosh, O U Salman, S Queyreau, and L Truskinovsky. Slip-dominated structural transitions. *Phys. Rev. Materials* 9, 073604, 2025
- [P5] O U Salman, A. Finel, L Truskinovsky. Inertia-induced power-law scaling in martensites. *Math. Mech. Solids*, 90, 91-107, 2025.

3.1 Introduction

Solid-to-solid phase transformations represent one of the most fascinating phenomena in materials science, offering both fundamental scientific insights and transformative technological applications. These transformations, which occur without melting or vaporization, fundamentally alter a material's crystal structure, symmetry, and properties while maintaining its solid state. This chapter presents my investigations into two distinct yet equally important classes of these transformations: reconstructive transitions exemplified by the BCC-HCP transformation, and diffusionless martensitic transformations in shape memory alloys. The second class encompasses martensitic transformations—cooperative, diffusionless structural changes that underpin the remarkable behavior of shape memory alloys (SMAs). These materials can "remember" their original shape and return to it upon heating, even after significant deformation. This unique property emerges from a reversible transformation between high-temperature austenite and low-temperature martensite phases, characterized by a group-subgroup symmetry relationship and therefore, can be described by the conventional Landau theory. The transformation proceeds through coordinated atomic displacements without diffusion, creating a crystallographically reversible pathway that enables both the shape memory effect and superelasticity.

Reconstructive phase transitions, such as the BCC-HCP transformation, are the most widespread type of structural transformations in solids. In contrast, these transitions lack the simplifying group-subgroup relationship and

therefore cannot be described by the conventional Landau theory. The development of the equally encompassing theory of reconstructive transitions is still a challenge given that they involve breaking of chemical bonds and are characterized by micro-inhomogeneous configurations with slip, twinning, and stacking faults apparently intertwined.

3.2 Slip-dominated structural transitions

Having established the theoretical framework for the crystallography and continuum mechanics, we now turn our attention to reconstructive phase transitions, where the parent and product phases have fundamentally different crystal structures and cannot be related by simple elastic deformation alone. We use molecular dynamics to show that plastic slip is a crucial component of the transformation mechanism of a square-to-triangular structural transition which is a stylized analog of many other reconstructive phase transitions. To justify our conclusions we use an atomistically-informed mesoscopic representation of the field of lattice distortions in molecular dynamics simulations. Our approach reveals a hidden alternating slip distribution behind the seemingly homogeneous product phase which points to the fact that lattice invariant shears play a central role in this class of phase transformations. While the underlying pattern of anti-parallel displacements may be also interpreted as microscopic shuffling, its precise crystallographic nature strongly suggests the plasticity-centered interpretation.

The BCC-HCP reconstructive transition is one of the most representative [92–99]. Its mechanism was proposed by Burgers based on crystallographic analysis [100–107]. A salient feature of the Burgers mechanism is an interplay between a homogeneous shear and a superimposed alternating shuffling. The latter was interpreted as anti-parallel shifting of atomic layers which emerged as a result of softening of a finite wavelength phonon. However, the origin of such softening could not be addressed based on crystallography only and various attempts to interpret it included references to structural mechanics, energetics and kinetics [98, 101, 108–116]. Similar problem exists for the FCC-HCP reconstructive phase transition which can be accomplished crystallographically by the coordinated anti-parallel gliding of Shockley partials on every second close-packed crystallographic plane [117, 118]. For both of these iconic reconstructive transformations the fundamental *raison d'être* for the corresponding antagonistic displacements still remains obscure [117, 119–133], which is disappointing given that the emerging pattern of anti-parallel, crystallographically specific, nanoscale coordinated displacements is exactly the distinguishing feature of reconstructive transitions which places them outside the classical Landau picture [134–136].

In this paper we propose a novel general interpretation of the shuffling phenomenon. Our conclusions are backed by the systematic molecular dynamics (MD) studies of a prototypical model which unambiguously links the apparent shuffling with highly cooperative plastic slip. Specifically, we study the simplest transition between 2D square (S) and triangular (T) lattices [32, 74, 137]. While this square-to-hexagonal reconstructive phase change is of interest by itself [138–151], it can be considered as a stylized, low dimensional, Bravais lattice based, analog of both emblematic BCC-HCP and FCC-HCP reconstructive transitions [68, 69, 152].

To reveal the underlying plastic slip in our MD simulations, we shift attention from the conventional description of the transformation history in terms of *individual* atoms to the novel description in terms of evolving atomic *neighborhoods*. This way of post-processing of MD data allows us to map the transformation path into the configurational space of the mesoscopic metric tensors. The purely geometrical periodic tessellation of the latter creates the possibility to distinguish unambiguously between elastic and plastic deformations [32, 137, 153]. The application of such atomistically-informed representation of lattice distortions in the case of S-T transition reveals that its fundamentally non-affine mechanism involves alternating lattice invariant shears. We show that the crystallographically specific nature of such shears points towards a plasticity-centered interpretation of the underlying reconstructive transition.

To corroborate the results of the MD numerical experiments, we also performed parallel studies of an athermal molecular statics model. The obtained qualitative agreement among the two models, which differ in their microscopic details, points to the possibility that the proposed slip-related interpretation of the mechanism of the S-T transition

is a robust feature of a broad class of reconstructive transformations.

3.2.1 Preliminaries

We first discuss the proposed novel approach to the interpretation of the results of MD simulations. The main idea is to use individual atomic position data to extract the local values of the deformation gradients. This amounts to post-processing the instantaneous MD data which are then interpreted as representing piecewise linear strain fields [154–158].

Indeed, by denoting the reference discrete atomic positions \mathbf{x} and the deformed atomic positions \mathbf{y} , we can define the *approximate* deformation gradient \mathbf{F} by minimizing the error function

$$\sum \| \Delta\mathbf{y} - \mathbf{F}\Delta\mathbf{x} \|^2 \quad (3.1)$$

with summation over the pairs of elements inside the chosen neighborhood of a given site [159–165]. Suppose first that in a two-dimensional lattice a reference point is represented by a vector $\mathbf{x} = \{x_1, x_2\}$ while its known deformed position is represented by the vector $\mathbf{y} = \{y_1, y_2\}$. Then, the *exact* value of the deformation gradient

$$F_{iI} = \frac{\partial y_i}{\partial x_I}, \quad (3.2)$$

known as well; note that in (3.2) the indexes i, I refer to deformed and reference coordinate systems, respectively. Now, if in MD simulations $\mathbf{R}^{\alpha\beta}$ and $\mathbf{r}^{\alpha\beta}$ are the vectors connecting atom α with its neighbor β in the reference and in the actual configurations, the approximate deformation gradient can be obtained by minimizing mean-square difference (3.1) between the actual displacements of the neighboring atoms relative to the chosen central atom and the relative displacements that they would have had if they were in a region of uniform strain. In Fig. 3.1 we schematically show a deformation of an atomic neighborhood. Given that we deal with weakly distorted lattices the sampling neighborhood is limited here to two complementary triangular domains. In other words, as a representative atomic neighborhood we have chosen two non collinear nearest neighbors and one of the second nearest neighbors. In general, the result of the proposed approximation procedure can be written in the form [165]

$$F_{iI}^\alpha = \omega_{iM}^\alpha (\eta_{iM}^\alpha)^{-1}, \quad (3.3)$$

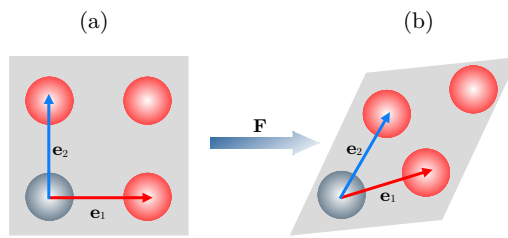


Figure 3.1: The schematic description of the deformation of the chosen ‘atomic neighborhood’ ; (a), (b) show the reference and the deformed states, respectively.

where

$$\omega_{iM}^\alpha \equiv \sum_{\beta=1}^n r_i^{\alpha\beta} R_M^{\alpha\beta}, \quad \eta_{iM}^\alpha \equiv \sum_{\beta=1}^n R_I^{\alpha\beta} R_M^{\alpha\beta}. \quad (3.4)$$

After the approximate deformation gradient

$$\mathbf{F} = \partial\mathbf{y}/\partial\mathbf{x} \quad (3.5)$$

is recovered, we can compute the atomistic metric tensor

$$\mathbf{C} = \mathbf{F}^T \mathbf{F}. \quad (3.6)$$

The possibility of mapping the results of MD simulations into the \mathbf{C} -space is of great interest because its crucial subspace,

$$\det(\mathbf{C}) = 1, \quad (3.7)$$

is naturally tessellated by the action of the global symmetry group of Bravais lattices as introduced in the previous chapter.

Additional insights can be obtained if we also project the energy landscape into the \mathbf{C} -space. To construct such a landscape it is sufficient to apply homogeneous deformation \mathbf{C} to a sufficiently large set of atoms, while accounting for all microscopic interactions. One can then use the Cauchy-Born rule [166, 167] and write

$$\phi(\mathbf{C}) = \frac{1}{2\Omega} \sum_{\mathbf{x}} \sum_{\mathbf{x}^c \in \mathcal{N}(\mathbf{x})} V(\sqrt{R_i C_{ij} R_j}), \quad (3.8)$$

where $V(r)$ is a pairwise interaction potential, R_i are the vectors representing reference points and the internal summations extend over all points \mathbf{x}^c belonging to the cut-off neighborhood $\mathcal{N}(\mathbf{x})$. In our work to ensure that a square lattice is the ground state we used the potential in the form [168]

$$V(r) = a/r^{12} - c_1 \exp[-b_1(r - r_1)^2] - c_2 \exp[-b_2(r - r_2)^2]. \quad (3.9)$$

Here r_1 is the lattice constant and r_2 is the second nearest neighbor distance and we used the parameter values $c_1 = c_2 = 2$ and $b_1 = b_2 = 8$; the choice $r_2/r_1=1.425$ produced the square ground state with a lattice constant equal to 1.0659 Å.

Note that it is sufficient to use (3.8) inside the minimal periodicity domain \mathcal{D} . The globally symmetric potential $\phi(\mathbf{C})$ can be then extended to the whole \mathbf{C} -space using the $GL(2, \mathbb{Z})$ periodicity. We recall that it implies the mapping of an arbitrary metric tensor \mathbf{C} into the domain D which produces its Lagrange-reduced image $\tilde{\mathbf{C}} = \mathbf{m}^T \mathbf{C} \mathbf{m}$ where \mathbf{m} is a unimodular integer-valued matrix. Since $\tilde{\mathbf{C}}$ is an image of \mathbf{C} inside the minimal periodicity domain, we can compute the value of the energy $\phi(\mathbf{C})$ by simply applying the equality $\phi(\mathbf{C}) = \phi(\tilde{\mathbf{C}})$ where $\phi(\tilde{\mathbf{C}})$ is obtained by our Cauchy-Born recipe (3.8).

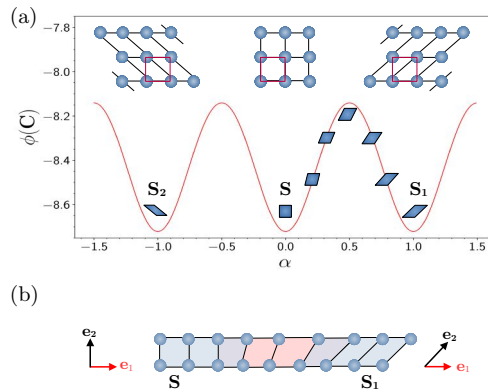


Figure 3.2: (a) Schematic representation of the strain energy $\phi(\mathbf{C})$ as a function of a simple shear amplitude α (see the text). The insets schematically depict the equivalent square lattice configurations S_2 , S and S_1 . (b) Schematic presentation of an edge dislocation.

Before we discuss the resulting energy landscape $\phi(\mathbf{C})$, it is instructive to schematically illustrate the structure of such a landscape around lattice invariant shears, which are crystallographically specific affine volume preserving deformations that map an infinite lattice into itself. We recall that the general lattice invariant shears are described by the deformation gradients represented by the integer valued unimodular matrices \mathbf{m} , see [153, 169] for the details.

To this end we can start with a square lattice (S) and deform it homogeneously applying the simple shear

$$\mathbf{F}(\alpha) = \mathbf{1} + \alpha \mathbf{e}_1 \otimes \mathbf{e}_2, \quad (3.10)$$

where α denotes the amplitude of shear, while $\mathbf{e}_1, \mathbf{e}_2$ represent unit base vectors along x and y directions, respectively.

Our Fig. 3.2(a) presents a schematic structure of the strain energy landscape $\phi(\mathbf{C})$ along such a one parametric family of homogeneous deformations. As we increase the parameter α from zero, which corresponds to a minimum of the energy, the function $\phi(\alpha)$ first reaches its maximum but then decreases reaching again a symmetry related minimum at $\alpha = 1$. At this point an equivalent lattice is obtained. Similarly, negative increment of α transforms at $\alpha = -1$ the original lattice configuration into yet another symmetric configuration with exactly the same energy. The insets of Fig. 3.2(a) schematically describe three equivalent lattice configuration S, S_1 and S_2 corresponding to three equivalent energy minima. Note that if we remove the bonds in those insets and leave only atoms, the corresponding three atomic configurations will be indistinguishable. Furthermore, our Fig. 3.2(b) presents a schematic structure of an edge dislocation which can be viewed as a ‘domain wall’ between a sheared (S_1 in this case) and undeformed (S) ‘phases’.

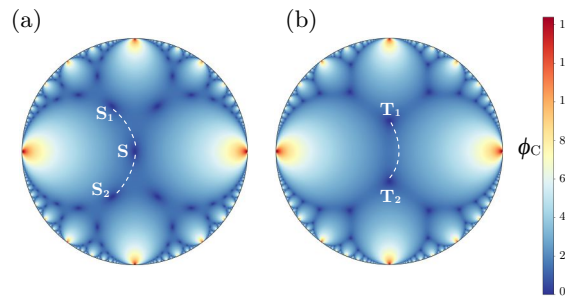


Figure 3.3: (a) Schematic presentation of an edge dislocation linking equivalent square lattices on a Poincaré disk. (b) Similar edge dislocation in the case of triangular lattice. Dashed lines represent examples of lattice invariant simple shear paths. The colors represent the strain energy level.

The complete $GL(2, \mathbb{Z})$ invariant energy landscape, emerging if we apply the Cauchy-Born rule, is shown in Fig. 3.3 (a,b). The parameters are chosen to ensure that the square lattice represent the ground state in Fig. 3.3 (a) while the triangular lattice is the ground state in Fig. 3.3 (b). In both cases the simple shear paths connecting equivalent zero energy lattice configurations are shown by white dashed curves. Thus, the equivalent square lattices S, S_1 and S_2 are linked in Fig. 3.3 (a) via the simple shear path (3.10). Similarly, the equivalent triangular lattices T_1 and T_2 can be linked via two symmetric simple shear paths only one of which is shown in Fig. 3.3(b). These paths can be viewed as a rough representation on the corresponding Poincaré disks of the cores of the associated edge dislocations.

3.2.2 Molecular dynamics

We reiterate that the goal of our MD numerical experiments was to reproduce pressure induced prototypical reconstructive phase transition from a square crystal phase (S , plane space group p4mm) to a close-packed hexagonal lattice crystal phase, interpreted here as triangular lattice (T , plane space group p6mm). The particle interaction potential was chosen in the form (3.9) where we used the fixed ratio $r_2/r_1=1.425$ to ensure that at zero pressure a square lattice with a lattice constant equal to 1.0659 \AA is in the ground state. We used a cutoff distance $r_c = 2.5 \text{ \AA}$ where the potential was smoothly reduced to zero. All the molecular dynamics simulations were carried out using LAMMPS which includes velocity Verlet algorithm [170].

We simulated 10^4 atoms with periodic boundary conditions (PBC) and typically performed 10^7 MD steps ($= 1 \text{ ns}$) in each run. First the square crystal was equilibrated within NVT ensemble with 10^5 time step sizes each equal

to $\Delta t = 0.0001$ ps. The pressure control protocol was implemented within isothermal-isobaric (NPT) ensemble till the square phase was marginalized. As

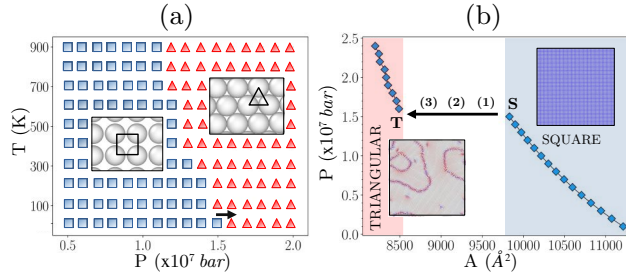


Figure 3.4: MD simulated square-to-triangular transition: (a) kinetic T-P phase diagram showing only the direct transition; (b) the same transition in P-V (area A) performed at $T = 10$ K (as indicated in (a) by an arrow).

typically done in NPT ensemble, it was the volume (area A in our 2D system) of the simulation domain that was changed to reach the target pressure [171]. To construct phase diagram, a broad range of temperatures (10 K - 900 K) and pressures (0.1×10^7 bar - 2.4×10^7 bar) was covered. Instead, to study microstructure formation we fixed temperature at $T = 10$ K.

The obtained (kinetic) T-P phase diagram addressing only the direct S-T transition is shown in Fig. 3.4(a). The predicted negative slope of the stability/coexistence curve agrees with similar numerical experiments [172–174] and is also consistent with the equilibrium data for BCC-HCP transformation in iron [175]. In Fig. 3.4(b), the same S-T transition is shown in P-A coordinates at fixed temperature $T = 10$ K. A salient feature of the observed phenomenon is that a originally pure-crystalline homogeneous square lattice transforms into a highly inhomogeneous polycrystalline texture. This is illustrated in more detail in Figure 3.5 where we zoom in into fragments of the product triangular lattice and show in the insets differently oriented hexagonal grains. The observed misorientation angles between the grains are not arbitrary. Thus, our Fig. 3.6(a) shows a fragment of the product triangular lattice featuring two grains and one can see that the basis vectors in one grain need to be rotated by 30° to transform into the basis vectors of the other grain. It is also clear that the purely crystalline grains are separated by dislocation-rich grain boundaries.

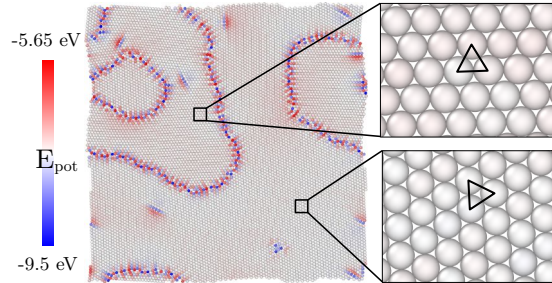


Figure 3.5: Multigrain configuration of transformed triangular lattice (T) colored according to the potential energy of each atom. The atomic structure of two triangular grains with 30° misorientation is illustrated in the insets.

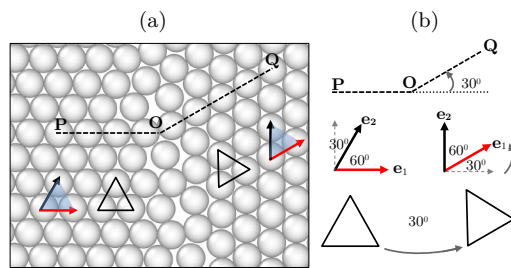


Figure 3.6: (a) A fragment of the product polycrystalline triangular phase showing two misoriented grains separated by a grain boundary; (b) basis vector e_1 and e_2 in both grains.

To rationalize the observed orientation relations, we now take advantage of the proposed novel mapping of the results of MD simulations into the \mathbf{C} -space. We begin by showing in Fig. 3.7(a) a fragment of the \mathbf{C} -space centered around the point S (taken in this case as the reference). Our Fig. 3.7(a) shows more vividly that an unbiased (pressure or temperature induced) $S \rightarrow T$ transition would be necessarily represented by two simultaneous and parallel transformation paths: $S \rightarrow T_1$ and $S \rightarrow T_2$. Both describe pure shear deformations traversing configurations with rhombic symmetry. Note that, while in Fig. 3.7(a) we show only the isochoric projection of the \mathbf{C} -space; it will be explained below that the actual $S \rightarrow T_1$ and $S \rightarrow T_2$ transitions in our MD numerical experiments also carry an attendant volumetric contraction.

Since the description in terms of metric tensors does not account for rigid rotations, it cannot be used to rationalize the observed orientation relationships between neighboring grains. To this end we need to advance from

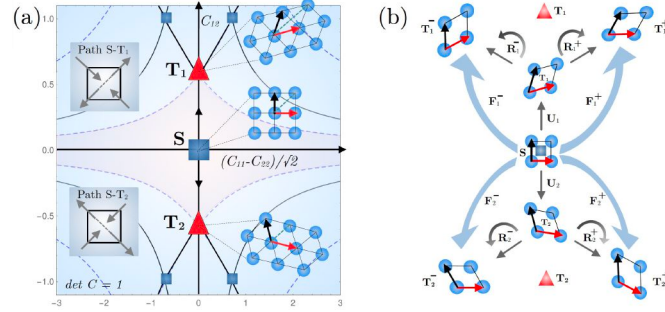


Figure 3.7: (a) A fragment of the configurational space of metric tensors \mathbf{C} showing the original square lattice (point S) and two equivalent versions of the triangular lattice (points T_1 and T_2). Solid arrows are directed along the two symmetric pure shear (rhombic) paths $S \rightarrow T_1$ and $S \rightarrow T_2$; the *elastic domain* is shown in pink; (b) A schematic structure of the four equivalent transformation paths in the extended configurational space of metric tensors \mathbf{F} .

\mathbf{C} -space to the larger \mathbf{F} -space, where expectedly an even more complex picture emerges, see our Fig. 3.7(b). Thus, the “deformation variants” in \mathbf{C} -space multiply as “orientation variants” in \mathbf{F} -space where the same metric can describe several deformation states which differ by the orientations of the basis vectors.

To be more quantitative, we observe that along the pure shear path $S \rightarrow T_1$ the stretch tensor

$$\mathbf{U} = \mathbf{U}_\diamond(\lambda) = \sqrt{\mathbf{C}_\diamond} \quad (3.11)$$

can be written in the form [176]

$$\mathbf{U}_\diamond(\lambda) = \frac{1}{2} \begin{bmatrix} \lambda + \frac{1}{\lambda} & \lambda - \frac{1}{\lambda} \\ \lambda - \frac{1}{\lambda} & \lambda + \frac{1}{\lambda} \end{bmatrix}, \quad (3.12)$$

where $\lambda = 1$ at the square phase S and $\lambda = \lambda_* = 3^{1/4}$ at the triangular phase T_1 . Along the apparently synchronous path $S \rightarrow T_2$ the stretch tensor is

$$\mathbf{U} = \mathbf{U}_\diamond(1/\lambda). \quad (3.13)$$

Note next, that both target mappings $\mathbf{U}_1 = \mathbf{U}_\diamond(\lambda_*)$ and $\mathbf{U}_2 = \mathbf{U}_\diamond(\lambda_*^{-1})$, correspond to area preserving stretchings along two opposite diagonals of a square lattice cell with one of the diagonals becoming longer than the other. These mappings, however, do not fully characterize the complete $S \rightarrow T$ transition because the underlying rigid rotation remains unspecified.

Thus, to ensure geometric compatibility of the variants T_1 and T_2 with the original square phase S , a clockwise rotation $\mathbf{R}^+(\vartheta)$ and anti clockwise rotation $\mathbf{R}^-(\vartheta)$ with $\vartheta = \pm 15^\circ$ have to be added to \mathbf{U}_1 and \mathbf{U}_2 . With such rotations included, we obtain four equivalent triangular lattices T_1^+ , T_1^- , T_2^+ and T_2^- . They are represented schematically in Fig. 3.7(b). The corresponding deformation gradients combining stretches with rotations can be

written in the form

$$\mathbf{F}_{1,2}^{\pm} = \mathbf{R}_{1,2}^{\pm} \mathbf{U}_{1,2}, \quad (3.14)$$

where

$$\mathbf{R}_1^{\pm} = \frac{1}{\sqrt{\cosh \alpha}} \begin{bmatrix} \cosh(\alpha/2) & \pm \sinh(\alpha/2) \\ \mp \sinh(\alpha/2) & \cosh(\alpha/2) \end{bmatrix}, \quad (3.15)$$

and $\alpha = 2 \ln \lambda_*$. Note that clockwise and counter clockwise rotations are denoted via ‘+’ and ‘-’ respectively. One can see that the lattice compatibility is achieved because the rotations (3.15) align the basis vector \mathbf{e}_1 , which has been already rotated by the stretches $\mathbf{U}_o(\lambda_*)$ and $\mathbf{U}_o(1/\lambda_*)$, with the horizontal direction.

We have now all the elements needed to explain the observed misorientation of the variants T_1 and T_2 in Fig. 3.5 and Fig. 3.6. Let us, for instance, evaluate the relative rotation between the T_1^+ and T_1^- neighboring triangular grains shown in Fig. 3.7. Recall that these coexisting variants are obtained from the square phase S via deformation gradients $\mathbf{F}_1^{\pm} = \mathbf{R}_1^{\pm} \mathbf{U}_1$. Given that $\lambda_* = 3^{1/4}$ and $\alpha = 2 \ln(\lambda_*)$, the corresponding misorientation angles are

$$\vartheta_{\pm} = \sin^{-1} \left[\pm \frac{\sinh(\alpha/2)}{\sqrt{\cosh(\alpha)}} \right] \frac{180^\circ}{\pi} = \pm 15^\circ. \quad (3.16)$$

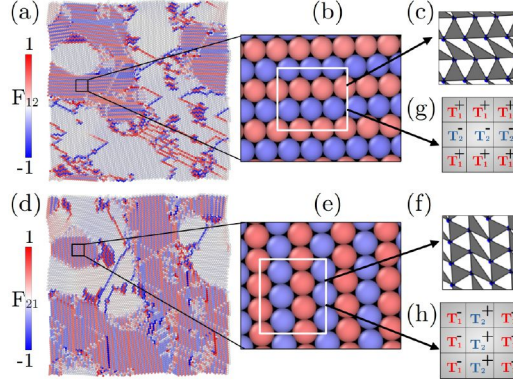


Figure 3.8: In (a), (d) we depict the MD simulated fields F_{12} and F_{21} in the transformed triangular phase. Zoomed-in views of fragments from (a,d) are presented in (b,e) where we see the corresponding atomic configurations visualized using OVITO [177]. In (c,f) we show triangulation representations corresponding to zoomed-in fragments from (b,e). In (g,h) we identify the corresponding variants $T_{1,2}^{\pm}$.

One can see that the rotations $\mathbf{R}_1^+(\vartheta)$ and $\mathbf{R}_1^-(\vartheta)$ align the basis vectors \mathbf{e}_1 and \mathbf{e}_2 of the T_1 lattice with the horizontal and vertical directions, respectively. The resulting misorientation angle between the variants T_1^+ and T_1^- is exactly 30° as we have seen in Fig. 3.6(a). Similarly, analysis for the coexisting variants T_2^+ and T_2^- shows that the corresponding misorientation angle is again 30° ; as we show below, the variants T_2^+ and T_2^- also coexist in neighboring grains separated by a grain boundary.

Indeed, our Fig. 3.8(a,d) confirms that all four variants $T_{1,2}^{\pm}$ are encountered in the grain textures obtained in the MD numerical experiments. Moreover, one can see that both atomic configuration, reached at the end of the S-T transformation, feature alternating rows/columns of positive and negative components of the deformation gradients, F_{12}^{\pm} and F_{21}^{\pm} , see Fig. 3.8(b,e). In other words, we observe two types of nano-scale mixtures: either T_1^+ and T_2^- , in Fig. 3.8(g), or T_1^- and T_2^+ , in Fig. 3.8(h). In Fig. 3.8(c,f) we show the associated Delaunay triangulation visualizing the non-affine deformation behind the apparently homogeneous lattice structure inside each of the grains.

To stress that our Fig. 3.5 and Fig. 3.8 show the outcome of the same MD numerical experiment, we present them together in Fig. 3.9. Both figures display the same transformed triangular crystal with the only difference that in Fig. 3.5 atoms are colored according to their potential energies, see the reproduction in Fig. 3.9(a), whereas in Fig. 3.8, which we present now as Fig. 3.9 (b,c), atoms inside two different triangular phase grains are colored according to the value of the particular components of the deformation gradient: F_{12} in Fig. 3.9(b) and F_{21} in

Fig. 3.9(c).

More specifically, the fragment A, shown in Fig. 3.9(a) and reproduced in Fig. 3.9(b), emphasizes the component F_{12} . It presents an example of a horizontal nano-twinning which can be also viewed as crystallographically specific finite shuffling. Instead, the fragment B, shown in Fig. 3.9(a) and reproduced in Fig. 3.9(c) emphasizes the component F_{21} . In this case the nano-twinning is vertical. Note that the special coloring of the grains in Fig. 3.9(b,c) is chosen in such a way that the gray areas always indicate that either $F_{12}=0$ or $F_{21}=0$.

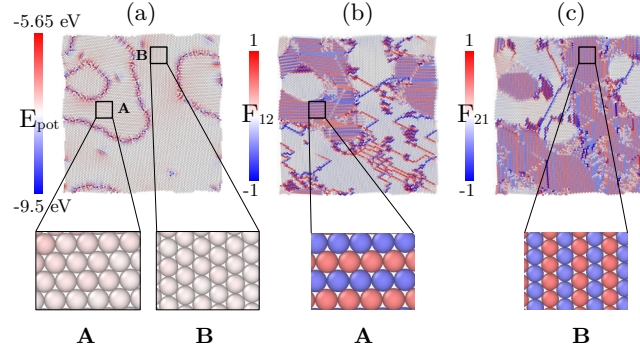


Figure 3.9: Transformed triangular polycrystal in MD numerical experiment with atoms colored using: (a) potential energies per atom, (b) F_{12} and (c) F_{21} . Two fragments A and B are also shown as insets.

The obtained numerical results suggest that the standard representation of MD data, interpreting the outcome of S-T transition as a polycrystal with misoriented homogeneous grains, is deceptive. Instead, the new way of representing such data reveals crystallographically specific nano-twinning disguised as rigid rotations. Moreover, given that the obtained antiparallel atomic displacements correspond exactly to lattice invariant shears, it is natural to interpret the resulting pattern as representing alternating plastic slips. The emerging perspective on the nature of the S-T transition complements and broadens previous studies of its mechanism which apparently overlooked the possibility that the product phase can be represented at the atomic level as a fine mixture of elementary variants [30, 32, 102, 135–137, 145, 172, 174, 178–181].

Note next that in our MD simulations the distribution of the values of the metric tensors \mathbf{C} evolved during the S-T transition. Thus, the transformation starts when all the values of \mathbf{C} were exactly the same and their distribution was fully localized. At the end of the transformation, when the T phase was nominally reached, the configurational points spread all over the \mathbf{C} -space. In Fig. 3.10, we show a fragment of the computed energy landscape around the reference configuration S which includes the two target configurations T_1 and T_2 . We mapped into the same \mathbf{C} -space all the atomic strains while showing separately the three stages (1-3) of the S-T transition indicated in Fig. 3.4(b).

Specifically, in Fig. 3.10(a) we illustrate the very beginning of the transformation when all atomic strains populate the marginally stable square configuration S located at the origin. At the intermediate stage of the transformation, shown in Fig. 3.10(b), we observe spreading of

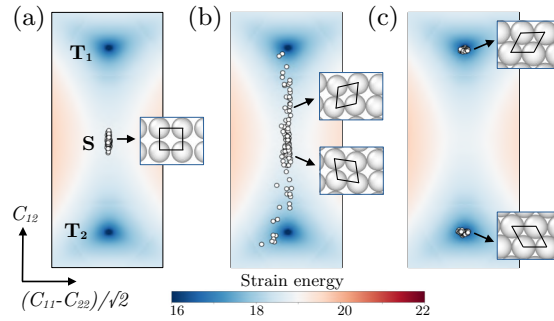


Figure 3.10: Gradual progression of the $S \rightarrow T$ transformation in **C**-space at three different stages corresponding to points (1-3) indicated in Fig. 3.4(b). Fragments of the initial square and the transformed rhombic and triangular configurations are shown in the insets. The energy landscape is visible at the background.

atomic strains along the two symmetric rhombic (pure shear) paths. The configurational points visibly advance towards two energy wells representing the variants T_1 and T_2 . We stress that both paths are pursued simultaneously. As a result, the transformed triangular phase emerges as comprised of strains populating almost equally both target energy wells T_1 and T_2 , see Fig. 3.10(c).

3.2.3 Molecular statics

In addition to standard finite temperature MD numerical experiments, we also used athermal zero temperature molecular statics (MS) protocols. This allowed us to investigate the sensitivity of the observed features of the S-T transition to temperature.

Recall that in MD simulations, we used the external pressure to induce the transition. Since in MS the thermodynamic pressure is an ambiguous concept and only virial pressure can be computed confidently, we have chosen to induce the S-T transition by changing the potential parameter of the potential [168]. Specifically, to observe triangular lattice we lowered the parameter r_2/r_1 from the original value 1.425 to 1.375 where the square lattice was almost elastically marginalized. In Figure 3.11 we

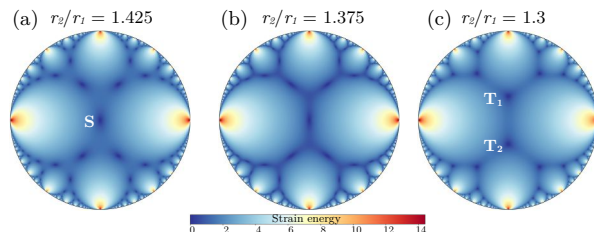


Figure 3.11: Strain energy landscape (color coded) in the configurational **C**-space (Poincaré disk) at three different values of the Boyer parameter r_2/r_1 . Letters indicate the square (S) and the two relevant triangular minima (T_1 , T_2).

illustrate the corresponding evolution of the energy landscape in the **C**-space (Poincaré disk). One can see that the location of energy minima shift from square configuration ‘S’ in Fig. 3.11(a) to triangular configurations ‘ T_1 ’ and ‘ T_2 ’ in Fig. 3.11(c).

Periodic boundary conditions were maintained throughout the simulation. Initially, a stable planar square crystal was prepared with 10^4 atoms using the same potential as in our MD simulations. Then, to induce the S-T transition in a near marginal state at $r_2/r_1 \approx 1.375$, we introduced a small disturbance by displacing all the atoms at random distances (about 0.9 % of the lattice parameter) along both x and y directions. Afterwards, the parameter was lowered further till the value $r_2/r_1 = 1.3$ where the instability took place and the conjugate gradient algorithm was used to perform local energy minimization and to locate the new equilibrium configuration.

Our numerical simulations of S-T transition using MS protocol exhibited all the main elements of the transformation mechanism observed in MD experiments. In particular, our Fig. 3.12(a-h) show that the lattice scale

alternate plastic slips involving both, atomic rows and atomic columns, have been recovered. More specifically, we observed in neighboring grains the same alternating mixtures of configurations T_1^+ , T_2^- (realized via alternating F_{12}^\pm) and of configurations T_1^- , T_2^+ (realized via

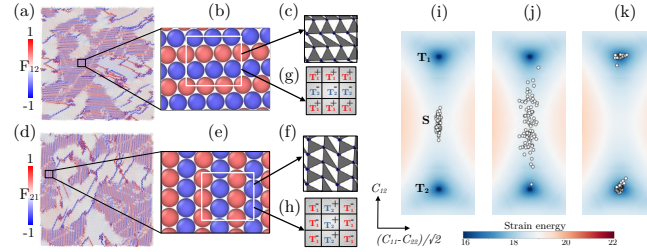


Figure 3.12: (a), (d) The distribution of deformation gradient components F_{12} and F_{21} in the transformed triangular phase obtained in MS simulations. Zoomed-in views of fragments from (a,d) are presented in (b,e) and triangulation representations of (b,e) are shown in (c,f) respectively. (g,h) shows the corresponding variants $T_{1,2}^\pm$. (i)–(k) Evolution of the atomistic strain distribution in the \mathbf{C} -space.

alternating F_{21}^\pm), see Fig. 3.12(g,h). The evolution of the strain populations inside the \mathbf{C} -space indicates basically the same mechanism involving concurrent symmetric pure shears, see our Fig. 3.12(i–k). As in our MD experiments, the spreading of atomic strains via rhombic valleys towards the triangular energy minima T_1 and T_2 took place in the form of propagating fronts separating the receding micro-homogeneous state from the expanding micro-inhomogeneous, pseudo-shuffled mixture states.

A minor difference between MD and MS numerical experiments is that in the latter the S-T transformation proceeded in almost isochoric conditions. To explain this effect we computed the radial distribution function

$$g(r) = \frac{1}{\pi r^2 N \rho} \sum_{i=1}^N \sum_{j \neq i}^N \langle \delta(\mathbf{r} - |\mathbf{r}_j - \mathbf{r}_i|) \rangle, \quad (3.17)$$

where $\mathbf{r}_j - \mathbf{r}_i$ is the distance between the atoms i and j , $r = |\mathbf{r}|$, $\rho = N/A$ is the density, N is the total number of atoms, A is the area of the system and the averaging is over angular variables. As we show in Fig. 3.13(a,b), the S-T transition results in the change of the value of the lattice constant from 1.0659 \AA [r_0 in Fig. 3.13(a)] in the ‘S’ phase to 1.14 \AA [r_{eq} in Fig. 3.13(b)] in the ‘T’ phase. The corresponding areas of the unit cell are: $r_0^2 = 1.1361 \text{ \AA}^2$ for the square lattice and $\frac{\sqrt{3}}{2} r_{eq}^2 = 1.125 \text{ \AA}^2$ for the triangular lattice (with its rhombic cell). While the ratio of the two areas is almost equal to one, $\frac{\text{area}_{\square}}{\text{area}_{\triangle}} = 1.009$, still during S-T transition the packing fraction increases. Indeed, if the triangular/hexagonal lattice is closed-packed, its square counterpart is not. Specifically, the packing fraction, defined as the ratio of the area occupied by the atoms inside the unit cell and that of the

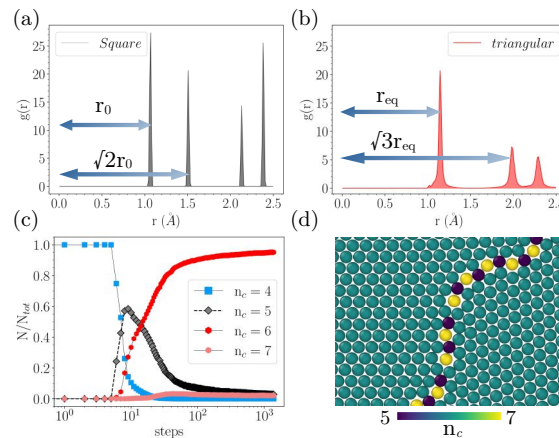


Figure 3.13: Radial distribution functions $g(r)$ for the initial square lattice (a) and for the transformed triangular crystal (b). In (c) we show the variation during the S-T transition of the fractions of atoms (N/N_{tot}) characterized by different coordination (n_c). A fragment of the misoriented triangular grains with atoms colored according to their coordination is shown in (d).

3.3 Discussion

In this chapter we showed that tracking the history of atomic-scale metric tensors in MD simulations offers a unique perspective on the intricate micro-pattern formation during reconstructive phase transitions. The proposed interpretation of MD numerical experiments reveals previously hidden details of the deformation paths allowing one to analyze systematically the underlying relation between elastic and inelastic modes.

It is appropriate to discuss here our results vis-à-vis the closely related previous 2D modeling work of Kastner *et al.* [182–185] who obtained somewhat similar conclusions despite considering a conceptually different model. In their work Kastner *et al.* used binary Lennard-Jones potential to model S-T transition in a 2D double-lattice where sub lattices were displaced by a shift/shuffle which served in their model as an independent order parameter. During their version of S-T transformation nested square unit cells were sheared into diamonds and then the interstitial atoms where first shuffled towards one of the sharp-angled corners, producing the hexagonal structure which then incorporated both sub-lattices.

Note first that in such a model there are two shear- and two shuffle-directions possible, thus *four* variants of hexagonal (triangular) phase can be identified. Instead, in our model of S-T transition in monoatomic lattices there are no shuffles and therefore there are only *two* variants of hexagonal phase. In fact, the main message of our work is that shuffle can be understood as nano-twinning involving only two variants (two energy wells). In other words, we show that quasi-shuffling does not need to be postulated separately: it can emerge in a model with two martensitic variants (instead of four) in a form of alternating nano-twinning which is a fundamentally novel observation. More generally, Kastner *et al.* interpreted their MD simulations as a model of ‘weak’ Landau-type martensitic phase transitions in shape memory alloys where the role of plasticity is usually minimal as their results also confirmed. Instead, our model deals with ‘strong’ reconstructive phase transitions where plasticity is usually thought to be playing a crucial role as it is also convincingly demonstrated by our work. We reiterate that the problematic interpretation of S-T transition as ‘weak’ is due to the fact that the two wells T_1 and T_2 are located exactly on the boundary of the *same* fundamental domain if the latter is centered around a square phase. However, as we show, they clearly belong to two *different* elastic periodicity domains if we center them around a triangular phase. In this perspective, mixing of these two wells should be considered as plastic rather than elastic deformation.

Despite the different modeling assumptions, Kastner *et al.* also observed in their numerical experiments the emergence of compatible twin variants with no lattice misfit and effectively zero interfacial energy. Their twins are characterized by alternating shear directions of unit cells (but with identical shuffle directions of sub-lattices) forming a “herring-bone pattern.” However, in contrast to our observations, their twinning mostly takes place at meso or macro scale. In particular, since they did not have our method of history recovery, they could not see whether their rotated grains are internally nano-twinned. Still, the model of Kastner *et al.* apparently allowed for the formation of some irreversible ‘defects’. Thus, they showed that during the reverse T-S transformation (unloading), their model material exhibited some plastic slip producing point defects which either glided to the surface, forming a kink, or piled up at obstacles in the bulk. In our terms, they observed a nano-scale mixing of the variants of the product phase which, however, only took place in the form of isolated defects. Instead, we observed that nominally plastic deformation takes place as a bulk phenomenon, in particular, it is responsible for the relative rotation of crystalline grains. In fact, we anticipate that the micro-mechanisms which we showed to be operative during our prototypical S-T transitions, contain some generic elements common to most reconstructive transitions including the iconic BCC-HCP and FCC-HCP transitions.

To draw some specific parallels between the observed transformation paths in 2D and the mechanism of, say, a reconstructive BCC-HCP transition in 3D [69, 137, 175], we first observe that the latter involves volume preserving pure shear deformation in addition to shuffling. However, these two phenomena appear to be well separated in time and therefore it is commonly believed that they can be formally decoupled [186]. We can then, following [102], neglect the Landau-type component of the transformation by associating the primary order parameter with the shuffle.

Note next that a classical shuffle mode would have naturally emerged in our picture of S-T transition if in our recovery of atomistic deformation gradients we had used a double unit cell [187]. Usually the BCC-HCP shuffle is perceived as proceeding via softening of an optical mode with the formation of an intermediate orthorhombic configuration. The idea is that such lowering of symmetry is maintained until the system locks-in in the higher symmetry configuration [188]. Our analysis suggests that instead of gradual softening, the emerging crystallographically specific anti-parallel shifts of consecutive planes can be viewed as a layer by layer pattern formation inside a single unit-cell (with some homogeneous adjustment layer-wise). Moreover, in the lock-in state the implied micro-heterogeneous coexistence of different variants of the orthorhombic phase, collectively recovering the HCP symmetry, can be interpreted as a special nano-twinning with individual twins distinguished by a lattice invariant shear. It is the large transformation strain in the lock-in conditions which drives the scale of such effective twinning to atomic dimensions.

The proposed analogy should be, of course, viewed only in a metaphoric sense as the actual BCC-HCP transition in 3D remains fundamentally different from the S-T transition in 2D. Thus, it is not clear whether the experimentally confirmed path for BCC-HCP transition [101] can be indeed decomposed into full plastic slips or instead represented by alternating stacking faults resulting from the passage of partial dislocations. Interestingly, the reconstructive FCC-HCP transition appear to be an example of the latter possibility as in this case instead of ‘fully’ plastic deformation we see the micro-deformation which can be interpreted as only ‘partially’ plastic. Indeed, during FCC-HCP transition the HCP phase appears to be emerging from an anti-parallel coordinated gliding of Shockley partials [122–124, 189, 190]. In the setting of S-T transformation the implied nano-scale stacking fault laminates [117, 132] would correspond to the layering of the type T_1 -S- T_2 . Since in our model the S phase is fully destabilized at the transformation threshold, such ‘partially’ plastic laminates are not observed with partials appearing only transiently as it is clear from our Fig. 3.15(a).

Our Fig. 3.14 illustrates in more detail the final strain distribution. The histogram representation of the strain distribution in Fig. 3.14(a) shows in logarithmic scale that most of the elements are in either T_1 or T_2 energy wells; this is also seen in its 2D projection shown in the Fig. 3.14(b).

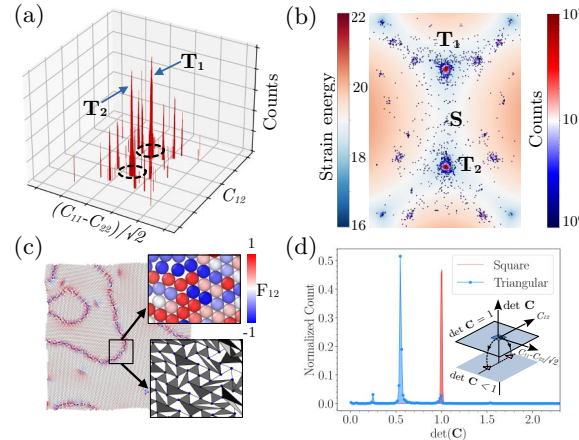


Figure 3.14: The S-T transition in the C -space. (a) 3D histogram representation of the strain distribution in triangular phase; ‘counts’ axis has a logarithmic scale. (b) the same strain distributions shown against the corresponding energy landscape. (c) A highly deformed atomic fragment around the grain boundary; both deformation gradient distribution and the deformed triangulation network are shown in the two insets. (d) The distribution of $\det C$ in the initial square (red) and the final triangular lattices (blue).

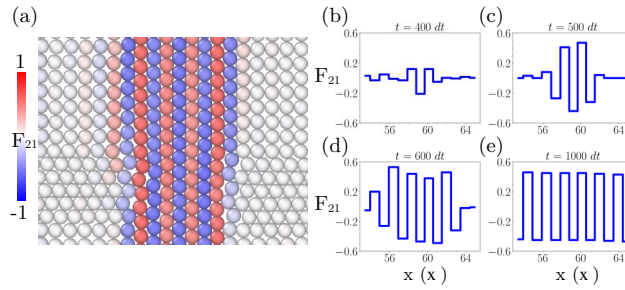


Figure 3.15: (a) Layer-by-layer propagation of the deformation gradient (here only F_{21} component) during S-T transformation; (b-e) transient spatial configurations of the deformation gradient showing the formation of an ideally periodic pattern.

Note however, that in addition to the most populated triangular configurations T_1 and T_2 , several other locations outside the T_1 and T_2 energy wells are also occupied. Most of them reflect the structure of grain boundaries like the one shown in Fig. 3.14(c). In Fig. 3.14(d) we illustrate the fact that the S-T transformation is accompanied by a volumetric contraction as the original single crystal S phase with $\det \mathbf{C} = 1$ finally transforms into the final polycrystal T phase with $\det \mathbf{C} = 0.55$.

A more detailed analysis of the stage-by-stage transformation process in the physical space, illustrated in Fig. 3.15(a), shows how the alternating micro-slips, represented by interdigitated fields F_{12} or F_{21} , are actually developing. One can see that the apparently shuffled microstructure grows layer-by-layer. More specifically, the associated nano-scale ‘zipping’ takes place through back and forth transverse propagation of Shockley partials. The possibility of such coordinated motion of surface steps has been also observed in other systems [191]. At macro scale this micro dynamics remains hidden and the transformation appears as proceeding through front propagation. While such front leaves behind a pattern of anti-parallel micro-displacements, what emerges at the macroscale is a rigid rotation of a perfect triangular lattice, see Fig. 3.15(b–e).

We stress that the revealed microscale pattern remains concealed behind the conventional interpretation of MD experiments which would present the product phase as homogeneous inside each of the grains. Instead, the proposed novel way of interpreting MD data shows that such apparently homogeneous phase is a disguised atomic scale mixture of two different but equivalent energy wells. Since the corresponding variants are geometrically compatible and the interfaces between them are energy free, the effectively plastic nature of such apparent lattice rotations has been so far hidden.

To complement the obtained picture of the direct S-T transition, we have also performed some numerical experiments where we also observed the reverse T-S transition. More specifically, we performed MD cyclic loading of our samples. The resulting hysteresis loop can be viewed as representing a succession of two, S \rightarrow T and T \rightarrow S, reconstructive transitions.

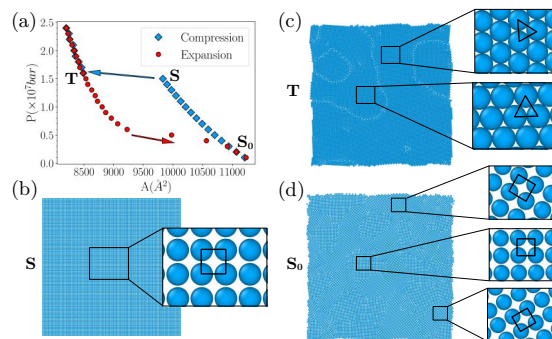


Figure 3.16: S \rightarrow T \rightarrow S reconstructive transitions in preliminary MD simulations. (a) P-V(area A) phase diagram of the complete compression-expansion cycle. With the letters S, T, and S_0 we denote : pristine square, transformed triangular lattice under compression and transformed square lattice after the subsequent expansion. Insets in (b), (c), and (d) show microscopic configurations with their associated multi-grain compositions.

In Fig. 3.16(a) we show the implied compression-tension sequence on the P-A plane. As in our previous numerical experiments, we started with a defect-free (pristine) 2D square crystal, see Fig. 3.16(b), and performed isotropic compression (by increasing hydrostatic pressure) to induce the transformation into a triangular phase. The resulting configuration of misoriented triangular grains at $P = 1.6 \times 10^7$ bar is shown in Fig. 3.16(c). We then further slightly increased the pressure up to 2.4×10^7 bar before reversing the direction of loading through gradual expansion the system via the reduction of pressure. This brought the system back into the square phase which was no longer homogeneous. Instead, we observed a texture of misoriented square grains shown in Fig. 3.16(d). While the nature of the underlying rotations will be discussed separately, here we only mention that successive $S \rightarrow T \rightarrow S \rightarrow T \rightarrow \dots$ transformations progressively increase the complexity of the variant mixture with eventual convergence to a plasticity-dominated shakedown state.

3.3.1 Conclusions

We provided compelling evidence that the proposed new perspective can reveal previously hidden details of the deformation paths of reconstructive phase transitions. The emerging new interpretation of MD data goes much beyond the conventional reasoning in terms of gamma surfaces. In particular, it brings to the forefront for the first time the dominant role in the formation of polycrystalline textures at reconstructive phase transformations of lattice invariant shears, see also [137].

Given that reconstructive phase transitions could not be rationalized in the framework of the conventional Landau theory of phase transitions, our novel approach offers a compromise: we effectively interpret lattice invariant shears as representing quasi-Landau phases. Our work can be then viewed as a response to the challenge of the development of a Landau-type theory of reconstructive transitions, offering a paradigm changing, plasticity-centered interpretation of the corresponding transformation paths. The discovered slip-dominated mechanism of reconstructive phase transitions is purely geometrical and is therefore insensitive to microscopic details. Therefore it can be viewed as a robust feature of a broad class of structural transformations including the iconic BCC-HCP and FCC-HCP transitions, where lattice invariant shears would emerge under the guise of microscale shuffling. Needless to say that we expect our theoretical predictions to stimulate considerable experimental efforts aimed at the recovery of the predicted nano-twinning patterns in realistic crystals far beyond the toy model of square to hexagonal transition.

Finally, we mention that our results have implications for the whole field of solid state physics as we build a new bridge between the microscopic stability of crystals and their macroscopic mechanical behavior usually addressed through engineering phenomenological plasticity theory. An important theoretical advance is the development of a broader perspective on structural phase transitions which goes beyond the classical Landau approach.

Chapter 4

Plastic flow in crystals

Selected peer-reviewed articles

- [P1] R Baggio, O U Salman, L Truskinovsky. Nucleation of dislocations by pattern formation. *Eur. J. Mech. A Solids*, 99, (3), 104897, 2023.
- [P2] R Baggio, O U Salman, L Truskinovsky. Inelastic rotations and pseudoturbulent plastic avalanches in crystals. *Phys. Rev. E*, 107, 025004, 2023.
- [P3] O U Salman, R Baggio, B Bacroix, G Zanzotto, N Gorbushin. Discontinuous yielding of pristine micro-crystals. *C. R. Physique*, 22 (S3), 1-48, 2021
- [P4] P Zhang, O U Salman, J Weiss, L Truskinovsky. Fluctuations in crystalline plasticity. *Phys. Rev. E*, 102, 023006, 2020.
- [P5] O U Salman, R Baggio, Homogeneous Dislocation Nucleation in Landau Theory of Crystal Plasticity, appeared in the book *Mechanics and Physics of Solids at Micro- and Nano-Scales*, (2019)
- [P6] R Baggio, E Arbib, P Biscari, S Conti, L Truskinovsky, G Zanzotto, and O U Salman, Landau-Type Theory of Planar Crystal Plasticity, *Phys. Rev. Lett.* 123, 205501, (2019)
- [P7] P Zhang, O U Salman, J Y Zhang, G Liu, J Weiss, L Truskinovsky and J Sun, Taming intermittent plasticity at small scales, *Acta Mater.* 128, 351-364, (2018)

4.1 Introduction

Despite decades of intense research, the phenomenon of *plastic yield* in crystalline solids remains enigmatic [192–201]. This phenomenon manifests as an abrupt loss of elastic rigidity, marking the transition from predominantly reversible to irreversible deformation. Two fundamental questions emerge when considering crystals under quasi-static loading: first, why does the memory of local atomic neighborhoods—which ensures elastic response—suddenly deteriorate, allowing the system to break its connection with deformation history; second, what governs the nature of post-yield plastic flow, which frequently exhibits intermittent fluctuations and scale-free spatial organization?

This work addresses these questions within the specific context of quasi-brittle plastic yielding in pristine (defect-free) crystals [9, 38, 39, 169, 202–204]. A remarkable aspect of this phenomenon is that similar quasi-brittle yielding

behavior occurs in glassy materials that lack crystalline symmetry and are structurally similar to liquids [205–214], suggesting fundamental commonalities in yielding mechanisms across different material structures.

Recent investigations of submicron crystal mechanics have revealed that traditional dislocation plasticity mechanisms undergo dramatic changes when sample dimensions fall below the micrometer scale. These small-scale crystals exhibit size-dependent strength with stress-strain responses characterized by pronounced intermittency and scale invariance across multiple length scales, independent of crystal symmetry. The measured and computed scaling exponents display unusual size dependence, challenging conventional understanding of plastic deformation.

Paradoxically, while macroscale plasticity typically associates with ductility, submicron crystal plasticity exhibits major stress drops and strain bursts reminiscent of brittle fracture. This brittleness—traditionally attributed to dislocation-free crystals—reemerges in nanoparticles and nanopillars that appear to "break plastically" through the generation of numerous globally correlated dislocations. These system-spanning events present significant challenges for controlling plastic deformation at submicron scales and compromise the reliable operation of ultra-small mechanical devices.

Quasi-brittle yielding is a salient feature of well-annealed glassy materials. In this chapter, we show that almost the same phenomenon characterizes plastic yielding in model 2D perfect crystals. In such systems the elastic stage of deformation terminates with a nonlinear elastic instability resulting in massive nucleation of dislocations. As we show this system spanning (first) yield type event effectively converts the atomic configuration from crystalline to a glassy. The subsequent deformation closely resembles quasi-brittle yielding of the ensuing pseudo-amorphous system. To corroborate these claims we present a detailed study of dislocation dynamics in a prototypical square crystal subjected to quasi-static loading. Our main tool is the mesoscopic tensorial model of crystal plasticity that we introduced. In addition to overall strain response response, the MTM approach allows one to capture intermittent statistics of dislocation avalanches. In close parallel to what is known about plasticity of glassy systems, here we also discover that both pre- and post- (second) yield avalanches in emerging 'amorphous crystal' exhibit power law statistics with matching exponents indicating marginal stability of the associated defect configurations.

4.2 Numerical experiments

4.2.1 A Single Dislocation

We begin by studying the core structure/energy of a single isolated dislocation and the long-range properties of a single dislocation introduced in the finite element mesh in MTM. To check whether the constructed MTM is adequate, we compare the output with MS simulations for crystals with triangular symmetry. We will show that while long-range elasticity is fulfilled, the dislocation core given in MTM smooths the elastic singularity because of coarse-graining, yet qualitatively gives reasonable output.

Molecular static simulations are employed to investigate the core and long-range elastic properties of a single isolated dislocation in a bi-dimensional triangular crystal. The simulations were performed using the LAMMPS open software [170].

The atoms interact via standard pairwise 6–12 LJ interatomic potentials. The potential is parametrized through the two parameters $\epsilon_{\text{LJ}} = 0.5e_{\text{LJ}}$ and $\sigma_{\text{LJ}} = 2 \sin(\pi/10)l_{\text{LJ}}$, corresponding to the energy and length scales of interaction, respectively. In the following, all quantities will be expressed in terms of the LJ units e_{LJ} and l_{LJ} .

This interatomic potential is slightly modified to be a twice continuously differentiable function [215]. To do so, the expression of the LJ potential for interatomic distances greater than $R_i = 2$ is replaced by a quartic polynomial which vanishes at a cutoff distance $R_{\text{cut}} = 2.5$ as reported in Fig. 1a. For two atoms i and j separated by a distance r_{ij} , it reads:

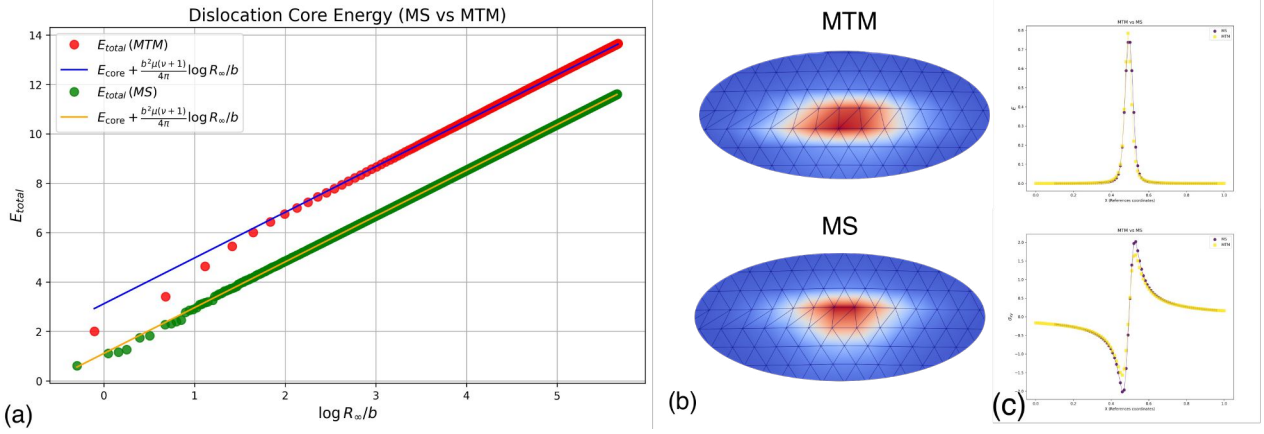


Figure 4.1: MTM vs. MS: (a) the dislocation core energy (MTM energy translated for clarity); (b), the nodal energy field ; and (c), the stress field in in MS and MTM.

$$V(r_{ij}) = \begin{cases} 4\epsilon_{\text{LJ}} \left[\left(\frac{\sigma_{\text{LJ}}}{r_{ij}} \right)^{12} - \left(\frac{\sigma_{\text{LJ}}}{r_{ij}} \right)^6 \right] + A, & r_{ij} < R_i \\ \sum_{k=0}^4 C_k (r_{ij} - R_i)^k, & r_{ij} \in [R_i, R_{\text{cut}}] \\ 0, & r_{ij} > R_{\text{cut}} \end{cases} \quad (4.1)$$

where $A = C_0 - 4\epsilon_{\text{LJ}} \left[\left(\frac{\sigma_{\text{LJ}}}{R_i} \right)^{12} - \left(\frac{\sigma_{\text{LJ}}}{R_i} \right)^6 \right]$ and

$$C_1 = \frac{\epsilon_{\text{LJ}} \sigma_{\text{LJ}}^6 (R_i^6 - 2\sigma_{\text{LJ}}^6)}{R_i^{13}} \quad (4.2)$$

$$C_2 = \frac{12\epsilon_{\text{LJ}} \sigma_{\text{LJ}}^6 (26\sigma_{\text{LJ}}^6 - 7R_i^6)}{R_i^{14}} \quad (4.3)$$

$$C_3 = -\frac{3C_1 + 4C_2(R_{\text{cut}} - R_i)}{3(R_{\text{cut}} - R_i)^2} \quad (4.4)$$

$$C_4 = \frac{C_1 + C_2(R_{\text{cut}} - R_i)}{2(R_{\text{cut}} - R_i)^3} \quad (4.5)$$

We used the cluster configuration, in which the atom positions at the edges of a cylindrical crystal are fixed after being displaced following the Volterra elastic solution displacement field \mathbf{u}^V . We introduced an edge dislocation with a horizontal slip plane and Burgers vector \mathbf{b} in the center of the cylinder. Since the material is isotropic, the elastic solution is exact and the displacement field is given by [216]:

$$u_1 = \frac{b}{2\pi} \left[\text{atan}2(X_2, X_1) + \frac{(1+\nu)X_1 X_2}{2(X_1^2 + X_2^2)} \right] \quad (4.6)$$

$$u_2 = -\frac{b}{2\pi} \left[\frac{(1-\nu) \ln(X_1^2 + X_2^2)}{4} + \frac{(1+\nu)(X_1^2 - X_2^2)}{4(X_1^2 + X_2^2)} \right] \quad (4.7)$$

Note that this two-dimensional solution corresponds to the plane strain solution with a remapping of Poisson's ratio. In the MTM model, the same displacement field is applied to the finite element nodes, whereas the strain-energy density is calculated by performing the sum in Eq. 2.13 in which the interatomic potential given in Eq. 4.1 is used.

After the minimization of the MTM and MS functionals, we obtain the equilibrium configuration shown in Fig. 4.1. In panel (a), we compare the dislocation core energies; in panel (b), the nodal dislocation energies; and in panel (c), the nodal energy and shear component of the Cauchy stress. Note that while the long-range elasticity

is perfectly reproduced in MTM, the dislocation core energy is quantitatively different. To quantify the difference, one can extract the core energy of a single dislocation using the total energy, which can be shown to follow the form:

$$E_{\text{tot}} = E_{\text{core}} + \frac{\mu b^2}{4\pi} \ln R_\infty \quad (4.8)$$

Here, E_{core} can be found by fitting the single parameter E_{fit} since all other parameters are known. We found a core energy of 1.11626 in MS and 1.10 in MTM, which are qualitatively close. A more conclusive quantitative comparison between the two models requires further study of properties such as the Peierls stress, which is currently under investigation.

4.2.2 Amorphisation of a perfect crystal

Quasi-brittle yielding is a salient feature of well-annealed glassy materials. Here we show that the same behavior is characteristic of plastic yielding in perfect crystals after they experience mechanically driven elastic instability leading to massive nucleation of dislocations. We argue that such 'preparation' effectively converts the atomic configuration from crystalline to quasi-amorphous. To understand the nature of subsequent quasi-brittle yield we study mechanical response of a prototypical 2D crystal subjected to quasistatic loading. In this section, we show that both pre- and post-yield dislocation avalanches exhibit power law statistics with matching exponents whose value is indicative of marginal stability.

The complexity of plastic yield in crystalline solids is exacerbated by the fact that both pre- and post-yield plastic flows often exhibit intermittent fluctuations and scale-free organization of dislocations [192–201]. These features are also typical for amorphous plasticity [205–214]. To build a conceptual link between the two phenomena, we study in this paper a relatively transparent prototypical example of a 2D square crystal subjected to quasistatic loading.

To prepare a 'generic' crystal we start with a pristine dislocation-free configuration and bring it to the point of mechanical instability which is resolved through massive dislocation nucleation. We argue that such 'preparation' effectively converts the atomic configuration from crystalline to quasi-amorphous [202, 217, 218]. We show that the subsequent plastic flow begins with a hardening stage, which involves a superposition of spatially localized dislocation rearrangements. Such 'microplasticity' regime is terminated abruptly with a quasi-brittle system-size event leading to the formation of multi-grain pattern arranged in the form of global shear bands. The post-yield plastic flow is characterized by a stress plateau with superimposed fluctuations representing broadly distributed intermittent dislocation avalanches. Similar quasi-brittle yield is known to be characteristic of plastic response of well-annealed glasses [219–227]. While the implied correspondence may look surprising in view of the absence of dislocations in amorphous plasticity, we recall that behind both phenomena is an evolving elastic incompatibility [228–232] with underlying elementary mechanical events represented by shear eigenstrains [233–235].

Our conclusions are based on a detailed study of dislocation dynamics in a prototypical square crystal subjected to quasistatic loading by shear strain applied along one of the slip directions. Our main tool is a novel mesoscopic tensorial model of crystal plasticity representing a conceptual trade-off between continuum and atomic descriptions [9, 38, 39, 77, 153, 169, 204, 236]. Crucially, it allows one to capture the intermittent nature of dislocation avalanches [10, 237]. In contrast, other computational approaches [7, 46, 51, 53, 56, 238–258] struggle to simultaneously reproduce the correct statistics of plastic fluctuations, account for large lattice rotations, and adequately represent the crystallographic nature of lattice-invariant shears [24, 37, 137, 259, 260].

The MTM approach assumes that mesoscale material elements experience an effective periodic energy landscape accounting for lattice-invariant shears. Within this Landau-type continuum framework with infinitely many equivalent energy wells [9, 32, 34, 35, 38, 39, 76, 77, 153, 169, 204, 236, 261–266], plastically deformed crystals emerge as multi-phase mixtures of equivalent phases. Despite operating with engineering concepts of stress and strain, MTM correctly captures both long-range elastic interactions between dislocations and their short-range interactions, including topological changes such as nucleation and annihilation [66, 68–75, 267].

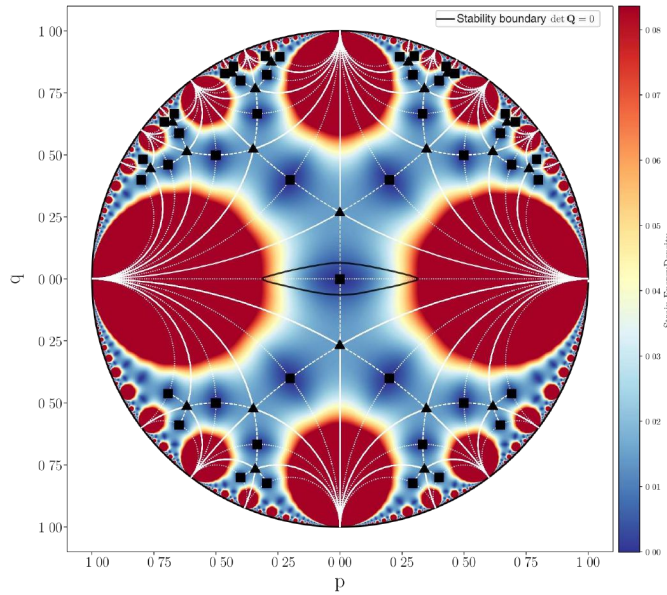


Figure 4.2: Strain-energy density landscape in the space of shear strains visualized on a Poincaré disk. The stereographic projection maps points from the configuration space (constrained by $\det \mathbf{C} = 1$) to the disk via the coordinate transformation $t = 2/(2 + C_{11} + C_{22})$, $p = t(C_{11} - C_{22})/2$, $q = tC_{12}$, ensuring that all physically accessible states map to the interior of the unit disk ($p^2 + q^2 < 1$). Thin white lines show the tessellation into equivalent periodicity domains related by $GL(2, \mathbb{Z})$ transformations. Colors represent energy levels. Stability boundaries from equation (2.32) are shown by the thick black line around the reference energy well.

Suppose that $\mathbf{y} = \mathbf{y}(\mathbf{x})$ is the deformation where \mathbf{y} and \mathbf{x} are positions of material point in the current and reference configurations. Due to frame indifference constraint, the strain energy density of an elastic solid can depend on the deformation gradient $\mathbf{F} = \nabla \mathbf{y}$, only through the metric tensor $\mathbf{C} = \mathbf{F}^T \mathbf{F}$ which then plays the role of the order parameter.

The elastic energy density $\phi = \phi(\mathbf{C})$ should also respect the symmetry of an underlying Bravais lattices going beyond the conventional continuum mechanics point group. Thus, in the corresponding 2D continuum theory one should require that $\phi(\mathbf{C}) = \phi(\mathbf{m}^T \mathbf{C} \mathbf{m})$, where \mathbf{m} belongs to $GL(2, \mathbb{Z}) = \{\mathbf{m}, m_{IJ} \in \mathbb{Z}, \det(\mathbf{m}) = \pm 1\}$. In view of this global symmetry, the surface $\det \mathbf{C} = 1$ in the 3D space (C_{11}, C_{22}, C_{12}) is tessellated into an infinite number of equivalent periodicity domains. The structure of the minimal tensorial periodicity domain \mathcal{D} , is discussed in the previous section; if the energy density is known in one of such domains, it can be extended to the whole configurational space by symmetry.

In our numerical experiments we used the simplest function $\phi(\mathbf{C})$ with required periodicity discussed in the second chapter. In Fig. 2.2 we illustrate the corresponding multi-well energy landscape with bottoms of the wells corresponding to lattice invariant deformations. One can show that such a landscape contains a network of low energy valleys along the directions representing plastic 'mechanisms', simple shears parallel to crystallographic slip planes. Along these valleys the energy wells correspond to the equivalent replicas of the reference square lattice.

The presence of a complex system of energy barriers separating individual quantized lattice invariant shears makes the function $\phi(\mathbf{C})$ highly nonconvex. Therefore, as in every Landau type continuum theory, the corresponding scale free problem is highly degenerate. Instead of conventional Ginzburg-type gradient regularization, we introduce in MTM a uniform mesoscale grid and attribute elastic response to discrete elements whose linear size h is then viewed as a physical parameter of the model. In other words, we reduce the space of admissible deformations to a finite dimensional set of compatible, piece-wise affine mappings.

It is clear that the ensuing mechanically driven system will experience a rich repertoire of instabilities. In particular, under quasistatic loading conditions the incremental elastic energy minimization will lead to a succession of jump discontinuities representing elastic branch switching events. The corresponding energy losses will then mimic dissipative processes which will merge in the continuum limit producing what is known as rate-independent plasticity [268].

In our numerical experiments, a square crystal sample was discretized with $N \times N$ nodes, which were triangulated into $2N^2$ finite elements. We used $N = 400$. We loaded our athermal system quasi-statically by applying the affine displacement field $\mathbf{u}(\alpha, \mathbf{x}) = (\bar{\mathbf{F}}(\alpha) - \mathbb{1})\mathbf{x}$, with $\bar{\mathbf{F}}(\alpha) = \mathbf{I} + \alpha \mathbf{e}_1 \otimes \mathbf{e}_2$, where \mathbf{e}_i is the orthonormal basis of the reference lattice. Such loading was chosen to represent simple shear along one of the principal slip directions, with shear amplitude α serving as the loading parameter. By changing this parameter in strain increments of order 10^{-6} , we advanced the loading, and after each increment the displacement field was updated by the energy minimization algorithm. To implement periodic boundary conditions, we use the following algorithm: To simulate an effectively infinite crystal under controlled macroscopic affine deformation, we use the method of domain replication. Starting from the computational domain Ω_0 with dimensions $L_x \times L_y$, we generate a periodic lattice of domains using translation vectors $\mathbf{t}_n = \begin{pmatrix} n_x L_x \\ n_y L_y \end{pmatrix}$, where $\mathbf{n} = (n_x, n_y) \in \{-1, 0, 1\}^2$. Let $\bar{\mathbf{F}}(\alpha)$ denote the macroscopic deformation gradient tensor at the parameter value α . Under such affine deformation, the position of replicated domains relative to the central domain Ω_0 is given by: $\mathbf{R}_n = \bar{\mathbf{F}}(\alpha) \cdot \mathbf{t}_n$, where \mathbf{R}_n represents the displacement vector of the origin of the domain associated with \mathbf{t}_n . Then, for a node located at position \mathbf{x}_i in the central domain Ω_0 , its periodic image, associated with the translation vector \mathbf{t}_n , is at: $\mathbf{x}_i^{(n)} = \mathbf{x}_i + \mathbf{R}_n = \mathbf{x}_i + \bar{\mathbf{F}}(\alpha) \cdot \mathbf{t}_n$. Such correspondence ensures that the macroscopic deformation gradient $\bar{\mathbf{F}}(\alpha)$ is consistently applied across all periodic images of Ω_0 . After establishing the positions of all nodes across the nine domains (original domain Ω_0 and its eight periodic images), we perform a Delaunay triangulation on the complete set of particles: $\mathcal{P} = \{\mathbf{x}_i : i \in \mathcal{I}_0\} \cup \{\mathbf{x}_i^{(n)} : i \in \mathcal{I}_0, n \neq \mathbf{0}\}$, where \mathcal{I}_0 denotes the set of particle indices in the original domain and $\mathbf{0} = (0, 0)$ corresponds to the null translation vector. Using the obtained global triangulation \mathcal{T} , we select the triangles that have at least one vertex belonging to the original domain Ω_0 . However, since triangles near periodic boundaries may be identified multiple times through different domain images, we enforce uniqueness by mapping all vertex indices to their representatives in Ω_0 and using the sorted tuple of these representatives as a canonical identifier. A triangle is included in $\mathcal{T}_{\text{unique}}$ only upon its first encounter, ensuring each physical triangle is counted exactly once. This selection procedure ensures that: (i) Each triangle in the computational mesh is counted exactly once, eliminating redundancy from the periodic extension; (ii) All triangles connected to the original domain are included, maintaining proper connectivity across periodic boundaries; (iii) The triangulation naturally incorporates the macroscopic deformation through the deformed positions of the periodic images. The selected set of triangles $\mathcal{T}_{\text{unique}}$ forms the computational mesh for the MTM calculations while implementing the periodic boundary conditions and ensuring consistency with the applied macroscopic deformation gradient $\bar{\mathbf{F}}(\alpha)$.

To 'prepare' a generic sample we first loaded a pristine (defect-free) crystal. The associated purely elastic homogeneous deformation became unstable at a critical value of the loading parameter $\alpha = \alpha_c \approx 0.138$, which is well approximated by the value corresponding to the loss of positive definiteness of the acoustic tensor, see [269–271]. The stability envelop of the homogeneous solution for any shear deformation is shown by the thick black line around the reference first energy well calculated using Eq. 2.32. At this level of the load, the homogenous solution ceases to be stable and a short-wave instability develops as described in [169]. The breakdown of an elastic state took the form of a major system-size inelastic deformation transforming a perfect crystal into a dislocation-rich quasi-amorphous configuration, see Fig. 4.3 where the highest stress levels correspond to the location of dislocation cores. Note that the stabilization of the global dynamic restructuring process can be expected to produce only a marginally stable state.

Having 'prepared' a generic sample, we continued to load it using the same athermal quasistatic loading protocol. The ensuing stress-strain response of our quasi-amorphous crystal is illustrated in Fig. 4.4. Note the presence of irregularly placed elastic branches interrupted by abrupt stress drops; the latter represent intermittent plastic avalanches which involve partial or complete unlocking of dislocation structures. One of these avalanche-type events, representing a major multi-stage stress drop, stands out, which suggests that there are two different regimes. While the first regime is characterized by plastic hardening, the second regime, represented by a stress plateau, suggests quasi-stationary plastic flow, see Fig. 4.4. It is natural to interpret the abrupt system-size event dividing these two regimes as a quasi-brittle plastic yield.

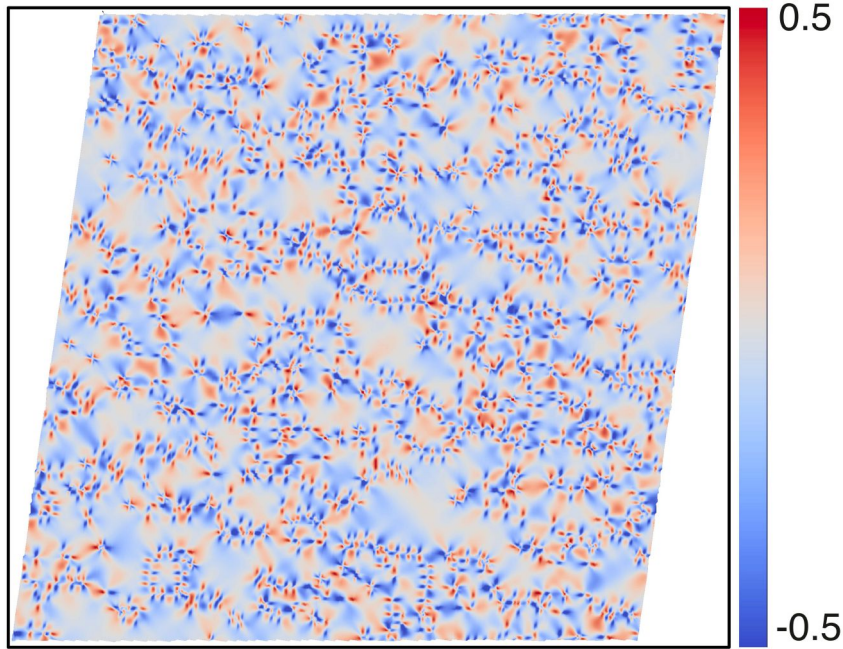


Figure 4.3: Dislocated configuration emerging after a homogeneous lattice is mechanically driven to the threshold of elastic instability. Colors indicate the level of the shear component of the Cauchy stress tensor.

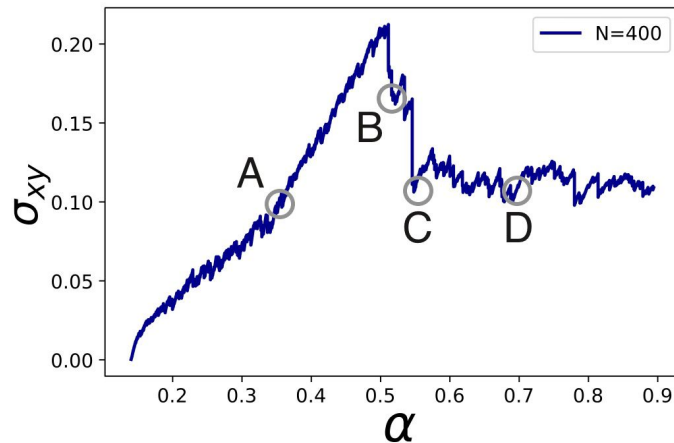


Figure 4.4: Stress-strain response of a quasi-amorphous crystal shown in Fig. 4.3.

Fig. 4.5 shows the stress field in a typical pre-yield state. Its comparison to Fig. 4.3 suggests that the restructuring is relatively minor with mostly preexisting mobile dislocations moving between the locking sites formed by immobilized dislocations. In other words, dislocations appear to be confined inside the effective cages where they can pile up but from where they can only rarely escape by breaking the existing locks. Overall, such a quasi-elastic regime preceding macroscopic quasi-brittle yield can be characterized as 'microplasticity' which is known to be characteristic of pre-yield behavior for both crystalline and amorphous solids [195, 272–276].

The quasi-elastic regime ends with discontinuous yield which is highly reminiscent of mechanical response of well annealed 'brittle' glasses; the phenomenon of plastic brittleness is also a characteristic feature of sub-micron crystal samples with high initial purity [277–287]. As we see in Fig. 4.4, the global restructuring event takes the form of a two-stage transition $A \rightarrow B \rightarrow C$. The snapshots of the spatial dislocation microconfigurations in the states B and C are shown in Fig. 4.6 where we already see the evidence of a collective dislocation activity which leads to the emergence of global structures in the form of system-spanning shear bands.

Additional important details can be seen in Fig. 4.7 where we illustrate the strain-energy density field in state C . Here, for instance, one can distinguish dislocations of different sign via Delaunay triangulation (see inset in Fig. 4.7): nodes with five (seven) neighbors are shown in blue (red), and dislocations correspond to adjacent

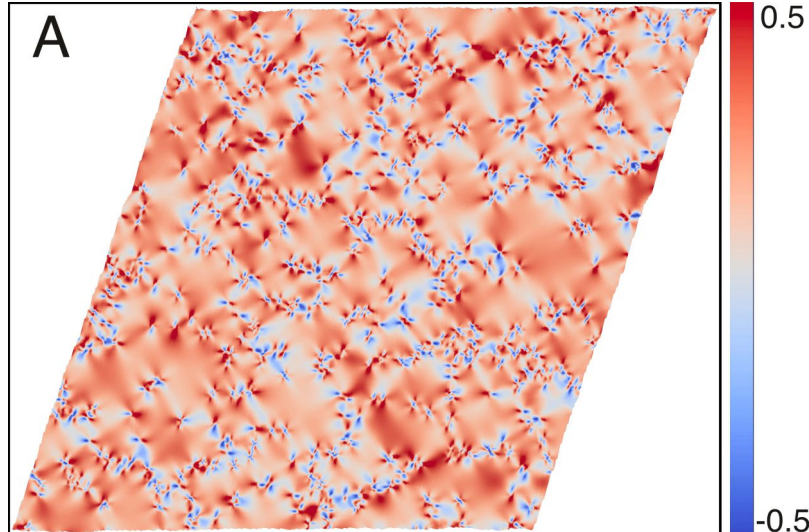


Figure 4.5: Dislocated configuration in a typical pre-yield state characterizing the stage of 'microplasticity'. The state *A* is marked in Fig. 4.4. Colors indicate the level of the shear component of the Cauchy stress tensor.

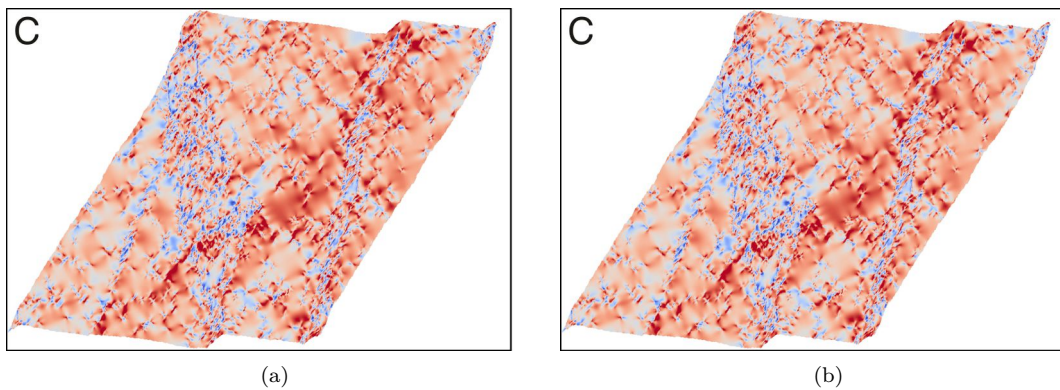


Figure 4.6: Dislocated configuration characterizing different stages of unfolding of the quasi-brittle system size event. The states *B* and *C* are marked in Fig. 4.4. Colors indicate the level of the shear component of the Cauchy stress tensor.

pairs where the ordering 5-7 or 7-5 determines the sign. It also becomes visible that the shift from 'local' to 'global' dislocation rearrangements leads to the development of dislocation-free rotated patches of the original lattice forming the polycrystalline grain texture inside the shear bands. The misorientation of neighboring grains is controlled by the overall compatibility of the deformation field. The emergence of special highly optimized grain boundaries, in particular, the ubiquitous presence in such patterns of low energy $\Sigma 5$ grain boundaries, has been discussed in [39], see also [288–290].

The post-yield regime characterized by relative stabilization of the average stress level can be interpreted as a quasi-stationary non-equilibrium steady state. A representative snapshot of the microconfiguration of the crystal in state *D* is shown in Fig. 4.8 where we see further development of the polycrystalline grain texture. The intermittent avalanches characterizing this regime represent bigger grains occasionally merging to form larger grains while small grains continue to nucleate. In this way the process of self-organization of dislocations within the widening shear bands continues to produce additional scales developing into a global hierarchical structure. Overall the system transitions from isolated dislocation motion to collective dislocation behavior as it gains access to a much broader repertoire of large-scale relaxation mechanisms. A detailed analysis of the avalanche structure shows that while in the pre-yield regime plastification occurs primarily in isolated, linear arrangements of transformed elements showing minimal branching, the configuration of a typical post-yield avalanche reveals extended plastified regions with complex branching.

The value of the power-law exponent $\epsilon = 1.0$ is a signature of an archetypically 'wild' crystal plasticity in the

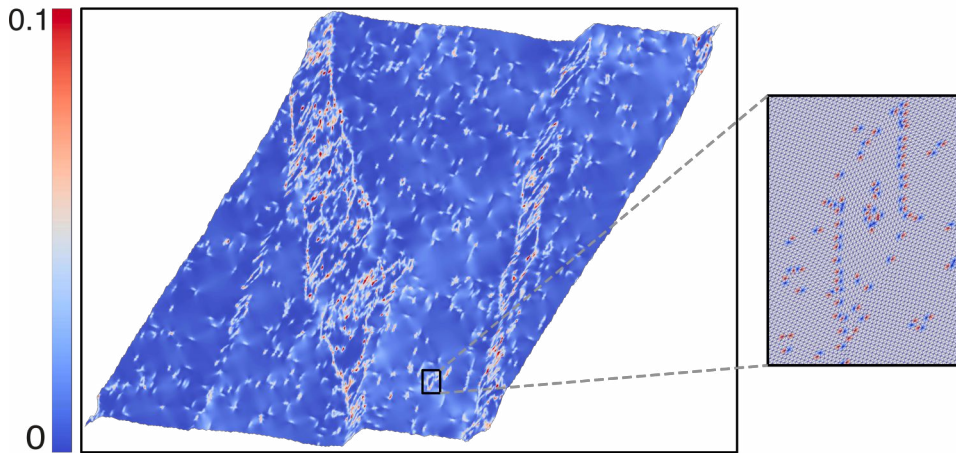


Figure 4.7: The micro-configuration configuration corresponding to the state C marked in Fig. 4.4. Colors indicate the magnitude of strain-energy density. The inset shows a single grain and details the dislocation structure of the grain boundaries.

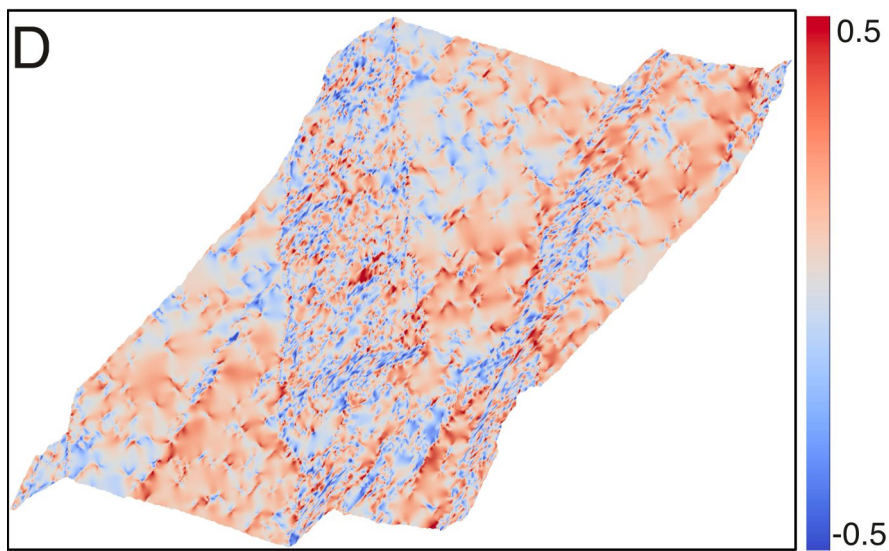


Figure 4.8: Mature shear bands in the regime of stationary post-yield plastic flow represented by the state D marked in Fig. 4.4. Colors indicate the level of the shear component of the Cauchy stress tensor.

sense of [237]. The same value was obtained in discrete dislocation dynamics studies of disorder-free 2D samples containing a fixed number of preexisting dislocations [246, 291] and also recorded in numerical experiments on pristine crystals using a scalar version of the MTM [9]. The exponent $\epsilon = 1.0$ has been previously interpreted in crystal plasticity framework as representing either dislocation jamming or self-induced glassiness [217, 292–294]. The latter conclusion is corroborated by the fact that the same value of the exponent is routinely recorded in the studies of plastic flows in structural glasses [207, 295, 296].

A theoretical understanding of the relation between the emergence of the power law exponent value $\epsilon = 1.0$ and the structure of the underlying energy landscapes has been developed in the theory of spin glasses, where it was shown that the hierarchical (ultrametric) organization of energy wells in the phase space results in an intermittent, scale-free response to quasistatic deformation [297–300] and that in the mean-field limit the associated distribution of energy avalanches must be of a power law with $\epsilon = 1.0$. In this context it was also understood that the reason behind this value of the exponent is the marginal stability of the system [297, 301, 302].

Since glasses represent liquids at a quenching threshold, their marginal stability is not surprising, for instance, similar marginality is exhibited by jammed states of granular matter. If such marginally rigid systems are mechanically driven, the proximity to unstable modes makes the mechanical response inherently intermittent, effectively mixing statics (stability) and dynamics (instability). Recall that our 'quasi-amorphous crystal' also emerged from

arrested dynamics with the system being stabilized close to the threshold of mechanical stability. One can argue that in such cases the self-generated disorder brings the system directly from solid to glassy state. Since we observe the same value of exponent $\epsilon = 1.0$ in both pre- and post-yield regimes, we may conclude that the achieved marginality is not even affected by the quasi-brittle yielding event. This may mean that the brittle yielding does not compromise the global organization of the emerged energy landscape while obviously affecting the reachability of its different subdomains [303–305].

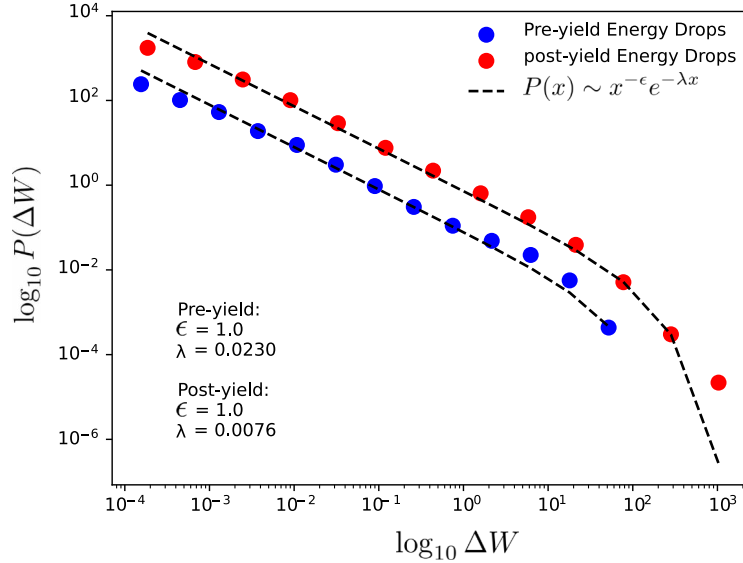


Figure 4.9: Probability distribution of energy drops during avalanches in pre- and post-yield regimes.

Note next that the pre-yielding value of the cutoff parameter $\lambda = 0.0230$ is drastically different from its post-yielding value $\lambda = 0.0076$. The approximately three-fold decrease of the value of λ after yielding indicates that large energy drops become substantially more probable in the post-yield regime. The emergent collective behavior in this regime manifests itself in a much broader extent of avalanche activity reaching the size of the system and in this sense the system shows the signs of divergence of the characteristic length $l \sim 1/\lambda$.

This conjecture is supported by the observation that shear bands in the post-yield regime traverse the whole computational domain which is in stark contrast to unequivocally subextensive localized dislocation rearrangements taking place in the pre-yield regime. The physical nature of the implied criticality is presently actively debated [9, 306–310].

Finally we mention that if intermittent fluctuations in amorphous plasticity are usually modeled in terms of elasto-plastic models [219, 296, 311, 312], the MTM approach to crystal plasticity is very similar, basically operating within the same finite element setting. The difference is that the phenomenological yield thresholds are modeled in MTM by elastic instabilities reflecting the structure of the geometrically conditioned energy landscape while the fixed elastic propagators are replaced by the solution ‘on the fly’ of the corresponding nonlinear elasticity problems. The implied nonlinearity is also of universal nature as it originates from the geometrically exact description of deformation allowing one to handle adequately both finite rotations and elastic compatibility.

In this paper we performed a series of numerical experiments aimed at deeper understanding of the phenomenon of plastic yield in model 2D crystals in the limit of zero strain rate and negligible thermal effects. While it is known that quasi-brittle yielding is a salient feature of well-annealed glassy materials, we showed that generic crystals can exhibit remarkably similar phenomenology after the necessary level of annealed disorder emerges from dislocation self-organization after the breakdown of an affine elastic configuration. One of our main findings is that in the ensuing quasi-amorphous crystals both pre- and post-yield avalanches exhibit power law statistics with matching exponents indicative of hierarchical structure of the underlying energy landscape and marginal stability of the associated mechanical system. It would also be intriguing to explore whether crystals with higher triangular symmetry exhibit similar behavior and to assess whether the specific choice of strain-energy density functional

plays a crucial role in these phenomena. More work is needed to turn our initial insights into an understanding of similar phenomena in realistic 3D crystals with HCP, FCC and BCC symmetry. In particular, only a 3D model will distinguish adequately between edge and screw dislocations, and will be suitable to handle realistic dislocation entanglements. It will then be able to capture such important physical effects as dislocation climb, cross slip and forest hardening.

The value of the power-law exponent $\epsilon = 1.0$ has been encountered in the studies of crystal plasticity even if in somewhat different contexts. Thus, it was found to be a signature of an archetypically “wild” crystal plasticity in the sense of [237]. An almost the same value of the power-law exponent $\epsilon = 1.0$ was obtained in discrete dislocation dynamics (DDD) studies. In their numerical experiments conducted on disorder-free 2D samples containing a fixed number of preexisting dislocations the authors associated exactly this value of the power-law exponent with extended range of steady plastic flow [246, 291]. The exponent $\epsilon = 1.0$ was also recorded in numerical experiments involving pristine crystals conducted using the scalar version of the MTM [9]. Overall, in the literature on crystal plasticity the exponent $\epsilon = 1.0$ has been previously linked with either dislocation jamming or self-induced glassiness [217, 292, 293, 313].

Some theoretical understanding of the relation between the emergence of the power law exponent value $\epsilon = 1.0$ and the structure of the underlying energy landscapes has been obtained in the case of spin glasses. Thus, it was shown that the hierarchical (ultrametric) organization of energy wells in the phase space results in an intermittent, scale-free response to quasi-static deformation [297–300]. Moreover, it was shown that in the mean-field limit the associated distribution of the dissipated energy must necessarily follow power law with exponent exactly equal to $\epsilon = 1.0$. It was also understood that the reason behind this value of the exponent is the marginal stability of the system [297, 301, 302]. Note that the same arguments have been used to rationalize the observation of the same exponent $\epsilon = 1.0$ in numerical studies of quasi-elastic flow of structural glasses [207, 295, 296].

We recall that marginality of structural glasses is usually linked to the fact that they emerge when liquid is brought exactly to its quenching threshold. Similar type of marginality is also exhibited by jammed states of granular matter that are also expected to be at the threshold between liquid and solid behavior. In both cases ‘rigidity’ results from the fact that dynamics has just subsided which explains why the ensuing stability is only marginal. In such states the closeness to unstable modes makes the mechanical response inherently intermittent, effectively mixing dynamics and statics. In the same spirit, the recovery of the exponent $\epsilon = 1.0$ in our numerical experiments may be suggesting that our ‘amorphous crystal’ is posited exactly at the threshold of mechanical stability. This is, in fact, not surprising since the stabilization in the ‘amorphous crystal’ state was achieved exactly at the end of the first system-size avalanche. Apparently, the associated fast time dynamics brought into the system exactly the level of self-generated disorder needed to transform a stable (elastic) state into a marginally stable (glassy) state. Since we observe the same value of exponent $\epsilon = 1.0$ in both pre- and post-yield regimes, the achieved marginality is not even affected by the catastrophic yielding event. This may mean that the brittle yielding transition does not compromise the global organization of the emerged energy landscape while obviously affecting the reachability of its different subdomains.

In contrast to the exponent ϵ , the cutoff parameter λ differs drastically between the pre-yielding regime, where $\lambda = 0.0230$, and post-yielding regime, where $\lambda = 0.0076$, even though in both cases we deal with the same system size. The approximately three-fold decrease in λ after yielding indicates that large energy drops become substantially more probable in the post-yield regime. This is a clear evidence of an emergent collective behavior which manifests itself in a much broader extent of the post-yield avalanches. Effectively we observe in the post-yield regime an evidence of a divergence of the characteristic length

$$l \sim 1/\lambda. \quad (4.9)$$

This conjecture is supported by the observation that shear bands in the post-yield regime traverse the whole computational domain reaching the size of the system. This is in stark contrast to unequivocally subextensive localized rearrangements taking place in the pre-yield regime. It is appropriate to evoke here that the divergence

of the correlation length is one of the major indicators that the system has reached a critical state. The physical nature of the associated generic (extended) criticality is presently actively debated [226, 306–308, 310, 314].

Finally we mention that our results clearly indicate that the values of parameters ϵ and λ reflect different aspects of the self-organization processes taking place during plastic deformation. The persistence of ϵ over the yielding transition and the variability of λ raises important question about the physical nature of the associated quasi-abrupt emergence of complex long-range correlations which ultimately transforms crystallinity into glassiness.[303, 315, 316].

4.3 Rebonding algorithm

In the preceding section, we demonstrated that the MTM model, founded on the minimization of strain-energy density while respecting $GL(2, \mathbb{Z})$ -symmetries, successfully captures the essential mechanics of crystal deformation. The model's theoretical elegance and computational efficiency make it a valuable tool for simulating large-scale crystal behavior.

However, a closer examination of the finite element kinematics reveals a significant practical limitation. As the crystal undergoes the extreme deformations—with local shear strains often exceeding several hundred percent—the underlying triangular mesh that keeps the initial connectivity fixed becomes severely distorted. Individual elements shear to accommodate these deformations, resulting in highly anisotropic and poorly conditioned triangulations. This geometric degradation is not without consequences: *it influences the kinematic constraints and results in lock-in effects of dislocation passing through dislocation free but already sheared regions*. Note that this effect is present in any variant of MTM type of models [317–322] and is not addressed so far. Regions of high distortion can introduce spurious numerical artifacts, alter the effective material response, and compromise the fidelity of damage localization predictions.

Figure 4.10 provides a clear visualization of this mesh distortion issue. The color-coded strain-energy distribution shows strong localization in highly sheared regions, while the inset detail reveals the extreme geometric distortion of individual triangular elements—illustrating the source of the kinematic constraints and lock-in effects discussed above.

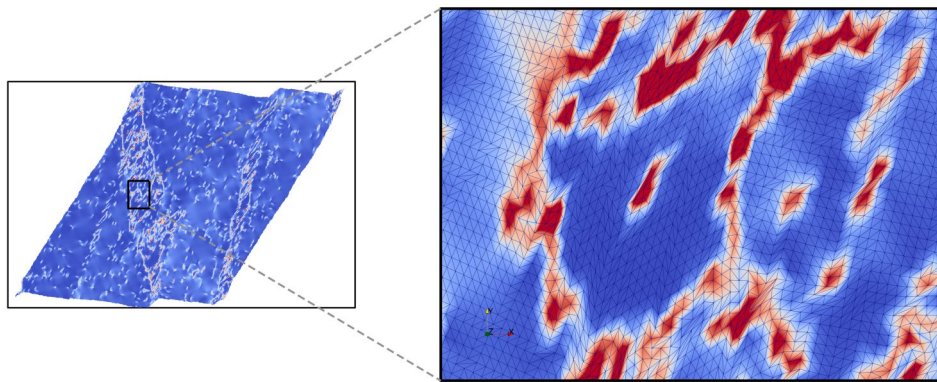


Figure 4.10: Microconfiguration corresponding to state C marked in Fig. 4.4. Color indicates strain-energy density magnitude. The inset highlights a region of severe deformation in which triangular elements undergo large distortions while preserving the initial nodal connectivity.

To address this challenge, we introduce a novel *rebonding algorithm* that dynamically adapts the mesh connectivity during the deformation process. Rather than allowing triangles to deform indefinitely, the algorithm strategically re-establishes bonds—effectively re-triangulating—when geometric quality metrics fall below prescribed thresholds. This approach preserves the mechanical integrity of the simulation while maintaining consistency with the underlying variational framework. In what follows, we detail the mathematical formulation of the rebonding criterion, its integration within the computational framework, and its impact on both mesh quality and solution

accuracy.

The rebonding algorithm is activated whenever the metric tensor of a finite element exits a carefully defined domain in metric space. Specifically, we monitor the condition

$$-\frac{1}{2} \min(C_{11}, C_{22}) < C_{12} < \min(C_{11}, C_{22}), \quad (4.10)$$

which defines a region that encapsulates the reference square lattice (at $C_{11} = C_{22} = 1$, $C_{12} = 0$) and the equilateral triangular lattice (at $C_{11} = C_{22} = \gamma^2$, $C_{12} = \gamma^2/2$ with $\gamma = (4/3)^{1/4}$). This domain is visualized in Figure 4.11 using the Poincaré disk representation of the metric space. Crucially, all lattice-invariant shears—those transformations that preserve the lattice structure under $GL(2, \mathbb{Z})$ symmetries—lie precisely on the boundaries of this domain (shown as dashed lines in Figure 4.11). Therefore, when an element’s metric violates these bounds, it signals that a lattice-invariant shear transformation has occurred, triggering the rebonding procedure. The rebonding algorithm itself consists of a Delaunay triangulation applied to the current nodal positions, from which new finite elements are constructed. This Delaunay retriangulation restores optimal mesh quality—maximizing the minimum angle of triangles—while respecting the crystallographic structure. This geometric criterion ensures that mesh adaptation occurs exactly when needed: at the moment when further element distortion would represent a physically equivalent but numerically degraded lattice configuration.

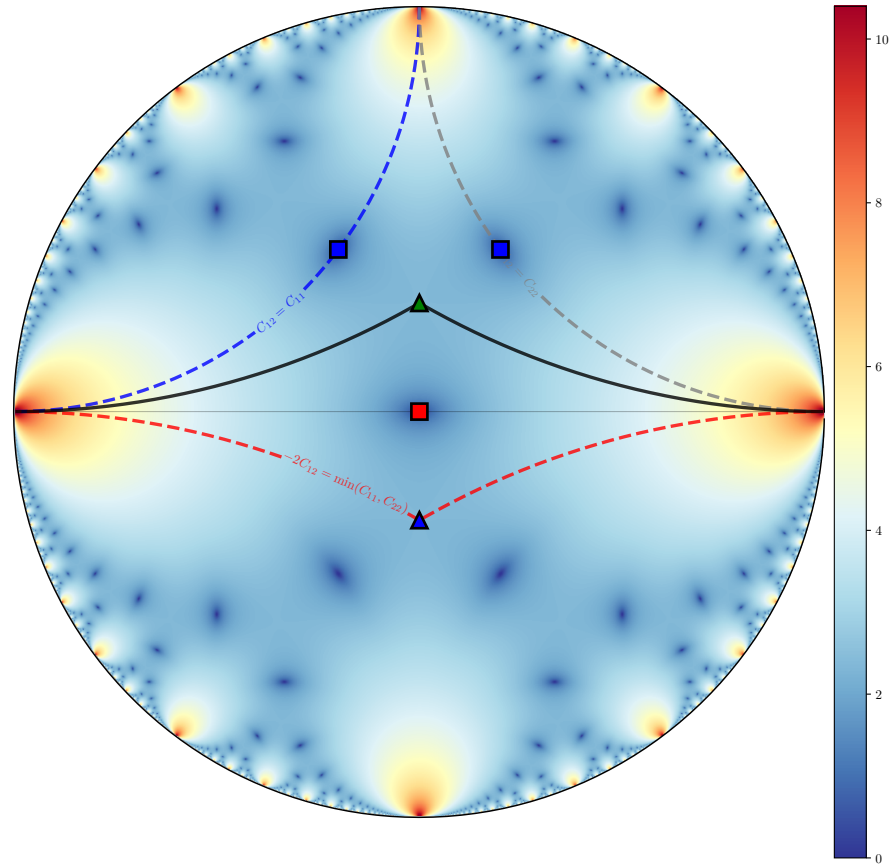


Figure 4.11: Poincaré disk representation of the metric space showing the fundamental domain (interior region bounded by dashed lines) defined by $-\frac{1}{2} \min(C_{11}, C_{22}) < C_{12} < \min(C_{11}, C_{22})$. The red square ($C_{11} = C_{22} = 1$, $C_{12} = 0$) and red triangle ($C_{11} = C_{22} = \gamma^2$, $C_{12} = \gamma^2/2$) mark the original reference states for the square and equilateral triangular lattices, respectively. Blue markers indicate their first $GL(2, \mathbb{Z})$ copies, representing equivalent lattice configurations obtained through lattice-invariant shear transformations. Boundary lines represent: $C_{12} = C_{11}$ (blue), $C_{12} = C_{22}$ (gray), and $-2C_{12} = \min(C_{11}, C_{22})$ (red). The rebonding algorithm is triggered when a single element metrics exit this domain.

The rebonding algorithm operates iteratively: (i) solve the mechanical equilibrium equations via energy minimization, (ii) compute the metric tensor C_{ij} for each finite element and verify that $-\frac{1}{2} \min(C_{11}, C_{22}) < C_{12} <$

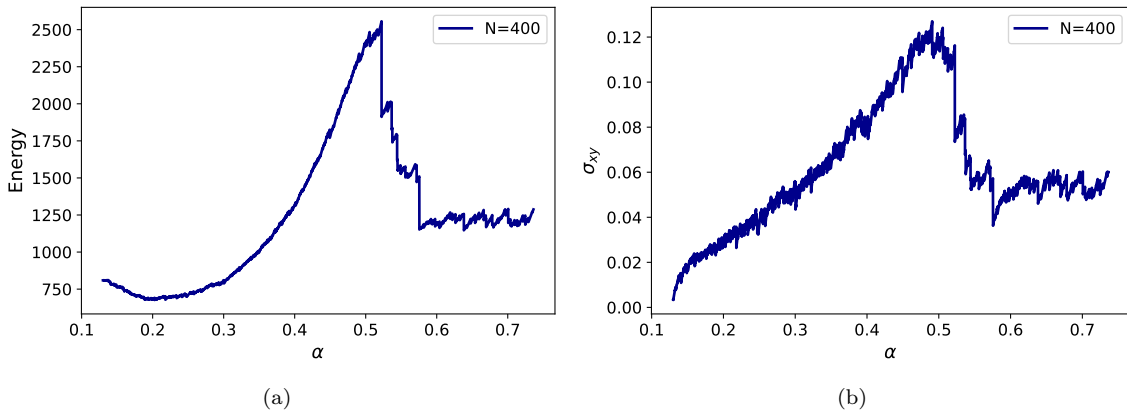


Figure 4.12: (a) Strain-energy density and (b) stress-strain response of the quasi-amorphous crystal shown in Fig. 4.3 with the rebonding algorithm activated.

$\min(C_{11}, C_{22})$, (iii) if any element violates this constraint, perform Delaunay retriangulation of the current nodal positions and return to step (i). The iteration terminates when all element metrics lie within the domain, ensuring both mechanical equilibrium and optimal mesh quality. The results of applying this algorithm to the quasi-amorphous crystal are reported in Fig. 4.12. Qualitatively, the response remains similar to the fixed-connectivity simulation: the system exhibits a hardening microplastic regime characterized by gradual energy accumulation, followed by a brittle plastic event manifested as the formation of shear bands.

Figure 4.13 illustrates the microstructural evolution throughout the deformation process with the rebonding algorithm activated. The initial configuration (Fig. 4.13a) shows a quasi-amorphous structure. As deformation progresses into the microplastic regime (Fig. 4.13b), the subsequent plastic flow shows again a hardening stage, which involves a superposition of spatially localized dislocation rearrangements, indicated by regions of elevated off-diagonal Cauchy stress components. In the post-yield state (Fig. 4.13c), the system exhibits fully developed shear bands characterized by intense stress localization. The dynamic mesh adaptation throughout this process ensures that these shear bands are captured accurately without the kinematic lock-in effects that plagued the fixed-connectivity simulations shown in Fig. 4.10. The clear visualization of stress patterns demonstrates that the rebonding algorithm not only maintains numerical stability but also preserves the physical fidelity of the deformation mechanisms.

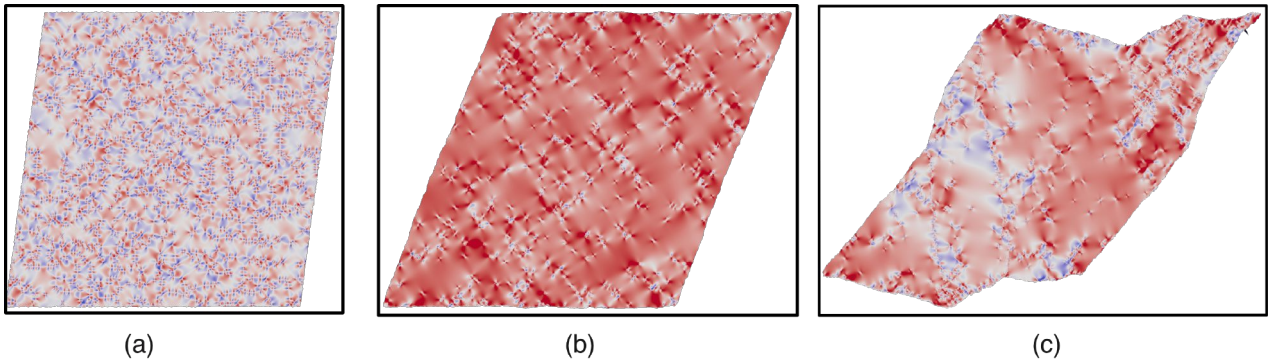


Figure 4.13: Microstructural evolution with the rebonding algorithm: (a) initial configuration, (b) microplastic regime with localized deformation, and (c) post-yield state showing shear band formation. Colors indicate non-diagonal component of Cauchy stress levels.

The dramatic improvement in solution quality is further evident in Fig. 4.14, which shows the strain-energy density field in the post-yield state. The inset magnifies a region where several interfaces among differently rotated crystal patches can be identified, revealing both the grain structure and the underlying mesh quality. In stark contrast to the severely distorted elements in Fig. 4.10, the mesh here remains well-conditioned with nearly equilateral triangles even in highly strained regions. This geometric regularity translates directly to physical

clarity: grain boundaries emerge as sharp, well-defined interfaces rather than smeared or artificially broadened zones. The energy localization patterns are crisp and free from the numerical artifacts that previously obscured the underlying crystallographic structure. This comparison underscores the essential role of the rebonding algorithm in maintaining both computational robustness and physical interpretability of the results.

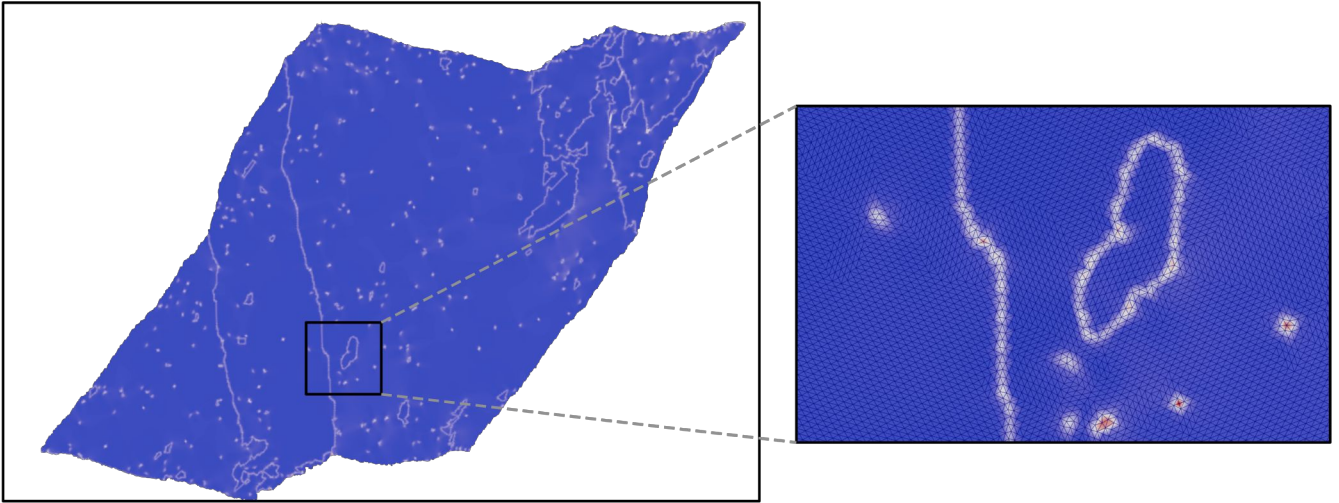


Figure 4.14: Strain-energy density field in the post-yield state with the rebonding algorithm. The inset shows a magnified view of the mesh structure, revealing well-defined grain boundaries and sharp localization patterns. The improved mesh quality eliminates the spurious artifacts present in fixed-connectivity simulations (cf. Fig. 4.10), enabling clear identification of crystallographic defect structures.

4.4 Conclusions

We performed a series of numerical experiments aimed at deeper understanding of the phenomenon of plastic yield in highly idealized 2D crystals in the limit of zero strain rate and negligible thermal effects. To capture the intricate underlying dislocation dynamics we used a relatively novel theoretical and computational tool: a mesoscopic tensorial model (MTM) of crystal plasticity representing a conceptual trade-off between continuum and atomic descriptions.

While it is known that quasi-brittle yielding is a salient feature of well-annealed glassy materials, here we used the MTM approach to show that plastic yielding in model pristine crystals leads to a remarkably similar phenomenology. More specifically, our numerical experiments revealed that plastic yielding in somewhat stylized ideal crystals can be represented as a two stage process.

During the first-stage-yielding massive dislocation nucleation results in the formation of an effectively glassy state. More precisely, a system size avalanche, representing nonlinear elastic instability, a fast time self-organization phenomenon combining nucleation and the proliferation of defects which effectively transform a pristine crystal into what we call an ‘amorphous crystal’.

We note that the emergence of such quasi-amorphous state after a massive dislocation nucleation event is not completely surprising. Thus, the mechanical response of conventional poly-crystalline solids is usually qualified as isotropic and is treated by continuum plasticity theory similar to how it treats other amorphous solids. What we see is that at least some features of amorphous response may be acquired by pristine crystals even before the polycrystalline texture develops. In other words, the necessary level of annealed disorder may result from dislocation self-organization at an almost molecular level.

The second-stage-yielding is preceded by pseudo-elastic deformation of a quasi-amorphous solid associated with only minimal dislocation activity. The activity of defects remains localized as in the case of ‘caged’ rearrangements in amorphous solids. This nominally-elastic stage of plastic deformation which is sometimes interpreted as ‘micro-plasticity’, ends abruptly with a catastrophic phenomenon closely resembling quasi-brittle yield in well-annealed

glasses. We therefore interpret this system spanning event as a transition to the actual plastic yield in a pseudo-amorphous system. The subsequent plastic flow takes the form of intermittent development of a grain texture at almost constant stress. It involves local and global rearrangements of the dislocation structure which takes the form of an evolving system of shear bands.

One of our main findings is that in both pre- and post (second) yield regimes, plastic flow proceeds by local instabilities at the level of single elastic elements which are organized in hierarchical way due to the presence of long range elastic interactions. This self-organization is behind dislocational avalanches which takes place at constant applied strain but which result in stress or energy drops exhibiting power law statistics. Similarly distributed energy and stress drops have been long known to be a signature of amorphous plasticity. The use of the MTM approach allowed us to discover that even the exponents, characterizing power law distributed avalanches, are similar in some model systems representing amorphous and crystalline plasticity. In particular, in full agreement to what is known about plasticity of glassy systems, here we also found that both pre- and post (second) yield avalanches exhibit power law statistics with matching exponents. This supports our idea of an 'amorphous crystal' which is characterized by the marginal stability of the associated defect configuration indicative of a hierarchical structure of the underlying energy landscape.

More work would be needed to convert our initial insights, revealing various peculiar aspects of the behavior of an over simplified prototypical system, into a deep physical understanding of the phenomenon of plastic yield in realistic 3D crystals with, say HCP, FCC and BCC symmetry. For instance, while the developed model deals only with quasi-statically loaded, low dimensional defect free model crystals at zero temperature, it effectively underplays such important physical effects of realistic crystal plasticity as dislocation climb, cross slip, dislocation pinning and forest hardening, to mention just a few. Most importantly, only a 3D model will distinguish adequately edge, screw, and mixed dislocations, and will be suitable to handle topologically nontrivial dislocation entanglements. The 3D model addressing crystallographically nontrivial crystal structures will also allow one to study the effects of the orientation of the samples in the loading device which are known to affect strongly the complexity of the emerging dislocation patterns. To account adequately for all these important physical effects, one would also need to quantitatively calibrate the 3D version of the MTM by a systematic comparing with parallel MD simulations and developing a rigorous conceptual bridge between the notions used to describe atomic and mesoscopic scales.

From a computational perspective, an important technical advancement presented in this thesis is the introduction of a novel rebonding algorithm that addresses the mesh distortion artifacts inherent in all MTM-type models. By dynamically adapting the mesh connectivity through Delaunay retriangulation whenever element metrics exit a carefully defined domain in metric space, this algorithm eliminates the kinematic lock-in effects that previously compromised solution fidelity in regions of extreme deformation. While the examples provided here demonstrate the algorithm's effectiveness in quasi-amorphous crystal systems, more comprehensive investigations are currently underway. These ongoing studies examine the algorithm's performance across a broader range of scenarios, including dislocation-grain boundary interactions, dislocation-crack interactions, and nanoindentation, with results to be reported in forthcoming publications. This computational tool will prove essential in extending the MTM framework to the more complex 3D systems and realistic loading conditions discussed above.

Chapter 5

Fracture Phenomena: Gradient-Enhanced Materials and Damage Pattern Evolution

Selected peer-reviewed articles

- [P1] O.U. Salman, L. Truskinovsky, "Delocalizing fracture," *Journal of the Mechanics and Physics of Solids* 154, 104517, (2021).
- [P2] O.U. Salman, G. Vitale, "Continuum theory of bending-to-stretching transition," *Phys. Rev. E* 100, 051001(R), Rapid Communication (2019).
- [P3] M.M. Terzi, O.U. Salman, D. Faurie, A.A. Baldelli, "Navigating local minima and bifurcations in brittle thin film systems with irreversible damage," *Computer Methods in Applied Mechanics and Engineering* 445, 118201, (2025)

Having explored the complex phenomena of plasticity and phase transitions in materials, we now turn our attention to another fundamental aspect of material behavior: failure mechanisms. While plasticity represents the capacity of materials to accommodate deformation through irreversible structural rearrangements, and phase transitions involve collective reorganization of material structure, failure represents the ultimate limit of material integrity where catastrophic loss of load-bearing capacity occurs.

The study of material failure encompasses a rich variety of physical phenomena, from the nucleation and propagation of cracks to the evolution of distributed damage zones. Understanding these failure mechanisms is crucial not only from a fundamental scientific perspective but also for the design of safer and more resilient engineering structures. The complexity of failure processes arises from the inherently multi-scale nature of the underlying physics, where atomic-scale bond breaking cascades through microstructural features to manifest as macroscopic fracture.

In this chapter, we investigate two distinct approaches to understanding material failure. First, we examine how strain-gradient effects can be leveraged to mitigate brittle fracture, exploring the potential of designed materials to enhance fracture resistance through controlled microstructural gradients. This work demonstrates how modern material design principles can be applied to improve failure characteristics by manipulating local stress and strain distributions.

Second, we analyze conventional fracture through the lens of gradient damage models, focusing on the emergence

of local minima, pattern formation, and evolutionary dynamics in damage systems. This approach provides insights into the fundamental mechanisms governing crack initiation, propagation, and the complex interactions between multiple damage sites.

Together, these two studies illustrate the breadth of approaches available for understanding and controlling material failure, from proactive design strategies that prevent failure to mechanistic models that describe failure evolution. Through this dual perspective, we aim to contribute to both the fundamental understanding of fracture mechanics and the practical development of failure-resistant materials.

5.1 Fracture Phenomena: Gradient-Enhanced Materials and Damage Pattern Evolution

Brittle materials typically fail through the development of a macro-crack that originates from a microscopic flaw and propagates by concentrating singular stresses near the crack tip [323, 324]. This extreme stress concentration arises from the nonconvexity of the inter-atomic potential [325, 326], which leads to elastic softening and the associated loss of ellipticity in the equilibrium equations [327, 328]. In engineering applications, the formation of system-spanning macro-cracks is generally undesirable due to the resulting low toughness and catastrophic failure dynamics [329, 330].

Many ingenious strategies for mitigating brittleness and enhancing ductility have been proposed, including toughening through microcracking [331, 332], exploiting phase transformations [333, 334], and utilizing multi-level failure mechanisms [335, 336]. The underlying principle is to prevent unstable crack propagation [337] by creating obstacles and dissipation centers [338–340] that trap the system in metastable configurations [341, 342]. These crack re-channeling mechanisms can be tailored to achieve high energy absorption, enabling nominally brittle artificial materials to rival their natural ductile counterparts [343–345].

In this chapter, we propose a different approach to fracture delocalization that can be viewed as rigidity mitigation [346]. The underlying concept is to counteract the material's progressive softening by strengthening *nonlocal* interactions that promote stress redistribution and prevent strain localization. This is achieved through a distributed compliant metamaterial substructure whose elasticity is *bending*-dominated and serves to transmit these interactions.

As a proof of principle, we present the simplest prototype of such a mechanical system. Our intentionally simplified model aims to elucidate the transition from conventional elastic behavior under small tensile loading (with no damage) to bending-dominated elastic response under substantial tensile loading (with significant damage) by making this transition analytically tractable. We demonstrate that this transition prevents softening-induced strain localization, instead enabling the system to redistribute strain globally such that each brittle sub-element fails independently. The proposed design relies on stabilizing compliant mechanical modes through bending rigidity and has bio-mimetic origins, structurally imitating known prototypes in nature [347, 348]. Such variable-connectivity structures can now be fabricated artificially using additive manufacturing techniques [349].

Our composite design is deliberately minimalist as we assemble it using the most simple local and nonlocal elastic sub-structures. The local sub-structure is represented by a chain of springs with Lennard-Jones-type nonconvex potential. The nonlocal sub-structure is a zero-stiffness pantograph composed of inextensible but flexible beams connected through ideal pivots [350–352]. The two sub-structures are coupled in such a way that in the initial state, where all breakable springs are intact, the whole system is over-constrained [353, 354]. As the structure is stretched, the geometrical constraints force the breakable elements to fail, and the composite mechanical system progressively transforms into an under-constrained one with dominating bending (gradient) elasticity. While we use only a particular nonlocal sub-structure in our analysis, other floppy designs could be used as well, see for instance, [355] and examples in our concluding Section. A general analysis of the nonlocality in such systems can be found in the theory of high contrast elastic composites [356, 357]. Contrary to what is known for usual composite materials, higher-order derivatives in the homogenized representation of such systems, appear

already at the leading order [358–360].

If, in the absence of a floppy reinforcement, a series of breakable springs loaded in tension fails abruptly with a formation of a single macro-crack, e.g., [361]. Instead, we show that the same system with a floppy reinforcement breaks gradually and exhibits distributed microcracking. The whole process can be interpreted as damage *spreading* and viewed as a propagation of a *diffuse* front separating affine and non-affine deformation configurations. Most remarkably, due to the presence of nonlocal reinforcement, the affine deformation is recovered at a sufficiently large stretching with strain uniformity being *rebuilt* by bending elasticity. Such re-entrant homogeneity of deformation distinguishes the proposed metamaterial structures from the conventional brittle solids because the latter cannot *heal* the acquired non-affinity in monotone loading.

We show that in the continuum framework, our metamaterial structure can be modeled as a softening elastic solid with a strain gradient term in the energy representing bending elasticity. The ensuing continuum model takes the classical Ginzburg-Landau form with macroscopic strain playing the role of order parameter [362, 363]. However, to describe fracture, the usual double-well energy has to be replaced by Lennard-Jones type potential. A model of this type was considered in [364], but under a constitutive condition which effectively erased the healing effect. Another closely related model is the strain-gradient-regularized damage mechanics [365], though in this framework, our crucial assumption that the nonlocal stiffness is damage-independent has been so far considered as unrealistic [366]. A conceptual link can also be built between our approach and models developed to describe ductile fracture in plastic solids when an effective local energy is complemented by a weakly nonlocal term describing strain gradient hardening [367, 368].

To elucidate the possibility of fracture delocalization *patterns* in our model we also consider a version with elastic background, particularly relevant for biological applications [369]. In this setting, the ‘effectively ferromagnetic’ interactions, implied by bending elasticity, compete with ‘effectively anti-ferromagnetic’ interactions brought by the elastic background [370]. The resulting mechanically frustrated system is shown to generate complex periodic arrangements of alternating affine and non-affine behavior.

5.2 The design idea

To motivate further developments, consider a conventional mass-spring chain constrained to remain on a straight line, see Fig. 5.1. The goal of this basic pre-model is to mimic the mechanical behavior of a softening nonlinear elastic material. To this end, we assume that the springs are ‘breakable’ and that their mechanical response is described by a non-convex elastic potential of Lennard-Jones type.

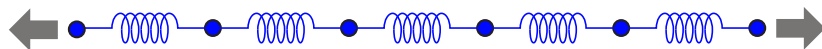


Figure 5.1: The simplest (not reinforced) mass-spring chain. Particles are connected in series by breakable springs and the whole system is loaded in tension.

Define the horizontal displacement $u_i = x_i - x_i^0$ of the mass point with index i where x_i is its actual coordinate and $x_i^0 = ai$ is its reference coordinate. The energy of this system can be written in dimensionless form

$$E_S(\mathbf{u}) = a \sum_{i=0}^{N-1} f\left(\frac{u_{i+1} - u_i}{a}\right). \quad (5.1)$$

where $a = 1/(N - 1)$ is dimensionless reference length. For our numerical illustrations, where we deal exclusively with tension, it will be sufficient to use an analytically convenient expression for the elastic potential $f(\varepsilon_i) = \varepsilon_i^2/(2 + \varepsilon_i^2)$ where we introduce the discrete strain $\varepsilon_i = (u_{i+1} - u_i)/a$, see Fig. 5.2.

Suppose next that the chain is stretched quasi-statically in a hard device so that $u_0 = -\bar{\varepsilon}/2$ and $u_{N-1} = \bar{\varepsilon}/2$, were $\bar{\varepsilon} > 0$ is the average strain which plays the role of loading parameter. To find the macroscopic response we

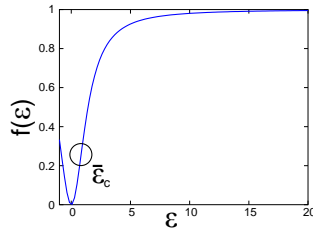


Figure 5.2: The elastic potential of Lennard-Jones-type describing the mechanical response of a ‘breakable’ spring loaded in tension. The compression range is not shown because it is not used in this study. The inflection point $\bar{\varepsilon}_c$ marks the instability of the affine response for the simplest chain with nearest neighbor interactions shown in Fig. 5.1.

need to solve for each value of $\bar{\varepsilon}$ the equilibrium equations

$$\partial E_S / \partial u_i = 0, \quad 1 < i < N - 2. \quad (5.2)$$

Knowing that continuous branches of equilibria can terminate, we need to prescribe the branch switching strategy defined by the dynamic extension of the model. Such extension should ensure that the system re-stabilizes after an instability in a dissipative way and in quasi-static setting reduces to the selection of a new locally stable equilibrium branch with necessarily lower energy. In this paper, we will compare two dynamic strategies.

Having the *structural mechanics* applications in view, we should be choosing the new equilibrium branch using the local energy minimizing (LEM) criterion which mimics the zero viscosity limit of an overdamped viscous dynamics. Under this protocol, the quasi-static loading will maintain the system in a metastable state (local minimum of the energy (5.1)) till it ceases to exist and then, during an isolated switching event, select the new equilibrium branch using the steepest descent algorithm [268].

With the *biomechanical* applications in view, where temperatures are different from zero and the energy scale of thermal fluctuations is comparable to the existing energy barriers, we also discuss the global energy minimizing (GEM) strategy. It implies that at each value of the loading parameter, the system is able to minimize the energy globally. Physically, this branch selection strategy indicates the parametric thermal equilibration with the subsequent zero-temperature limit. While for macroscopic engineering structures, the global energy minimization does not make much sense in the context of fracture, at sufficiently small scales (encountered, for instance, in cells and tissues) and over sufficiently large times, thermal fluctuations can be thought as exploring enough of phase space to make global minima relevant.

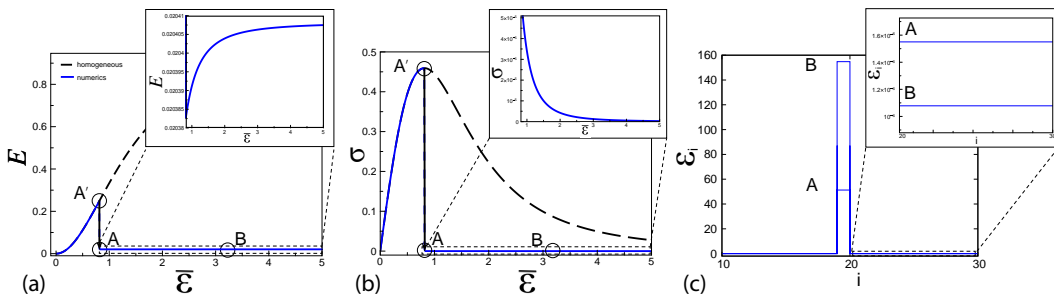


Figure 5.3: The LEM response of a mass-spring chain with breakable springs subjected to quasi-static tensile loading in a hard device: (a) the equilibrium elastic energy $\bar{E}_S(\bar{\varepsilon})$ and, (b) the equilibrium stress $\sigma(\bar{\varepsilon}) = d\bar{E}_S/d\bar{\varepsilon}$, (c) the equilibrium strain profiles $\varepsilon_i(\bar{\varepsilon})$, $i = 1, \dots, N$. Hypothetical affine response is compared with numerical simulations following the LEM protocol. Insets: (a,b) the response of the broken chain beyond point A, (c) the state of the unloaded springs in points A and B. Here $N = 50$.

While for the system with energy (5.1) both LEM and GEM responses can be studied *analytically*, we use here this simple case to detail our numerical approach. For instance, in Fig. 5.3 we illustrate the classical brittle fracture with ultimate (lattice scale) strain localization. Here we apply the LEM strategy while stretching the

chain with $N = 50$. The incremental energy minimization is based on L-BFGS algorithm [81] (imitating gradient flow), which builds a positive definite Hessian approximation for (5.2) allowing one to make a quasi-Newton step lowering the total energy [371]. Such iterations continue till the increment in the energy becomes sufficiently small. We then use the obtained approximate solution as an initial guess \mathbf{w} to solve, using LU factorization [82], the linear equations for the correction $\Delta\mathbf{w}$

$$K_{ij}\Delta w_j + \Delta f_i = 0, \quad (5.3)$$

where $K_{ij} = \partial^2 E_S / \partial u_i \partial u_j$ is the discrete stiffness matrix, and Δf_i are the bulk forces. The displacement field is updated in this way till the gradient norm of Eq. 5.2 is smaller than 10^{-8} which furnishes the actual solution of the problem. The loading is performed by monotonically increasing the value of the displacements of boundary nodes $u_0 = -\bar{\varepsilon}/2$ and $u_{N-1} = \bar{\varepsilon}/2$ in increments of 10^{-6} . The Hessian matrix K_{ij} is also used to assess the stability of the obtained equilibrium configurations. To determine the GEM path we simply chose at each value of $\bar{\varepsilon}$ the equilibrium configuration with the lowest energy.

In Fig. 5.3 we show separately the equilibrium macroscopic energy, $\bar{E}_S(\bar{\varepsilon})$, the equilibrium macroscopic stress $\sigma(\bar{\varepsilon}) = d\bar{E}_S/d\bar{\varepsilon}$ and the equilibrium distribution of the microscopic strains ε_i in individual springs. The homogeneous (affine) configuration remains locally stable till the value $\bar{\varepsilon} = \bar{\varepsilon}_c$ is reached, where $\bar{\varepsilon}_c$ is defined by the instability condition $\partial^2 f / \partial \varepsilon^2 = 0$, see Fig. 5.2. As the homogeneous state becomes unstable, the stress drops to almost zero and then continues to diminish further as the loading parameter increases, see the inset in Fig. 5.3(b). During the stress drop, the strain abruptly localizes at the scale of the lattice, see Fig. 5.3(c). The location of the ensuing macro-crack is accidental and was chosen by an initial imperfection. Subsequent loading increases the crack opening while further unloading the rest of the sample, see Fig. 5.3(c). Under the GEM protocol, similar isolated macroscopic crack forms before the point $\bar{\varepsilon}_c$ is reached, see for instance, [361], however, the subsequent growth of this crack follows the same equilibrium branch as in LEM case. The main difference is that under the LEM strategy, the dissipation during the brittle failure process is finite, while under the GEM strategy the dissipation is identically zero.

After the major stress drop the subsequent loading does not create additional damage and the response reduces to the increase of the amplitude of the localized strain. Note also that during the stress drop, the system does not fully unload because some (weakening) elastic interaction between the newly formed crack lips always exists. A 1D model of brittle fracture where stress drops to zero while the boundary layers near the lips remain have been recently proposed in [372].

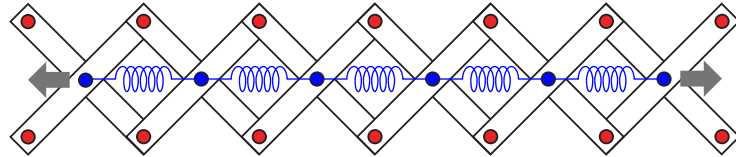


Figure 5.4: The reinforced chain of breakable springs. The pantograph floppy frame constitutes a sub-structure. The system is loaded in tension.

To de-localize brittle fracture, we now reinforce the series connection of breakable springs by adding a *sub-structure* whose role is to ensure that the strain is uniformly redistributed. The simplest sub-structure of this type is a *pantograph* frame made of inextensible but bendable beams connected by ideal pivots, see Fig. 5.4. While it has zero longitudinal macroscopic stiffness, (it does not resist affine deformations) the non-affine longitudinal deformations remain energetically penalized due to the finite bending rigidity of individual beams. If we again assume that the composite system shown in Fig. 5.4 is constrained to remain on a straight line, we can write the elastic energy of the bending beams in the form

$$E_B(\mathbf{u}) = a \sum_{i=1}^{N-1} \frac{\lambda_1^2}{2} \left(\frac{u_{i+1} + u_{i-1} - 2u_i}{a^2} \right)^2, \quad (5.4)$$

where λ_1 is a dimensionless length proportional to a with the coefficient depending on the bending stiffness of the beams [350]. The total energy of the composite system is then

$$E(\mathbf{u}) = E_S(\mathbf{u}) + E_B(\mathbf{u}), \quad (5.5)$$

where $E_S(\mathbf{u})$ is given by (5.1). We will again load the system in a hard device with $\bar{\varepsilon}$ serving as the loading parameter. No other constraints are imposed, making the ends of the reinforced structure effectively ‘moment free’ [373].

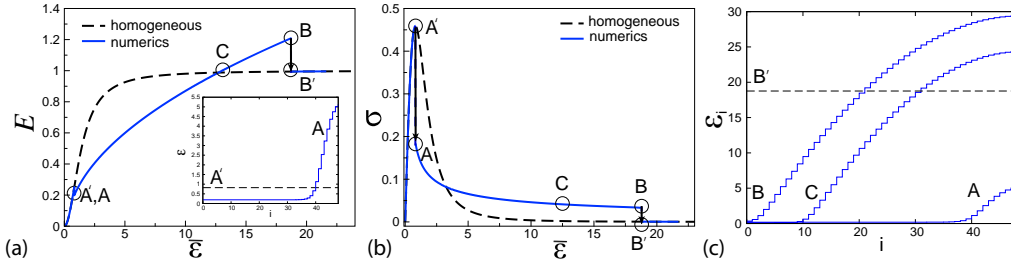


Figure 5.5: Mechanical response of the pantograph reinforced chain subjected to tensile loading in a hard device and following LEM dynamic protocol: (a) the equilibrium elastic energy $E(\bar{\varepsilon})$; (b) the equilibrium stress $\sigma(\bar{\varepsilon})$; (c) typical strain profiles. Inset details the transformation the homogeneous (affine) state A' into an inhomogeneous (non-affine) state A which takes the form of the nucleation of distributed damage at the boundary of the sample. The affine state is recovered when the inhomogeneous state B , describing a developed damage zone, transforms back into the homogeneous state B' . This re-homogenization transformation would have happened at C if the system followed the global minimum path. Here, $N = 50$, $\lambda_1 = 0.02236$.

The mechanical response of the pantograph-reinforced chain under the LEM protocol is illustrated in Fig. 5.5. To obtain the response curves, we used the same numerical approach as in the case of the non-reinforced chain. The energy minimizer is again affine at sufficiently small values of the loading parameter. At a critical value of the load (point A') the homogeneous state becomes unstable, meaning that the corresponding local minimizer ceases to exist. The local energy minimization, imitating overdamped dynamics, produces the drop in stress and brings the system to a new local minimum (point A). However, instead of an *isolated* localized crack, the failure process now produces a *diffuse* nucleus of strain non-affinity. The strain profiles, see Fig. 5.5(c), suggest that the transition $A' \rightarrow A$ leads to the formation of a damaged (micro-cracked) zone. The fact that it forms on one of the boundaries of the sample is a consequence of the zero moment boundary condition which effectively weakens the boundaries.

As the loading continues, the damage spreads through the structure, see the configurations C and B in Fig. 5.5(c). The increase of the total energy accompanies the process of successive microcracking while the stress progressively declines, see Fig. 5.5(b). The ‘de-localized’ failure zone advances into the sample from A to B as more and more springs get effectively broken, see Fig. 5.5(c). Note that the advancing zone of strain non-affinity does not have a sharp front but, instead, propagates as a diffuse wave.

According to LEM dynamics, another critical value of the loading parameter is at point B where the damage instantaneously spreads through the remaining, still-intact part of the sample, and the deformation becomes affine again all over the sample (transition $B \rightarrow B'$). This is the second dissipative event as the energy, in addition to stress, drops abruptly. The newly acquired homogeneous response remains energy minimizing at larger strains, see Fig. 5.5(a-c). Note that the total dissipation in this composite system, measured by the area under the resulting stress-strain curve shown in Fig. 5.5(b), is higher than in the case of the simple non-reinforced chain, see Fig. 5.3(b).

The GEM response of the pantograph-reinforced system will be roughly similar with the transition $A' \rightarrow A$ taking place at smaller values of the loading parameter chosen by the corresponding Maxwell condition. Similarly, the re-stabilization of the affine state will take place earlier than under LEM protocol, at the point C , rather than B , see Fig. 5.5(a-c). Despite these two abrupt stress drops along the GEM path, no energy is dissipated in such a process with all the work of the loading device absorbed by the system.

We have seen that if the simplest LEM model of a breakable chain produces conventional localized fracture with an abrupt drop of stress and low dissipation, the LEM model of a pantograph-reinforced chain shows an unusual de-localized fracture with a gradual decrease of stress and higher energy dissipation. Instead of breaking into two pieces, the pantograph-reinforced chain *fragments* uniformly into N equal pieces. The brittle response of the original system is then replaced by a ductile one with stable *softening* behavior and larger effective toughness. We remark that the advantages of embedding brittle elements into a compliant matrix are well known in both engineering (fiberglass) and biology (extra-cellular matrix). A certain peculiarity of our toughening mechanism is that it produces overall softening behavior instead of the more conventional hardening utilized, for instance, in ceramic matrix composites [374].

5.3 Continuum analog

The model shown in Fig. 5.4 was designed as a prototype of an inherently discrete system (metamaterial). However, such nonlinear discrete systems are not analytically transparent and therefore the origin of their unusual mechanical behavior is not apparent. Some theoretical insights can be obtained if we consider their mathematically more tractable continuum analogs.

Suppose that the (dimensionless) lattice parameter a is sufficiently small. We can then look for a continuum model which, in the limit $a \rightarrow 0$, is asymptotically equivalent to our discrete model. Since the formal, scale-free asymptotic limit of the discrete theory produces a degenerate model [375, 376], we should aim at (*quasi*) continuum description preserving the lowest order terms in the small parameter a .

Approximations of different order, based on the idea of Γ -convergence, were discussed in [377]. However, since here we are interested in local minimization of the energy, Γ -limits are not adequate, and we need to use instead the parallel approach based on the computation of point-wise limits [378, 379]. The simplest low-order quasi-continuum approximation of this type can be obtained if we use formal asymptotic expansions of the linear finite difference operators in a . Using these ideas we formally replace the discrete energy functional $E(\mathbf{u})$ in (5.5) by its (quasi) continuum analog

$$E(u) = \int_0^1 \left(f(\varepsilon) + \frac{\lambda_1^2}{2} \varepsilon'^2 \right) dx, \quad (5.6)$$

where $\varepsilon(x) = u'(x)$ is the continuum strain variable and $u(x)$ is the corresponding displacement field. The energy density in (5.6) maintains the additive structure of its discrete analog with the first term representing the stretching energy of the breakable springs and the second term describing the bending energy of the pantograph substructure. The 'redressed' parameter λ_1 , whose exact value will not be of interest in our qualitative study, is assumed to be strain independent given that the beams can be viewed as much stiffer than springs. It brings into the ensuing (quasi)continuum model a dimensionless length scale which does not fade away with loading as in models of un-supported mass-springs chains [364]. For numerical illustrations we continue to use the particular function $f(\varepsilon) = \varepsilon^2 / (2 + \varepsilon^2)$.

To model the system loaded in a hard device, we again set $u(0) = -\bar{\varepsilon}/2$, $u(1) = \bar{\varepsilon}/2$ where $\bar{\varepsilon} > 0$ is the imposed strain. Given that the boundaries are moment free, we also use the natural higher order boundary conditions $u''(0) = u''(1) = 0$. Under these assumptions the homogeneous (affine) configuration $u^0(x) = (\bar{\varepsilon}/2)(2x - 1)$ is an equilibrium state at all values of the loading parameter $\bar{\varepsilon}$.

Due to the softening nature of the energy density f , the homogeneous configuration can be expected to become unstable in tension. To find the critical value of the loading parameter we need to study the linear problem for the perturbation $s(x) = u(x) - u^0(x)$

$$-\lambda_1^2 s'''' + \frac{\partial^2 f}{\partial \varepsilon^2}(\bar{\varepsilon}) s'' = 0, \quad (5.7)$$

with the boundary conditions $s(0) = s(1) = s''(0) = s''(1) = 0$. The system becomes linearly unstable when the second variation of the energy (5.6) loses its positive definiteness and the problem (5.7) acquires a nontrivial solution. The largest eigenvalue of the linear operator with constant coefficients in the left hand side of (5.7) is

$-\lambda_1^2\pi^4 - (\partial^2 f / \partial \varepsilon^2)(\bar{\varepsilon})\pi^2$ and the corresponding eigenvector is $s(x) \sim \sin(\pi x)$ [380, 381]. Therefore, the homogeneous solution is stable for $(\partial^2 f / \partial \varepsilon^2)(\bar{\varepsilon}) > -\lambda_1^2(\pi)^2$ and the loss of stability takes place at the smallest $\bar{\varepsilon}$ such that $(\partial^2 f / \partial \varepsilon^2)(\bar{\varepsilon}) = -\lambda_1^2\pi^2$. The higher order modes $s(x) \sim \sin(n\pi x)$ with $n > 1$ bifurcate at the values of the loading parameter satisfying

$$\frac{\partial^2 f}{\partial \varepsilon^2}(\bar{\varepsilon}) = -\lambda_1^2(n\pi)^2. \quad (5.8)$$

The corresponding *stability boundaries*, representing solutions of (5.8) at different values of n and λ_1 , are illustrated in Fig. 5.6(a,b) for the case of our special $f(\varepsilon)$. In Fig. 5.6(a,b) we show that, independently of the value of the parameter λ_1 , the wavelength of the critical perturbation always corresponds to $n_c = 1$.

Note a remarkable feature of the stability diagrams shown in Fig. 5.6(a,b). If λ_1 is sufficiently small, the homogeneous (affine) configuration is stable in the two disconnected domains: when the applied stretch is sufficiently small $\bar{\varepsilon} \leq \bar{\varepsilon}_c^*$ and when it is sufficiently large $\bar{\varepsilon} \geq \bar{\varepsilon}_c^{**}$, with the same critical mode number ($n_c = 1$) responsible for both instabilities, see Fig. 5.6(c). This observation points to the existence of the re-entrant behavior characteristic for the isola-center bifurcations [382–384]. When the dimensionless parameter λ_1 is sufficiently large (large bending modulus or small system size), the affine configurations are stable in the whole range of loadings. In such ‘overconstrained’ regimes, failure becomes ‘dissipationless,’ taking place gradually and uniformly throughout the whole system.

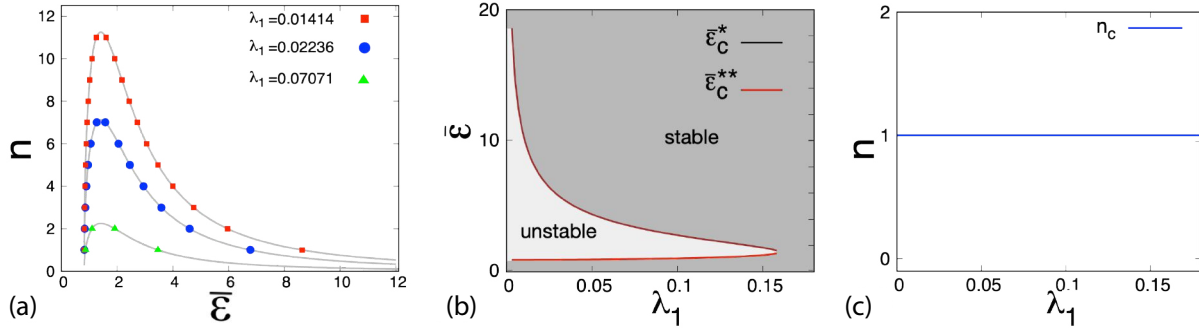


Figure 5.6: Linear stability boundaries for the homogeneous state in the continuum model of pantograph-reinforced chain: (a) bifurcation points, (b) critical strains $\bar{\varepsilon}_c^*$ and $\bar{\varepsilon}_c^{**}$ bounding the unstable domain (c) critical wavenumber n_c vs λ_1 .

The metastable non-affine configurations can be found by solving the nonlinear equilibrium equation

$$-\lambda_1^2 u''' + \frac{\partial^2 f}{\partial \varepsilon^2}(u') u'' = 0, \quad (5.9)$$

with the chosen boundary conditions for $u(x)$. The whole set of solutions of the nonlinear equation (5.9) can be obtained in quadratures, e.g., [380, 381, 385]. For the general problem with an arbitrary convex-concave potential $f(\varepsilon)$, different equilibrium branches can be parametrized by the unstable wave number n at the point of bifurcation from the trivial homogeneous solution; the latter itself can be associated with $n = 0$. One can show that all branches $u_n(x)$ with $n > 1$ are all unstable [380, 381, 386]. It can be also shown that the branch with $n = 1$ which bifurcates from the trivial homogeneous branch of equilibria at $\bar{\varepsilon}_c^*$ does it subcritically and that it reconnects to it at $\bar{\varepsilon}_c^{**}$ also subcritically [381].

These general observations are confirmed numerically in the case of our special potential $f(\varepsilon)$, see Fig. 5.7(a) and Fig. 5.8(a,b). Equilibrium branches were found using a pseudo-arc length continuation technique, implemented in the software AUTO [387]. It solves the nonlinear equation Eqs. 5.9 with the relative end displacement treated as a continuation parameter. To discretize the boundary-value problem, it uses collocation with Lagrange polynomials, and in our simulations, we had $N = 200$ mesh points with $N_c = 5$ collocation nodes and activated mesh adaptation.

To study stability we checked numerically the positive definiteness of the second-variation

$$\delta^2 E(u)(v, v) = \int_0^1 [(\partial^2 f / \partial \varepsilon^2)(u') v' v' + \lambda_1^2 v'' v''] dx, \quad (5.10)$$

where v are the test functions respecting the boundary conditions. We discretized the integral (5.10) to construct the stiffness matrix \mathbf{K} and then investigated numerically the sign of the minimal eigenvalue κ of the corresponding finite quadratic form [82]. To this end, we used one-dimensional finite elements based on third-order polynomial shape functions containing four unknown constants (cubic Hermite interpolation) [388]. This implies that four shape functions were used in each two-node element (4 degrees of freedom), and we used a uniform mesh with an element size $h_e = 1/1000$. The discrete solution $u'(x_i)$ provided at discrete nodes x_i by AUTO was first interpolated using B-spline basis function of degree 3 [389] and then used to calculate the integral 5.10 using a three-point Gauss integration scheme; the fixed boundary conditions were imposed by removing from the stiffness matrix \mathbf{K} the row and columns at $x = 0$ and $x = 1$. As a result, the second variation (5.10) was approximated by a finite sum with $K_{ij} = \int_0^1 [(\partial^2 f / \partial \varepsilon^2)(u') \mathcal{N}'_i \mathcal{N}'_j + \lambda_1^2 \mathcal{N}''_i \mathcal{N}''_j] dx$, where $\mathcal{N}_i(x)$ is the shape function of node i [388].

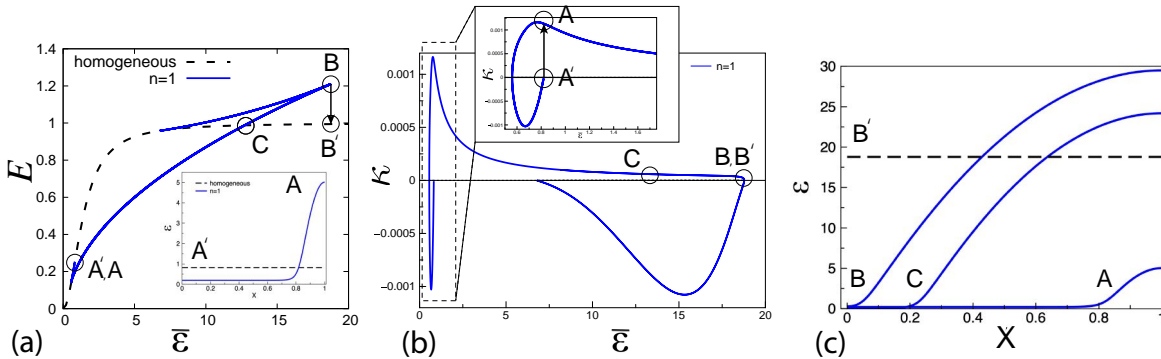


Figure 5.7: The LEM mechanical response in tensile loading for the continuum model of a pantograph reinforced chain: (a) equilibrium energy-strain relation for the branch $n = 1$ with the lowest energy, (b) smallest eigenvalue of the second variation for the mode $n = 1$ as a function of the loading parameter $\bar{\varepsilon}$. The inset in (a) shows the nucleation of the diffuse damage zone near the boundary of the sample (transition $A' \rightarrow A$). In point B the non-affine state transforms into the affine state (transition $B \rightarrow B'$). Along the global energy minimization path (GEM response) the re-entry type transformation would take place in point C. Here $\lambda_1 = 0.02236$.

In Fig. 5.7(a) we show the macroscopic energy-strain relation for the system following the LEM protocol. The non-affine branch with $n = 1$ bifurcates from the trivial branch at point A' . Since the bifurcation is subcritical, the system jumps from the homogeneous state A' to the inhomogeneous state A located on the only other stable equilibrium branch (with $n = 1$), see the inset in Fig. 5.7(a). During this abrupt transition, the stress drops, and the energy is dissipated, see Fig. 5.8(b). As the loading parameter increases, the system follows the $n = 1$ branch till it reaches the turning point B . From there the system abruptly returns to the homogeneous (affine) branch $n = 0$ as a result of a dissipative transition accompanied with another stress drop, see Fig. 5.8(b). Further loading preserves the affine nature of the strain configuration which has recovered its stability. In Fig. 5.7(b) we show the strain dependence of the lowest eigenvalue of the second variation κ for the equilibrium branch with $n = 1$. As we see, this branch bifurcates from the branch with $n = 0$ at the point A' as an unstable one. However, the non-affine state A , where the LEM solution jumps, is stable as the corresponding $\kappa > 0$. The branch $n = 1$ loses stability again at the turning point B where $\kappa = 0$.

We remark that the *global* structure of the nontrivial branch $n = 1$ is similar to the one obtained in the Ginzburg-Landau model with a double-well potential, e.g. [380]. The same topological structure of the bifurcation diagram is observed in a model with a single-well potential because the separation and the reconnection of the nontrivial branch $n = 1$ with the trivial branch $n = 0$ takes place outside the energy wells, in the spinodal region, which is effectively present in both types of theories.

The structure of the associated local energy minimizers is illustrated in Fig. 5.7(c). The abrupt nucleation

of the first domain of non-affinity takes place at the point A' corresponding to $\bar{\varepsilon}_c^* > \bar{\varepsilon}_c$. In the linear regime, the unstable bifurcating mode has a characteristic size of the system, but in the nonlinear regime, it partially localizes near one of the boundaries (transition A'→A). As the applied strain $\bar{\varepsilon}$ increases, the non-affine state of distributed damage proliferates towards the other boundary of the sample; note that it remains diffuse as successive springs continue to break. Observe *broad* transition layers, separating the non-affine domains which contain broken springs (domains where $\partial^2 f / \partial \varepsilon^2 < 0$) and the dominating elasticity is of the bending (gradient) type, from the affine domains which contain intact springs (domains where $\partial^2 f / \partial \varepsilon^2 > 0$) and the dominating elasticity is of the classical 'stretching' type. The fully affine configuration is recovered through the discontinuous event which marks the complete annihilation of the stretching dominated domain (transition B→B').

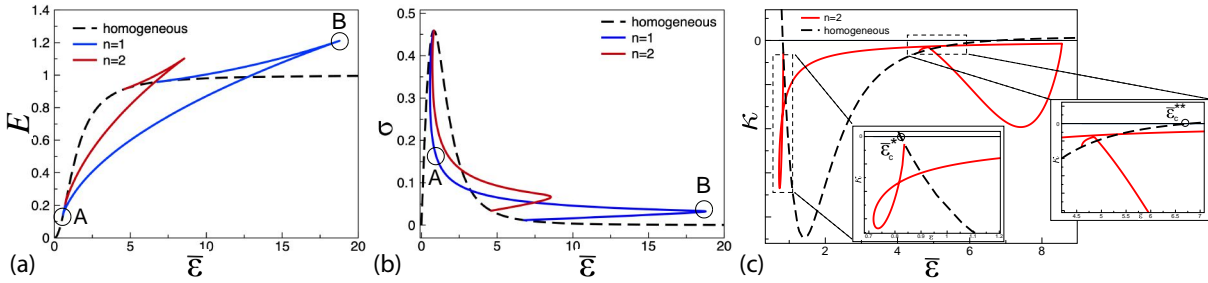


Figure 5.8: The mechanical response in the continuum model of a pantograph reinforced chain : (a) equilibrium energy-strain relations showing the two lowest energy branches, (b) the corresponding stress-strain relations, (c) minimal eigenvalues of the second variation for branches with $n = 0$ (homogeneous) and $n = 2$ (unstable).

Since branches with $n = 0$ and $n = 1$ are the only ones containing stable fragments, the GEM path can also be read off our Fig. 5.7(a). Thus, the global energy minimizing transition from $n = 0$ to $n = 1$ branch takes place slightly before point A' while the reverse transition occurs at point C. It involves the instantaneous breaking of almost half of the springs and precedes considerably the analogous transition in the LEM model taking place at the point B, see Fig. 5.7(c).

An unstable equilibrium branch with $n = 2$, which does not participate in either LEM, or GEM paths, is illustrated in Fig. 5.8. It describes saddle points but exhibits similar isola-center bifurcation. The instability of this branch is illustrated Fig. 5.8(c) where we show the strain dependence of the lowest eigenvalue of the second variation κ for branches with $n = 0$ and $n = 2$. Note that since the $n = 2$ branch bifurcates from the trivial state as the second eigenvalue of the second variation becomes negative, the curve $\kappa(\bar{\varepsilon})$ in Fig. 5.8(c) corresponding to $n = 2$ originates on $n = 1$ branch rather than $n = 0$ branch. It is also clear from Fig. 5.8(a) that the branch $n = 2$ corresponds to a higher energy level than the branch $n = 1$ and, therefore, independently of the local stability analysis, it cannot make appearance in principle along the GEM path.

Our analysis shows that the behavior of the (quasi)continuum model is qualitatively similar to the behavior of the corresponding discrete model, compare Fig. 5.5 and Fig. 5.7. In particular, both models predict the abrupt emergence and subsequent proliferation of the non-affine zones which contain inhomogeneously ruptured springs. Similarly, both models predict the abrupt recovery of the affine state as the rupture process saturates.

Note that the non-affine states, stabilized by bending (gradient) elasticity, can be characterized at the macro-scale in terms of damage mechanics. It provides a homogenized description of de-localized microcracking which is relevant when the competing localized macro-cracking is inhibited. The nonlocal stress redistribution, facilitated by an under-constrained sub-system of stress-transmitting backbones, may be considered a factor contributing to such inhibition.

5.4 Elastic background

To show that the de-localized damage can also appear in the form of periodic *patterns*, we now consider our pantograph-reinforced chain coupled to an elastic (Winkler's) background. Breakable networks embedded in soft

elastic matrices are structural elements in many engineering materials and biological materials, see for instance, [390–392].

To achieve analytical transparency, we again assume that the parameter a is sufficiently small and adopt the quasi-continuum description encapsulated in (5.6). Under the simplifying assumption that the elastic background is uniformly pre-stretched with the same strain $\bar{\varepsilon}$ as the composite chain, we can write the energy of the system in the form [393, 394]

$$E(u) = \int_0^1 \left(f(\varepsilon) + \frac{\lambda_1^2}{2} \varepsilon'^2 + \frac{\lambda_2^{-2}}{2} (u - u^0)^2 \right) dx, \quad (5.11)$$

where $u^0(x) = (\bar{\varepsilon}/2)(2x - 1)$ and λ_2 is a new dimensionless length scale characterizing the strength of the coupling; note that in (5.11) the elastic energy of the background is effectively subtracted. In what follows, we use the same boundary conditions on $u(x)$ as in the case of the unsupported chain.

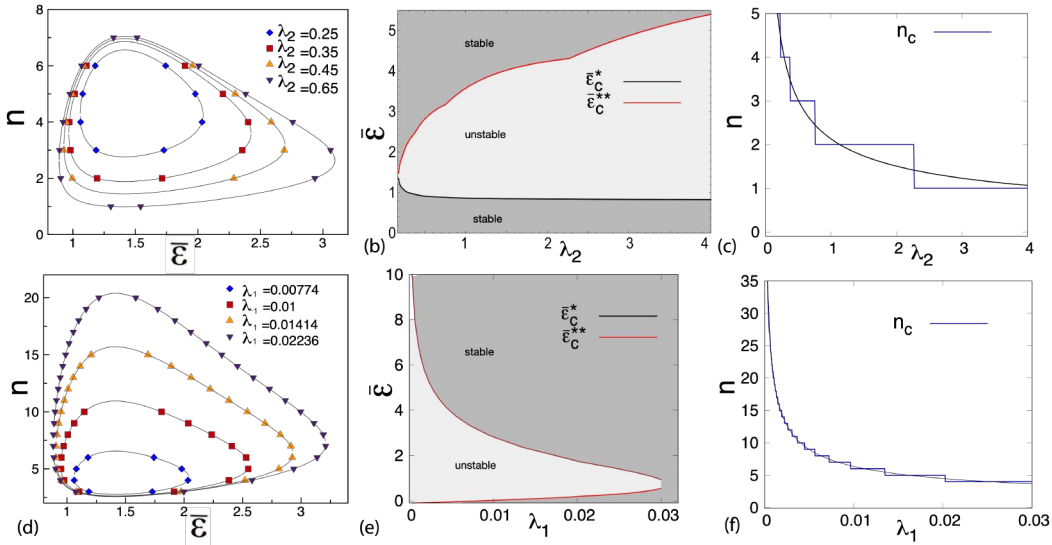


Figure 5.9: Linear stability limits for the homogeneous state in the continuum model of pantograph reinforced chain coupled to an elastic background: (a,d) bifurcation points, (b,e) critical strains ($\bar{\varepsilon}_c^*$, $\bar{\varepsilon}_c^{**}$); (c,f) critical modes n_c . Parameters: in (a-c) $\lambda_1 = 0.02236$. In (d-f) $\lambda_2 = 0.25$.

In the model with energy (5.11), the bifurcation condition for the trivial branch can be found from the equation generalizing (5.8)

$$\lambda_1^2(n\pi)^4 + \frac{\partial^2 f}{\partial \varepsilon^2}(\bar{\varepsilon})(n\pi)^2 + \lambda_2^{-2} = 0. \quad (5.12)$$

We again obtain that there are upper and lower critical strains $\bar{\varepsilon}_c^*$ and $\bar{\varepsilon}_c^{**}$ corresponding to the same mode number n_c so the bifurcation from the trivial branch is always of isola-center type. The difference from the case without the foundation is that now one can have $n_c \neq 1$, see Fig. 5.9. To interpolate critical thresholds we neglect the discreteness and write the approximating relations $\partial^2 f / \partial \varepsilon^2(\bar{\varepsilon}_c) = -2(\lambda_1/\lambda_2)$ and $n_c = \pi^{-1}(\lambda_1\lambda_2)^{-1/2}$. The expression for the critical wavenumber suggests that the instability is of Turing type [395, 396].

The dependence of solutions of (5.12) on parameters λ_1 and λ_2 is illustrated in Fig. 5.9(a,d); the parametric dependence of the corresponding bifurcation thresholds $\bar{\varepsilon}_c^*$ and $\bar{\varepsilon}_c^{**}$ is shown in Fig. 5.9(b,e). One can see that the non-affinity can be suppressed if the bending rigidity λ_1 is sufficiently large or if λ_2 and the foundation coupling is stiff. However, the effect of the bending in this respect is much stronger than the effect of the coupling, which needs to be infinitely stiff to eliminate non-affinity completely. Note also that the wave number of the unstable mode tends to zero when either λ_1 or λ_2 disappears, see Fig. 5.9(c,f). Interestingly, the whole configuration of the boundaries in Fig. 5.9(a,d) strongly resembles similar diagrams appearing in the fully nonlinear 3D theories of wrinkles in stretched elastic sheets [397].

The study of the post-bifurcational behavior is based on the nonlinear equilibrium equation

$$-\lambda_1^2 u''' + \frac{\partial^2 f}{\partial \varepsilon^2}(u') u'' - \lambda_2^{-2} (u - u^0) = 0. \quad (5.13)$$

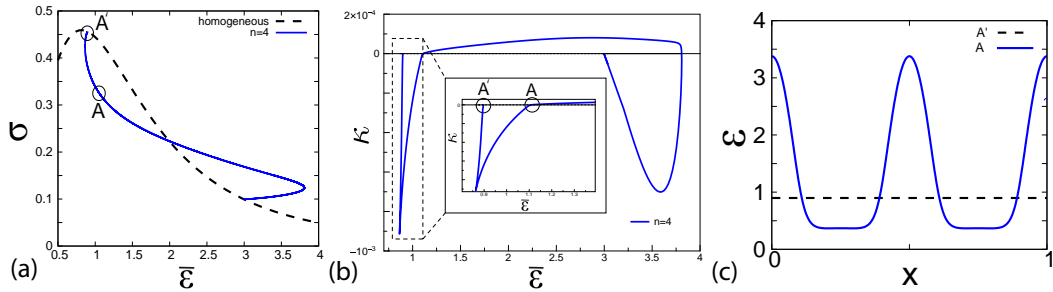


Figure 5.10: Mechanical response in the continuum model of pantograph reinforced chain coupled to an elastic background: (a) strain-stress relation along the first unstable branch $n = 4$; (b) the smallest eigenvalue of the second variation for the same branch as a function of the loading parameter $\bar{\varepsilon}$; (c) equilibrium strain profiles associated with the states A' and A . Parameters: $\lambda_1 = 0.0167$, $\lambda_2 = 0.45$.

Eq. (5.13) describes the interplay between the localization tendency due to nonconvexity of the energy $f(u')$ and the delocalizing effect of weakly nonlocal bending elasticity brought by the pantograph reinforcement. This competition is in turn affected by the bias towards homogeneity brought by the interaction with an elastic foundation. The two harmonic reinforcements can be compared in terms of the effective interaction kernels [394]. Thus, the pantograph sub-structure brings sign-definite, ferromagnetic-type interaction favoring coarsening of the damaged microstructure. Instead, the Winkler's foundation brings a sign indefinite, anti-ferromagnetic type interaction favoring microstructure refinement. The complexity of the emerging post-bifurcation behavior reflects the general frustration due to the presence of these competing tendencies.

Since the solution of (5.13) in quadratures is not available, we need to resort to numerical methods. Our computational approach is the same as in the case without foundation and is based on the use of the AUTO continuation algorithm [387]. The stability of equilibrium branches is again assessed by the numerical evaluation of the smallest eigenvalue of the second variation, which is now

$$\delta^2 E(u)(v, v) = \int_0^1 [(\partial^2 f / \partial \varepsilon^2)(u') v' v' + \lambda_1^2 v'' v'' + \lambda_2^{-2} v v] dx. \quad (5.14)$$

The corresponding stiffness matrix is $K_{ij} = \int_0^1 [(\partial^2 f / \partial \varepsilon^2)(u') \mathcal{N}'_i \mathcal{N}'_j + \lambda_1^2 \mathcal{N}''_i \mathcal{N}''_j + \lambda_2^{-1} \mathcal{N}_i \mathcal{N}_j] dx$.

Our first illustration concerns the nucleation event at $\bar{\varepsilon} = \bar{\varepsilon}_c^*$. The bifurcated equilibrium branch, corresponding to $n = 4$, is shown in Fig. 5.10(a). One may expect the instability at the point A' to result in the transition $A' \rightarrow A$ where the non-affine configuration A also lies on the $n = 4$, see Fig. 5.10(c). However, the study of the smallest eigenvalue of the second variation (5.14) for the equilibrium branch $n = 4$ shows that the corresponding state A at $\bar{\varepsilon} = \bar{\varepsilon}_c^*$ is unstable, see Fig. 5.10(b). According to this figure there is a finite gap separating the first point of instability of the homogeneous state and the first stable equilibrium with $n = 4$, see point A in Fig. 5.10(a,b).

The presence of competing interactions in this problem suggests that the stable pattern, emerging from the decomposition of the homogeneous state, may be *different* from the one implied by the linear stability analysis. The global picture is presented in Fig. 5.11(a,c) where we show the energy-strain and the stress-strain relations along the equilibrium branches with $n = 3, \dots, 6$. They all bifurcate from the homogeneous branch around $\bar{\varepsilon}_c^* = 0.897334$, for instance the second bifurcation point (after the one with $n = 4$) at $\bar{\varepsilon}_c = 0.903472$ corresponds to the branch with $n = 3$.

The detailed picture is shown in Fig. 5.11(b,d) where we see that, in view of the instability of the $n = 4$ branch in the interval of interest, the only configuration reachable from point A' by energy minimization is the one corresponding to point A^* on the $n = 3$ branch. The local stability of this branch is illustrated in the inset in Fig. 5.12(c). Moreover, in this range of strains, the equilibrium branch with $n = 3$ also delivers the *global* minimum of the energy.

Considering GEM dynamics, we can conclude that the transition from the trivial branch $n = 0$, taking place at the point G (Fig. 5.11), also leads to the branch with $n = 3$. According to Fig. 5.11(a,c) the next transition along

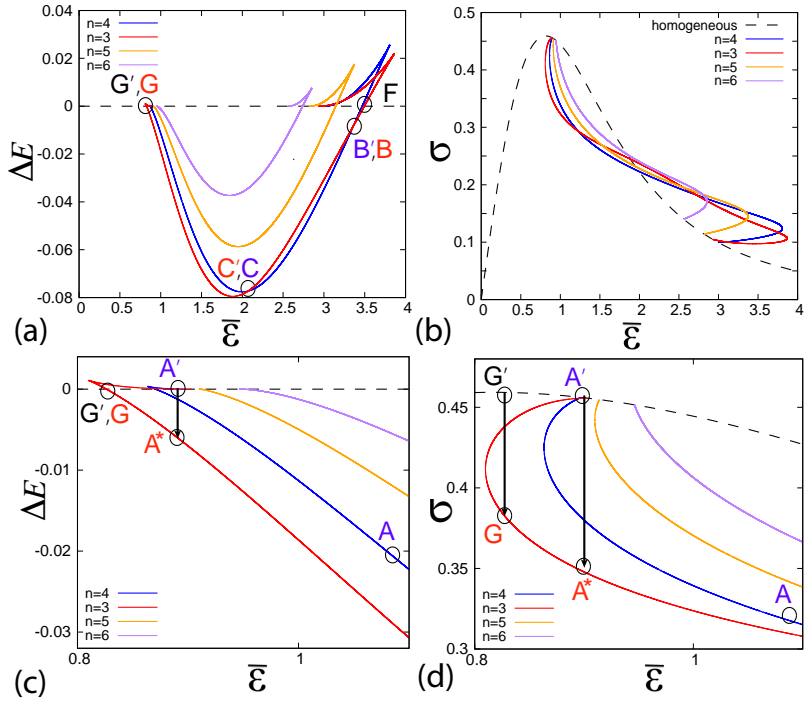


Figure 5.11: Mechanical response in the continuum model of a pantograph reinforced chain coupled to an elastic foundation: (a) the energy difference between the non-affine and affine equilibrium configurations; (b) macroscopic strain-stress relations along different equilibrium branches; (c,d) magnified versions of (a) and (b) near the first instability point. The transition $A' \rightarrow A^*$ takes place along the LEM path while the transitions $G' \rightarrow G$, $C' \rightarrow C$, $B' \rightarrow B$ and $F \rightarrow F'$ are the equilibrium branch switching events taking place along the GEM path. Parameters: $\lambda_1 = 0.0167$, $\lambda_2 = 0.45$.

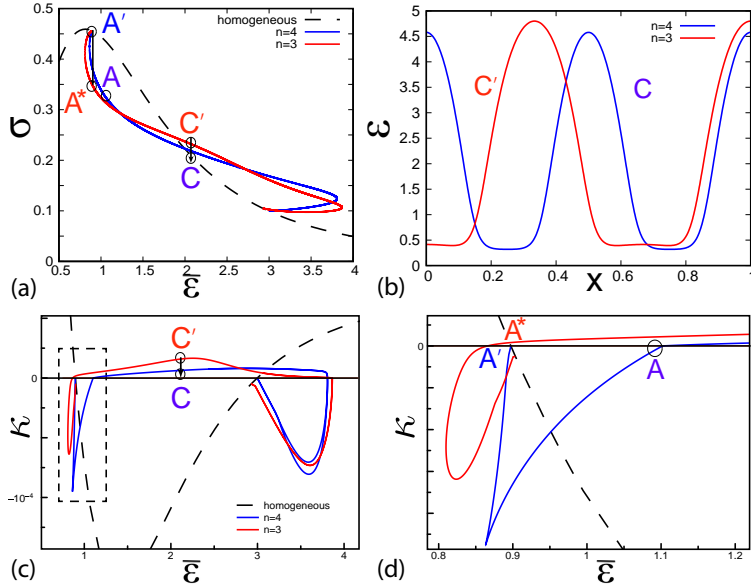


Figure 5.12: Zoom in on the particular branch switching events along LEM and GEM paths shown in Fig.5.11: (a) stress-strain response, (b) equilibrium configurations C and C' with the same energy, (c) smallest eigenvalue of the second variation for the branches with $n = 3$ and $n = 4$, (d) zoom in on (c) around the first instability along the LEM path. Symmetry is lost during the transition $A' \rightarrow A^*$ while symmetry is acquired during the $C' \rightarrow C$ transition. Parameters: $\lambda_1 = 0.0167$, $\lambda_2 = 0.45$.

the GEM path takes place at point C' and brings the system back to $n = 4$ equilibrium branch. Then, at point B' the system returns again on the $n = 3$ branch and finally stabilizes on the trivial $n = 0$ branch at point F . In Fig. 5.12(b) and Fig. 5.13(b) we provide evidence that these GEM transitions are between locally stable states.

Our Fig. 5.12(c) and Fig. 5.12(d) illustrate the nature of the restructuring of the equilibrium configurations

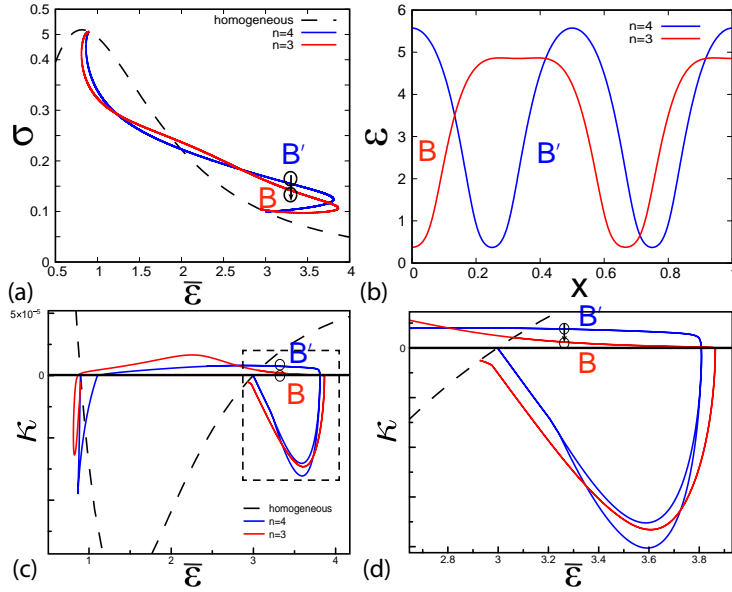


Figure 5.13: Zoom in on the particular branch switching events along LEM and GEM paths shown in Fig. 5.11: (a) stress-strain response, (b) equilibrium configurations B and B' with the same energy, (c) smallest eigenvalue of the second variation for the branches with $n = 3$ and $n = 4$, (d) zoom in on (c) around the transition $B' \rightarrow B$ along the GEM path. Symmetry is lost during the $B' \rightarrow B$ transition. Parameters: $\lambda_1 = 0.0167$, $\lambda_2 = 0.45$.

during these transitions. Thus, as the loading parameter $\bar{\epsilon}$ increases, the non-symmetric configuration produced at point G , which contains two domains of non-affinity and corresponds to the branch with $n = 3$, evolves till another strain threshold is reached where the system undergoes the transformation $C' \rightarrow C$ to the symmetric configuration corresponding to $n = 4$. As a result, the second surface-bound damage zone appears, see Fig. 5.12(c). Then, during the reverse transition $B' \rightarrow B$ the symmetry is lost and one of the surface-bound damage zone disappears again, see Fig. 5.13(c). Finally, the symmetry is recovered when the affine configuration stabilizes at point F .

In contrast to the complexity of the GEM path, the LEM dynamics produces much simpler set of transitions. Without going into details, we only mention that after the dissipative $A \rightarrow A^*$ transition the system remains on the $n = 3$ branch all the way till its reaches the turning point where another dissipative transition to the homogeneous branch $n = 0$ takes place (not shown in either of the figures).

Note that the parameters in Fig. 5.11, Fig. 5.12 and Fig. 5.13 were chosen arbitrarily with the only consideration that the number of the domains of nonaffinity is relatively small. It is straightforward to see that the microcracking pattern in this problem may be arbitrarily complex, for instance in the limit $\lambda_1 \rightarrow 0$ the number of cracks tends to infinity. In fact, by choosing the bending resistance of the metamaterial sub-structure and the degree of coupling with the elastic environment, one can effectively control the complexity of the emerging microstructures.

More generally, the above analysis shows that, despite the constituents' brittle nature, the material response of the pantograph-reinforced chain is incompatible with the conventional scenario of highly localized cracking. Instead, the model predicts the emergence of de-localized damage zones, which, in the presence of elastic background, advance from multiple sources and form regular patterns. Competitive interactions ensure that a monotonously loaded system experiences a series of instabilities where symmetries may be lost and re-acquired. The interplay between two internal length scales in this problem may be a source of the considerable complexity in the spatial distribution of damage.

5.5 Conventional fracture: Evolution in a Gradient Damage Fracture Model

5.5.1 Introduction

If a nonlocal sub-structure is absent, the remaining local sub-structure represents a conventional brittle material that can be simulated in the continuum limit by gradient damage model [14–18] or any other phase-field model of fracture [19–22]. Since one internal length scale is also present in the conventional fracture mechanics and another one can be added through the coupling to an elastic foundation, one may ask if the pantograph-based sub-structure brings anything fundamentally different. To answer this question we consider in this Section a continuum model of fracture where cracks are described by a phase-field [17, 21, 398]. In this setting, we will show that neither damage-spreading nor re-entrant behavior takes place. Even when the elastic environment is added, the broad microcracking domains, characteristic of our metamaterial response, do not appear. Instead, we observe in this case only the conventional pattern of highly localized macro-cracks.

Structural Model The structure is a multilayer composite: a brittle thin film, whose material is identified by the state function W , bonded to a substrate which is either stiff or elastically compliant, see Figure 5.14. The thin film is a one-dimensional membrane with thickness h and length L with $L \gg h$, subject to a combination of imposed displacements by the substrate and loadings at the boundary (see Figure 5.14).

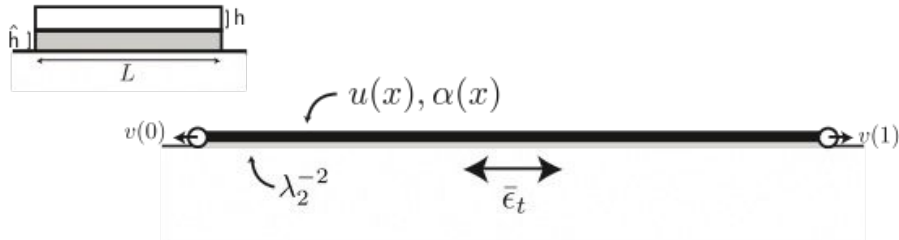


Figure 5.14: Illustration of the thin film model (nondimensional). A thin film (black bar) is bonded to a compliant substrate (gray) via an elastic foundation (light gray) of effective stiffness Λ^{-2} , where Λ is its characteristic length scale. The displacement $u(x)$ and damage variable $\alpha(x)$ are defined on the film, while $v(x)$ is the trace of the substrate's displacement at the interface. Boundary conditions prescribe the displacement $v(0), v(1)$, compatible with the time-parametrized average substrate strain $\bar{\epsilon}_t$. The inset shows the original 3D geometry before dimension reduction: a bilayer composed by a film of thickness h bonded through an interfacial layer of thickness \hat{h} over a domain of length L .

In phase-field theories of fracture, the solid's elasticity is typically modeled as linear with damage-dependent stiffness degradation. The damage state is captured by a scalar order parameter $\alpha(x)$, where $\alpha = 0$ represents the intact state and $\alpha = 1$ the fully broken state. The gradient of this parameter controls the energy cost of damage localization [14].

For a one-dimensional system without external constraints, the total energy takes the form

$$E(u, \alpha) = \int_0^1 \left[f(\varepsilon, \alpha) + \frac{\lambda_1^2}{2} (\alpha')^2 \right] dx, \quad (5.15)$$

where $\varepsilon(x) = u'(x)$ is the strain field. The local energy density consists of two contributions:

$$f(\varepsilon, \alpha) = \frac{1}{2} g(\alpha) \varepsilon^2 + h(\alpha). \quad (5.16)$$

The first term represents linear elasticity with damage-modulated stiffness $g(\alpha)$, while $h(\alpha)$ captures the intrinsic energy cost of damage formation. The gradient penalty in (5.15) introduces an internal length scale λ_1 that regularizes damage localization.

Equilibrium configurations satisfy the coupled field equations:

$$\begin{cases} \nabla \cdot [g(\alpha) \nabla u] = 0 & \text{(mechanical equilibrium)} \\ -\lambda_1^2 \alpha'' + \frac{1}{2} g'(\alpha) |\nabla u|^2 + h'(\alpha) = 0 & \text{(damage evolution)} \end{cases} \quad (5.17)$$

where primes denote derivatives with respect to the argument.

To mimic in this framework our numerical experiments with the breakable chain, see Fig. 5.1, we make the standard assumptions that $g(\alpha) = (1 - \alpha)^2$, and $h(\alpha) = \alpha^2$. If we also choose the boundary conditions in the form $u(0) = -\bar{\varepsilon}/2$, $u(1) = \bar{\varepsilon}/2$ and $\alpha'(0) = \alpha'(1) = 0$, the homogeneous solution, representing in this case the principal branch of equilibria, takes the form

$$u^0(x) = (\bar{\varepsilon}/2)(2x - 1), \quad \alpha^0(x) = \bar{\varepsilon}^2/(2 + \bar{\varepsilon}^2). \quad (5.18)$$

The effective elastic energy along the trivial branch is

$$f^0(\varepsilon) = f(\varepsilon, \alpha^0(\varepsilon)) = \varepsilon^2/(2 + \varepsilon^2). \quad (5.19)$$

whose similarity with potential adopted in the study of our Ginzburg-Landau elastic model justifies the assumptions for $g(\alpha)$ and $h(\alpha)$. We may therefore perceive the phase-field model as a version of an elastic theory with the softening energy $f^0(\varepsilon)$ [399].

To assess the linear stability of the homogeneous solution (5.19), we linearize (5.17) around the base state and seek nontrivial perturbations $s(x) = u(x) - u^0(x)$ and $\tau(x) = \alpha(x) - \alpha^0$. Following standard stability analysis, we find that the eigenmodes take the form $s(x) \sim \sin(n\pi x)$ and $\tau(x) \sim \cos(n\pi x)$, where n is the mode number. The bifurcation condition emerges as

$$(n\pi)^2 = -\frac{4\bar{\varepsilon}^2 \partial^2 f^0 / \partial \varepsilon^2(\bar{\varepsilon})}{\lambda_1^2 [\partial f^0 / \partial \varepsilon(\bar{\varepsilon}) \cdot \bar{\varepsilon} - \partial^2 f^0 / \partial \varepsilon^2(\bar{\varepsilon})]}, \quad (5.20)$$

where all derivatives are evaluated at the homogeneous state. Figure 5.15(a) shows how the bifurcation points depend on the internal length λ_1 . Notably, the fundamental mode $n_c = 1$ always becomes unstable first, as illustrated in Fig. 5.15(c), mirroring the behavior observed in the pantograph-reinforced chain.

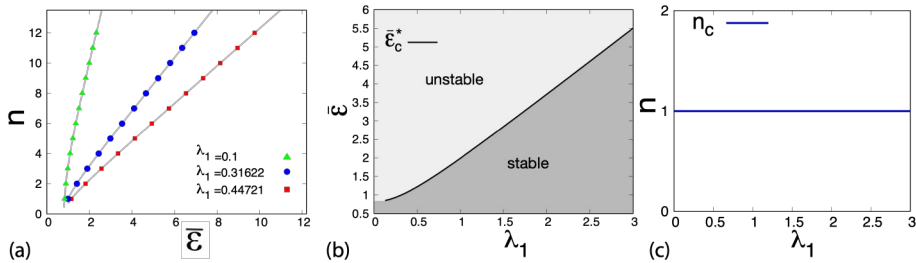


Figure 5.15: Stability study of the homogeneous (affine) state in the phase-field model of a unreinforced breakable chain: (a) stability boundaries (bifurcation points) depending on the regularization parameter λ_1 ; (b) critical strains $\bar{\varepsilon}_c^*$; (c) critical mode n_c .

To see the difference, we now consider the λ_1 dependence of the critical strain $\bar{\varepsilon}_c$ which can be found from the equation

$$\bar{\varepsilon}_c (4\bar{\varepsilon}_c^2 - \lambda_1^2 \pi^2) \frac{\partial^2 f^0 / \partial \varepsilon^2(\bar{\varepsilon}_c)}{\partial f^0 / \partial \varepsilon(\bar{\varepsilon}_c)} + \lambda_1^2 \pi^2 = 0. \quad (5.21)$$

It takes particularly simple form for our choice of the potential $f^0(\varepsilon)$ when we can write $\lambda_1^2 \pi^2 = 3\bar{\varepsilon}_c^2 - 2$, see Fig. 5.15(b). Now, in contrast to the case of the pantograph-reinforced chain, see Fig. 5.4, the affine configuration does not re-stabilizes after the initial instability and the 'broken' configuration always remains non-affine, see

Fig. 5.15(b). Such response is in full agreement with the behavior of a simple breakable chain, see Fig. 5.1, but despite the presence of gradient term in (5.15), the effect of the pantograph reinforcement is lost.

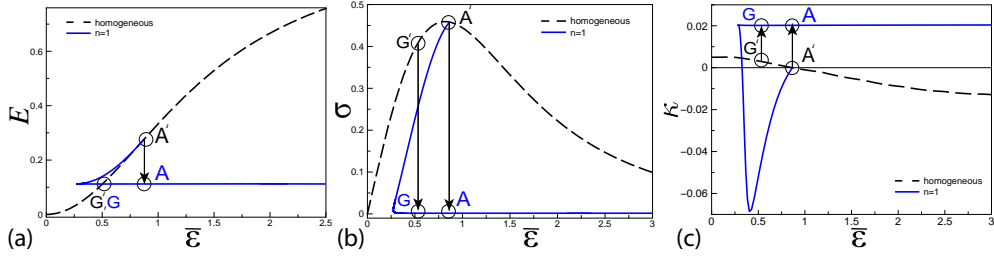


Figure 5.16: Mechanical response in the phase-field model of unreinforced chain along the LEM ($A' \rightarrow A$ transition) and the GEM ($G' \rightarrow G$ transition) loading paths: (a) macroscopic energy-strain relation; (b) macroscopic stress-strain relation; (c) smallest eigenvalue of the second variation for the homogeneous branch as a function of the loading parameter $\bar{\epsilon}$. Single macroscopic crack nucleation takes the form of $A' \rightarrow A$ transition. Here, $\lambda_1 = 0.158114$.

The fracture localization (vs de-localization) in the phase-field model is illustrated in Fig. 5.16. We combine there the solutions of the nonlinear system (5.17) corresponding to LEM and GEM protocols. To confirm the local stability of the configurations found by our LEM algorithm, we computed the lowest eigenvalue of the second variation

$$\delta^2 E(u, \alpha)(v, w) = \int_0^1 [(1-\alpha)^2 v'^2 - 4(1-\alpha)u'v'w + (2+u'^2)w^2 + \lambda_1^2 w'^2] dx, \quad (5.22)$$

where v and w are test functions. The stiffness matrix is then

$$\mathbf{K} = \begin{bmatrix} \int_0^1 [(1-\alpha)^2 \mathcal{N}'_i \mathcal{N}'_j] dx & -2 \int_0^1 (1-\alpha) u' \mathcal{N}'_i \mathcal{N}_j dx \\ -2 \int_0^1 (1-\alpha) u' \mathcal{N}_i \mathcal{N}'_j dx & \int_0^1 [(2+u'^2) \mathcal{N}_i \mathcal{N}_j + \lambda_1^2 \mathcal{N}'_i \mathcal{N}'_j] dx \end{bmatrix}, \quad (5.23)$$

where the shape functions $\mathcal{N}_i(x)$ can be now chosen simply quadratic.

According to Fig. 5.16, the LEM dynamics, which reduces to local energy minimization, is characterized by a major dissipative event in the form of the transition $A' \rightarrow A$ from the branch $n = 0$ to the branch $n = 1$. Instead, the GEM dynamics, which implies global energy minimization, is epitomized by an earlier and smaller non-dissipative transition $G' \rightarrow G$, also from the branch $n = 0$ to the branch $n = 1$. Note that the metastable section of the non-affine equilibrium branch $n = 1$ in Fig. 5.16 was constructed using again the pseudo-arclength continuation technique implemented in the software package AUTO [387].

We observe, see Fig. 5.16(a,b), that the stretching response of this continuum system is basically the same as for the simple chain with breakable elements. The fact that the crack forms on one of the boundaries is due to a small bias provided by the phase-field related boundary conditions. After the major stress drop the subsequent loading does not create additional damage and the response reduces to the increase of the amplitude of the localized strain. Note again that during the stress drop, the system does not fully unload because some (weakening) elastic interaction between the newly formed crack lips always exists. The noteworthy difference between the behavior of the original discrete system and its phase-field analog is the smearing out of the crack due to the gradient regularization, see Fig. 5.17(a,b). If the strain remains sufficiently localized, the damage parameter shows an extended boundary layer whose structure, however, is fundamentally different from the diffuse damage configuration generated in the pantograph-reinforced chain.

Our example shows that the phase-field framework cannot be used alone to build a continuum model of the pantograph-reinforced structure. In particular, we show that due to weaker regularization through α vs regularization through $\bar{\epsilon}$, the standard phase-field model does not capture the reentry nature of the bifurcation and therefore misses the main effect: the recovery of the homogeneous state at a large levels of stretching. We have seen that in phase-field theory, fracture remains localized independently of the loading, and the phenomenon of diffuse microcracking does not take place.

Below we show that the introduction of an elastic foundation in the phase-field framework fixes the problem

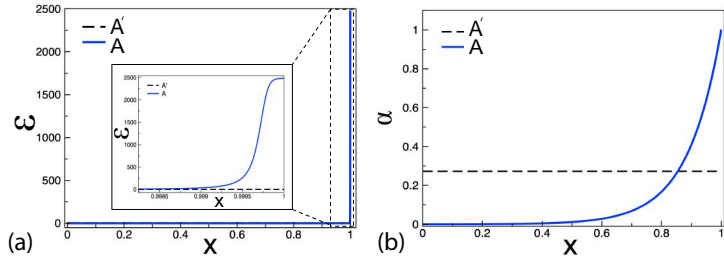


Figure 5.17: The detailed picture of the $A' \rightarrow A$ transition shown in Fig. 5.16. The macroscopic crack is nucleated near the boundary of the sample: (a) strain profile, (b) damage parameter profile (b). Here, $\lambda_1 = 0.158114$.

only partially. In this case, the return to the affine configuration at large levels of stretch is secured due to the ultimate dominance of the elastic foundation, however, the task of recovering the diffuse microcracking remains elusive.

Indeed, consider the energy functional of the form

$$E = \int_0^1 \left(f(\varepsilon, \alpha) + \frac{\lambda_1^2}{2} (\alpha')^2 + \frac{\lambda_2^{-2}}{2} (u - u^0)^2 \right) dx, \quad (5.24)$$

where again $u^0(x) = (\bar{\varepsilon}/2)(2x-1)$. We keep the same boundary conditions as in the case without elastic foundation. Then again the equilibrium equations

$$\begin{cases} -(g(\alpha)u')' + \lambda_2^{-2}(u - u^0) = 0 \\ -\lambda_1^2 \alpha'' + \frac{1}{2}(u')^2 \frac{\partial g}{\partial \alpha} + \frac{\partial h}{\partial \alpha} = 0. \end{cases} \quad (5.25)$$

We can now apply the same computational approach as in the foundation free case while appropriately modifying the expression for the second variation $\delta^2 E(u, \alpha)(v, w) = \int_0^1 [(1-\alpha)^2 v'^2 + \lambda_2^{-2} v^2 - 4(1-\alpha)u'v'w + (2+u'^2)w^2 + \lambda_1^2 w'^2] dx$.

The wavenumber of nontrivial perturbations can be found from the equation

$$\lambda_1^2 \frac{g(\alpha^o)}{\frac{\varepsilon^2}{2} \frac{\partial^2 g}{\partial \alpha^2}(\alpha^o) + \frac{\partial^2 h}{\partial \alpha^2}(\alpha^o)} (n\pi)^4 + \left(g(\alpha^o) + \frac{(\lambda_1/\lambda_2)^2 - (\varepsilon \frac{\partial g}{\partial \alpha}(\alpha^o))^2}{\frac{\varepsilon^2}{2} \frac{\partial^2 g}{\partial \alpha^2}(\alpha^o) + \frac{\partial^2 h}{\partial \alpha^2}(\alpha^o)} \right) (n\pi)^2 + \lambda_2^{-2} = 0, \quad (5.26)$$

In terms of the effective elastic energy density $f^0(\varepsilon)$ the bifurcation condition for $\bar{\varepsilon}_c$ reads

$$\left[\frac{\lambda_1^2}{\lambda_2^2} \frac{f^0(\bar{\varepsilon}_c)}{\bar{\varepsilon}_c^2} + \frac{\partial^2 f^0}{\partial \varepsilon^2}(\bar{\varepsilon}_c) \right]^2 - \frac{\lambda_1^2}{\lambda_2^2} \frac{1}{\bar{\varepsilon}_c^2} \left[\frac{1}{\bar{\varepsilon}_c} \frac{\partial f^0}{\partial \varepsilon}(\bar{\varepsilon}_c) - \frac{\partial^2 f^0}{\partial \varepsilon^2}(\bar{\varepsilon}_c) \right] = 0. \quad (5.27)$$

Then the critical mode number n_c is

$$(n_c \pi)^2 = - \frac{(\lambda_1/\lambda_2)^2 \frac{f^0(\bar{\varepsilon}_c)}{\bar{\varepsilon}_c^2} + \frac{\partial^2 f^0}{\partial \varepsilon^2}(\bar{\varepsilon}_c)}{\frac{\lambda_1^2}{2\bar{\varepsilon}_c^2} \left[\frac{1}{\bar{\varepsilon}_c} \frac{\partial f^0}{\partial \varepsilon}(\bar{\varepsilon}_c) - \frac{\partial^2 f^0}{\partial \varepsilon^2}(\bar{\varepsilon}_c) \right]}. \quad (5.28)$$

The parametric dependence of the solutions of (5.26), is illustrated in Fig. 5.18(a,d). We see the return of the closed loops as in the case of a pantograph-reinforced chain, see Fig. 5.9(a,d). The loops becomes larger as $\lambda_2 \rightarrow \infty$, and in the limit, we recover the loopless case of classical brittle fracture, see Fig. 5.15(a). Such ‘opening’ of the stability boundaries is reminiscent of the theory of wrinkles in stretched elastic sheets as one moves from the fully nonlinear 3D theory for, say neo-Hookean material, to a simplified Foppl-von Karman theory [397].

In Fig. 5.18(b,e), we show the parametric dependence of the critical strain, see (5.27). Due to the presence of an elastic background, the re-entry behavior of the affine configuration is recovered with the emergence of the two critical strains $\bar{\varepsilon}_c^*$ and $\bar{\varepsilon}_c^{**}$ representing, respectively, the lower and upper limits of stability for the homogeneous

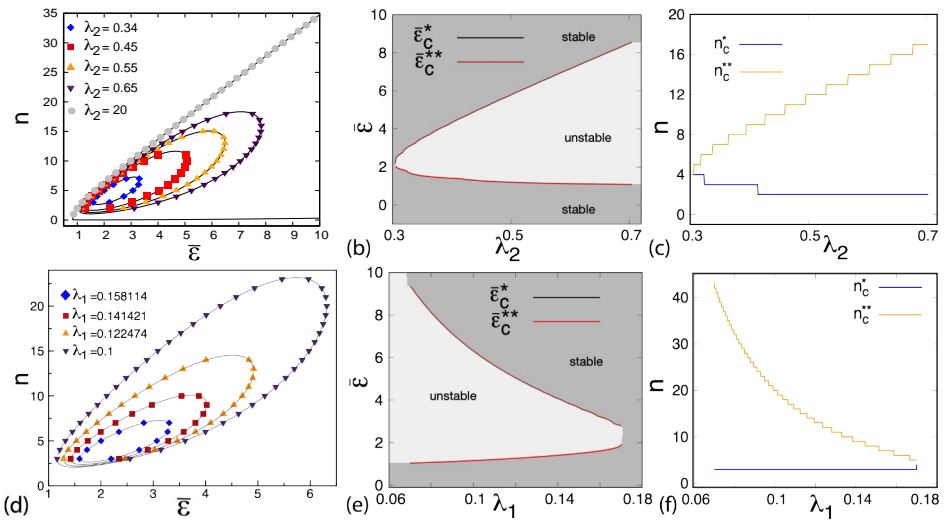


Figure 5.18: Linear stability of a homogeneous state in the continuum (phase-field) model of breakable chain coupled to an elastic background. Parametric study: (a,d) bifurcation points; (b,e) critical strains $\bar{\varepsilon}_c^*$ and $\bar{\varepsilon}_c^{**}$; (c,f) instability mode numbers n_c^* and n_c^{**} . In (a-c) $\lambda_1 = 0.158114$ and in (d-f) $\lambda_2 = 0.34$.

state, see Fig. 5.18 (b,e). The parametric dependence of the critical wavenumber n_c , shown in Fig. 5.18(c,f), departs from what we have seen in the model of pantograph-reinforced chain on an elastic foundation as the critical wavenumber $n_c(\bar{\varepsilon}_c^*)$ is now different from the critical wavenumber $n_c(\bar{\varepsilon}_c^{**})$. We can link this result with the fact that the re-stabilization (or healing) of the affine state at large levels of stretching is enforced by a different physical mechanism in our two settings: the bending induced ‘weak’ nonlocality of ‘ferromagnetic’ type in the case of the pantograph-reinforced breakable chain, and the elastic foundation-induced ‘strong’ nonlocality of anti-ferromagnetic type in the case of the chain coupled to an elastic foundation.

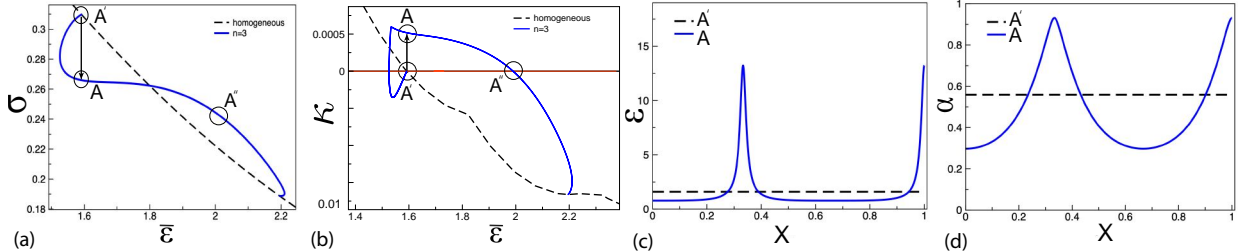


Figure 5.19: First instability along the LEM path in the continuum model of a breakable chain coupled to an elastic background: (a) macroscopic strain-stress response showing the discontinuous transition $A' \rightarrow A$ from affine to non-affine states at the critical strain $\bar{\varepsilon}_c^*$; (b) smallest eigenvalue of the second variation for the branch with $n = 0$ and $n = 3$ as a function of the loading parameter $\bar{\varepsilon}$; (c,d) strain and damage parameter profiles before and after the $A' \rightarrow A$ transition. Parameters: $\lambda_1 = 0.158114$, $\lambda_2 = 0.34$.

Consider now the post-bifurcational response under the LEM protocol. The stress-strain response, following the first instability at the point A' , is illustrated in Fig. 5.19(a) for a particular choice of parameters λ_1 and λ_2 . The branch switching transition $A' \rightarrow A$ brings the system from the trivial branch with $n = 0$ to the nontrivial equilibrium branch with $n = 3$, and the linear stability of the ensuing non-affine configuration is illustrated in Fig. 5.19(b) where we show that in point A the smallest eigenvalue of the corresponding second variation is positive. In Fig. 5.19(c,d) we show that during this symmetry breaking transition two localized cracks nucleate simultaneously: one inside the domain and one on the boundary. Due to the subcritical nature of the bifurcation, the dissipative transition $A' \rightarrow A$ is accompanied by an abrupt stress drop, see Fig. 5.19(a). As we see from Fig. 5.19(b), the equilibrium configurations with $n = 3$ loses linear stability at the point A'' . To describe the subsequent transformations, we need to reconstruct the global picture and consider equilibrium configurations with different values of n . The corresponding solutions of the nonlinear system (5.25) are shown in Fig. 5.20 where

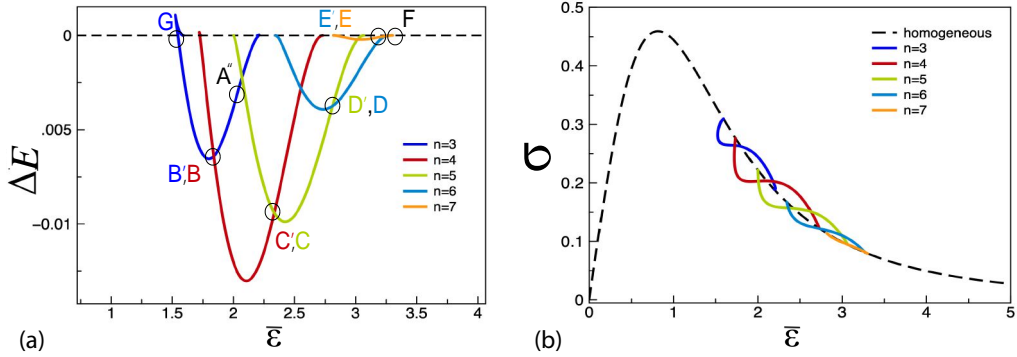


Figure 5.20: Mechanical response in the continuum (phase-field) model of a breakable chain on elastic foundation deformed according to the GEM protocol: (a) the energy difference between the affine and non-affine configurations, letters G,B,C,D,E,F indicate dissipation-free branch switching events; (b) the corresponding macroscopic strain-stress relations. Parameters: $\lambda_1 = 0.158114$, $\lambda_2 = 0.34$.

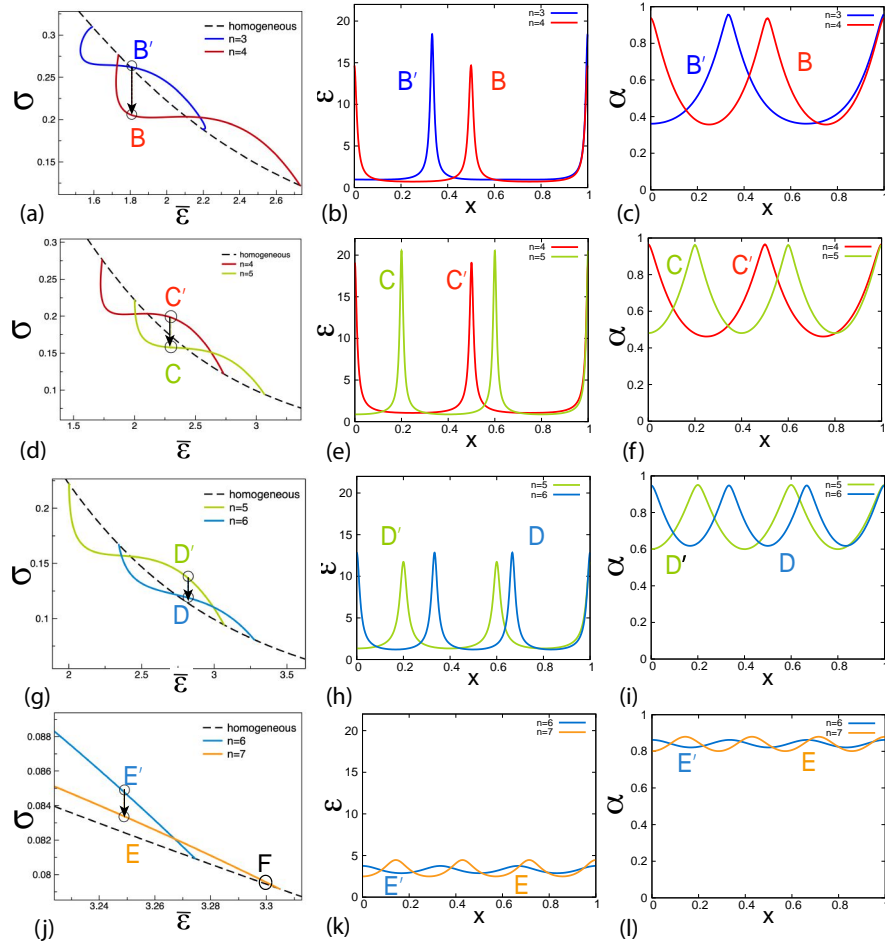


Figure 5.21: Zoom in on various dissipation-free GEM transitions depicted in Fig. 5.20: (a,d,g,j) stress-strain relations, (b,e,h,k) strain profiles, (c,f,i,l) damage parameter profiles. Parameters: $\lambda_1 = 0.158114$, $\lambda_2 = 0.34$.

we collected information about the equilibrium branches with $n = 3, \dots, 7$.

We observe that under the LEM protocol, the only available transition from point A'' is to the branch with $n = 4$, which is locally stable in the corresponding range of applied strains $\bar{\epsilon}$. Beyond this point, a sequence of dissipative LEM transitions takes place with more and more cracks appearing sequentially, till finally, at a sufficiently large value of the loading parameter, the strain localization abruptly disappears, and the damage becomes uniformly distributed. The detailed picture of the LEM response will be laid out elsewhere, while below, for a difference, we summarize the system's behavior along the GEM dynamic path.

The access to the equilibrium branches shown in Fig. 5.20 allow one to describe all the successive branch

switching events in the process of quasi-static stretching. The nature of the corresponding transitions is illustrated in Fig. 5.21 which should be compared with the analogous Fig. 5.12 and Fig. 5.13 showing the succession of the GEM transitions in the system reinforced by pantograph substructure.

We observe in Fig. 5.20 that along the GEM path the first non-symmetric, two-crack configuration nucleates non-dissipatively at the point G' . The corresponding transition $G' \rightarrow G$ marks the switch from the branch $n = 0$ to the branch $n = 3$, see Fig. 5.20(a). The next GEM transition at point B' to the branch $n = 4$ takes place before the corresponding linear instability limit, marked by the point A'' is reached, see Fig. 5.20(a). The configuration which emerges as a result of the non-dissipative transition $B' \rightarrow B$ is illustrated in Fig. 5.21 (a-c). As we see, the non-symmetric two-crack configuration transforms into the symmetric three-crack configuration with one localized crack in the center and two localized cracks around the boundaries. The next GEM transition $C' \rightarrow C$ breaks the symmetry again, creating a three-crack configuration with two localized cracks inside and one localized crack on the boundary. Then, the symmetry is recovered during the transition $D' \rightarrow D$ when the four-crack configuration emerges with two localized cracks inside and two localized cracks around the boundaries. Finally, after yet another symmetry breaking transition $E' \rightarrow E$ the affine configuration is retrieved at the point F .

Note that with each successive GEM transition, both the strain $\varepsilon(x)$ and the measure of damage $\alpha(x)$ become less localized. In particular, just before the affine state is recovered, that sample appears almost unstressed with slight modulation of strain but with the level of damage almost uniformly *high*. In such configuration, which absorbs all the work of the loading device, the elastic strain is systematically replaced by the inelastic strain. Instead, along the corresponding LEM path, the energy is dissipated instead of being accumulated.

Note also that in the phase-field model, even in the presence of an elastic background, cracks remain *localized* almost all the way till they disappear in the state entirely dominated by the elastic background. Their number increases with stretch, however, in contrast to the model of pantograph-reinforced chain, the extended *domains* of distributed damage do not appear. In this sense, the reinforcement through the elastic foundation *is not* equivalent to the reinforcement through the bending dominated sub-structure. Therefore, the floppy substructure is indeed the crucial element of the proposed metamaterial design.

5.5.2 Irreversible evolutions and stability

In our previous analysis of the phase-field model, we neglected the irreversibility constraint—arguably the model’s most fundamental feature—to isolate the essential mechanics of bifurcation. We now briefly consider the irreversible case, where damage can only increase, which profoundly affects the stability analysis.

The irreversibility constraint restricts admissible perturbations to a cone K_0^+ rather than the full tangent space X_0 . More precisely, admissible perturbations in the fully reversible case belong to the tangent space $T_y X_t = X_0$ associated with X_t (respectively, $T_y X_t = \widetilde{X}_0$) which is a linear vector space, whereas in the irreversible case admissible perturbations constitute the closed convex cone K_0^+ (respectively, \widetilde{K}_0^+). Consequently, stability must be assessed through the constrained variational inequality:

$$\delta^2 E(y^{\text{hom}})(y - y^{\text{hom}}, y - y^{\text{hom}}) > 0, \quad \forall y - y^{\text{hom}} \in K_0^+, \quad (5.29)$$

where for brevity, we denote by $y := (u, \alpha)$. This constraint fundamentally alters the stability landscape. Defining $t_s := \inf_t \{\delta^2 E(y^{\text{hom}})(\zeta, \zeta) = 0, \text{ for some } \zeta \in K_0^+\}$ as the stability threshold and recalling that t_b denotes the bifurcation threshold, the inclusion $K_0^+ \subset X_0$ implies that $t_b \leq t_s$. Equality holds only when the first bifurcation mode has a definite sign.

This reveals a crucial distinction in the irreversible setting: *bifurcation and stability are decoupled*. A system may lose uniqueness (bifurcate) while remaining stable on the homogeneous branch. In other words, alternative equilibrium paths may emerge, yet the homogeneous solution persists as a stable, observable state beyond the bifurcation point.

In our simplified one-dimensional setting through an illustrative numerical computation with the same material

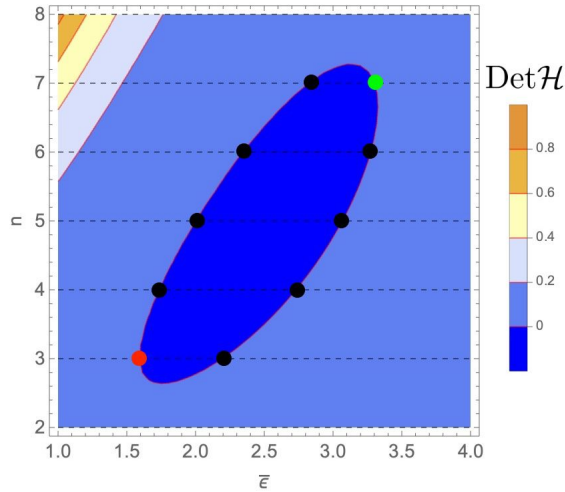


Figure 5.22: Determinant $\det H$ for homogeneous solution α_h ($\ell = 0.16$, $\Lambda = 0.34$) for a rigid foundation;. Closed loops indicate re-entry behavior at large deformations. Black dots: bifurcations from homogeneous solution; red/green dots: critical strains $\bar{\epsilon}^*$ (red) and $\bar{\epsilon}^{**}$ (yellow) (lower/upper stability limits). Critical wave numbers differ between limits: $n_c(\bar{\epsilon}^*) \neq n_c(\bar{\epsilon}^{**})$.

parameters as above, enforcing irreversibility. Irreversibility manifests both as a point-wise constraint and as a global nonlinearity in the perturbation space. Firstly, it rules out transitions between branches that require a local decrease of damage in favor of a global decrease of energy (e.g. from branch $n = 3$ to branch $n = 4$, see profiles in the Fig. 5.21 of the transition $B \mapsto C$). On the other hand, irreversibility is a global constraint that changes the structure of the perturbation space, by only allowing positive perturbations in the damage field. Consequently, irreversible evolutions are qualitatively different from the unconstrained case.

The following example illustrates the subtle scenario in which two stable irreversible solutions are computed, one of which branches off the homogeneous solution at a bifurcation point without any instability. Despite lack of uniqueness of the response enabled by the existence of bifurcations, the second computation shows that the system can robustly navigate the purely homogeneous branch, satisfying a sufficient condition for stability (hence for observability) of the computed trajectory. This juxtaposition underscores a critical sensitivity in that the numerical bifurcation induced by the solver may not reflect an actual instability transition of the physical system, but rather an artifact of the computational method.

We compute an irreversible evolution using the same parameters as in the rigid substrate model cf. Figure 5.22, using two different numerical methods: first, the quasi-Newton L-BFGS/CG method (via ALGLIB) and second, a Newton solver based on PETSc's reduced-space (active set) algorithms for variational inequalities (via SNES), [400]. In the first case, the numerical solution of first order optimality conditions with irreversibility constraints is tackled leveraging the `minbleic` subpackage of the Alglib library [81], via an active set method that handles inequality constraints $\delta E(y_t)(y - y_t) \geq 0$, $\forall y - y_t \in K_0^+$. Active inequality constraints correspond to nodes where damage necessarily evolves. Indeed, owing to the complementarity conditions (5.30)₃ given by

$$\dot{\alpha}_t \geq 0 \quad -\phi_t(\alpha_t) \leq 0 \quad \phi_t(\alpha_t)\dot{\alpha}_t = 0, \quad (5.30)$$

damage evolves ((5.30)₁ holds with a strict inequality) in regions where the system satisfies first order optimality conditions (5.30)₂ with an equality. At first order, this is handled by projecting the energy gradient onto the subspace orthogonal to the set of active constraints, ensuring the solver proceeds in directions that respect irreversibility. This projection modifies the search space as the set of active constraints evolves at each load, requiring the algorithm to re-evaluate the target function, the constraints, and the constrained subspace at each variation of damage. This guarantees that the damage field respects the irreversibility condition throughout the evolution. This robust and accurate enforcement of the first-order criticality, essential for the fidelity of phase-field models in fracture mechanics, however introduces a significant computational overhead. Indeed, every time a constraint

activates or deactivates (e.g., when a node reaches or leaves the energy optimality threshold), the constraint matrix is reorthogonalized. This operation has a computational cost of $O(n + \Delta k)k$, where n is the total number of degrees of freedom, k is the number of active constraints, and Δk represents the incremental changes in the active set. Furthermore, each evaluation of the target energy functional incurs an additional computational cost $O(n)$. By our choice of kinematic boundary conditions and the one-dimensional setting the damage criterion is attained as soon as the load is nonzero, hence this re-evaluation of constraints is performed for all nodes.

To solve the second-order cone-constrained inequality (5.29), both our solvers employ a numerical method based on the orthogonal decomposition of the Hilbert space X_0 according to two mutually polar cones K_0^+ and K^* , cf. [401, 402]. Given an element z in X_0 , there exists a unique decomposition into two orthogonal components, $x \in K_0^+$ and $y \in K^*$, where x and y are the closest elements to z in K_0^+ and K^* , respectively.

This decomposition allows us to project the second order problem into the cone and ensure that the eigen-solution satisfies the constraints imposed by irreversibility. This is particularly useful in mechanics and physics when dealing with unilateral constraints or problems where the solution space is naturally bounded by physical considerations (e.g., non-negative stress, plastic deformations, etc.)

We implement a simple iterative Scaling-and-Projection algorithm [402] which depends upon one numerical parameter, a scaling factor $\eta > 0$, and an initial guess. Given a convex cone K and an initial guess z_0 (not necessarily in the cone), the algorithm operates by first projecting the vector into the cone, $x^{(k=0)} = P_K(z_0)$, then iteratively computing the eigenvalue estimate using the Rayleigh quotient

$$\lambda^{(k)} = \frac{x^{(k)^T} H x^{(k)}}{\|x^{(k)}\|}, \quad (5.31)$$

where H is the (projected) Hessian operator. Then, we compute the residual vector $y^{(k)} = Hx^{(k)} - \lambda^{(k)}x^{(k)}$ and obtain the next iterate $x^{(k+1)} = v^{(k)}/\|v^{(k)}\|$ where $v^{(k)} = P_K(x^{(k)} + \eta y^{(k)})$. The algorithm is repeated until convergence is achieved on $x^{(k)}$. Note that, in the cone-constrained case, the residual vector $y^{(k)}$ need not be zero at convergence.

We compare spectral information from the two solver setups (see Figure 5.24), namely: i) Quasi-Newton (with approximate Hessian, L-BFGS/CG): shown with large orange and blue markers, ii) Newton-based solver (with exact Hessian, PETSc/SNES): shown with small red and black circles. In both cases, we display: the bifurcation spectrum (blue markers, black circles), and the cone-constrained stability spectrum (orange markers, red circles). At small loads both solvers follow the homogeneous path, consistent with theoretical predictions and the uniqueness of the solution below the bifurcation threshold, despite the homogeneous branch being stable. As the load increases, however, a slight oscillation appears in the damage field before the theoretical bifurcation load \bar{e}_b , for the Quasi-Newton solver. This is clearly appreciated evaluating the L^2 -norm of the damage gradient, marking the onset of spatial localisation, see the figure inset. The damage profile corresponding to the theoretical bifurcation already deviates slightly from homogeneity, at a load approximately 20% smaller than the bifurcation point. These early oscillations are reminiscent of the $n = 3$ bifurcation mode computed analytically. The bottom panel of Figure 5.24 presents the spectral diagram for the irreversible problem, displaying the smallest eigenvalues of the bifurcation (ball) and stability (cone-constrained) problems. This early transition, marked by oscillations is a spurious bifurcation driven by the numerical approximation rather than a loss of physical stability. In contrast, the Newton-based solver correctly tracks the stability of the homogeneous solution across the bifurcation point, showing strictly positive, albeit discontinuous, cone eigenvalues throughout. Corresponding trajectories are shown in the equilibrium map in Figure 5.20. This behavior highlights the sensitivity of the system. While irreversibility implemented at first order by the active-set method guarantees damage monotonicity, the Hessian approximation performed by the Quasi-Newton method disrupts the stability information, showing how approximate quasi-Newton methods may drift away from physically meaningful trajectories.

The full Newton PETSc solver, leveraging full Hessian information, maintains fidelity to the underlying variational structure and avoids spurious instabilities. There is qualitative difference in the spectral regularity: the

bifurcation inf-spectrum (infimum of eigenvalue across time) is continuous and piecewise smooth, while the stability inf-spectrum (cone-constrained infimum eigenvalue) is globally discontinuous. Our numerical experience is that the cone-constrained eigenvalue is sensitive to the initial guess. At low loads (the spectral branches labelled *a* and *b* in Figure 5.24–(bottom)), when the initial guess lies outside the admissible cone, the projection performed to bootstrap the second order solver returns a trivial zero mode, resulting in an overestimation of the smallest eigenvalue. At higher loads, the bifurcation mode providing the initial guess lies closer to the admissible set, and the spectral estimate becomes more accurate. We sample eigenmodes at the bifurcation load $\bar{\epsilon}_b$ (marked **A** and **B** in the bottom panel of Figure 5.24), associated to the homogeneous state. Their corresponding profiles are displayed in Figure 5.23–(left) and -right, respectively. Altogether, this underscores that not all observed bifurcations in numerical simulations are physical. In constrained systems, numerical artefacts arising from the choice of solver or approximation strategy can spuriously trigger localisation and corrupt the stability information encoded in the (singular) energy curvatures. The stability and bifurcation spectra are essential tools to distinguish physical transitions from purely numerical effects.

Finally, note that the bifurcation spectrum is singular at $\bar{\epsilon}_t = 0$ because the damage criterion is attained as soon as the load is non-zero, and the space of admissible rate perturbations changes suddenly from $H_0^1(0, 1) \times \emptyset$ at $\bar{\epsilon}_t = 0$ to the full space $X_0 = H_0^1(0, 1) \times H^1(0, 1)$ for $\bar{\epsilon}_t > 0$ which includes all (sufficiently smooth) damage rate perturbations. Despite the occurrence of negative eigenvalues for the bifurcation problem, the eigenvalues of the stability problem are all positive, which is a sufficient condition to determine the stability (and thus, the observability) of the computed homogeneous evolution.

This section has established the theoretical framework for understanding bifurcations and stability in phase-field fracture models. The careful distinction between variational bifurcation and constrained stability, coupled with appropriate numerical methods, provides the foundation for predicting damage localization. For a comprehensive discussion of these topics, including extensive numerical studies and practical applications, we refer the reader to [403].

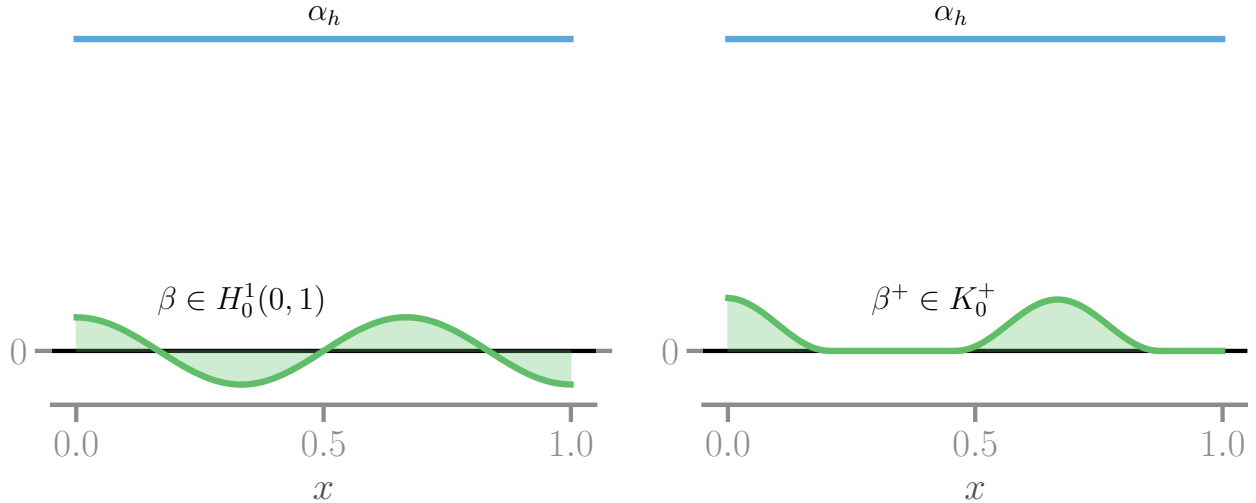


Figure 5.23: Damage field profiles (blue) and inf-eigenvectors (green) at bifurcation load $\bar{\epsilon}_b$ for the bifurcation problem (left) and the constrained stability problem (right). At bifurcation, damage α_h is homogeneous. The bifurcation field β is an eigenmode on the branch $n = 4$ (cf. Fig. 5.21). The stability problem's inf-eigenvector (β^+ on the right) is associated to an eigenvalue $\lambda = 2 \cdot 10^{-2} > 0$. These solution profiles respectively correspond to points **A**, **B** in Fig. 5.24(bottom)

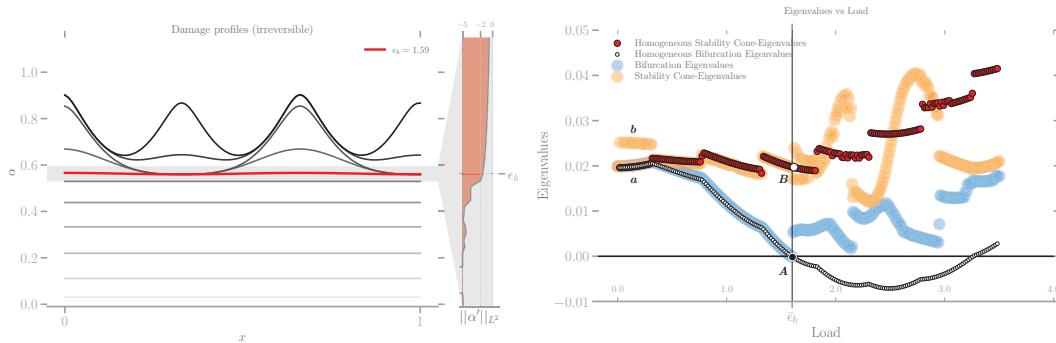


Figure 5.24: **Top:** Damage profiles from a Quasi-Newton solver with irreversibility. At first, the solution is homogeneous (bottom, light gray). As the load increases, small perturbations (oscillations) appear before the theoretically predicted bifurcation point $\bar{\epsilon}_b$, highlighted in red. This indicates a spurious numerical bifurcation due to solver sensitivity. **Inset (Top Right):** As a diagnostic, the L^2 norm of the damage gradient highlights the emergence of spatial non-homogeneity (oscillations). The red line corresponds to the theoretical bifurcation load, tick marks indicate value of the norm (base-10 logarithmic scale). **Bottom:** We compare the smallest eigenvalues computed from two numerical approaches: a Quasi-Newton solver (visualized using large blue and orange markers) and a full Newton solver (visualized using small circles, black/white and red markers). For each method, we compute two types of spectra: the bifurcation spectrum (light blue and black/white markers), which measures the loss of uniqueness of equilibrium solutions, and the stability spectrum (orange and red markers), which reflects the system's resistance to perturbations under the irreversibility constraint. The two solvers agree up to the critical bifurcation load, and diverge beyond. The full Newton solver with exact Hessian properly captures the stability of the homogeneous solution, showing its stability even after bifurcation (indicating the solution remains observable, though non-unique). This discrepancy reveals that Quasi-Newton methods, due to their partial Hessian information, can trigger premature (unphysical) transitions. In contrast, Newton-type methods with full Hessian accurately preserve stability information. Spectral Detail: the difference between cone (stability) and ball (bifurcation) eigenvalue problems also reflects in the structure of their spectra (piecewise continuous vs. smooth). Their solutions are sampled at points A and B, corresponding to the zero (singular) bifurcation eigenmode (A, cf. Fig 5.23-left) and to a stable mode not causing transition (B, cf. Fig 5.23-right).

5.6 Conclusions

While some natural materials break with the formation of a single macro-crack, other natural materials exhibit multiple, almost diffuse macro-cracking. The difference between the two classes of material behavior is reflected in the nomenclature of *fracture* and *damage* mechanics. The two are often presented as separate disciplines addressing fundamentally distinct failure modes; a closely related antithesis is between brittle and quasi-brittle (ductile) responses.

Various attempts have been made to explain the difference between these two failure mechanisms by linking them, for instance, to preexisting defects [340, 404] or to the convexity properties of the cohesive energy [335, 405]. Under the assumption that "to understand, is to build", we posed in this paper the problem of designing an artificially engineered metamaterial that can be potentially switched from one of these failure modes to another.

Our main idea is that the range of stress redistribution, exemplified by the effective rigidity, may serve as the factor affecting, at least in some cases, the localization properties of fracture phenomenon [346]. In particular, we conjectured that the transition from 'stretching dominated' to 'bending dominated' elasticity [347, 351, 406] will favor strain delocalization and will be able to change the character of the cracking process from brittle-like to ductile-like.

To check this possibility, we followed various earlier insights and proposed the simplest conceptual design of a high-toughness, pseudo-ductile metamaterial with nominally brittle sub-elements. Using this toy example we showed that by affecting the nature of the structural connectivity inside an elastic system, one can transform a brittle structure, which fails with the formation of highly localized cracks, into an apparently ductile structure exhibiting de-localized damage. The desired nominal ductility is achieved by elastic coupling of a conventional stretching-dominated brittle sub-structure with another floppy sub-structure that can transmit bending-dominated nonlocal elastic interactions.

To substantiate these conclusions, we solved a series of elementary 1D model problems showing how the presence of a floppy sub-structure can suppress strain localization and induce the formation of diffuse zones of microcracking. To facilitate the analysis we developed an asymptotically equivalent continuum theory of Ginzburg-Landau type with strain as the order parameter. Since the local part of the corresponding energy is represented by a *single-well* potential with sub-linear growth, the nonlocal (gradient) term becomes relevant ‘volumetrically’ even though there is a small coefficient in front of it. This is unusual, given that in the conventional theory of phase transitions, a similar term is only relevant for the description of narrow transition zones. We showed that in tensile loading, the proposed Ginzburg-Landau elastic model reproduces the behavior of the original discrete model adequately, including the intriguing re-entrant *isola-center* bifurcation. The main lesson is that the re-stabilization of the affine response can be accomplished by bending rather than stretching elasticity.

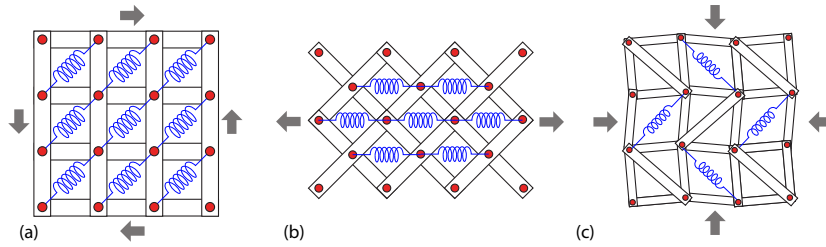


Figure 5.25: Three examples of the 2D spring systems reinforced by floppy substructures with bending dominated elasticity that can be expected to exhibit fracture de-localization under: (a) shear, (b) uni-axial tension, (c) bi-axial (hydrostatic) compression.

The analysis of the same system coupled to an elastic background revealed a complex succession of fracture patterns. Depending on the presence or absence of the floppy reinforcing substructure, the emerging microstructures include either diffuse zones of microcracking or isolated macrocracks. Our ability to manipulate such patterns in specially designed metamaterials can mimic living cells’ ability to assemble and dis-assemble various load-carrying ‘frames’ that are fine-tuned to match the particular types of loading. The presence in the space of the loading parameters of a finite range where the mechanical response of the system is non-affine may be of interest to industrial applications. For instance, it implies that under monotone driving, the appropriately designed metamaterial can produce a transient, information-carrying failure pattern that first comes out but then gets erased.

The proposed *prototypical* design of the pantograph-reinforced mass-spring chain serves only as a proof of concept, and the technologically relevant 3D brittle metamaterials, reinforced by bending-dominated floppy networks, would still have to be designed and fabricated. This task, however, is not unrealistic, given the already existing 3D printing capabilities which open access to high-contrast composite networks with inextensible but bendable elements. Three potentially interesting 2D designs of this type, involving *floppy* substructures with bending dominated elasticity, and expected to show fracture delocalization in either shear, uni-axial tension or bi-axial (hydrostatic) compression, are shown in Fig. 5.25. They demonstrate how the *harnessed* floppiness can be used to achieve high toughness in low-weight structures.

Finite size effects were also largely neglected. Interesting problems will be raised by the development of rigorous finite strain continuum approximations in higher dimensions accounting for both ‘local’ and ‘nonlocal’ sub-structures. The associated continuum problems are of higher-order, requiring the development of new analytical and numerical approaches.

Chapter 6

Perspectives

6.1 Atomistic-Continuum Framework for Failure Precursors in Crystalline Solids

The mechanics of crystalline solids at small scales presents a fundamental paradox: while these materials exhibit extraordinary strength, their performance is often undermined by unpredictable instabilities like shear banding and fracture. A key feature of their deformation is the presence of intermittent mechanical fluctuations, detectable as acoustic emission. Contrary to being simple noise, these fluctuations exhibit long-tailed distributions and complex correlations characteristic of critical systems. They contain essential information about the material's evolving microstate, yet traditional continuum models, which rely on smooth constitutive laws, inherently ignore them.

Building upon the previously introduced Mesoscopic Tensorial Model (MTM), our central ambition is to leverage this framework to create a new paradigm for materials modeling that explicitly incorporates these fluctuations. We aim to develop a predictive, physics-based approach that directly links macroscopic failure modes to the underlying discrete lattice structure through the MTM's unique capabilities. Our goal is to move beyond phenomenological descriptions and build engineering tools capable of forecasting material failure by interpreting its earliest microscopic precursors. The ultimate technological objectives are to control the brittle-to-ductile transition and to develop novel, fluctuation-based non-destructive diagnostic techniques.

Leveraging the MTM for Failure Prediction:

The MTM framework, as established earlier, provides the ideal foundation for bridging atomistic reality and continuum engineering. Having demonstrated its ability to overcome the limitations of both molecular dynamics (computationally expensive) and conventional crystal plasticity (overly phenomenological), we now focus on its application to failure precursor detection and prediction.

The model's effectiveness stems from its unique energy formulation built upon a globally periodic landscape that reflects the discrete symmetry of the underlying crystal lattice. This periodicity, governed by the group of integer-valued matrices $GL(N, \mathbb{Z})$, naturally encodes all possible lattice-invariant shears. In this framework, plastic deformation emerges as a sequence of escapes from one energy well to an equivalent one, while dislocations appear naturally as topological defects—boundaries between regions that have slipped by different integer lattice vectors.

For failure analysis, the MTM's key advantages include:

- Coherent integration of atomic-scale failure mechanisms with continuum mechanics fields (stress, strain), enabling multi-scale failure prediction as illustrated in our framework (Fig. 6.1).
- Capture of large strains, geometric non-linearities, and full crystal anisotropy during failure processes without ad-hoc assumptions.
- Natural modeling of complex dislocation interactions and their role in failure initiation and propagation.
- Direct access to the energy landscape fluctuations that serve as precursors to macroscopic failure events.

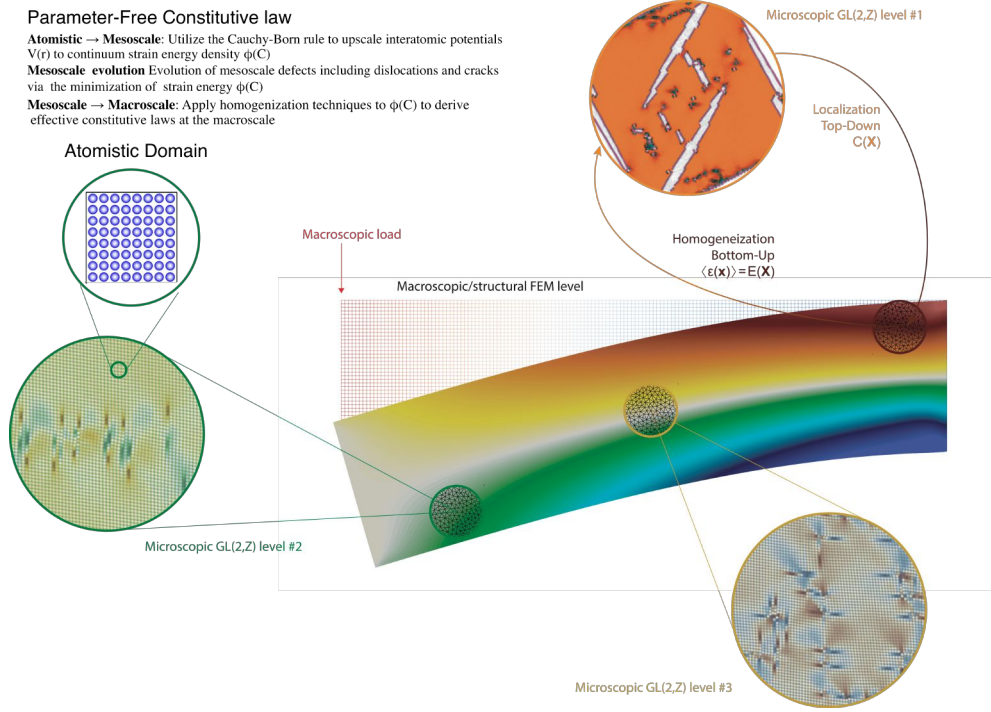


Figure 6.1: The proposed multi-scale coupling strategy.

Key Achievements and Proof of Concept: Our framework is not merely theoretical; we have achieved significant results that validate its power and potential.

- **Quantitative Validation:** The MTM accurately reproduces fundamental dislocation properties. As shown in Fig. 4.1, the model's predictions for dislocation core energy and local stress fields match molecular statics simulations with remarkable precision, all without phenomenological fitting.
- **Capturing Critical Dynamics:** Our 2D simulations successfully model dislocation nucleation in a pristine crystal and the subsequent intermittent plastic flow. The model naturally generates system-spanning avalanches, and the resulting distribution of dissipated energy follows a truncated power-law, consistent with experimental observations and theories of criticality, see Fig. 4.9.
- **Extension to 3D and Complex Physics:** We have successfully extended the MTM to 3D, a critical step for engineering relevance. Our 3D model can now simulate the behavior of FCC crystals, including complex phenomena like the dissociation of perfect dislocations into Shockley partials, their interaction, and subsequent annihilation (Fig. 6.2).
- **Pathway to Fracture Modeling:** By incorporating atomistically-informed energy potentials that soften under tension, our model can capture volumetric failure mechanisms. This enables the spontaneous nucleation of voids and micro-cracks alongside dislocations, opening a direct path to studying the brittle-to-ductile transition (Fig. 6.3).

1. **Finalize and Deploy a Robust 3D MTM:** We will complete the implementation for BCC and HCP lattices, essential for modeling a wider range of engineering materials. This involves using advanced lattice reduction algorithms and a Cauchy-Born approach to construct the 3D energy potentials. We will then simulate fundamental 3D mechanisms like cross-slip, Frank-Read sources, and forest hardening to validate the model against established theory and experiment.
2. **Develop a Predictive Model of Plasticity-Fracture Interaction:** We will use material-specific interatomic potentials (e.g., EAM) to construct realistic, multi-well Landau energy functions. This will allow us to quantitatively study the brittle-to-ductile transition by modeling the competition between dislocation emission from a crack tip and crack propagation. We will investigate the role of microstructure by explicitly modeling dislocation-grain boundary interactions.

3. **Identify Failure Precursors in Cyclic Loading:** A major goal is to understand fatigue. We will subject our virtual samples to cyclic loading and systematically track the evolution of avalanche statistics (e.g., energy, size, duration). We aim to identify robust statistical signatures that act as long-range precursors to catastrophic failure, linking the evolution of internal micro-damage to the external acoustic signals.
4. **Create a Coupled FE-MTM Multi-scale Framework:** To bridge the model to engineering scales, we will develop a strongly coupled framework where macroscopic finite elements (FE) are enriched with our MTM model. This will enable simulations of macroscopic components while resolving the critical defect physics locally. This tool will be used to reconstruct experimental fatigue life (Wöhler) curves from first principles, capturing their inherent statistical variability.

Impact and Dissemination: This project promises to significantly advance our fundamental understanding of material failure. By developing a framework that bridges scales from the atomistic to the continuum, we will provide a powerful tool for designing more reliable materials and structures. The findings will have a broad impact on industries where structural integrity is paramount. In line with open-science principles, our 2D code is already publicly available on GitHub, and we commit to maintaining this repository, publishing our 3D code, and making all simulation data accessible to ensure transparency and reproducibility.

6.1.1 Fracture in thin films:

Flexible electronic devices on polymer substrates hold promise for applications such as wearable sensors, flexible displays, and smart textiles. While polymers are lightweight and inexpensive, the inorganic thin films that provide optical, magnetic, or electronic functionality are prone to early fracture under bending or stretching. Intrinsic solutions based on ductile materials (e.g., Cu, Au, or flawless alumina) remain limited. Instead, multi-material systems with nanometric architectures appear more promising for achieving both robustness and multifunctionality.

To address this challenge, I collaborated with **D. Faurie (LSPM)** and **A. Léon-Baldelli (d'Alembert)**

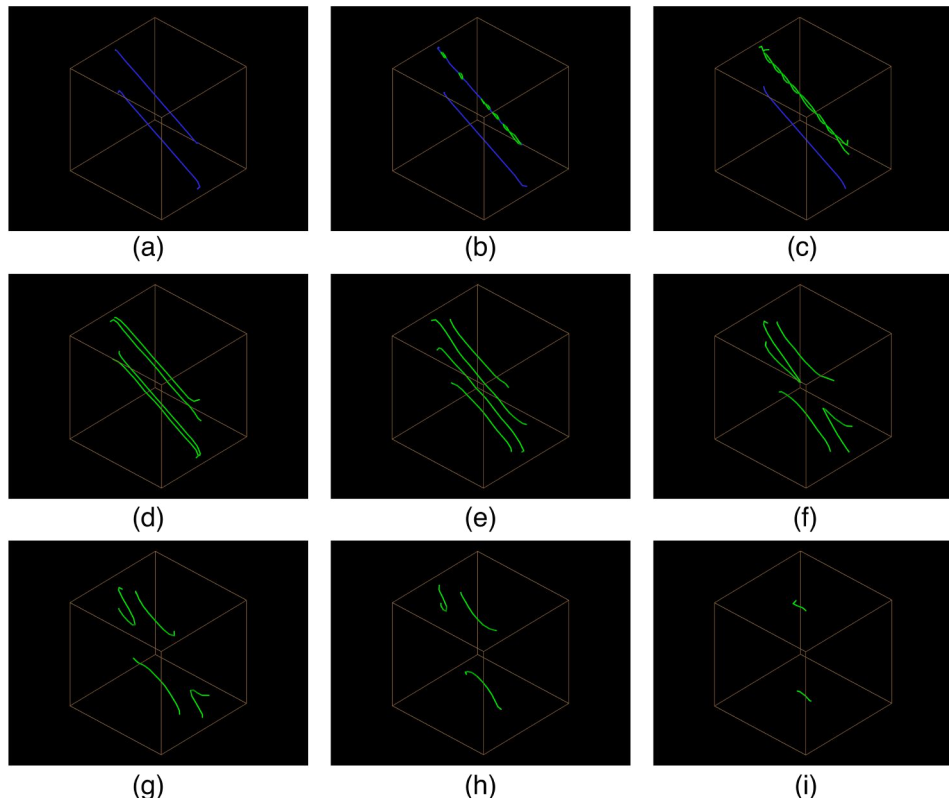


Figure 6.2: A 3D simulation showing the complete lifecycle of a dislocation dipole, from dissociation into partials to mutual annihilation.

and supervised postdoctoral researchers M. Degeiter and M. Terzi through the ANR-FWF NANOFILM project. We first developed a 1D phase-field model and performed a bifurcation analysis to predict crack nucleation, rigorously analyze the stability of solutions returned by existing algorithms, and propose a new strategy based on second-order information of the energy landscape to obtain stable crack-evolution paths (see [Terzi et al., CMAME 445, 118201, 2025](#)). Building on this foundation, we extended the framework to 2D with a deformable substrate and implemented both a fully stable FFT-based solver coupled with quasi-Newton methods and a traditional FEM solver incorporating variational irreversibility to enforce damage irreversibility. Representative results are shown in Fig. 6.4, highlighting fracture patterns under uniaxial and biaxial loading. Looking ahead, we aim to incorporate substrate plasticity into the modeling—which is known to alter crack-pattern evolution—and to develop a comprehensive numerical framework for fracture in flexible systems. The numerical developments carried out in this work are openly available at <https://github.com/cnrs-oguzumut/smooth-crack>.

(iii) Multiscale Modeling of Metallic Glass Deformation: From Atomic Heterogeneities to Macroscopic Failure

The mechanics of metallic glasses presents a fundamental challenge that bridges atomic-scale physics and continuum mechanics. Unlike crystalline materials where defects can be referenced against well-defined lattice structures, metallic glasses lack this reference state, making plastic deformation inherently more complex. The recent ANR-

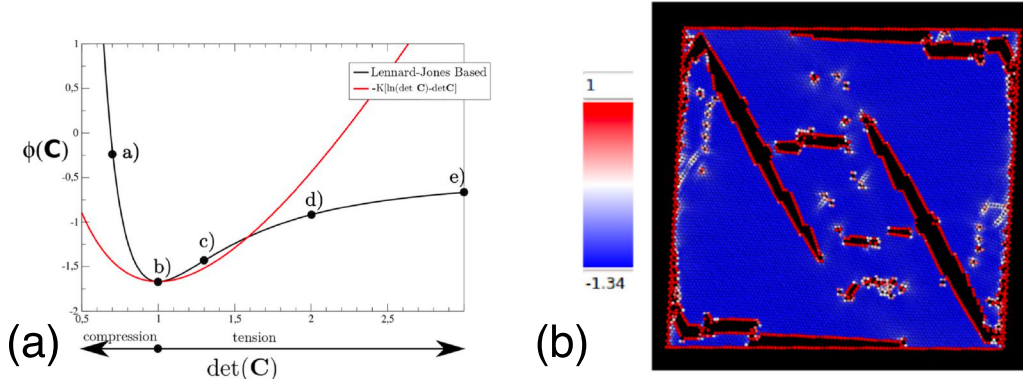


Figure 6.3: The MTM's ability to model fracture by using a volumetric energy potential derived from atomistics, allowing voids and cracks to form.

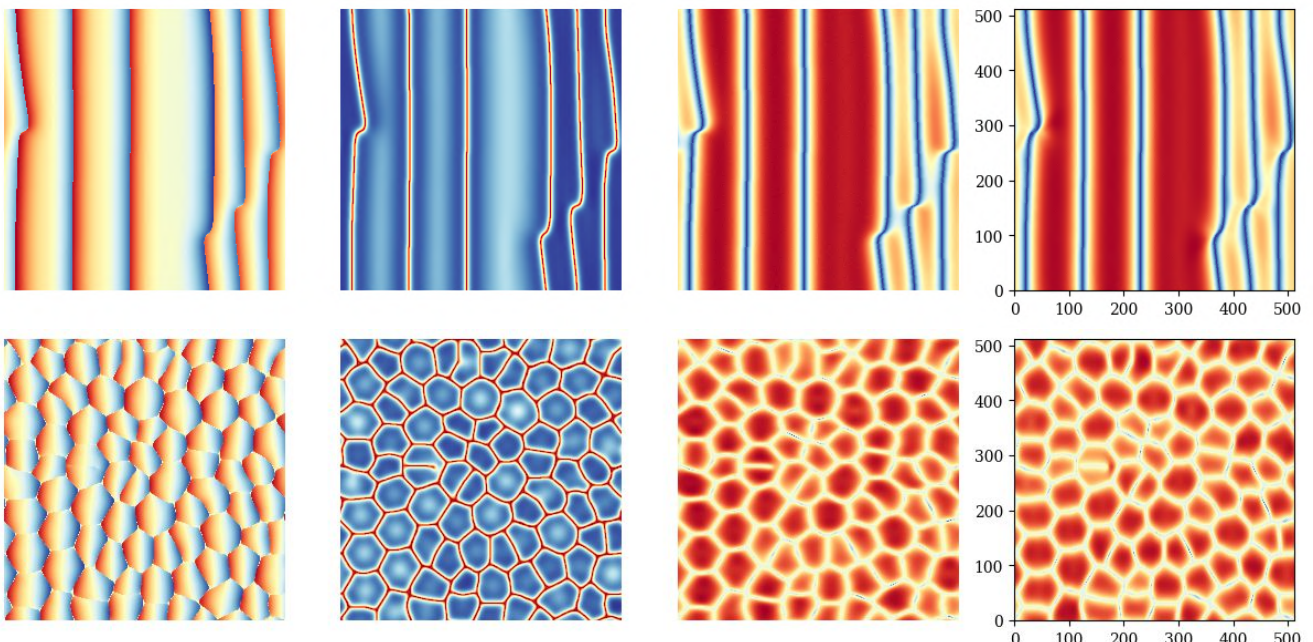


Figure 6.4: Fracture patterns in thin films under mechanical loading. Top: uniaxial loading, bottom: biaxial loading. Each panel shows (from left to right) the displacement, phase-field, and stress fields.

FWF Super-Glasses project, conducted in collaboration with **Dr. Matteo Ghidelli (LSPM-CNRS)** and **Dr. Christoph Gammer (ESI, Austrian Academy of Sciences)**, addresses this challenge through a systematic multiscale approach that links atomic-scale structural heterogeneities to macroscopic mechanical behavior.

The project's central ambition is to understand and control the brittle-to-ductile transition in metallic glasses by manipulating local chemical composition and structural state. Traditional approaches to improving metallic glass ductility focus on introducing crystalline phases or creating multilayer architectures. However, these strategies do not address the fundamental atomic-scale mechanisms governing shear transformation zones (STZs) and shear band formation. Our theoretical framework aims to provide this missing link through first-principles modeling coupled with mesoscale coarse-graining strategies.

The project team has been successfully established with the recent recruitment of a PhD student who will focus on the experimental synthesis of ZrCu-O thin film metallic glasses and their structural characterization. We are currently in the process of recruiting a 2-year postdoctoral researcher who will lead the development of machine learning force fields and the implementation of the mesoscale elasto-plastic modeling framework.

Atomistic Foundation and Machine Learning Force Fields: The computational strategy employs ab initio molecular dynamics (AIMD) coupled with density functional theory (DFT) to investigate model ZrCu and PdSi systems with controlled oxygen addition (0-20 at.%). A key innovation is the implementation of machine learning force fields (MLFF) in VASP 6.x, enabling ultrafast compositional screening by replacing quantum mechanical calculations with trained molecular dynamics simulations. This approach allows systematic investigation of how oxygen concentration and structural state (free volume) influence the brittle-to-ductile transition.

The atomistic models span multiple length scales: 300 atoms for AIMD calculations providing quantum mechanical accuracy, and hundreds of thousands of atoms for large-scale MD simulations using LAMMPS with trained force fields. To quantify plastic rearrangements during mechanical loading, we calculate vibrational modes and derive quantities such as participation ratios and phonon order parameters. These metrics provide quantitative information about the topology of STZs and their evolution under stress, moving beyond phenomenological descriptions toward predictive understanding.

Mesoscale Coarse-Graining Strategy: A critical innovation is the development of a mesoscale elasto-plastic model that captures essential physics of amorphous plasticity at larger length scales. Unlike crystalline materials where the Cauchy-Born rule combined with crystal symmetries adequately describes mesoscale behavior, amorphous solids require fundamentally different approaches. We construct probability distributions of plastic thresholds by isolating patches of equal area from atomistic systems and measuring local yield stresses—a methodology analogous to our earlier work on crystal plasticity but adapted for the unique challenges of amorphous materials.

The mesoscale strain-energy density is systematically derived from MD simulations rather than relying on phenomenological multi-well potentials typically used in amorphous plasticity models. This approach captures nanoscale heterogeneity in non-linear mechanical response as a function of both structural state and oxygen concentration. The framework extends beyond the limitations of two-dimensional Lennard-Jones systems that dominate current theoretical work, providing realistic descriptions for metallic systems with directional bonding.

Scale-Bridging Experimental Validation: Our theoretical predictions guide experimental synthesis of thin film metallic glasses (TFMGs) with controlled composition and structural state. The collaboration with Ghidelli's group at LSPM focuses on ZrCu-O systems, while Gammer's team at ESI investigates PdSi-O systems. This division allows systematic comparison of metal-metal versus metal-metalloid systems under identical modeling frameworks.

Experimental validation employs advanced characterization techniques including 4D-STEM for nanoscale strain mapping, in situ SEM micropillar compression for mechanical testing, and atom probe tomography for precise chemical analysis. The integration of experimental observations with theoretical predictions enables iterative refinement of both models and synthesis protocols.

Technological Objectives and Impact: The project aims to establish design principles for bulk metallic glasses with enhanced ductility through controlled chemical and structural heterogeneities. Preliminary results demonstrate that oxygen addition creates regions of strong covalent bonding surrounded by more loosely packed areas,

fundamentally altering STZ dynamics. Even modest oxygen concentrations (<5 at.

The mesoscale model enables investigation of brittle-to-ductile transitions at length scales inaccessible to atomistic simulations while maintaining direct connection to underlying atomic mechanisms. This capability is essential for understanding how local heterogeneities influence macroscopic shear band formation and propagation.

Future Directions and Broader Impact: This work establishes a computational framework that can be extended to other amorphous systems, including oxide glasses and polymers. The machine learning force field methodology provides a pathway for high-throughput screening of glass-forming compositions with tailored properties. The mesoscale modeling approach offers a bridge between fundamental science and engineering applications, enabling the design of metallic glasses for structural applications where both strength and ductility are required.

The collaboration integrates French expertise in synthesis and mechanical characterization with Austrian leadership in advanced electron microscopy and Austrian Academy computational resources. This international partnership exemplifies the multidisciplinary approach necessary for addressing complex materials challenges that span multiple length and time scales.

Through this systematic approach combining first-principles calculations, mesoscale modeling, and experimental validation, we aim to transform metallic glass design from empirical trial-and-error toward predictive materials engineering based on fundamental understanding of atomic-scale mechanisms.

Appendix A

Algorithm

A.1 Appendix: Numerical Algorithm

Preprocessing:

Generate finite element mesh of domain Ω and identify boundary nodes on $\partial\Omega$

Initialize displacement vector $\mathbf{u} = \mathbf{0}$ for all nodes

Loading Loop:

Apply loading through displacement $\mathbf{u}(\alpha) = (\bar{\mathbf{F}}(\alpha) - \mathbf{I})\mathbf{x}$ for boundary nodes on $\partial\Omega$, where $\bar{\mathbf{F}}(\alpha)$ is the applied deformation gradient with amplitude α

Phase 1: L-BFGS Minimization

repeat

 Construct deformation gradient \mathbf{F} in each element

 Construct metric tensor $\mathbf{C} = \mathbf{F}^T \mathbf{F}$ in each element

 Perform Lagrange reduction to calculate reduced metric tensor \mathbf{C}_D and matrix \mathbf{m}

 Calculate first Piola-Kirchhoff stress tensor

 Obtain nodal forces and total strain energy W^t

 Update displacement vector \mathbf{u}^t such that $W^t < W^{t-1}$

until $|W^t - W^{t-1}| < \text{tol}$

Phase 2: Newton-Raphson Refinement

Initialize with converged displacement \mathbf{u}^t from L-BFGS

repeat

 Construct deformation gradient \mathbf{F} in each element

 Construct metric tensor $\mathbf{C} = \mathbf{F}^T \mathbf{F}$ in each element

 Perform Lagrange reduction to calculate \mathbf{C}_D and \mathbf{m}

 Calculate tensor \mathbf{A}

 Assemble stiffness matrix \mathbf{K} and residual forces \mathbf{R}

 Perform Newton step: $\mathbf{u}^{t+1} = \mathbf{u}^t - \mathbf{K}^{-1} \mathbf{R}$

until $|\mathbf{R}^t| < \text{tol}$

Load Increment:

Increase loading amplitude: $\alpha \leftarrow \alpha + \delta\alpha$

Return to loading loop for next increment

Appendix B

Curriculum Vitae

Oğuz Umut SALMAN

oguzumut.salman@cnrs.fr
<https://cnrs-oguzumut.github.io/scientific-profile/>
+33(0)783146245

Professional Experience

CNRS (2015–Present)

Chargé de recherche

Researcher - Centre National Research Scientific (CNRS) in Mechanics, FRANCE
Lecturer - Université Sorbonne Paris Nord, FRANCE

CNR-IENI (2013–2015)

Scientific researcher

Post-Doctoral Fellow - CNR-IENI Milano, ITALY
Advanced Grant of the European Research Council: Size Effects in Fracture and Plasticity

Harvard University (2012–2013)

Post-doc

Post-Doctoral Fellow - The Aisenberg Biomineralization and Biomimetic Laboratory, Harvard University, USA

Bosphorus University (2011–2012)

Post-doc

Post-Doctoral Fellow - The Physics Department under the supervision of M. Mungan

Ecole Polytechnique (2009–2011)

Post-doc

Post-Doctoral Fellow - Solid Mechanics Laboratory (LMS), Ecole Polytechnique, FRANCE

Education

- Ph.D. in Physics (2005–2009) - Université Pierre et Marie Curie, Paris, FRANCE

- M.Sc. in Materials Science and Nano-Objects (2004–2005) - Ecole Polytechnique, Palaiseau, FRANCE
- B.S. in Physics (2000–2004) - Istanbul Technical University, Physics Department, Istanbul, TURKEY

Skills

Languages: Turkish (Native), French (Fluent), English (Fluent)

Programming: C, C++, Fortran, Mathematica, Matlab, Parallel coding (OpenMP-MPI), ABAQUS, FreeFem++, GPU Programming

Publications

In all my publications, I contributed to the design and implementation of the research, the analysis of the results, the development of numerical code, and the writing of the manuscript. Most of the results were obtained using my existing code libraries.

Pre-prints

- J. Smiri, O.U. Salman, I.R. Ionescu, "Orientation attractors in velocity gradient driven processes for large plastic deformations of crystals," arXiv preprint arXiv:2504.13714, (2025)
- J. Smiri, O.U. Salman, I.R. Ionescu, "Dislocation-density based crystal plasticity: stability and attractors in slip rate driven processes," arXiv preprint arXiv:2504.02413, (2025)

Published

- J. Smiri, J. Paux, O. U. Salman, and I. R. Ionescu, "Large plastic deformation of voids in crystals", Int. J. Solids Struct. 324, 113657 (2026).
- O.U. Salman, A. Finel, L. Truskinovsky, "Inertia induced power-law scaling," Mathematics and Mechanics of Solids, 1-39 (2025)
- M.M. Terzi, O.U. Salman, D. Faurie, A.A. Baldelli, "Navigating local minima and bifurcations in brittle thin film systems with irreversible damage," Computer Methods in Applied Mechanics and Engineering 445, 118201, (2025)
- K. Ghosh, O.U. Salman, S. Queyreau, L. Truskinovsky, "Slip-dominated structural transitions," Physical Review Materials 9 (7), 073604, Editors' Choice, (2025)
- M. Lamari, P. Kerfriden, O.U. Salman, V. Yastrebov, K. Ammar, S. Forest, "A time-discontinuous elasto-plasticity formalism to simulate instantaneous plastic flow bursts," International Journal of Solids and Structures 309, 11317, (2024)
- J. Smiri, O.U. Salman, M. Ghidelli, and I.R. Ionescu, "Accounting for localized deformation: a simple computation of true stress in micropillar compression experiments," Experimental Mechanics 64 (9), 1435-1442, arXiv:2310.06476, (2024)
- R. Baggio, O.U. Salman, L. Truskinovsky, "Nucleation of dislocations by pattern formation," European Journal of Mechanics-A/Solids 99, 104897, (2023)
- R. Baggio, O.U. Salman, L. Truskinovsky, "Inelastic rotations and pseudoturbulent plastic avalanches in crystals," Phys. Rev. E 107, 025004, (2023)

- C. Baruffi, A. Finel, Y. Le Bouar, B. Bacroix, O.U. Salman, "Atomistic simulations of temperature-driven microstructure formation in pure Titanium," Computational Materials Science 203, 111057, Editor's choice, (2022)
- O.U. Salman, I.R. Ioanescu, "Tempering the mechanical response of FCC micro-pillars: an Eulerian plasticity approach," Mechanics Research Communications, Volume 114, June, (2021)
- O.U. Salman, L. Truskinovsky, "Delocalizing fracture," Journal of the Mechanics and Physics of Solids 154, 104517, (2021)
- O.U. Salman, R. Baggio, B. Bacroix, G. Zanzotto, N. Gorbushin, "Discontinuous yielding of pristine micro-crystals," Comptes Rendus. Physique 22 (S3), 1-48, (2021)
- P. Zhang, O.U. Salman, J. Weiss, L. Truskinovsky, "Fluctuations in crystalline plasticity," Comptes Rendus. Physique 22 (S3), 1-3707, (2021)
- P. Zhang, O.U. Salman, J. Weiss, L. Truskinovsky, "Variety of scaling behaviors in nanocrystalline plasticity," Phys. Rev. E, 102, 023006, arXiv:2004.08579, hal-02644607, (2020)
- Edited by I.R. Ionescu, S. Queyreau, C. R. Picu, O.U. Salman, "Mechanics and Physics of Solids at Micro- and Nano-Scales," ISBN: 978-1-786-30531-2 February (2020)
- O.U. Salman, R. Baggio, "Homogeneous Dislocation Nucleation in Landau Theory of Crystal Plasticity," appeared in the book Mechanics and Physics of Solids at Micro- and Nano-Scales, (2019)
- R. Baggio, E. Arbib, P. Biscari, S. Conti, L. Truskinovsky, G. Zanzotto, and O.U. Salman, "Landau-Type Theory of Planar Crystal Plasticity," Phys. Rev. Lett. 123, 205501, (2019)
- O.U. Salman, G. Vitale, L. Truskinovsky, "Continuum theory of bending-to-stretching transition," Phys. Rev. E 100, 051001(R), Rapid Communication (2019)
- O.U. Salman, B. Muite, A. Finel, "Origin of stabilisation of macrotwin boundaries in martensites," The European Physical Journal B 92 (1), 20, (2019)
- C. Baruffi, A. Finel, Y. Le Bouar, B. Bacroix, O.U. Salman, "Overdamped Langevin Dynamics simulations of grain boundary motion," Materials Theory, 3,4 (2019)
- P. Franciosi, M. Spagnuolo, O.U. Salman, "Mean Green operators of deformable fiber networks embedded in a compliant matrix and property estimates," Continuum Mechanics and Thermodynamics, Volume 31, Issue 1, pp 101–132, (2019)
- A. Ask, S. Forest, B. Appolaire, K. Ammar, O.U. Salman, "A Cosserat crystal plasticity and phase field theory for grain boundary migration," Journal of the Mechanics and Physics of Solids 115, 167-194, (2018)
- P. Zhang, O.U. Salman, J.-Y. Zhang, G. Liu, J. Weiss, L. Truskinovsky and J. Sun, "Taming intermittent plasticity at small scales," Acta Mater., 128, 351-364, (2018)
- M. Jedrychowski, B. Bacroix, O.U. Salman, J. Tarasiuk, S. Wronski, "Investigation of SIBM driven recrystallization in alpha Zirconium based on EBSD data and Monte Carlo modeling," Materials Science and Engineering 89, 012029, (2016)
- A. Taloni, O.U. Salman, S. Zapperi, "Volume Changes During Active Shape Fluctuations in Cells," Phys. Rev. Lett. 114, 208101, (2015) - (Highlighted in Nature Physics and APS Physics Journals)
- O. Schylgo, O.U. Salman, A. Finel, "Martensitic phase transformations in Ni-Ti base shape memory alloys: Landau Theory," Acta Materialia 60, 6784-6792, (2012)

- O.U. Salman, A. Finel, R. Delville, D. Schryvers, "The role of phase compatibility in martensite," *J.Appl.Phys.*, 111, 103517, (2012)
- O.U. Salman, L. Truskinovsky, "On the critical nature of the plastic flow: one and two dimensional models," *International Journal of Engineering Science*, 59:219-254, (2012)
- O.U. Salman, L. Truskinovsky, "Minimal discrete automaton behind crystal plasticity," *Phys. Rev. Lett.* 106, 175503, (2011)
- A. Finel, O.U. Salman, "Phase Field Methods: microstructures, mechanical properties and complexity," *Comptes Rendus Physique*, Vol. 11, Issues 3-4, p. 245-256, (2010)
- O.U. Salman, "Criticality in martensite," DOI: 10.4171/OWR/2009/57, *Mathematisches Forschungsinstitut, Oberwolfach*, (2009)
- R. Delville R. D. James, O.U. Salman, A. Finel and D. Schryvers, "Transmission electron microscopy study of low-hysteresis shape memory alloys," DOI:10.1051/esomat/200902005, *ESOMAT 2009*, 02005 (2009)
- B. Muite, O.U. Salman, "Computations of geometrically linear and nonlinear Ginzburg-Landau models for martensitic pattern formation," in *ESOMAT 2009* edited by E. Sciences, P. Sittner, V. Paidar, L. Heller, H. Seiner, 587 p. 03008, (2009)
- S. Ugur, O.U. Salman, G. Tepehan, F. Tepehan, O. Pekcan, "Fluorescence study on Al_2O_3 polystyrene latex composite film formation," *Polymer composites* 26 (3), 352-360, (2005)

Current Research Funding

- **ARN-FWF: Super-Glasses (Project Leader)** - *Nanoengineering metallic glasses through chemical and structural heterogeneities*, 2 Ph.D. + 2 post-doc grant for LSPM
- **MITI - 80PRIME: BE-ST (Project Leader)** - *Physical nature of BEnding-to-STretching phase transition in semiflexible fibers networks*, Ph.D. grant (2023-2026)
- **ANR: MESOCRYSP (Project Partner)** - *Discrete Mesoscale Plasticity*, 2 Post-Docs (2021-2025)

Current Supervision

Ph.D. Students:

- P. Soyfer: Physical nature of bending-to-stretching phase transition in semi-flexible fiber networks (2024-2027)
- G. Tejedor: Numerical modeling of mesoscopic crystal plasticity (2023-2026)
- E. Lundheim: Effect of disorder on dislocation avalanches (2023-2026)

Completed Supervision

Ph.D. Students and Post-Docs:

- Ph.D: J. Smiri, "Eulerian finite element modeling of ductile fracture in micro-scale crystals," financé par une bourse de l'Université Sorbonne Paris Nord, co-directeur (36 mois), 2021-2024 (soutenue)

- Ph.D: M. Aissaoui, "Acoustic emission study of intermittent plasticity: the role of disorder, crystal orientation and symmetry," financé par une bourse de l'Université Sorbonne Paris Nord, co-directeur (36 mois), 2021-2024 (soutenue)
- Post-Doc: K. Ghosh, "Modeling of coupling of phase transition with crystal plasticity in Zirconium and Titanium through Landau theory," financé par ANR-JCJC, (18 mois), 2022-2024
- Post-Doc: M. Terzi, "A low dimensional representation of 6D metric space via machine learning for the development of a new 3D Landau theory of crystal plasticity," financé par ANR-MESOCRYSP et ANR-FWF: NANOFILM, (24 mois), 2021-2023
- Post-Doc: M. Degeiter, "Modeling of Fracture in thin films through phase-field approach," financé par Labex, 2019-2022
- Post-Doc: N. Gorbushin, "Landau-type modeling of marginal stability in plasticity," financé par ANR-PRCI-SUMMIT, 2019-2021
- Post-Doc: A. Ask, "Modélisation de Recristallisation Concours coup de pouce, Fédération francilienne de mécanique, FRANCE," financé par Concours coup de pouce de F2M, (2015-2016), (actuellement ingénieur de recherche à l'ONERA)
- Ph.D: R. Baggio, "Multi-Scale Modeling of Plasticity," financé par une bourse de l'Université Sorbonne Paris Nord, co-directeur, soutenue en décembre 2019, (post-doc à l'INRIA-Bordeaux et Université de Corse)
- Ph.D: M. Spagnuolo, "Modélisation continue des structures pantographiques," bourse européenne Inspire, UE, co-directeur, soutenue en septembre 2019
- Ph.D: C. Baruffi, "Modélisation des mécanismes de vieillissement et d'endommagement dans les alliages métalliques," bourse ONERA, FRANCE, soutenue en décembre 2018 (actuellement embauchée à ASML Netherlands, a reçu le prix Jacques Dalla Torre 2019 pour son travail de thèse)
- Ph.D: P. Zhang, supervision de la dernière année de sa thèse à Paris, collaboration Chine/France, soutenue en 2018, (actuellement professeur assistant à l'Université Jiaotong de Xi'an)

Teaching

Visiting Professor - Lund University Mechanical Department, Advanced Mechanics Master lectures, Sweden (2022-2024)

Lecturer - Modeling of Functional Materials Master 2 Course: Statistical mechanics, Theory of elasticity and Finite Element theory, Université Sorbonne Paris Nord, FRANCE (2015-Present)

Open-Source Codes

The C++ code implementing the crystal plasticity model based on $GL(2, \mathbb{Z})$ invariance and fracture in thin films can be found at: <https://cnrs-oguzumut.github.io/scientific-profile>

Bibliography

- [1] J. Ortin, A. Planes, and L. Delaey. *Hysteresis in shape-memory materials*. Academic Press, 2004.
- [2] H. Mughrabi, T. Ungár, W. Kienle, and M. Wilkens. Long-range internal stresses and asymmetric X-ray line-broadening in tensile-deformed [001]-orientated copper single crystals. *Philos. Mag. A*, 53(6):793–813, 1986.
- [3] D. Faurie, F. Zighem, P. Godard, G. Parry, T. Sadat, D. Thiaudière, and P.-O. Renault. In situ x-ray diffraction analysis of 2D crack patterning in thin films. *Acta Mater.*, 165:177–182, 2019.
- [4] Y. Xu, S. Joseph, P. Karamched, K. Fox, D. Rugg, Fionn P. E. Dunne, and D. Dye. Predicting dwell fatigue life in titanium alloys using modelling and experiment. *Nat. Commun.*, 11(1):5868, 2020.
- [5] Y. Xu, Felicity F. Worsnop, D. Dye, and Fionn P. E. Dunne. Slip intermittency and dwell fatigue in titanium alloys: a discrete dislocation plasticity analysis. *J. Mech. Phys. Solids*, 179:105384, 2023.
- [6] Dennis M. Dimiduk, C. Woodward, R. Lesar, and Michael D. Uchic. Scale-free intermittent flow in crystal plasticity. *Science*, 312(5777):1188–1190, 2006.
- [7] P.Y. Chan, G. Tselenis, J. Dantzig, Karin A. Dahmen, and N. Goldenfeld. Plasticity and dislocation dynamics in a phase field crystal model. *Phys. Rev. Lett.*, 105(1):015502, 2010.
- [8] Julia R. Greer, Warren C. Oliver, and William D. Nix. Size dependence of mechanical properties of gold at the micron scale in the absence of strain gradients. *Acta Mater.*, 53(6):1821–1830, 2005.
- [9] P. Zhang, O.U. Salman, J. Weiss, and L Truskinovsky. Variety of scaling behaviors in nanocrystalline plasticity. *Phys. Rev. E*, 102(2-1):023006, 2020.
- [10] J. Weiss, P. Zhang, O.U. Salman, G. Liu, and L. Truskinovsky. Fluctuations in crystalline plasticity. *C. R. Phys.*, 22(S3):163–199, 2021.
- [11] F. Roters, P. Eisenlohr, L. Hantcherli, D. D. Tjahjanto, T. R. Bieler, and D. Raabe. Overview of constitutive laws, kinematics, homogenization and multiscale methods in crystal plasticity finite-element modeling: Theory, experiments, applications. *Acta Mater.*, 58(4):1152–1211, 2010.
- [12] Prajwal A. Sabnis, S. Forest, Nagaraj K. Arakere, and Vladislav A. Yastrebov. Crystal plasticity analysis of cylindrical indentation on a ni-base single crystal superalloy. *Int. J. Plast.*, 51:200–217, 2013.
- [13] D. Tkalich, G. Cailletaud, Vladislav A. Yastrebov, and A. Kane. A micromechanical constitutive modeling of WC hardmetals using finite-element and uniform field models. *Mech. Mater.*, 105:166–187, 2017.
- [14] G. I. Barenblatt and V. M. Prostokishin. A mathematical model of damage accumulation taking into account microstructural effects. *Eur. J. Appl. Math.*, 4(3):225–240, 1993.
- [15] M. Frémond and B. Nedjar. Damage, gradient of damage and principle of virtual power. *Int. J. Solids Struct.*, 33(8):1083–1103, 1996.

- [16] B. Bourdin, G. A. Francfort, and J. J. Marigo. Numerical experiments in revisited brittle fracture. *J. Mech. Phys. Solids*, 48(4):797–826, 2000.
- [17] E. Lorentz and S. Andrieux. Analysis of non-local models through energetic formulations. *Int. J. Solids Struct.*, 40(12):2905–2936, 2003.
- [18] A. Benallal and J. J. Marigo. Bifurcation and stability issues in gradient theories with softening. *Modell Simul Mater Sci Eng*, 15(1):S283, 2006.
- [19] L. Ambrosio and V. M. Tortorelli. Approximation of functional depending on jumps by elliptic functional via t-convergence. *Commun. Pure Appl. Math.*, 43(8):999–1036, 1990.
- [20] I. S. Aranson, V. A. Kalatsky, and V. M. Vinokur. Continuum field description of crack propagation. *Phys. Rev. Lett.*, 85(1):118–121, 2000.
- [21] A. Karma, D. A. Kessler, and H. Levine. Phase-field model of mode iii dynamic fracture. *Phys. Rev. Lett.*, 87:045501, 2001.
- [22] L. O. Eastgate, J. P. Sethna, M. Rauscher, T. Cretegny, et al. Fracture in mode I using a conserved phase-field model. *Phys. Rev. E*, 65(3):10, 2002.
- [23] P. Engel. *Geometric Crystallography: An Axiomatic Introduction To Crystallography*. Springer Science & Business Media, Dordrecht, 2012.
- [24] M. Pitteri and G. Zanzotto. *Continuum models for phase transitions and twinning in crystals*. Chapman and Hall/CRC, Boca Raton, 2002. ISBN 9781-58488-240-4.
- [25] Ganesh R. Bhimanapati, Z. Lin, V. Meunier, Y. Jung, J. Cha, S. Das, D. Xiao, Y. Son, Michael S. Strano, Valentino R. Cooper, L. Liang, Steven G. Louie, E. Ringe, W. Zhou, Steve S. Kim, Rajesh R. Naik, Bobby G. Sumpter, H. Terrones, F. Xia, Y. Wang, J. Zhu, D. Akinwande, N. Alem, Jon A. Schuller, Raymond E. Schaak, M. Terrones, and Joshua A. Robinson. Recent advances in Two-Dimensional materials beyond graphene. *ACS Nano*, 9(12):11509–11539, 2015.
- [26] J. Chen, G. Schusteritsch, Chris J. Pickard, Christoph G. Salzmann, and A. Michaelides. Two dimensional ice from first principles: Structures and phase transitions. *Phys. Rev. Lett.*, 116(2):025501, 2016.
- [27] V.V. Hoang and N.T. Hieu. Formation of Two-Dimensional crystals with square lattice structure from the liquid state. *J. Phys. Chem. C*, 120(32):18340–18347, 2016.
- [28] K. Zhang, Y. Feng, F. Wang, Z. Yang, and J. Wang. Two dimensional hexagonal boron nitride (2D-hBN): synthesis, properties and applications. *J. Mater. Chem.*, 5(46):11992–12022, 2017.
- [29] D. Akinwande, Christopher J. Brennan, J. Scott Bunch, P. Egberts, Jonathan R. Felts, H. Gao, R. Huang, J. Kim, T. Li, Y. Li, Kenneth M. Liechti, N. Lu, Harold S. Park, Evan J. Reed, P. Wang, Boris I. Yakobson, T. Zhang, Y. Zhang, Y. Zhou, and Y. Zhu. A review on mechanics and mechanical properties of 2D materials—graphene and beyond. *Extreme Mech. Lett.*, 13:42–77, 2017.
- [30] V.V. Hoang and N.H. Giang. Compression-induced square-triangle solid-solid phase transition in 2D simple monatomic system. *Physica E*, 113:35–42, 2019.
- [31] Jerald L. Ericksen, Millard F. Beatty, and Michael A. Hayes. *Mechanics and Mathematics of Crystals: Selected Papers of J. L. Ericksen*. World Scientific, 2005.
- [32] S. Conti and G. Zanzotto. A variational model for reconstructive phase transformations in crystals, and their relation to dislocations and plasticity. *Arch. Ration. Mech. Anal.*, 173(1):69–88, 2004.

- [33] M. Pitteri. Reconciliation of local and global symmetries of crystals. *J. Elast.*, 14:175–190, 1984.
- [34] G. Parry. On the elasticity of monatomic crystals. *Math. Proc. Cambridge Philos. Soc.*, 80(1):189–211, 1976.
- [35] G. P. Parry. On the crystallographic point groups and on cauchy symmetry. In Cambridge University Press, editor, *Mathematical Proceedings of the Cambridge Philosophical Society*, volume 82, pages 165–175, 1977.
- [36] Gareth P. Parry. Low-dimensional lattice groups for the continuum mechanics of phase transitions in crystals. *Arch. Ration. Mech. Anal.*, 145(1):1–22, 1998.
- [37] L. Michel. Fundamental concepts for the study of crystal symmetry. *Phys. Rep.*, 341(4):265–336, 2001.
- [38] R. Baggio, O.U. Salman, and L. Truskinovsky. Homogeneous nucleation of dislocations as a pattern formation phenomenon. *Eur. J. Mech. A/Solids*, 99:104897, 2023.
- [39] R. Baggio, O. U. Salman, and L. Truskinovsky. Inelastic rotations and pseudoturbulent plastic avalanches in crystals. *Phys. Rev. E*, 107(2-2):025004, 2023.
- [40] H. Emmerich, Hartmut Löwen, Raphael Wittkowski, Thomas Gruhn, Gyula I. Tóth, György Tegze, and László Gránásy. Phase-field-crystal models for condensed matter dynamics on atomic length and diffusive time scales: an overview. *Adv. Phys.*, 61(6):665–743, 2012.
- [41] A. Skaugen, L. Angheluta, and Jorge Viñals. Separation of elastic and plastic timescales in a phase field crystal model. *Phys. Rev. Lett.*, 121(25):255501, 2018.
- [42] V. Skogvoll, A. Skaugen, L. Angheluta, and Jorge Viñals. Dislocation nucleation in the phase-field crystal model. *Phys. Rev. B Condens. Matter*, 103(1):014107, 2021.
- [43] V. Skogvoll, M. Salvalaglio, and L. Angheluta. Hydrodynamic phase field crystal approach to interfaces, dislocations, and multi-grain networks. *Model. Simul. Mat. Sci. Eng.*, 30(8):084002, 2022.
- [44] L. Kubin. *Dislocations, mesoscale simulations and plastic flow*, volume 5. Oxford University Press, 2013.
- [45] V. Bulatov, Farid F. Abraham, L. Kubin, B. Devincre, and S. Yip. Connecting atomistic and mesoscale simulations of crystal plasticity. *Nature*, 391(6668):669–672, 1998.
- [46] B. Devincre, T. Hoc, and L. Kubin. Dislocation mean free paths and strain hardening of crystals. *Science*, 320(5884):1745–1748, 2008.
- [47] S. Sandfeld, T. Hochrainer, M. Zaiser, and P. Gumbsch. Continuum modeling of dislocation plasticity: Theory, numerical implementation, and validation by discrete dislocation simulations. *J. Mater. Res.*, 26(5):623–632, 2011.
- [48] Yong S. Chen, W. Choi, S. Papanikolaou, M. Bierbaum, and James P. Sethna. Scaling theory of continuum dislocation dynamics in three dimensions: Self-organized fractal pattern formation. *Int. J. Plast.*, 46:94–129, 2013.
- [49] D. Rodney, Y. Le Bouar, and A. Finel. Phase field methods and dislocations. *Acta Mater.*, 51:17–30, 2001.
- [50] Y. M. Jin and A. G. Khachaturyan. Phase field microelasticity theory of dislocation dynamics in a polycrystal: Model and three-dimensional simulations. *Philos. Mag. Lett.*, 81(9):607–616, 2001.
- [51] Yu U. Wang, Yongmei M. Jin, and A. G. Khachaturyan. Phase field microelasticity modeling of dislocation dynamics near free surface and in heteroepitaxial thin films. *Acta Mater.*, 51(14):4209–4223, 2003.
- [52] A. Ruffini and A. Finel. Phase-field model coupling cracks and dislocations at finite strain. *Acta Mater.*, 92:197–208, 2015.

- [53] M. Javankakht and Valery I. Levitas. Phase field approach to dislocation evolution at large strains: Computational aspects. *Int. J. Solids Struct.*, 82:95–110, 2016.
- [54] E. B. Tadmor, M. Ortiz, and R. Phillips. Quasicontinuum analysis of defects in solids. *Philos. Mag. A*, 73(6):1529–1563, 1996.
- [55] V. B. Shenoy, R. Miller, E. b Tadmor, D. Rodney, R. Phillips, and M. Ortiz. An adaptive finite element approach to atomic-scale mechanics—the quasicontinuum method. *J. Mech. Phys. Solids*, 47(3):611–642, 1999.
- [56] R.E. Miller and E.B. Tadmor. The quasicontinuum method: Overview, applications and current directions. *J. Comput.-Aided Mater. Des.*, 9(3):203–239, 2002.
- [57] M. Dobson, R. S. Elliott, M. Luskin, and E. B. Tadmor. A multilattice quasicontinuum for phase transforming materials: Cascading cauchy born kinematics. *J. Comput.-Aided Mater. Des.*, 14:219, 2007.
- [58] V. Sorkin, R. S. Elliott, and E. B. Tadmor. A local quasicontinuum method for 3D multilattice crystalline materials: Application to shape-memory alloys. *Modell. Simul. Mater. Sci. Eng.*, 22(5):055001, 2014.
- [59] V. Shenoy, V. Shenoy, and R. Phillips. Finite temperature quasicontinuum methods. *Mater. Res. Soc. Symp. Proc.*, 538(465):465, 1998.
- [60] L. M. Dupuy, E. B. Tadmor, R. E. Miller, and R. Phillips. Finite-temperature quasicontinuum: molecular dynamics without all the atoms. *Phys. Rev. Lett.*, 95(6):060202, 2005.
- [61] Ellad B. Tadmor and Ronald E. Miller. *Modeling Materials: Continuum, Atomistic and Multiscale Techniques*. Cambridge University Press, 2011.
- [62] Krystyn J. Van Vliet, J. Li, T. Zhu, S. Yip, and S. Suresh. Quantifying the early stages of plasticity through nanoscale experiments and simulations. *Phys. Rev. B*, 67(10):104105, 2003.
- [63] T. Zhu, J. Li, Krystyn J. Van Vliet, S. Ogata, S. Yip, and S. Suresh. Predictive modeling of nanoindentation-induced homogeneous dislocation nucleation in copper. *J. Mech. Phys. Solids*, 52(3):691–724, 2004.
- [64] W. A. Curtin and Ronald E. Miller. Atomistic/continuum coupling in computational materials science. *Model. Simul. Mat. Sci. Eng.*, 11(3):R33–R68, 2003.
- [65] David L. McDowell. Multiscale modeling of interfaces, dislocations, and dislocation field plasticity. In Sinisa Mesarovic, Samuel Forest, and Hussein Zbib, editors, *Mesoscale Models: From Micro-Physics to Macro-Interpretation*, pages 195–297. Springer International Publishing, Cham, 2019.
- [66] C. Denoual, A. Caucci, L. Soulard, and Y. Pellegrini. Phase-field reaction-pathway kinetics of martensitic transformations in a model Fe3Ni alloy. *Phys. Rev. Lett.*, 105(3):035703, 2010.
- [67] A. Vattré and C. Denoual. Polymorphism of iron at high pressure: A 3D phase-field model for displacive transitions with finite elastoplastic deformations. *J. Mech. Phys. Solids*, 92:1–27, 2016.
- [68] Y. Gao, Y. Wang, and Y. Zhang. Deformation pathway and defect generation in crystals: a combined group theory and graph theory description. *IUCrJ*, 6(1):96–104, 2019.
- [69] Y. Gao, Y. Zhang, and Y. Wang. Determination of twinning path from broken symmetry: A revisit to deformation twinning in bcc metals. *Acta Mater.*, 196:280–294, 2020.
- [70] Y. Gao. A cayley graph description of the symmetry breaking associated with deformation and structural phase transitions in metallic materials. *Materialia*, 9:100588, 2020.

- [71] Y. Gao, Y. Zhang, Larry K. Aagesen, J. Yu, M. Long, and Y. Wang. Defect-free plastic deformation through dimensionality reduction and self-annihilation of topological defects in crystalline solids. *Phys. Rev. Res.*, 2(1):013146, 2020.
- [72] P. Biscari, M. F. Urbano, A. Zanzottera, and G. Zanzotto. Intermittency in crystal plasticity informed by lattice symmetry. *J. Elast.*, 123(1):85–96, 2015.
- [73] E. Arbib, P. Biscari, L. Bortoloni, C. Patriarca, and G. Zanzotto. Crystal elasto-plasticity on the poincaré half-plane. *Int. J. Plast.*, 130:102728, 2020.
- [74] E. Arbib, P. Biscari, C. Patriarca, and G. Zanzotto. Ericksen-landau modular strain energies for reconstructive phase transformations in 2D crystals. *J. Elast.*, 155(3):747–761, 2023.
- [75] E. Arbib, N. Barrera, P. Biscari, and G. Zanzotto. Reconstructive martensitic phase transitions: intermittency, anti-transformation, plasticity, irreversibility. *J. Appl. Mech.*, 92(1):1–24, 2025.
- [76] G. P. Parry. Low-dimensional lattice groups for the continuum mechanics of phase transitions in crystals. *Arch. Rational Mech. Anal.*, 145(1):1–22, 1998.
- [77] O.U. Salman and L. Truskinovsky. Minimal integer automaton behind crystal plasticity. *Phys. Rev. Lett.*, 106(17):175503, 2011.
- [78] I. Fonseca. Variational methods for elastic crystals. *Arch. Ration. Mech. Anal.*, 97(3):189–220, 1987.
- [79] P. C. Hohenberg and A. P. Krekhov. An introduction to the ginzburg–landau theory of phase transitions and nonequilibrium patterns. *Phys. Rep.*, 572:1–42, 2015.
- [80] Bruce M. Irons. Engineering applications of numerical integration in stiffness methods. *AIAA J.*, 4(11):2035–2037, 1966.
- [81] S. Bochkanov and V. Bystritsky. Alglib. Available from: www.alglib.net, 2013.
- [82] C. Sanderson and R. Curtin. Armadillo: a template-based c++ library for linear algebra. *J Open Source Softw.*, 1(2):26, 2016.
- [83] M. Fishman, Steven R. White, and E. Miles Stoudenmire. The ITensor software library for tensor network calculations, 2020.
- [84] R.W. Ogden. *Non-linear Elastic Deformations*. Dover Publications, 2013.
- [85] Y. Grabovsky and L. Truskinovsky. Normality condition in elasticity. *J. Nonlinear Sci.*, 24(6):1125–1146, 2014.
- [86] P. Sagaut. Analysis and validation of large-eddy simulation data. In *Large Eddy Simulation for Incompressible Flows: An Introduction*, pages 305–322. Springer, Berlin, Heidelberg, 2006.
- [87] L. Davidson. Large eddy simulations: how to evaluate resolution. *Int. J. Heat Fluid Flow*, 30(6):1016–1025, 2009.
- [88] P. Franciosi. The concepts of latent hardening and strain hardening in metallic single crystals. *Acta Metall.*, 33(9):1601–1612, 1985.
- [89] A Cuitiño and M Ortiz. *The hardening of single crystals*, pages 39–52. Routledge, 2021.
- [90] P. R. Dawson. Computational crystal plasticity. *Int. J. Solids Struct.*, 37(1-2):115–130, 2000.
- [91] N. Bertin, R. Carson, Vasily V. Bulatov, J. Lind, and M. Nelms. Crystal plasticity model of BCC metals from large-scale MD simulations. *Acta Mater.*, 260:119336, 2023.

- [92] D. Bancroft, Eric L. Peterson, and S. Minshall. Polymorphism of iron at high pressure. *J. Appl. Phys.*, 27(3):291–298, 1956.
- [93] Kyle J. Caspersen, A. Lew, M. Ortiz, and Emily A. Carter. Importance of shear in the bcc-to-hcp transformation in iron. *Phys. Rev. Lett.*, 93(11):115501, 2004.
- [94] D. H. Kalantar, J. F. Belak, G. W. Collins, J. D. Colvin, H. M. Davies, J. H. Eggert, T. C. Germann, J. Hawrelak, B. L. Holian, K. Kadau, et al. Direct observation of the α - ε transition in shock-compressed iron via nanosecond x-ray diffraction. *Phys. Rev. Lett.*, 95(7):075502, 2005.
- [95] C. Baruffi, A. Finel, Y.L. Bouar, B. Bacroix, and O.U. Salman. Atomistic simulation of martensite microstructural evolution during temperature driven $\beta \rightarrow \alpha$ transition in pure titanium. *Nato. Sc. S. Ss. Iii. C. S.*, 203:111057, 2022.
- [96] David A. Young. *Phase diagrams of the elements*. Univ of California Press, 1991.
- [97] S. Banerjee and P. Mukhopadhyay. *Phase transformations: examples from titanium and zirconium alloys*. Elsevier, 2010.
- [98] H. Zong, P. He, X. Ding, and Graeme J. Ackland. Nucleation mechanism for hcp \rightarrow bcc phase transformation in shock-compressed zr. *Phys. Rev. B*, 101(14):144105, 2020.
- [99] G. Grimvall, B. Magyari-Kope, V. Ozolins, and Kristin A. Persson. Lattice instabilities in metallic elements. *Rev. Mod. Phys.*, 84(2):945, 2012.
- [100] W. G. Burgers. On the process of transition of the cubic-body-centered modification into the hexagonal-close-packed modification of zirconium. *Physica*, 1(7-12):561–586, 1934.
- [101] H. Mao, William A. Bassett, and T. Takahashi. Effect of pressure on crystal structure and lattice parameters of iron up to 300 kbar. *J. Appl. Phys.*, 38(1):272–276, 1967.
- [102] S. G. Srinivasan, D. M. Hatch, H. T. Stokes, A. Saxena, R. C. Albers, and T. Lookman. Mechanism for BCC to HCP transformation: generalization of the burgers model. *arXiv preprint cond-mat/0209530*, 2002.
- [103] W. A. Bassett and E. Huang. Mechanism of the body-centered cubic–hexagonal close-packed phase transition in iron. *Science*, 238(4828):780–783, 1987.
- [104] S. J. Wang, M. L. Sui, Y. T. Chen, Q. H. Lu, E. Ma, X. Y. Pei, Q. Z. Li, and H. B. Hu. Microstructural fingerprints of phase transitions in shock-loaded iron. *Scientific reports*, 3(1):1086, 2013.
- [105] K. Masuda-Jindo, S. R. Nishitani, and V.V. Hung. hcp-bcc structural phase transformation of titanium: Analytic model calculations. *Phys. Rev. B*, 70(18):184122, 2004.
- [106] S. Merkel, A. Lincot, and S. Petitgirard. Microstructural effects and mechanism of bcc-hcp-bcc transformations in polycrystalline iron. *Phys. Rev. B*, 102(10), 2020.
- [107] T. Lee, H. Ha, J. Kang, J. Moon, C. Lee, and S. Park. An intersecting-shear model for strain-induced martensitic transformation. *Acta Mater.*, 61(19):7399–7410, 2013.
- [108] D. Banerjee, K. Muraleedharan, and J. L. Strudel. Substructure in titanium alloy martensite. *Philos. Mag. A*, 77(2):299–323, 1998.
- [109] J. Zhao, D. Maroudas, and F. Milstein. Thermal activation of shear modulus instabilities in pressure-induced bc c \rightarrow hcp transitions. *Phys. Rev. B*, 62(21):13799, 2000.
- [110] C. Cayron. Angular distortive matrices of phase transitions in the fcc–bcc–hcp system. *Acta Mater.*, 111:417–441, 2016.

- [111] C. Cayron, F. Barcelo, and Y. de Carlan. The mechanisms of the fcc–bcc martensitic transformation revealed by pole figures. *Acta Mater.*, 58(4):1395–1402, 2010.
- [112] S. M. C. Van Bohemen, J. Sietsma, and S. Van der Zwaag. Experimental observations elucidating the mechanisms of structural bcc-hcp transformations in β -ti alloys. *Phys. Rev. B*, 74(13):134114, 2006.
- [113] A.H. Zahiri, J. Ombogo, M. Lotfpour, and L. Cao. Twinning in hexagonal close-packed materials: The role of phase transformation. *Metals*, 13(3):525, 2023.
- [114] M. Sanati, A. Saxena, T. Lookman, and R. C. Albers. Landau free energy for a bcc-hcp reconstructive phase transformation. *Phys. Rev. B Condens. Matter*, 63(22):224114, 2001.
- [115] J. B. Liu and Duane D. Johnson. Bcc-to-hcp transformation pathways for iron versus hydrostatic pressure: coupled shuffle and shear modes. *Phys. Rev. B*, 79(13):134113, 2009.
- [116] V. Riffet, B. Amadon, N. Bruzy, and C. Denoual. Role of dislocations in the bcc-hcp transition under high pressure: A first-principles approach in beryllium. *Phys. Rev. Mater.*, 4(6):063609, 2020.
- [117] Yongmei M. Jin, Armen G. Khachaturyan, Yu U. Wang, Chris R. Krenn, and Adam J. Schwartz. Crystallography of the $\delta \rightarrow \alpha$ martensitic transformation in plutonium alloys. *Metall. Mater. Trans. A.*, 36:2031–2047, 2005.
- [118] G.B. Olson and M. Cohen. A general mechanism of martensitic nucleation: Part i. general concepts and the FCC \rightarrow HCP transformation. *Metall. Trans. A*, 7:1897–1904, 1976.
- [119] E. Gartstein and A. Rabinkin. On the fcc \rightarrow hcp phase transformation in high manganese-iron alloys. *Acta Metall. Mater.*, 27(6):1053–1064, 1979.
- [120] H. Fujita and S. Ueda. Stacking faults and fcc to hcp transformation in 188-type stainless steel. *Acta Metall. Mater.*, 20(5):759–767, 1972.
- [121] T. Waitz and H. P. Karnthaler. The fcc to hcp martensitic phase transformation in CoNi studied by TEM and AFM methods. *Acta Mater.*, 45(2):837–847, 1997.
- [122] Y. Liu, H. Yang, G. Tan, S. Miyazaki, B. Jiang, and Y. Liu. Stress-induced FCC to HCP martensitic transformation in CoNi. *J. Alloys Compd.*, 368(1-2):157–163, 2004.
- [123] H. Yang and Y. Liu. Factors influencing the stress-induced fcc to hcp martensitic transformation in Co–32Ni single crystal. *Acta Mater.*, 54(18):4895–4904, 2006.
- [124] Y. Liu, H. Yang, Y. Liu, B. Jiang, J. Ding, and R. Woodward. Thermally induced fcc to hcp martensitic transformation in co-ni. *Acta Mater.*, 53(13):3625–3634, 2005.
- [125] B. Li, G. Qian, Artem R. Oganov, S.E. Boulfelfel, and R. Faller. Mechanism of the fcc-to-hcp phase transformation in solid ar. *J. Chem. Phys.*, 146(21), 2017.
- [126] H. Zhang, B. Wei, X. Ou, S. Ni, H. Yan, and M. Song. Atomic-scale understanding of the reversible HCP \leftrightarrow FCC phase transition mechanisms at $\{101\bar{1}\}$ twin tip in pure titanium. *Int. J. Plasticity*, 156:103357, 2022.
- [127] W. Guo, F. Han, G. Li, Y. Zhang, M. Ali, J. Ren, Q. Wang, and F. Yuan. Atomic scale investigation of FCC \rightarrow HCP reverse phase transformation in face-centered cubic zirconium. *J. Mater. Sci. Technol.*, 137:8–13, 2023.
- [128] S. Li, Philip J. Withers, W. Chen, and K. Yan. Atomic-scale investigation of the mechanisms of deformation-induced martensitic transformation at ultra-cryogenic temperatures. *J. Mater. Sci. Technol.*, 210:138–150, 2025.

- [129] F. Zhang, Y. Ren, Z. Pei, Q. Gao, Z. Lu, B. Wang, Y. Xue, X. Cao, K. Du, Y. Yang, et al. Cooperative dislocations for pressure-dependent sequential deformation of multi-principal element alloys under shock loading. *Acta Mater.*, 276:120150, 2024.
- [130] E. Farabi, N. Haghddadi, C. Czettl, J. Pachlhofer, G. S. Rohrer, S. P. Ringer, and S. Primig. On the fcc to hcp transformation in a co-ru alloy: Variant selection and intervariant boundary character. *Scripta Mater.*, 248:116127, 2024.
- [131] Robin Fréville, Agnès Dewaele, Nicolas Bruzy, Volodymyr Svitlyk, and Gaston Garbarino. Comparison between mechanisms and microstructures of α - γ , γ - ε , and α - ε - α phase transitions in iron. *Phys. Rev. B*, 107(10):104105, 2023.
- [132] A. D. Rosa, A. Dewaele, G. Garbarino, V. Svitlyk, G. Morard, F. De Angelis, M. Krstulović, R. Briggs, T. Irifune, O. Mathon, et al. Martensitic fcc-hcp transformation pathway in solid krypton and xenon and its effect on their equations of state. *Phys. Rev. B*, 105(14):144103, 2022.
- [133] E. Galindo-Nava. On a mathematical theory for the crystallography of shear transformations in metals: Unification of mechanisms. *Materialia*, 33:102033, 2024.
- [134] V. P. Dmitriev, S. B. Rochal, Yu M. Gufan, and P. Toledano. Definition of a transcendental order parameter for reconstructive phase transitions. *Phys. Rev. Lett.*, 60(19):1958, 1988.
- [135] Pierre Tolédano and Vladimir Dmitriev. *Reconstructive Phase Transitions*. WORLD SCIENTIFIC, 1996. URL <https://www.worldscientific.com/doi/abs/10.1142/2848>.
- [136] V. Dmitriev. *Discontinuous Phase Transitions in Condensed Matter: Symmetry Breaking in Bulk Martensite, Quasiperiodic and Low-Dimensional Nanostructures*. World Scientific, 2023.
- [137] K. Bhattacharya, S. Conti, G. Zanzotto, and J. Zimmer. Crystal symmetry and the reversibility of martensitic transformations. *Nature*, 428(6978):55–59, 2004.
- [138] M. R. Eskildsen, P. L. Gammel, B. P. Barber, U. Yaron, A. P. Ramirez, D. A. Huse, D. J. Bishop, C. Bolle, C. M. Lieber, S. Oxx, et al. Observation of a field-driven structural phase transition in the flux line lattice in ErNi₂B₂C. *Phys. Rev. Lett.*, 78(10):1968, 1997.
- [139] B. Keimer, Wan Y. Shih, Ross W. Erwin, Jeffrey W. Lynn, F. Dogan, and Ilhan A. Aksay. Vortex lattice symmetry and electronic structure in Y_{ba}₂cu₃O₇. *Phys. Rev. Lett.*, 73(25):3459, 1994.
- [140] D. Chang, C.-Y. Mou, B. Rosenstein, and C. L. Wu. Interpretation of the neutron scattering data on flux lattices of superconductors. *Phys. Rev. Lett.*, 80(1):145, 1998.
- [141] A. Holz. Defect states and phase transition in the two-dimensional wigner crystal. *Phys. Rev. B*, 22(8):3692, 1980.
- [142] L. Glasser and A. G. Every. Energies and spacings of point charges on a sphere. *J. Phys. A*, 25(9):2473, 1992.
- [143] V. Bayot, E. Grivei, S. Melinte, M. B. Santos, and M. Shayegan. Giant low temperature heat capacity of GaAs quantum wells near landau level filling $\nu=1$. *Phys. Rev. Lett.*, 76(24):4584, 1996.
- [144] M. Rao, S. Sengupta, and R. Shankar. Shape-deformation-driven structural transitions in quantum hall skyrmions. *Phys. Rev. Lett.*, 79(20):3998, 1997.
- [145] D. M. Hatch, T. Lookman, A. Saxena, and H. T. Stokes. Systematics of group-nonsubgroup transitions: Square to triangle transition. *Phys. Rev. B*, 64(6):060104, 2001.

- [146] T. Shirahata, K. Shiratori, S. Kumeta, T. Kawamoto, T. Ishikawa, S. Koshihara, Y. Nakano, H. Yamochi, Y. Misaki, and T. Mori. Structural transitions from triangular to square molecular arrangements in the quasi-one-dimensional molecular conductors (DMEDO-TTF) $2XF_6$ ($x = p$, as , and sb). *J. Am. Chem. Soc.*, 134(32):13330–13340, 2012.
- [147] X. Cheng, H. Gao, X. Tan, X. Yang, M. Prehm, H. Ebert, and C. Tschiertsche. Transition between triangular and square tiling patterns in liquid-crystalline honeycombs formed by tetrathiophene-based bolaamphiphiles. *Chem. Sci.*, 4(8):3317–3331, 2013.
- [148] W. Qi, Y. Peng, Y. Han, Richard K. Bowles, and M. Dijkstra. Nonclassical nucleation in a solid-solid transition of confined hard spheres. *Phys. Rev. Lett.*, 115(18):185701, 2015.
- [149] Y. Peng, F. Wang, Z. Wang, Ahmed M. Alsayed, Z. Zhang, Arjun G. Yodh, and Y. Han. Two-step nucleation mechanism in solid–solid phase transitions. *Nat. Mater.*, 14(1):101–108, 2015.
- [150] Y. Peng, W. Li, F. Wang, T. Still, Arjun G. Yodh, and Y. Han. Diffusive and martensitic nucleation kinetics in solid-solid transitions of colloidal crystals. *Nat. Commun.*, 8(1):14978, 2017.
- [151] Y. Peng, W. Li, T. Still, Arjun G. Yodh, and Y. Han. In situ observation of coalescence of nuclei in colloidal crystal-crystal transitions. *Nat. Commun.*, 14(1):4905, 2023.
- [152] C. Denoual and A. Vattre. A phase field approach with a reaction pathways-based potential to model reconstructive martensitic transformations with a large number of variants. *J. Mech. Phys. Solids*, 90:91–107, 2016.
- [153] R. Baggio, E. Arbib, P. Biscari, S. Conti, L. Truskinovsky, G. Zanzotto, and O.U. Salman. Landau-type theory of planar crystal plasticity. *Phys. Rev. Lett.*, 123(20):205501, 2019.
- [154] H. Inoue, Y. Akahoshi, and S. Harada. A molecular dynamics-aided fracture mechanics parameter and its application to a tensile problem. *Comput. Mech.*, 16(4):217–222, 1995.
- [155] N. P. Kruyt and L. Rothenburg. Micromechanical definition of the strain tensor for granular materials. *J. Appl. Mech.*, 63(3):706–711, 1996.
- [156] S. Sengupta, P. Nielaba, M. Rao, and K. Binder. Elastic constants from microscopic strain fluctuations. *Phys. Rev. E*, 61(2):1072, 2000.
- [157] Peter H. Mott, Ali S. Argon, and Ulrich W. Suter. The atomic strain tensor. *J. Comput. Phys.*, 101(1):140–150, 1992.
- [158] Donald K. Ward, W. A. Curtin, and Y. Qi. Mechanical behavior of aluminum–silicon nanocomposites: a molecular dynamics study. *Acta Mater.*, 54(17):4441–4451, 2006.
- [159] Michael L. Falk and James S. Langer. Dynamics of viscoplastic deformation in amorphous solids. *Phys. Rev. E*, 57(6):7192, 1998.
- [160] M. L. Falk. Molecular-dynamics study of ductile and brittle fracture in model noncrystalline solids. *Phys. Rev. B*, 60(10):7062, 1999.
- [161] M. F. Horstemeyer and M. I. Baskes. Strain tensors at the atomic scale. *MRS Online Proceedings Library (OPL)*, 578:15, 1999.
- [162] Michael R. Mitchell, T. Tlusty, and S. Leibler. Strain analysis of protein structures and low dimensionality of mechanical allosteric couplings. *Proc. Natl. Acad. Sci.*, 113(40):E5847–E5855, 2016.
- [163] P. Sartori and S. Leibler. Evolutionary conservation of mechanical strain distributions in functional transitions of protein structures. *Phys. Rev. X*, 14:011042, 2024.

- [164] J. Eckmann, J. Rougemont, and T. Thusty. Colloquium: Proteins: The physics of amorphous evolving matter. *Rev. Mod. Phys.*, 91(3):031001, 2019.
- [165] Jonathan A. Zimmerman, Douglas J. Bammann, and H. Gao. Deformation gradients for continuum mechanical analysis of atomistic simulations. *Int. J. Solids Struct.*, 46(2):238–253, 2009.
- [166] J. L. Ericksen. On the Cauchy–Born rule. *Math. Mech. Solids*, 13(3-4):199–220, 2008.
- [167] P. Ming et al. Cauchy–born rule and the stability of crystalline solids: static problems. *Arch. Rational Mech. Anal.*, 183(2):241–297, 2007.
- [168] L. L. Boyer. Molecular-dynamics study of the melting of hexagonal and square lattices in two dimensions. *Phys. Rev. B*, 53(6):3145, 1996.
- [169] O.U. Salman, R. Baggio, B. Bacroix, G. Zanzotto, N. Gorbushin, and L. Truskinovsky. Discontinuous yielding of pristine micro-crystals. *C. R. Phys.*, 22(S3):201–248, 2021.
- [170] Aidan P. Thompson, H. Metin Aktulga, R. Berger, Dan S. Bolintineanu, W. Michael Brown, Paul S. Crozier, Pieter J. in't Veld, A. Kohlmeyer, Stan G. Moore, T.D. Nguyen, et al. LAMMPS-a flexible simulation tool for particle-based materials modeling at the atomic, meso, and continuum scales. *Comput. Phys. Commun.*, 271:108171, 2022.
- [171] D. Frenkel and B. Smit. *Understanding Molecular Simulation: From Algorithms to Applications*. Academic Press, San Diego, 2nd edition, 2002.
- [172] Pablo F. Damasceno, Luis Gustavo V. Gonçalves, José Pedro Rino, and M. T. Rita de Cássia. Pressure-induced structural phase transitions in a two-dimensional system. *Phys. Rev. B*, 79(10):104109, 2009.
- [173] K.Y. Lee and John R. Ray. Mechanism of pressure-induced martensitic phase transformations: a molecular-dynamics study. *Phys. Rev. B*, 39(1):565, 1989.
- [174] F. Shuang, P. Xiao, L. Xiong, and W. Gao. Atomistic mechanisms of phase nucleation and propagation in a model two-dimensional system. *Proc. R. Soc. A.*, 478(2268):20220388, 2022.
- [175] A. Dewaele, C. Denoual, S. Anzellini, F. Occelli, M. Mezouar, P. Cordier, S. Merkel, M Véron, and E Rausch. Mechanism of the α - ϵ phase transformation in iron. *Phys. Rev. B*, 91(17), 2015.
- [176] C. Thiel, J. Voss, Robert J. Martin, and P. Neff. Shear, pure and simple. *Int. J. Non-Linear Mech.*, 112: 57–72, 2019.
- [177] A. Stukowski. Visualization and analysis of atomistic simulation data with OVITO—the open visualization tool. *Modelling and simulation in materials science and engineering*, 18(1):015012, 2009.
- [178] M. F. Laguna and E. A. Jagla. Classical isotropic two-body potentials generating martensitic transformations. *J. Stat. Mech.*, 2009(09):P09002, 2009.
- [179] M.F. Laguna. Testing conditions for reversibility of martensitic transformations with an isotropic potential for identical particles. *Phys. Status Solidi B*, 252(3):538–544, 2015.
- [180] M. Rechtsman, F. Stillinger, and S. Torquato. Designed interaction potentials via inverse methods for self-assembly. *Phys. Rev. E*, 73:011406, 2006.
- [181] Nikita P. Kryuchkov, Stanislav O. Yurchenko, Yury D. Fomin, Elena N. Tsiok, and Valentin N. Ryzhov. Complex crystalline structures in a two-dimensional core-softened system. *Soft Matter*, 14(11):2152–2162, 2018.

- [182] O. Kastner. Molecular-dynamics of a 2D model of the shape memory effect: Part i: Model and simulations. *Continuum Mech. Thermodyn.*, 15:487–502, 2003.
- [183] O. Kastner. Molecular-dynamics of a 2D model of the shape memory effect: Part II: Thermodynamics of a small system. *Continuum Mech. Thermodyn.*, 18(1):63–81, 2006.
- [184] O. Kastner and Graeme J. Ackland. Mesoscale kinetics produces martensitic microstructure. *J. Mech. Phys. Solids*, 57(1):109–121, 2009.
- [185] O. Kastner, G. Eggeler, W. Weiss, and Graeme J. Ackland. Molecular dynamics simulation study of microstructure evolution during cyclic martensitic transformations. *J. Mech. Phys. Solids*, 59(9):1888–1908, 2011.
- [186] Bertrand Dupé, Bernard Amadon, Yves-Patrick Pellegrini, and Christophe Denoual. Mechanism for the $\alpha \rightarrow \varepsilon$ phase transition in iron. *Phys. Rev. B*, 87(2):024103, 2013.
- [187] D.R. Trinkle III. *A theoretical study of the hcp to omega martensitic phase transition in titanium*. The Ohio State University, 2003.
- [188] D. Zahn and S. Leoni. Nucleation and growth in pressure-induced phase transitions from molecular dynamics simulations: Mechanism of the reconstructive transformation of NaCl to the CsCl-type structure. *Phys. Rev. Lett.*, 92(25):250201, 2004.
- [189] S. Mahajan, M. L. Green, and D. Brasen. A model for the FCC \rightarrow HCP transformation, its applications, and experimental evidence. *Metall. Trans. A*, 8(2):283–293, 1977.
- [190] J. Singh and S. Ranganathan. On the mechanism of f. c. c.- \rightarrow h. c. p. transformation. *Phys. Status Solidi A*, 73(1):243–248, 1982.
- [191] R. Béjaud, Julien Durinck, and Sandrine Brochard. The effect of surface step and twin boundary on deformation twinning in nanoscale metallic systems. *Nato. Sc. Ss. Iii. C. S.*, 145:116–125, 2018.
- [192] M. Zaiser. Scale invariance in plastic flow of crystalline solids. *Adv. Phys.*, 55(1-2):185–245, 2006.
- [193] W. Jian, M. Xiao, W. Sun, and W. Cai. Prediction of yield surface of single crystal copper from discrete dislocation dynamics and geometric learning. *J. Mech. Phys. Solids*, 186:105577, 2024.
- [194] M. Ortiz. Plastic yielding as a phase transition. *J. Appl. Mech.*, 66(2):289–298, 1999.
- [195] S. Papanikolaou, Y. Cui, and N. Ghoniem. Avalanches and plastic flow in crystal plasticity: an overview. *Modell. Simul. Mater. Eng.*, 26(1):013001, 2017.
- [196] J.M. Kosterlitz. Kosterlitz–thouless physics: a review of key issues. *Rep. Prog. Phys.*, 79(2):026001, 2016.
- [197] M. Khantha and V. Vitek. Mechanism of yielding in dislocation-free crystals at finite temperatures—part i. theory. *Acta Mater.*, 45(11):4675–4686, 1997.
- [198] T. Hochrainer, S. Sandfeld, M. Zaiser, and P. Gumbsch. Continuum dislocation dynamics: towards a physical theory of crystal plasticity. *J. Mech. Phys. Solids*, 63:167–178, 2014.
- [199] James S. Langer. Statistical thermodynamics of crystal plasticity. *J. Stat. Phys.*, 175(3):531–541, 2019.
- [200] P. M. Derlet and R. Maaß. The stress statistics of the first pop-in or discrete plastic event in crystal plasticity. *J. Appl. Phys.*, 120(22):225101, 2016.
- [201] Péter D. Ispánovity, István Groma, Géza Györgyi, Ferenc F. Csikor, and Daniel Weygand. Submicron plasticity: yield stress, dislocation avalanches, and velocity distribution. *Phys. Rev. Lett.*, 105(8):085503, 2010.

- [202] J. P. Sethna, M. K. Bierbaum, K. A. Dahmen, C. P. Goodrich, J. R. Greer, L. X. Hayden, and S. Zapperi. Deformation of crystals: Connections with statistical physics. *Annu. Rev. Mater. Res.*, 47(1):217–246, 2017.
- [203] F. Ghimenti, M. Ozawa, G. Biroli, and G. Tarjus. Shear-induced phase behavior and topological defects in two-dimensional crystals. *Phys. Rev. B*, 109(10):104114, 2024.
- [204] N. Perchikov and L. Truskinovsky. Quantized plastic deformation. *J. Mech. Phys. Solids*, 190:105704, 2024.
- [205] Krutarth M. Kamani and Simon A. Rogers. Brittle and ductile yielding in soft materials. *Proc. Natl. Acad. Sci. USA*, 121(22):e2401409121, 2024.
- [206] L. Berthier, G. Biroli, M. Lisa Manning, and F. Zamponi. Yielding and plasticity in amorphous solids. *arXiv preprint arXiv:2401.09385*, 2024.
- [207] B. Shang, P. Guan, and J. L. Barrat. Elastic avalanches reveal marginal behavior in amorphous solids. *Proc. Natl. Acad. Sci.*, 117(1):86–92, 2020.
- [208] J. Shang, Y. Wang, D. Pan, Y. Jin, and J. Zhang. The yielding of granular matter is marginally stable and critical. *Proc. Natl. Acad. Sci. USA*, 121(33):e2402843121, 2024.
- [209] M. Singh, M. Ozawa, and L. Berthier. Brittle yielding of amorphous solids at finite shear rates. *Phys. Rev. Mater.*, 4(2):025603, 2020.
- [210] D. Richard, E. Lerner, and E. Bouchbinder. Brittle-to-ductile transitions in glasses: Roles of soft defects and loading geometry. *MRS Bull.*, 46(10):902–914, 2021.
- [211] J. Pollard and Suzanne M. Fielding. Yielding, shear banding, and brittle failure of amorphous materials. *Phys. Rev. Res.*, 4(4):043037, 2022.
- [212] J. Lin, E. Lerner, A. Rosso, and M. Wyart. Scaling description of the yielding transition in soft amorphous solids at zero temperature. *Proc. Natl. Acad. Sci. U. S. A.*, 111(40):14382–14387, 2014.
- [213] G. Parisi, I. Procaccia, C. Rainone, and M. Singh. Shear bands as manifestation of a criticality in yielding amorphous solids. *Proc. Natl. Acad. Sci. USA*, 114(21):5577–5582, 2017.
- [214] Peter M. Derlet and Robert Maaß. Micro-plasticity in a fragile model binary glass. *Acta Mater.*, 209:116771, 2021.
- [215] A. Barbot, M. Lerbinger, A. Hernandez-Garcia, Reinaldo García-García, Michael L. Falk, Damien Vandembroucq, and Sylvain Patinet. Local yield stress statistics in model amorphous solids. *Phys. Rev. E*, 97(3-1):033001, 2018.
- [216] Peter M. Anderson, John P. Hirth, and J. Lothe. Theory of dislocations. *Cambridge University Press*, 2017.
- [217] A. Lehtinen, G. Costantini, Mikko J. Alava, S. Zapperi, and L. Laurson. Glassy features of crystal plasticity. *Phys. Rev. B*, 94(6):064101, 2016.
- [218] M. Ovaska, A. Lehtinen, M. J. Alava, L. Laurson, and S. Zapperi. Excitation spectra in crystal plasticity. *Phys. Rev. Lett.*, 119(26):265501, 2017.
- [219] A. Nicolas, Ezequiel E. Ferrero, K. Martens, and J. Barrat. Deformation and flow of amorphous solids: Insights from elastoplastic models. *Rev. Mod. Phys.*, 90(4), 2018.
- [220] D. Rodney, A. Tanguy, and D. Vandembroucq. Modeling the mechanics of amorphous solids at different length scale and time scale. *Model. Simul. Mat. Sci. Eng.*, 19(8):083001, 2011.
- [221] M. Popović, T. W. J. de Geus, and M. Wyart. Elastoplastic description of sudden failure in athermal amorphous materials during quasistatic loading. *Phys. Rev. E*, 98(4):040901, 2018.

- [222] A. Tanguy. Elasto-plastic behavior of amorphous materials: a brief review. *C. R. Phys.*, 22(S3):117–133, 2021.
- [223] M. Talamali, V. Petäjä, D. Vandembroucq, and S. Roux. Strain localization and anisotropic correlations in a mesoscopic model of amorphous plasticity. *C. R. Mécanique*, 340(4):275–288, 2012.
- [224] J. T. Parley and P. Sollich. Ductile and brittle yielding of athermal amorphous solids: A mean-field paradigm beyond the random-field ising model. *Phys. Rev. E.*, 110(4-2):045002, 2024.
- [225] S. Karmakar, E. Lerner, and I. Procaccia. Statistical physics of the yielding transition in amorphous solids. *Phys. Rev. E Stat. Nonlin. Soft Matter Phys.*, 82(5 Pt 2):055103, 2010.
- [226] M. Ozawa, L. Berthier, G. Biroli, A. Rosso, and G. Tarjus. Random critical point separates brittle and ductile yielding transitions in amorphous materials. *Proc. Natl. Acad. Sci.*, 115(26):6656–6661, 2018.
- [227] T. Divoux, E. Agoritsas, S. Aime, C. Barentin, J.-L. Barrat, R. Benzi, L. Berthier, D. Bi, G. Biroli, D. Bonn, P. Bourrianne, M. Bouzid, E. Del Gado, H. Delanoe-Ayari, K. Farain, S. Fielding, M. Fuchs, J. van der Gucht, S. Henkes, M. Jalaal, Y. M. Joshi, A. Lemaitre, R. L. Leheny, S. Manneville, K. Martens, W. C. K. Poon, M. Popovic, I. Procaccia, L. Ramos, J. A. Richards, S. Rogers, S. Rossi, M. Sbragaglia, G. Tarjus, F. Toschi, V. Trappe, J. Vermant, M. Wyart, F. Zamponi, and D. Zare. Ductile-to-brittle transition and yielding in soft amorphous materials: perspectives and open questions. *Soft Matter*, 20(35):6868–6888, 2024.
- [228] M. Moshe, I. Levin, H. Aharoni, R. Kupferman, and E. Sharon. Geometry and mechanics of two-dimensional defects in amorphous materials. *Proc. Natl. Acad. Sci.*, 112(35):10873–10878, 2015.
- [229] M. Baggio, M. Landry, and A. Zacccone. Deformations, relaxation, and broken symmetries in liquids, solids, and glasses: A unified topological field theory. *Phys. Rev. E.*, 105(2-1):024602, 2022.
- [230] M. J. Bowick and L. Giomi. Two-dimensional matter: order, curvature and defects. *Adv. Phys.*, 58(5):449–563, 2009.
- [231] M. Katanaev and I. Volovich. Theory of defects in solids and three-dimensional gravity. *Annals of Physics*, 216:1–28, May 1992.
- [232] F. Sozio and A. Yavari. Riemannian and euclidean material structures in anelasticity. *Math. Mech. Solids*, 25(6):1267–1293, June 2020.
- [233] G. Picard, A. Ajdari, F. Lequeux, and L. Bocquet. Elastic consequences of a single plastic event: A step towards the microscopic modeling of the flow of yield stress fluids. *Europhysics Journal E*, 15:371, 2004.
- [234] Z. Budrikis, D.F. Castellanos, S. Sandfeld, M. Zaiser, and S. Zapperi. Universal features of amorphous plasticity. *Nat. Commun.*, 8:15928, 2017.
- [235] W. Cai, A. Arsenlis, Christopher R. Weinberger, and Vasily V. Bulatov. A non-singular continuum theory of dislocations. *J. Mech. Phys. Solids*, 54(3):561–587, 2006.
- [236] O.U. Salman and L. Truskinovsky. On the critical nature of plastic flow: One and two dimensional models. *Int. J. Eng. Sci.*, 59:219–254, 2012.
- [237] J. Weiss, W. Ben Rhouma, T. Richeton, S. Dechanel, F. Louchet, and L. Truskinovsky. From mild to wild fluctuations in crystal plasticity. *Phys. Rev. Lett.*, 114(10):105504, 2015.
- [238] A. Arsenlis, W. Cai, M. Tang, M. Rhee, T. Oppelstrup, G. Hommes, T. G. Pierce, and V. V. Bulatov. Enabling strain hardening simulations with dislocation dynamics. *Modell. Simul. Mater. Eng.*, 15(6):553, 2007.

- [239] Luis A. Zepeda-Ruiz, A. Stukowski, T. Oppelstrup, N. Bertin, Nathan R. Barton, R. Freitas, and Vasily V. Bulatov. Atomistic insights into metal hardening. *Nat. Mater.*, 20(3):315–320, 2021.
- [240] M. Ponga, K. Bhattacharya, and M. Ortiz. Large scale ab-initio simulations of dislocations. *J. Comput. Phys.*, 407(109249):109249, 2020.
- [241] P. Lafourcade, G. Ewald, T. Carrard, and C. Denoual. Extraction of slip systems and twinning variants from a lagrangian analysis of molecular dynamics simulations. *Mech. Mater.*, 200(105189):105189, January 2025.
- [242] M. Salvalaglio, L. Angheluta, Z. Huang, A. Voigt, Ken R. Elder, and Jorge Viñals. A coarse-grained phase-field crystal model of plastic motion. *J. Mech. Phys. Solids*, 137:103856, 2020.
- [243] Z. Zhong, Y. Huang, Y. Gao, R. Li, S. Yao, K. Wang, W. Zhu, and W. Hu. Phase field crystal model simulation of transonic dislocations and mode 2 crack propagation. *Physica B Condens. Matter*, 706(417154):417154, 2025.
- [244] I. J. Beyerlein and A. Hunter. Understanding dislocation mechanics at the mesoscale using phase field dislocation dynamics. *Philos. Trans. A Math. Phys. Eng. Sci.*, 374(2066), 2016.
- [245] M. Koslowski, A. M. Cuitiño, and M. Ortiz. A phase-field theory of dislocation dynamics, strain hardening and hysteresis in ductile single crystals. *J. Mech. Phys. Solids*, 50(12):2597–2635, 2002.
- [246] Péter Dusán Ispánovity, Lasse Laurson, Michael Zaiser, István Groma, Stefano Zapperi, and Mikko J. Alava. Avalanches in 2D dislocation systems: plastic yielding is not depinning. *Phys. Rev. Lett.*, 112(23):235501, 2014.
- [247] D. Gómez-García, B. Devincre, and L. P. Kubin. Dislocation patterns and the similitude principle: 2.5D mesoscale simulations. *Phys. Rev. Lett.*, 96(12):125503, 2006.
- [248] G. Po, M. Lazar, D. Seif, and N. Ghoniem. Singularity-free dislocation dynamics with strain gradient elasticity. *J. Mech. Phys. Solids*, 2014.
- [249] S. Lu, J. Zhao, M. Huang, Z. Li, G. Kang, and X. Zhang. Multiscale discrete dislocation dynamics study of gradient nano-grained materials. *Int. J. Plast.*, 156(103356):103356, 2022.
- [250] N. Bertin, V. V. Bulatov, and F. Zhou. Learning dislocation dynamics mobility laws from large-scale MD simulations. *Npj Comput. Mater.*, 10(1):1–9, August 2024.
- [251] T. Nasir Tak and P. J. Guruprasad. A discrete dislocation dynamics framework for modelling plasticity in two-phase polycrystals. *Model. Simul. Mat. Sci. Eng.*, 33(4):045001, June 2025.
- [252] K. Starkey, G. Winther, and A. El-Azab. Theoretical development of continuum dislocation dynamics for finite-deformation crystal plasticity at the mesoscale. *J. Mech. Phys. Solids*, 139:103926, 2020.
- [253] Y. Zhang, R. Wu, and M. Zaiser. Continuum dislocation dynamics as a phase field theory with conserved order parameters: Formulation and application to dislocation patterning. *Model. Simul. Mat. Sci. Eng.*, 33(035011), 2025.
- [254] A. Acharya. An action for nonlinear dislocation dynamics. *J. Mech. Phys. Solids*, 161(104811), 2022.
- [255] A. Acharya, Anish R., and A. Sawant. Continuum theory and methods for coarse-grained, mesoscopic plasticity. *Scr. Mater.*, 54(5):705–710, 2006.
- [256] D. Rodney and R. Phillips. Structure and strength of dislocation junctions: An atomic level analysis. *Phys. Rev. Lett.*, 82(8):1704–1707, 1999.

- [257] B. Van Koten and B. Luskin. Analysis of energy-based blended quasi-continuum approximations. *SIAM J. Numer. Anal.*, 49:2182–2209, 2011.
- [258] Z. Zhang, J. Zhang, Y. Ni, C. Wang, K. Jiang, and X. Ren. Multiscale simulation of surface defect influence in nanoindentation by the quasi-continuum method. In *The 1st International Electronic Conference on Crystals*, volume 7, page 1113. MDPI, 2018.
- [259] P. Engel. *Geometric Crystallography: An Axiomatic Introduction to Crystallography*. Springer Netherlands, 1986.
- [260] Rolph Ludwig Edward Schwarzenberger. Classification of crystal lattices. *Proc. Cambridge Phil. Soc.*, 72(3):325–349, 1972.
- [261] J. L. Ericksen. Nonlinear elasticity of diatomic crystals. *Int. J. Solids Struct.*, 6(7):951–957, 1970.
- [262] Jerald L. Ericksen. Loading devices and stability of equilibrium. In R. W. Dickey, editor, *Nonlinear Elasticity*, pages 161–173. Academic Press, New York, 1973.
- [263] J. L. Ericksen. Special topics in elastostatics. *Adv. Appl. Mech.*, 17:189–244, 1977.
- [264] J. L. Ericksen. Some phase transitions in crystals. *Arch. Ration. Mech. Anal.*, 73(2):99–124, 1980.
- [265] Jerald L. Ericksen. Weak martensitic transformations in bravais lattices. *Arch. Ration. Mech. Anal.*, 107(1):23–36, 1989.
- [266] I. Folkins. Functions of two-dimensional bravais lattices. *J. Math. Phys.*, 32(7):1965–1969, 1991.
- [267] Y. Gao, T. Yu, and Y. Wang. Phase transformation graph and transformation pathway engineering for shape memory alloys. *Shape Memory and Superelasticity*, 6(1):115–130, 2020.
- [268] G. Puglisi and L. Truskinovsky. Thermodynamics of rate-independent plasticity. *J. Mech. Phys. Solids*, 53(3):655–679, 2005.
- [269] H. C. Simpson and S. J. Spector. Necessary conditions at the boundary for minimizers in finite elasticity. In *Mechanics and Thermodynamics of Continua: A Collection of Papers Dedicated to BD Coleman on His Sixtieth Birthday*, pages 159–179. Springer Berlin Heidelberg, Berlin, Heidelberg, 1989.
- [270] Y. Grabovsky and L. Truskinovsky. Marginal material stability. *J. Nonlinear Sci.*, 23:891–969, 2013.
- [271] D. J. Steigmann, M. Bîrsan, and M. Shirani. Hyperelastic solids: Purely mechanical theory. In *Lecture Notes on the Theory of Plates and Shells: Classical and Modern Developments*, pages 61–76. Springer Nature Switzerland, Cham, 2023.
- [272] R. Maaß and P. M. Derlet. Micro-plasticity and recent insights from intermittent and small-scale plasticity. *Acta Mater.*, 143:338–363, 2018.
- [273] G. Sparks and R. Maaß. Nontrivial scaling exponents of dislocation avalanches in microplasticity. *Phys. Rev. Mater.*, 2(12):120601, 2018.
- [274] G. Sparks, Y. Cui, G. Po, Q. Rizzardi, J. Marian, and R. Maaß. Avalanche statistics and the intermittent-to-smooth transition in microplasticity. *Phys. Rev. Mater.*, 3(8):080601, 2019.
- [275] Q. Rizzardi, P. M. Derlet, and R. Maaß. Intermittent microplasticity in the presence of a complex microstructure. *Phys. Rev. Mater.*, 6(7):073602, 2022.
- [276] J. Duan, Y. J. Wang, L. H. Dai, and M. Q. Jiang. Elastic interactions of plastic events in strained amorphous solids before yield. *Phys. Rev. Mater.*, 7(1), 2023.

- [277] H. Bei, S. Shim, G. M. Pharr, and E. P. George. Effects of pre-strain on the compressive stress-strain response of mo-alloy single-crystal micropillars. *Acta Mater.*, 56(17):4762–4770, 2008.
- [278] D. Chrobak, N. Tymiak, A. Beaber, O. Ugurlu, William W. Gerberich, and R. Nowak. Deconfinement leads to changes in the nanoscale plasticity of silicon. *Nat. Nanotechnol.*, 6(8):480–484, 2011.
- [279] Z. Wang, Z. Shan, J. Li, J. Sun, and E. Ma. Pristine-to-pristine regime of plastic deformation in submicron-sized single crystal gold particles. *Acta Mater.*, 60(3):1368–1377, 2012.
- [280] Y. Cui, G. Po, and N. Ghoniem. Influence of loading control on strain bursts and dislocation avalanches at the nanometer and micrometer scale. *Phys. Rev. B*, 95(6):064103, 2017.
- [281] Julia R. Greer and Jeff Th M. De Hosson. Plasticity in small-sized metallic systems: Intrinsic versus extrinsic size effect. *Prog. Mater Sci.*, 56(6):654–724, 2011.
- [282] S. S. Brenner. Tensile strength of whiskers. *J. Appl. Phys.*, 27(12):1484–1491, 1956.
- [283] S. S. Brenner. Growth and properties of “whiskers”. *Science*, 128(3324):569–575, 1958.
- [284] A. Sharma, J. Hickman, N. Gazit, E. Rabkin, and Y. Mishin. Nickel nanoparticles set a new record of strength. *Nat. Commun.*, 9(1):4102, 2018.
- [285] D. Mordehai, O. David, and R. Kositski. Nucleation-Controlled plasticity of metallic nanowires and nanoparticles. *Adv. Mater.*, 30(41):e1706710, 2018.
- [286] E. T. Lilleodden and W. D. Nix. Microstructural length-scale effects in the nanoindentation behavior of thin gold films. *Acta Mater.*, 54(6):1583–1593, 2006.
- [287] S. G. Corcoran, R. J. Colton, E. T. Lilleodden, and W. W. Gerberich. Anomalous plastic deformation at surfaces: Nanoindentation of gold single crystals. *Phys. Rev. B Condens. Matter*, 55(24):R16057–R16060, 1997.
- [288] A. P. Sutton. Grain-boundary structure. *Int. Met. Rev.*, 29(1):377–404, 1984.
- [289] L. Priester. *Grain boundaries: from theory to engineering*. Springer Science & Business Media, 2012.
- [290] V. Randle. *The role of the coincidence site lattice in grain boundary engineering*. CRC Press, London, England, 2024.
- [291] H. Salmenjoki, L. Laurson, and Mikko J. Alava. Avalanche correlations and stress-strain curves in discrete dislocation plasticity. *Phys. Rev. Mater.*, 5:073601, 2021.
- [292] M. Ovaska, L. Laurson, and Mikko J. Alava. Quenched pinning and collective dislocation dynamics. *Sci. Rep.*, 5:10580, 2015.
- [293] X. Zhang, X. Zhang, Q. Li, and F. Shang. Strain avalanches in microsized single crystals: Avalanche size predicted by a continuum crystal plasticity model. *Chin. Physics Lett.*, 33(10):106401, 2016.
- [294] Céline Ruscher and Jörg Rottler. Residual stress distributions in athermally deformed amorphous solids from atomistic simulations. *arXiv [cond-mat.dis-nn]*, 2019.
- [295] B. Tyukodi, D. Vandembroucq, and Craig E. Maloney. Avalanches, thresholds, and diffusion in mesoscale amorphous plasticity. *Phys. Rev. E*, 100(4-1):043003, 2019.
- [296] E. E. Ferrero and E. A. Jagla. Criticality in elastoplastic models of amorphous solids with stress-dependent yielding rates. *Soft Matter*, 15(44):9041–9055, 2019.
- [297] S. Franz and S. Spigler. Mean-field avalanches in jammed spheres. *Phys. Rev. E*, 95(2-1):022139, 2017.

- [298] M. Müller and M. Wyart. Marginal stability in structural, spin, and electron glasses. *Annu. Rev. Condens. Matter Phys.*, 6:177, 2015.
- [299] L. Berthier, G. Biroli, P. Charbonneau, Eric I. Corwin, S. Franz, and F. Zamponi. Gardner physics in amorphous solids and beyond. *J. Chem. Phys.*, 151(1):010901, 2019.
- [300] R. C. Dennis and E. I. Corwin. Jamming energy landscape is hierarchical and ultrametric. *Phys. Rev. Lett.*, 124(7):078002, 2020.
- [301] Ferenc Pázmándi, Gergely Zaránd, and Gergely T. Zimányi. Self-Organized criticality in the hysteresis of the Sherrington-Kirkpatrick model. *Phys. Rev. Lett.*, 83(5):1034–1037, 1999.
- [302] P.L. Doussal, Markus Müller, and Kay Jörg Wiese. Equilibrium avalanches in spin glasses. *Phys. Rev. B Condens. Matter Mater. Phys.*, 85(21), 2012.
- [303] I. Regev and T. Lookman. The irreversibility transition in amorphous solids under periodic shear. In *Understanding Complex Systems*, Understanding complex systems, pages 227–259. Springer International Publishing, Cham, 2017.
- [304] I. Regev and T. Lookman. Critical diffusivity in the reversibility–irreversibility transition of amorphous solids under oscillatory shear. *Journal of Physics: Condensed Matter*, 31, January 2017.
- [305] I. Regev, I. Attia, K. Dahmen, S. Sastry, and Muhittin M. Topology of the energy landscape of sheared amorphous solids and the irreversibility transition. *Phys. Rev. E.*, 103(6-1):062614, June 2021.
- [306] G. Grinstein. Generic scale invariance and self-organized criticality. In *Scale Invariance, Interfaces, and Non-Equilibrium Dynamics*, pages 261–293. Springer US, Boston, MA, 1995.
- [307] A. Zippelius, M. Fuchs, A. Rosso, James P. Sethna, and M. Wyart. Emergent dynamics in glasses and disordered systems: Correlations and avalanches. In *Spin Glass Theory and Far Beyond*, pages 277–305. WORLD SCIENTIFIC, 2023.
- [308] P. Charbonneau, E. Marinari, G. Parisi, F. Ricci-tersegno, G. Sicuro, F. Zamponi, and Mezard M. (Eds.). *Spin glass theory and far beyond: replica symmetry breaking after 40 years*. World Scientific, 2023.
- [309] N. Oyama, H. Mizuno, and A. Ikeda. Shear-induced criticality in glasses shares qualitative similarities with the gardner phase. *Soft Matter*, 19(32):6074–6087, August 2023.
- [310] Y. Xing, Y. Yuan, H. Yuan, S. Zhang, Z. Zeng, X. Zheng, C. Xia, and Y. Wang. Origin of the critical state in sheared granular materials. *Nat. Phys.*, 20(4):646–652, 2024.
- [311] S. Rossi, G. Biroli, M. Ozawa, G. Tarjus, and F. Zamponi. Finite-disorder critical point in the yielding transition of elastoplastic models. *Phys. Rev. Lett.*, 129:228002, 2022.
- [312] D. Fernández Castellanos, S. Roux, and S. Patinet. Insights from the quantitative calibration of an elastoplastic model from a lennard-jones atomic glass. *C. R. Phys.*, 22(S3):135–162, 2021.
- [313] C. Ruscher and J. Rottler. Correlations in the shear flow of athermal amorphous solids: a principal component analysis. *J. Stat. Mech.*, 2019(9):093303, 2019.
- [314] N. Oyama, T. Kawasaki, K. Kim, and H. Mizuno. Scale separation of shear-induced criticality in glasses. *Phys. Rev. Lett.*, 132(14):148201, 2024.
- [315] P. Charbonneau, J. Kurchan, G. Parisi, P. Urbani, and F. Zamponi. Fractal free energy landscapes in structural glasses. *Nat. Commun.*, 5(1):3725, 2014.

- [316] Y. Fu, Y. Jin, D. Pan, and I. Procaccia. Long-range angular correlations of particle displacements at a plastic-to-elastic transition in jammed amorphous solids. *Phys. Rev. Lett.*, 134(17):178201, 2025.
- [317] A. Onuki. Plastic flow in two-dimensional solids. *Phys. Rev. E Stat. Nonlin. Soft Matter Phys.*, 68(6 Pt 1):061502, 2003.
- [318] A. Carpio and L. L. Bonilla. Edge dislocations in crystal structures considered as traveling waves in discrete models. *Phys. Rev. Lett.*, 90(13):135502, 2003.
- [319] L. L. Bonilla, A. Carpio, and I. Plans. Dislocations in cubic crystals described by discrete models. *Physica A: Statistical Mechanics and its Applications*, 376:361–377, 2007.
- [320] A. Onuki, A. Furukawa, and A. Minami. Sheared solid materials. *Pramana*, 64(5):661–677, 2005.
- [321] A. Minami and A. Onuki. Nonlinear elasticity theory of dislocation formation and composition change in binary alloys in three dimensions. *Acta Mater.*, 55(7):2375–2384, 2007.
- [322] P-. A. Geslin, B. Appolaire, and A. Finel. Investigation of coherency loss by prismatic punching with a nonlinear elastic model. *Acta Mater.*, 71:80–88, June 2014.
- [323] K. Bertram Broberg. *Cracks and Fracture*. Elsevier, 1999.
- [324] E. Hans J. Herrmann and S. Roux. *Statistical Models for the Fracture of Disordered Media*. Elsevier, 1990.
- [325] M. F. Kanninen and C. L. Popelar. *Advanced fracture mechanics*. Oxford University Press, 1985.
- [326] L. Truskinovsky. Fracture as a phase transition. In R. Batra and B. M. F., editors, *Contemporary research in the mechanics and mathematics of materials*, pages 322–332. CIMNE, Barcelona, 1996.
- [327] N. Triantafyllidis and E. Aifantis. A gradient approach to localization of deformation. i. hyperelastic materials. *J. Elast.*, 16(3):225–237, 1986.
- [328] T. Belytschko, H. Chen, J. Xu, and G. Zi. Dynamic crack propagation based on loss of hyperbolicity and a new discontinuous enrichment. *Int J Numer Meth Engng*, 58(12):1873–1905, 2003.
- [329] I. Baker and P. R. Munroe. Improving intermetallic ductility and toughness. *Jom-j. Min. Met. Mat. S.*, 40(2):28–31, 1988.
- [330] J. G. Swadener, M. I. Baskes, and M. Nastasi. Molecular dynamics simulation of brittle fracture in silicon. *Phys. Rev. Lett.*, 89(8):085503, 2002.
- [331] A. G. Evans and K. T. Faber. Toughening of ceramics by circumferential microcracking. *J. Am. Ceram. Soc.*, 64(7):394–398, 1981.
- [332] K. T. Faber, T. Iwagoshi, and A. Ghosh. Toughening by stress-induced microcracking in two-phase ceramics. *J. Am. Ceram. Soc.*, 71(9):C–399, 1988.
- [333] B. Budiansky, J. W. Hutchinson, and J. C. Lambropoulos. Continuum theory of dilatant transformation toughening in ceramics. *Int. J. Solids Struct.*, 19(4):337–355, 1983.
- [334] D. J. Green. *Transformation Toughening Of Ceramics*. CRC Press, 1st edition edition, 2018.
- [335] G. Del Piero and L. Truskinovsky. Macro- and micro-cracking in one-dimensional elasticity. *Int. J. Solids Struct.*, 38(6):1135–1148, 2001.
- [336] A. Cherkaev and L. Slepyan. Waiting element structures and stability under extension. *Int. J. Damage Mech.*, 4(1):58–82, 1995.

- [337] S. M. Wiederhorn. Brittle fracture and toughening mechanisms in ceramics. *Annu. Rev. Mater. Sci.*, 14(1):373–403, 1984.
- [338] T. J. Davies and A. A. Ogwu. A possible route to improving the ductility of brittle intermetallic compounds. *J Alloys Compd.*, 228(1):105–111, 1995.
- [339] T. Yang, Y. L. Zhao, W. H. Liu, J. H. Zhu, J. J. Kai, and C. T. Liu. Ductilizing brittle high-entropy alloys via tailoring valence electron concentrations of precipitates by controlled elemental partitioning. *Mater. Res. Lett.*, 6(10):600–606, 2018.
- [340] H. Borja da Rocha and L. Truskinovsky. Rigidity-Controlled crossover: From spinodal to critical failure. *Phys. Rev. Lett.*, 124(1):015501, 2020.
- [341] R. Daniel, M. Meindlhumer, W. Baumegger, J. Zalesak, B. Sartory, M. Burghammer, et al. Grain boundary design of thin films: Using tilted brittle interfaces for multiple crack deflection toughening. *Acta Mater.*, 122:130–137, 2017.
- [342] M. T. Ebrahimi, D. S. Balint, A. P. Sutton, and D. Dini. A discrete crack dynamics model of toughening in brittle polycrystalline material by crack deflection. *Eng. Fract. Mech.*, 214:95–111, 2019.
- [343] H. Wu and G. Fan. An overview of tailoring strain delocalization for strength-ductility synergy. *Prog. Mater. Sci.*, 113:100675, 2020.
- [344] F. Liang, B. Zhang, Y. Yong, X. M. Luo, and G. P. Zhang. Enhanced strain delocalization through formation of dispersive micro shear bands in laminated ni. *Int. J. Plast.*, 132:102745, 2020.
- [345] K. Radi, D. Jauffres, S. Deville, and C. L. Martin. Strength and toughness trade-off optimization of nacre-like ceramic composites. *Composites Part B*, 183:107699, 2020.
- [346] M. M. Driscoll, B. G. G. Chen, T. H. Beuman, S. Ulrich, S. R. Nagel, and V. Vitelli. The role of rigidity in controlling material failure. *Proc. Natl. Acad. Sci.*, 113(39):10813–10817, 2016.
- [347] G. A. Buxton and N. Clarke. “bending to stretching” transition in disordered networks. *Phys. Rev. Lett.*, 98(23):238103, 2007.
- [348] C. P. Broedersz and F. C. MacKintosh. Modeling semiflexible polymer networks. *Rev. Mod. Phys.*, 86:995–1036, 2014.
- [349] A. A. Zadpoor. Mechanical meta-materials. *Mater. Horiz.*, 3(5):371–381, 2016.
- [350] J. J. Alibert, P. Seppecher, and F. Dell’Isola. Truss modular beams with deformation energy depending on higher displacement gradients. *Math. Mech. Solids*, 8(1):51–73, 2003.
- [351] E. van der Giessen. Materials physics: Bending maxwell’s rule. *Nat. Phys.*, 7(12):923–924, 2011.
- [352] P. Franciosi, M. Spagnuolo, and O. U. Salman. Mean green operators of deformable fiber networks embedded in a compliant matrix and property estimates. *Continuum Mech. Thermodyn.*, 31(1):101–132, 2019.
- [353] J. C. Maxwell. L. on the calculation of the equilibrium and stiffness of frames. *The London, Edinburgh, and Dublin Philosophical Magazine and Journal of Science*, 27(182):294–299, 1864.
- [354] C. R. Calladine. Buckminster fuller’s “tensegrity” structures and clerk maxwell’s rules for the construction of stiff frames. *Int. J. Solids Struct.*, 14(2):161–172, 1978.
- [355] M. Schenk and S. D. Guest. On zero stiffness. *Proc. Inst. Mech. Eng. Part C*, 228(10):1701–1714, 2014.
- [356] C. Pideri and P. Seppecher. A second gradient material resulting from the homogenization of an heterogeneous linear elastic medium. *Continuum Mech. Thermodyn.*, 9(5), 1997.

- [357] K. D. Cherednichenko, V. P. Smyshlyaev, and V. V. Zhikov. Non-local homogenized limits for composite media with highly anisotropic periodic fibres. *Proc. R. Soc. Edinburgh Sect. A Math. Mathematics*, 136(01), 2006.
- [358] M. Camar-Eddine and P. Seppecher. Determination of the closure of the set of elasticity functionals. *Arch. Ration. Mech. Anal.*, 170(3):211–245, 2003.
- [359] C. Boutin, J. Soubestre, M. S. Dietz, and C. Taylor. Experimental evidence of the high-gradient behaviour of fiber reinforced materials. *Eur. J. Mech.-A/Solids*, 42, 2013.
- [360] M. Bacca, D. Bigoni, F. Dal Corso, and D. Veber. Mindlin second-gradient elastic properties from dilute two-phase cauchy-elastic composites. part i: Closed form expression for the effective higher-order constitutive tensor. *Int. J. Solids Struct.*, 50(24):4010–4019, 2013.
- [361] L. Truskinovsky and G. Zanzotto. Ericksen’s bar revisited : Energy wiggles. *J. Mech. Phys. Solids*, 44(8):1371–1408, 1996.
- [362] L. Golubović and T. C. Lubensky. Nonlinear elasticity of amorphous solids. *Phys. Rev. Lett.*, 63(10):1082, 1989.
- [363] V. I. Marconi and E. A. Jagla. Diffuse interface approach to brittle fracture. *Phys. Rev. E*, 71:036110, 2005.
- [364] N. Triantafyllidis and S. Bardenhagen. On higher order gradient continuum theories in 1-d nonlinear elasticity. derivation from and comparison to the corresponding discrete models. *J. Elast.*, 33(3):259–293, 1993.
- [365] L. Placidi. A variational approach for a nonlinear 1-dimensional second gradient continuum damage model. *Continuum Mech. Thermodyn.*, 27:623–638, 2015.
- [366] D. T. Le, J. J. Marigo, C. Maurini, and S. Vidoli. Strain-gradient vs damage-gradient regularizations of softening damage models. *Comput Methods Appl Mech Eng*, 340:424–450, 2018.
- [367] L. Fokoua, S. Conti, and M. Ortiz. Optimal scaling in solids undergoing ductile fracture by void sheet formation. *Arch. Ration. Mech. Anal.*, 212(1):331–357, 2014.
- [368] L. Fokoua, S. Conti, and M. Ortiz. Optimal scaling laws for ductile fracture derived from strain-gradient microplasticity. *J. Mech. Phys. Solids*, 62:295–311, 2014.
- [369] L. Zhang, S. P. Lake, V. H. Barocas, M. S. Shephard, and R. C. Picu. Cross-linked fiber network embedded in an elastic matrix. *Soft Matter*, 9:6398–6405, 2013.
- [370] X. Ren and L. Truskinovsky. Finite scale microstructures in nonlocal elasticity. *J. Elast.*, 59(1-3):319–355, 2000.
- [371] T. F. C. Chan and H. B. Keller. Arc-Length continuation and multigrid techniques for nonlinear elliptic eigenvalue problems. *SIAM J Sci and Stat Comput*, 3(2):173–194, 1982.
- [372] P. Rosakis, T. J. Healey, and U. Alyanak. The inverse-deformation approach to fracture. *J. Mech. Phys. Solids*, 150:104352, 2021.
- [373] M. Charlotte and L. Truskinovsky. Linear elastic chain with a hyper-pre-stress. *J. Mech. Phys. Solids*, 50(2):217–251, 2002.
- [374] W. A. Curtin, B. K. Ahn, and N. Takeda. Modeling brittle and tough stress-strain behavior in unidirectional ceramic matrix composites. *Acta Mater.*, 46(10):3409–3420, 1998.
- [375] L. Truskinovsky. Fracture as a phase transition, in “contemporary research in the mechanics and mathematics of materials,” CIMNE, barcelona,(1996), 322–332. *Received August*, 2010.

- [376] A. Braides, G. D. Maso, and A. Garroni. Variational formulation of softening phenomena in fracture mechanics: The One-Dimensional case. *Arch. Ration. Mech. Anal.*, 146(1):23–58, 1999.
- [377] A. Braides and L. Truskinovsky. Asymptotic expansions by Γ -convergence. *Continuum. Mech. Thermodyn.*, 20(1):21–62, 2008.
- [378] X. Blanc, C. Le Bris, and P. L. Lions. From molecular models to continuum mechanics. *Arch. Ration. Mech. Anal.*, 164(4):341–381, 2002.
- [379] M. Charlotte and L. Truskinovsky. Towards multi-scale continuum elasticity theory. *Continuum. Mech. Thermodyn.*, 20(3):133–161, 2008.
- [380] A. E. Lifshits and G. L. Rybnikov. Dissipative structures and couette flow of a non-newtonian fluid. In *Doklady Akademii Nauk*, volume 281, pages 1088–1093, 1985.
- [381] A. E. Lifshitz and G. L. Rybnikov. Dissipative structures and couette flow in a non-newtonian fluid. *Soviet Physics Doklady*, 20:275, 1985.
- [382] D. Dellwo, H. B. Keller, B. J. Matkowsky, and E. L. Reiss. On the birth of isolas. *SIAM J. Appl. Math.*, 42(5), 1982.
- [383] M. Golubitsky and D. G. Schaeffer. A brief introduction to the central ideas of the theory. In M. Golubitsky and D. G. Schaeffer, editors, *Singularities and Groups in Bifurcation Theory: Volume I*, pages 1–50. Springer New York, New York, NY, 1985.
- [384] T. J. Healey, Q. Li, and R. B. Cheng. Wrinkling behavior of highly stretched rectangular elastic films via parametric global bifurcation. *J. Nonlinear Sci.*, 23(5):777–805, 2013.
- [385] L. Truskinovsky and G. Zanzotto. Finite-scale microstructures and metastability in one-dimensional elasticity. *Meccanica*, 30(5):577–589, 1995.
- [386] A. Novick-Cohen and L. A. Segel. Nonlinear aspects of the Cahn-Hilliard equation. *Physica D*, 10(3):277–298, 1984.
- [387] E. J. Doedel, A. R. Champneys, F. Dercole, T. Fairgrieve, Y. Kuznetsov, B. Oldeman, et al. *AUTO-07P: Continuation and Bifurcation Software for Ordinary Differential Equations*, 2008.
- [388] G. R. Liu and S. S. Quek. *The Finite Element Method: A Practical Course*. Butterworth-Heinemann, 2013.
- [389] B. Grimstad et al. SPLINTER: a library for multivariate function approximation with splines. <http://github.com/bgrimstad/splinter>, 2015.
- [390] J. M. van Doorn, L. Lageschaar, J. Sprakel, and J. van der Gucht. Criticality and mechanical enhancement in composite fiber networks. *Phys. Rev. E*, 95(4-1):042503, 2017.
- [391] D. H. Cortes and D. M. Elliott. Extra-fibrillar matrix mechanics of annulus fibrosus in tension and compression. *Biomech Model Mechanobiol*, 11(6):781–790, 2012.
- [392] B. Lynch, S. Bancelin, C. Bonod-Bidaud, J. B. Gueusquin, F. Ruggiero, M. C. Schanne-Klein, et al. A novel microstructural interpretation for the biomechanics of mouse skin derived from multiscale characterization. *Acta Biomater.*, 50:302–311, 2017.
- [393] A. Vainchtein, T. J. Healey, and P. Rosakis. Bifurcation and metastability in a new one-dimensional model for martensitic phase transitions. *CMAME*, 170(3–4):407–421, 1999.
- [394] X. Ren and L. Truskinovsky. Finite scale microstructures in nonlocal elasticity. *J. Elast.*, 59(1-3):319–355, 2000.

- [395] B. N. Belintsev, M. A. Livshits, and M. V. Volkenstein. Pattern formation in systems with nonlocal interactions. *Z. Phys. B: Condens. Matter*, 44(4):345–351, 1981.
- [396] K. Toko and K. Yamafuji. Bifurcation characteristics and spatial patterns in an integro-differential equation. *Physica D*, 44(3):459–470, 1990.
- [397] Q. Li and Timothy J. Healey. Stability boundaries for wrinkling in highly stretched elastic sheets. *J. Mech. Phys. Solids*, 97:260–274, 2016.
- [398] K. Pham, J. J. Marigo, and C. Maurini. The issues of the uniqueness and the stability of the homogeneous response in uniaxial tests with gradient damage models. *J. Mech. Phys. Solids*, 59(6):1163–1190, 2011.
- [399] Y. P. Pellegrini, C. Denoual, and L. Truskinovsky. Phase-field modeling of nonlinear material behavior. In K. Hackl, editor, *IUTAM Symposium on Variational Concepts with Applications to the Mechanics of Materials*, volume 21 of *IUTAM Bookseries*, pages 209–220. Springer Netherlands, 2010.
- [400] Satish Balay, Shrirang Abhyankar, Mark F. Adams, Jed Brown, Peter Brune, Kris Buschelman, Lisandro Dalcin, Alp Dener, Victor Eijkhout, William D. Gropp, Dmitry Karpeyev, Dinesh Kaushik, Matthew G. Knepley, Dave A. May, Lois Curfman McInnes, Richard Tran Mills, Todd Munson, Karl Rupp, Patrick Sanan, Barry F. Smith, Stefano Zampini, Hong Zhang, and Hong Zhang. PETSc users manual. Technical Report ANL-95/11 - Revision 3.15, Argonne National Laboratory, 2021. URL <https://www.mcs.anl.gov/petsc>.
- [401] J. J. Moreau. Décomposition orthogonale d'un espace hilbertien selon deux cônes mutuellement polaires. *Comptes rendus hebdomadaires des séances de l'Académie des sciences*, 255:238–240, 1962.
- [402] A. Pinto da Costa and A. Seeger. Cone-constrained eigenvalue problems: theory and algorithms. *Comput. Optim. Appl.*, 45(1):25–57, January 2010.
- [403] O. U. Terzi, M. M .and Salman, D. Faurie, and A. A. León Baldelli. Navigating local minima and bifurcations in brittle thin film systems with irreversible damage. *Comput. Methods Appl. Mech. Eng.*, 445(118201):118201, October 2025.
- [404] A. Shekhawat, S. Zapperi, and J. P. Sethna. From damage percolation to crack nucleation through finite size criticality. *Phys. Rev. Lett.*, 110(18):185505, 2013.
- [405] A. Rinaldi. Bottom-up modeling of damage in heterogeneous quasi-brittle solids. *Continuum. Mech. Thermodyn.*, 25(2-4):359–373, 2013.
- [406] O. U. Salman, G. Vitale, and L. Truskinovsky. Continuum theory of bending-to-stretching transition. *Phys. Rev. E*, 100(5-1):051001, 2019.